Lurking in the Shadows: Wide-Separation Gas Giants as Tracers of Planet Formation

Thesis by
Marta Levesque Bryan

In Partial Fulfillment of the Requirements for the
Degree of
Doctor of Philosophy

CALIFORNIA INSTITUTE OF TECHNOLOGY
Pasadena, California

2018
Defended May 1, 2018

Marta Levesque Bryan
ORCID: [0000-0002-6076-5967]

ACKNOWLEDGEMENTS

First and foremost I would like to thank Heather Knutson, who I had the great privilege of working with as my thesis advisor. Her encouragement, guidance, and perspective helped me navigate many a challenging problem, and my conversations with her were a consistent source of positivity and learning throughout my time at Caltech. I leave graduate school a better scientist and person for having her as a role model. Heather fostered a wonderfully positive and supportive environment for her students, giving us the space to explore and grow - I could not have asked for a better advisor or research experience.

I would also like to thank Konstantin Batygin for enthusiastic and illuminating discussions that always left me more excited to explore the result at hand. Thank you as well to Dimitri Mawet for providing both expertise and contagious optimism for some of my latest direct imaging endeavors. Thank you to the rest of my thesis committee, namely Geoff Blake, Evan Kirby, and Chuck Steidel for their support, helpful conversations, and insightful questions.

I am grateful to have had the opportunity to collaborate with Brendan Bowler. His talk at Caltech my second year of graduate school introduced me to an unexpected population of massive wide-separation planetary-mass companions, and lead to a long-running collaboration from which several of my thesis projects were born. I greatly appreciate his guidance on my first foray into direct imaging, as well as his continued support and perspective.

I would like to thank other collaborators who made important contributions to the science presented in this thesis, including Henry Ngo, BJ Fulton, Bjorn Benneke, Sasha Hinkley, Adam Kraus, and Eve Lee.

This thesis was also made possible by a number of extraordinary mentors who I encountered as an undergraduate. I would like to thank David Charbonneau, who I had the great fortune of meeting my first week of freshman year and who taught not one but five semesters of classes that I took. I am grateful for his invaluable support over the past decade, and for introducing me to exoplanets in the first place. Thank you also to David Latham for encouraging me and guiding me through my first two exoplanet research projects, and for helping me realize that I had found my research home base. I also want to thank Don Hall and John Kovac for providing mentorship and positive research experiences that encouraged me to continue on in astronomy.

Thank you to Bekki Dawson and Meredith Hughes for being my official women in science graduate student mentors while I was an undergrad, and for continuing to provide measured advice and perspective throughout my time at Caltech. Thank you also to Courtney Dressing and Leslie Rogers for their advice and encouragement.

I would also like to thank friends who have taken this journey with me. In particular, I would like to thank Michael Eastwood for his invaluable support through it all. Thank you also to Becky Jensen-Clem for being a wonderful officemate, friend, and potential twin. Finally, thank you to Anna Ho for being an amazing coffee shop work partner, yoga buddy, and all around friend.

A special thank you to my mom for her love and support since the very beginning, and for providing me with the opportunities and encouragement to get where I am today.

ABSTRACT

Over the past two decades, thousands of planets with an extraordinary diversity of properties have been discovered orbiting nearby stars. Many of these exoplanetary systems challenge our narrative for how planets form and evolve, motivating the search for observational clues to the underlying mechanisms that led to this diversity. In this quest, gas giant analogs to our own Jupiter and Saturn immediately stand out as the most visible relics of the planet formation process. They are products of their birth environment, with properties such as atmospheric and interior compositions, masses, and formation locations sculpted by protoplanetary disk and host star properties. They also actively shape their surroundings; early in their lifetimes, gas giants can alter the structure of the gas disk from which additional planetary bodies may coalesce and affect the transport of rocky and icy materials to the inner disk. After the gas has dissipated these same behemoths can push smaller planets around, causing them to migrate or even ejecting them from the system. Thus to explain the observed diversity of exoplanet systems, we must first understand how gas giant planets form and evolve.

This thesis presents four studies that harness multiple observational techniques to explore this question of how gas giant planets outside our solar system form and evolve. In the first study, we searched for massive, long-period companions to 123 known exoplanetary systems using the radial velocity method. We found 20 systems with statistically significant RV trends, and used these data to produce the first statistical analysis of the frequency of outer gas giant companions in systems hosting inner gas giant planets. These companions appear to be common, with an occurrence rate of 52±5% for planets between 1 - 20 M_{Jup} and 5 - 20 AU. We also found that systems hosting hot Jupiters are more likely than warm and cold Jupiters to have an outer gas giant companion, consistent with the predictions of dynamical migration models. Finally, we found that planets between 0.1-5 AU in multi-body systems have higher average eccentricities than isolated planets, suggesting that dynamical interactions among gas giant planets play an important role in the evolution of most planetary systems.

The second study explores the formation histories of wide-separation planetary-mass companions. One possible solution is to argue that these planets did not form in situ, but were instead scattered outward from their original formation locations via interactions with another body in the system. We carried out a near-infrared

imaging survey using NIRC2 at Keck to search for close-in substellar companions to a sample of seven systems with confirmed planetary-mass companions on wide orbits. While we initially identified eight candidate companions, a second epoch of astrometry confirmed all eight to be background objects. From these new epochs of astrometry we also found that two of the previously confirmed companions showed evidence for orbital motion, which we used to constrain their orbital eccentricities to low to moderate values, contradicting predictions from scattering simulations. Taken together, these two pieces of evidence present a compelling argument against scattering as the explanation for the wide orbits of these planetary-mass companions.

In the third study, we used near-IR high-resolution spectroscopy to measure rotational line broadening of three young (2-300 Myr) planetary-mass companions and combined these measurements with published rotation rates for two additional companions to provide the first look at the spin distribution of these objects. We compared this distribution to complementary rotation rate measurements for six brown dwarfs with masses < 20 M_{Jup} (three of which we measured), and found that these spin distributions are indistinguishable. This suggests either that these two populations formed via the same mechanism, or that processes regulating rotation rates are largely independent of formation history. We also found that the rotation rates for both populations are well below their break-up velocities and do not evolve significantly during the first few hundred million years after the end of accretion. This suggests that rotation rates are set early in a planetary-mass object's lifetime, possibly by interactions with a circumplanetary disk.

In the final study, we use radial velocity observations to search for massive, long-period gas giant companions in 65 systems hosting inner super-Earth ($1 - 4$ $R_\oplus$, $1 - 10$ $M_\oplus$) planets in order to constrain formation and migration scenarios for this population. We find 10 systems with statistically significant trends indicating the presence of an outer companion. We quantify our sensitivity to the presence of long period companions in these system by fitting the sample with a power law distribution and find an estimated occurrence rate of $39\pm7\%$ for companions between $0.5 - 20$ M_{Jup} and $1 - 20$ AU. A quantitative comparison to previous determinations of the frequency of Jupiter analogs indicates that the occurrence rate of Jupiter analogs in super-Earth systems appears to be higher than the occurrence rate of gas giant planets around field stars. We conclude that the presence of outer gas giant planets does not suppress the formation of inner super-Earths, and may instead facilitate their formation.

PUBLISHED CONTENT AND CONTRIBUTIONS

Bryan, M. L., B. Benneke, et al. (2018). "Constraints on the spin evolution of young planetary-mass companions". In: *Nature Astronomy* 2, pp. 138–144. DOI: 10.1038/s41550-017-0325-8. arXiv: 1712.00457 [astro-ph.EP].
M.L.B. conceived the project with input from coauthors, wrote observing proposals to get the data, led the observational program, reduced the data, analyzed the results, and wrote the paper.

Bryan, M. L., B. P. Bowler, et al. (2016). "Searching for Scatterers: High-Contrast Imaging of Young Stars Hosting Wide-Separation Planetary-Mass Companions". In: *The Astrophysical Journal* 827, 100, p. 100. DOI: 10.3847/0004-637X/827/2/100. arXiv: 1606.06744 [astro-ph.EP].
M.L.B. contributed to the observations, reduced the data, analyzed the results, and wrote the paper.

Bryan, M. L., H. A. Knutson, et al. (2016). "Statistics of Long Period Gas Giant Planets in Known Planetary Systems". In: *The Astrophysical Journal* 821, 89, p. 89. DOI: 10.3847/0004-637X/821/2/89. arXiv: 1601.07595 [astro-ph.EP].
M.L.B. analyzed the data, led the statistical analysis, and wrote the paper.

TABLE OF CONTENTS

LIST OF ILLUSTRATIONS

LIST OF TABLES

Chapter 1

INTRODUCTION

Over the past two decades, over 3,700 planets with an extraordinary diversity of properties have been discovered orbiting nearby stars (Fig. 1.1). Many of these exoplanetary systems challenge our narrative for how planets form and evolve, motivating the search for observational clues to the underlying mechanisms that led to this diversity. In this quest, gas giant analogs to our own Jupiter and Saturn immediately stand out as the most visible relics of the planet formation process. They are products of their birth environment, with properties such as atmospheric and interior compositions, masses, and formation locations sculpted by protoplanetary disk and host star properties. They also actively shape their surroundings; early in their lifetimes, gas giants can alter the structure of the gas disk from which additional planetary bodies may coalesce and affect the transport of rocky and icy materials to the inner disk. After the gas has dissipated these same behemoths can push smaller planets around, causing them to migrate or even ejecting them from the system. Thus to explain the observed diversity of exoplanet systems, we must first understand how gas giant planets form and evolve.

This thesis presents four studies that harness multiple observational techniques to explore this question of how gas giant planets outside our solar system form and evolve. One powerful approach to exploring the origins of gas giant planets is to study a population that is difficult to explain with conventional formation and migration models. Over the past decade, direct imaging searches for self-luminous giant planets, which utilize adaptive optics to search for faint objects located close to their host stars, have uncovered an unexpected population of young planetary-mass companions on extremely wide orbits (separations >50 AU) (Bowler, 2016). The masses of these companions straddle the deuterium burning limit, throwing into question whether these objects are high mass planets, or low mass brown dwarfs. To date nearly two dozen planetary-mass companions at large separations have been discovered, most of which are typically in their infancy, with ages less than 10 Myr old. This selection for extreme youth is simply because the younger the system, the brighter the planet, and the easier it is to detect. There are currently three competing models for how to form these objects, namely core accretion (Helled et al., 2014), disk instability (Helled et al., 2014), and direct collapse from molecular cloud

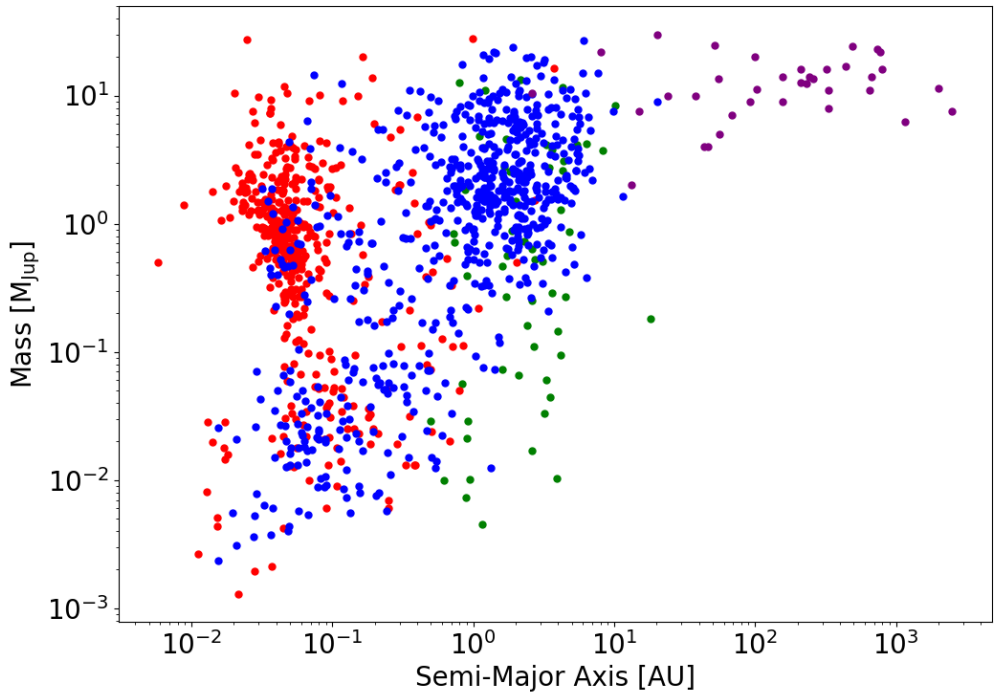

Figure 1.1: Current census of confirmed exoplanets with measured masses and semi-major axes as of April 2018. The colors represent different detection techniques; blue planets were discovered using the radial velocity (RV) method, red planets were discovered using the transit method, purple planets were discovered using the direct imaging method, and green points were discovered using the microlensing method.

fragmentation (Chabrier et al., 2014). While each of these mechanisms has its own significant hurdles to overcome in accounting for this population, these challenges can be succinctly summed up as: how can you form something very massive, very far away, and very quickly?

Another promising avenue is to consider gas giants as the architects of inner solar systems. Current transit surveys are only sensitive to planets as far out as Venus and Earth (Dressing and Charbonneau, 2015), while long-term radial velocity (RV) monitoring is beginning to detect Jupiter analogs around other stars but often misses smaller planets on interior orbits. This means that we are effectively trying to build narratives for exoplanetary systems where we are missing large pieces of the picture. It is difficult to imagine telling a story for the formation of the solar system, for instance, without knowing about both the inner rocky planets and the outer gas and ice giant planets. One practical solution to this problem is to search for the presence of outer gas giant planets in known planetary systems, and then compare the properties of systems that host gas giant planets to those that do not. Differences

in inner planet masses, separations, multiplicities, and orbital properties can paint a picture of the effect these gas giants have on the inner architectures of planetary systems. However, determining which stellar systems host long period gas giants is not trivial. While it has been suggested that gas giant planets preferentially form beyond the water ice line (the radius at which water freezes out) (Pollack et al., 1996; Alibert et al., 2005), current planet detection techniques such as the transit and RV methods have limited sensitivity to planets at these wide distances.

This thesis utilizes the radial velocity (RV) and direct imaging techniques to characterize the statistical properties of long-period gas giant planets. These observations allow us to explore competing explanations for several populations of exoplanets that challenge conventional formation models, including hot Jupiters, longer period gas giants on eccentric orbits, and short-period super-Earths. Hot Jupiters are the first class of exoplanets to be discovered simply because they are the easiest to detect. They are massive gas giant planets ($M > 0.5\ M_{Jup}$) orbiting very close to their host stars ($P_{orbit} < 10$ days). One of the longest remaining open questions in the field of exoplanets is: How do hot Jupiters form? Can a gas giant planet form so close to its host star, and if not, how did it migrate inwards? For years after hot Jupiters were first discovered, it was assumed that they formed beyond the water ice line ($\sim$ few AU) and migrated inwards to their present day locations (Pollack et al., 1996; Rafikov, 2006; Alibert et al., 2005; Lin, P. Bodenheimer, and Richardson, 1996; Wu and Murray, 2003; Beaugé and Nesvorný, 2012). However, more recent work suggests that hot Jupiters can form in situ (Batygin, P. H. Bodenheimer, and G. P. Laughlin, 2016). At present, whether or not hot Jupiters formed in situ or beyond the ice line and how if at all they migrated inwards remain open questions. More recently, Knutson et al. (2014) found that approximately half of all hot Jupiter systems have an outer gas giant companion. This finding raises the questions: Do hot Jupiters have more gas giant companions than other kinds of inner solar systems? Can we show that these companions directly impact the formation and evolution of hot Jupiters? By looking for outer gas giant companions in hot Jupiter systems and other systems hosting different populations of gas giants we can explore these questions.

Another population of planets that challenge current understandings of how planets form and evolve are gas giant planets at several AU that have eccentric orbits. The default expectation is that planets should have circular orbits, because planets are thought to form gently in a protoplanetary disk, and the gas in the disk will act

to damp out orbital eccentricity or inclination as these planets form. However, if there are dynamical interactions between planets in the same system after the gas dissipates, we expect these interactions to pump up the planets' orbital eccentricities (Chatterjee et al., 2008). While this population of long-period gas giant planets have eccentric orbits, they are in apparently single planet systems, leading to the question where did their eccentricities come from? One way to test these trends directly is to look for outer planetary companions in a large sample of systems, assessing whether these companions are associated with a larger orbital eccentricity for the inner planet.

The final population of planets that we targeted are super-Earths. Super-Earths are planets with masses and radii between 1 - 10 $M_{\oplus}$ and 1 - 4 $R_{\oplus}$, that have thus far been found with orbital periods typically less than 100 days. They are the most common class of exoplanet, with an estimated 30-50% of Sun-like stars hosting a super-Earth planet with an orbital period shorter than 100 days (Howard et al., 2012; Fressin et al., 2013). While we know that our own solar system gas giant planets significantly influenced the formation and evolution of our terrestrial planets (Batygin and G. Laughlin, 2015; Tsiganis et al., 2005; Morbidelli, Bitsch, et al., 2016; Morbidelli, Lunine, et al., 2012; Desch, Kalyaan, and Alexander, 2017), it is unknown how gas giant planets impact the formation and evolution of super-Earth systems. On the one hand, gas giant planets forming farther out in the disk might block the inward flow of solids into inner regions of the disk where rocky planets form, biasing these systems to forming smaller terrestrial planets close to the host star. In this case, we would expect few gas giant companions in super-Earth systems. On the other hand, gas giants might preferentially form out of more massive protoplanetary disks, which could provide more solids in the inner regions of the disk out of which more massive rocky bodies could form. In this case, it might be common for super-Earth systems to host gas giant companions. By searching for outer gas giant companions in these systems we can test these trends.

In this thesis, I present four studies that leverage multiple observational techniques to find and characterize long period gas giant planets as tracers of formation histories of exoplanetary systems. Chapter 2 describes a radial velocity (RV) and near-infrared imaging survey at Keck that produced the first statistical analysis of the frequency of outer gas giant companions in systems hosting inner gas giant planets. Chapter 3 discusses a direct imaging survey at Keck that strongly discounted scattering as a hypothesis for the origin of wide-separation gas giants. Chapter 4 describes a project

to measure rotation rates of wide-separation gas giant planets using near-infrared high-resolution spectra, and placed the first constraints on the angular momentum evolution of young planetary-mass objects. Chapter 5 details work using RV data to estimate the frequency of gas giant companions in systems hosting inner super-Earth planets. Finally, Chapter 6 presents future work, harnessing the observational techniques mastered over the course of this thesis to explore new questions targeting gas giant formation and evolution.

The remainder of this introduction will provide additional background information useful for understanding the context of these projects, focusing on current models of planet formation and observational techniques employed.

1.1 Models of Gas Giant Planet Formation and Migration

The most commonly invoked model of planet formation is the core accretion model. In the classical core accretion framework, planetary cores grow via successions of two-body collisions between solids until they are massive enough to retain a significant gaseous atmosphere. The planet then enters a phase where its atmosphere grows in hydrostatic equilibrium until the mass of the envelope reaches the mass of the core. At this point, a phase of runaway gas accretion begins, where the rate of growth is limited by the supply of gas in the disk. Accretion terminates once this gas is exhausted, either because the gas in the disk has dissipated or the planet has opened a gap in the disk (Pollack et al., 1996; Alibert et al., 2005). The longest phase of the formation process is hydrostatic growth of the atmosphere, which is on the order of disk dissipation timescales of 1 - 10 Myr. Thus in this framework, planetary cores need to form rapidly in order to reach the runaway gas accretion stage before the gas in the protoplanetary disk dissipates (Levison, Thommes, and Duncan, 2010). This led to the assumption that gas giant planets could likely only form outside the ice line, since with more solids (rock plus ice) available to build planet cores, these cores could reach a large enough mass fast enough to accrete a substantial envelope before the gas in the disk dissipated.

More recent core accretion models suggest that instead of building a core in the previously described bottom-up fashion from dust to cores, 10-100 km cores form quickly via streaming instabilities in the protoplanetary disk (A. N. Youdin and Goodman, 2005; A. Youdin and Johansen, 2007), and then grow rapidly by accreting cm-sized "pebbles" from the disk (Lambrechts and Johansen, 2012). This mechanism shortens the core formation timescale typically by one to three orders

of magnitude at distances of 5 AU.

In models of disk instability, planets form rapidly via the fragmentation of a gravitationally unstable disk. Generally, the disk needs to be relatively massive and cold enough to gravitationally collapse (Nelson et al., 1998; Mayer et al., 2002). However, achieving local gravitational instability does not guarantee disk fragmentation. In most scenarios, how effectively the disk radiates thermal energy determines whether or not the disk fragments. Models indicate that fragmentation is unlikely to occur at close separations (i.e. within 10 AU) due to high temperatures and pressures, and are most likely to form planets between 20 - 100 AU (Vazan and Helled, 2012; Boley, 2009).

Migration models for exoplanets can be divided into two broad categories. The first is smooth disk migration, in which exchanges of angular momentum with the disk causes a planet's orbit to gradually decay. This mechanism is expected to produce close to, if not completely, circular orbits that are well aligned with the spin axis of the host star (Goldreich and Tremaine, 1980; Lin and Papaloizou, 1986; Tanaka, Takeuchi, and Ward, 2002). The second migration channel is three-body interactions. These include the Kozai mechanism, in which the presence of a stellar or planetary companion causes the argument of periastron to undergo resonant librations, allowing the planet's orbit to exchange between mutual inclination and eccentricity. Alternatively, planet-planet scattering between planets could impart a large orbital eccentricity to the inner planet (Chatterjee et al., 2008; Nagasawa, Ida, and Bessho, 2008; Wu and Lithwick, 2011). This highly eccentric orbit can then shrink and circularize at short periods via tidal dissipation.

1.2 Radial Velocity Technique: Detecting Distant Gas Giants Using RV Trends

In a planetary system, both the planet and the host star will orbit the system's center of mass. As the star orbits this center of mass, its light will be periodically red-shifted and blue-shifted along our line of sight due to the Doppler effect. The more massive the planet is and the closer the planet is to the host star, the greater these Doppler shifts will be. Using a high-resolution spectrograph the Doppler shift of the stellar light can be measured with present day precisions down to $\sim$0.5 m s^{-1} (Fischer et al., 2014). By measuring the radial velocity of the star over a period of time, we can infer properties of planets in the system. For instance, since this motion is periodic, the period of the RV curve corresponds to the period of the planet's orbit. The shape of the RV curve provides information about the eccentricity of the planet's orbit,

and the amplitude of the RV curve yields the minimum mass Msin i of the planet. Equation 1.1 describes the RV semi-amplitude, which when measured can provide an estimate of the planet's minimum mass (Fischer et al., 2014). In this equation, e is the planet's eccentricity, M_P is the planet mass, i is the planet's orbital inclination, P is the planet's orbital period, and $M_\star$ is the stellar mass.

$$K = \frac{28.43 ms^{-1}}{\sqrt{1-e^2}} \frac{M_p \sin i}{M_{Jup}} \left(\frac{M_\star + M_P}{M_\odot} \right)^{-2/3} \left(\frac{P}{yr} \right)^{-1/3} \tag{1.1}$$

In Fig. 1.1 the planets discovered using the RV method are plotted in blue. From this plot it is evident that this technique is sensitive to planets spanning a wide range of masses at close separations, while it is largely limited to gas giant planets beyond ~1 AU.

In this thesis we are interested in detecting gas giant planets at wide separations. However, Fig. 1.1 indicates that the sensitivity of this technique decreases significantly past ~ 5 AU. To see why this is, let us consider the signal of a Jupiter analog, namely a 1 M_{Jup} planet orbiting a 1 $M_\odot$ star at 5 AU in a circular orbit. Computing the semi-amplitude K of this planetary system, we obtain K = 12.7 m s^{-1}. This signal is readily detectable by current RV instruments, but the period of this orbit is at the far end of typical RV time baselines (typically limited to gas giants at a few to 5 AU), meaning that the full orbit of a Jupiter analog might be barely mapped out given these RV baselines. So what happens if we want to detect gas giants with longer orbital periods than a given RV baseline? In this case, we would detect a long term trend in the RV data (Fig. 1.2). Given sensitivities defined by the time baseline of the data, number of data points, and uncertainties on those data points, we can use the duration and shape of the RV trend to constrain masses and separations of more distant gas giant planets in these systems.

1.3 Direct Imaging: Detecting High Mass Planets in Young Systems

The direct imaging technique is the only exoplanet detection technique that spatially resolves the planet's light separate from that of its host star; it utilizes adaptive optics to search for faint objects located close to their host stars, and gathers photons directly from the planet. Two primary challenges of this technique are the brightness ratio between the star and the planet, and the angular separation between the star and the planet. In short, collecting photons from the planet in the glare of the host star is difficult. As a result, planet detections made via direct imaging thus far have been limited to a parameter space where the planets are extremely young, massive,

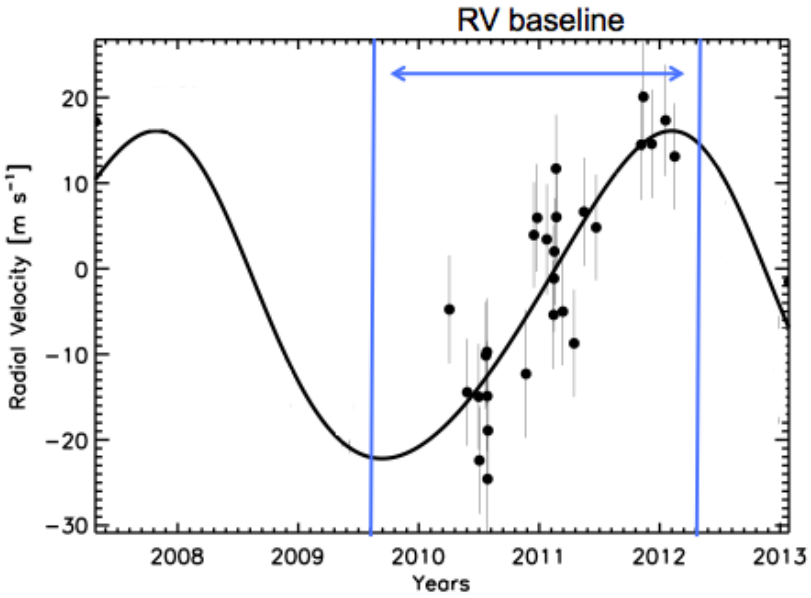

Figure 1.2: When the RV baseline is shorter than the orbital period of a companion in the system, we can still detect a long term trend in the RV data.

and far away from their host stars. To see why this is, let us first consider the flux ratio between a planet and its host star (Equation 1.2) (Seager, 2010).

$$\frac{f_p(\lambda, i, \alpha)}{f_s(\lambda)} = p(\lambda)\left(\frac{R_P}{a}\right)^2 \phi(i, \alpha) + \frac{B_\lambda(T_{\text{eff},p})R_P^2}{B_\lambda(T_{\text{eff},\star})R_\star^2} \tag{1.2}$$

In equation 1.2, the contrast between the planet and the star is given by a combination of reflected light (left-hand term), and thermal emission (right-hand term). The term $p(\lambda)$ is the geometric albedo as a function of wavelength, R_P is the planet radius, a is the planet's semi-major axis, and $\phi(i, \alpha)$ is the phase function, which indicates the fraction of the planet's disk that is illuminated given its orbital inclination i and phase angle α. The second half of the equation is due to the planet's thermal emission, where both the star and the planet are approximated as black bodies. R_P is the planet radius, $R_\star$ is the stellar radius, $T_{\text{eff},P}$ is the planet effective temperature, and $T_{\text{eff},\star}$ is the stellar effective temperature. At optical wavelengths, an Earth analog system is dominated by reflected light, and this Earth/Sun contrast is $\sim 10^{-10}$. Again taking an Earth analog system, at 10 um (approximately the peak of the Earth's thermal radiation), the contrast between the Earth and the Sun is $\sim 10^{-7}$. Given a distance of 10 pc, an Earth at 1 AU would be separated by 0.1 arcseconds away from its host star. Detecting this system is beyond current instrument capabilities.

Fortunately this situation becomes significantly more favorable when we consider young gas giant planets at wide separations. For the first few 100 Myr after a gas giant planet forms, it continues to radiate away energy from its formation and gravitational contraction; its infrared flux is dominated by this thermal emission. Fig. 1.3 shows how luminosity varies as a function of time for planetary to stellar masses (Bowler, 2016). From this figure, it is evident that particularly for the planetary mass regime, targeting young ages is critical to pushing down in mass, since the luminosity of a Jupiter mass planet varies by an order of magnitude between 1 and 10 Myr.

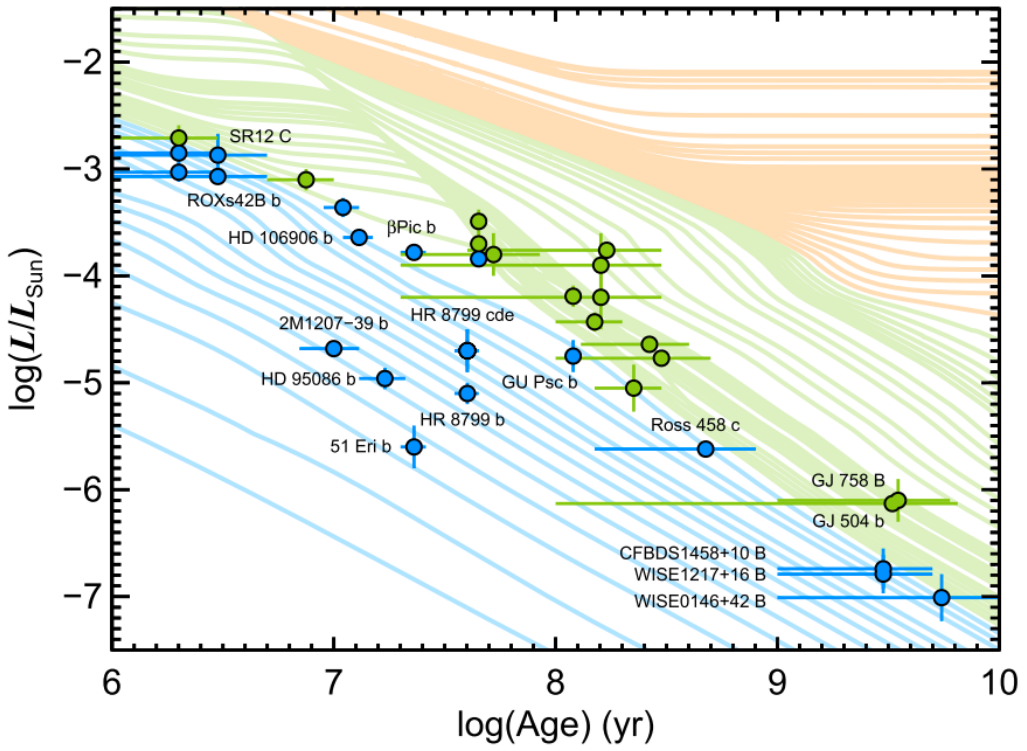

Figure 1.3: Directly imaged companions are plotted with evolutionary tracks (Baraffe et al., 2003). The blue tracks correspond to planetary masses (1 - 13 M_{Jup}), the green tracks correspond to brown dwarf masses (13 - 80 M_{Jup}), and the orange tracks correspond to stellar masses (Bowler, 2016).

To image planetary companions close to their host stars, a combination of adaptive optics and a coronagraph to block light from the star are typically used while taking observations. The coronagraph diameter defines the inner working angle for the observations, and scattered light from a combination of atmospheric aberrations and optical imperfections ("speckle noise") further limit achievable contrast close to the host star. Post-processing techniques can improve this contrast close to the host star (i.e. minimizing speckle noise) (Marois, Lafrenière, et al., 2006; Marois, Macintosh, and Véran, 2010; Soummer, Pueyo, and Larkin, 2012). Because the

achievable contrast depends on angular separation away from the host star, the distance of the system determines how physically close observations are able to probe in a given system. Typical separations for directly imaged planet detections are outside ~0.5 arcseconds (physical separations greater than ~ 50 AU). Direct imaging surveys make compromises between distance and age, as young star forming regions are typically at larger distances, while young moving groups can be found at closer distances. These trade-offs between age and distance (translating to limiting physical separation), are evidenced in Figure 1.4 (Bowler, 2016).

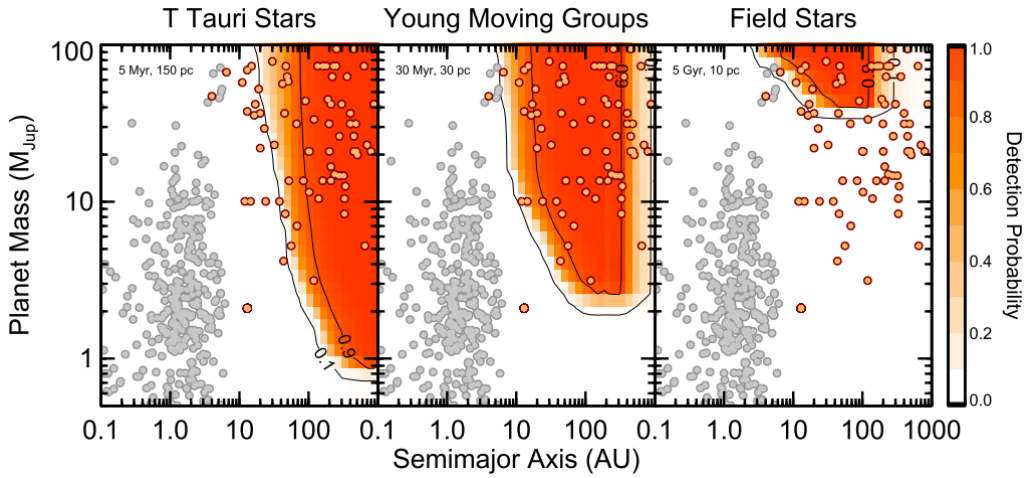

Figure 1.4: These panels show the typical sensitivities of observations of young T Tauri stars (5 Myr old, 150 pc away), stars in young moving groups (30 Myr old, 30 pc away), and field stars (5 Gyr old, 10 pc). The orange dots are direct imaging discoveries, while the grey points are discoveries made by the radial velocity method. These panels illustrate the trade-offs between age and distance; younger stars probe lower masses, but their larger distances lead to less sensitivity at separations interior to ~100 AU (Bowler, 2016).

In this thesis, we used NIRC2 at Keck to undertake a near-IR direct imaging search for additional planetary-mass companions in systems that already had a confirmed wide-separation planetary-mass companions (separation > 100 AU). While our targets spanned a wide range of ages and distances (1 - 400 Myr and 18 - 145 pc), all targets were chosen because they had previously been imaged using short integration times. Thus our comparatively deep imaging could push to lower masses at smaller separations. At 1" separation, we achieved contrasts between 10^{-4} – 10^{-5}. This translated to a sensitivity to high mass planets outside ~ 30 – 100 AU.

1.4 High-Resolution Spectroscopy: Measuring Rotation Rates

While the previous two sections addressed techniques to detect long period gas giant exoplanets, this section introduces a technique to characterize them. Directly

imaged planets have previously been observed using low resolution spectroscopy (R∼10s-100s), where these spectra were used primarily to determine spectral types and probe broad absorption features of molecules like CO, water, and methane (Bowler, Liu, et al., 2010; Barman et al., 2011; Oppenheimer et al., 2013; Kraus et al., 2014). Some of these directly imaged planets have also been observed using medium resolution spectroscopy (R∼1000s), which is able to resolve molecular bandheads and some absorption lines from molecules such as CO, CH4, and FeH (Konopacky et al., 2013; Naud et al., 2014; Bowler and Hillenbrand, 2015). These spectra have primarily been used to explore how derived effective temperatures and surface gravities from 1D model grids can be biased by effects from clouds and disequilibrium chemistry on the low and medium resolution spectra (Marley and Robinson, 2015).

With high-resolution spectra (R∼10,000s), individual absorption lines are resolved. Directly imaged planets represent a unique opportunity for the high-resolution spectroscopy technique; because directly imaged planets are still young and hot they are relatively bright at near-IR wavelengths, and their wide orbital separations allow us to observe them separately from their host stars using AO-fed echelle spectrographs. However, prior to this thesis only one directly imaged planetary-mass companion had been observed with a high-resolution spectrograph (CRIRES/VLT, R∼100,000). The spectrum of the companion β Pic b was used to measure rotational line broadening in order to constrain the projected rotation rate $v \sin i$ of the companion (Snellen et al., 2014). This was the first rotation rate measurement of a gas giant planet outside the solar system; a second rotation rate was later measured photometrically (rotational modulations yielded the rotational period of 2M1207b) (Zhou et al., 2016).

In this thesis, we used NIRSPEC at Keck (R∼30,000) to obtain near-IR high-resolution spectra of directly imaged planetary-mass companions. At present, NIRSPEC is the only near-IR spectrograph that can operate in conjunction with an AO system, which allows us to spatially separate the light from the host stars from the light from the companion for a wide range of separations. Our goal was to measure rotational line broadening in these high-resolution spectra. This effect occurs when an object spins about an axis. As one half of the disk rotates towards you, the light from that half of the disk is blue-shifted, and as the other half of the disk rotates away from you, that light is red-shifted. This leads to a broadening of the atmospheric spectral lines. Note that the observed broadening along the line of sight will depend

on the angle of inclination of the spin axis with respect to the observer; therefore the quantity that is actually measured when determining rotational line broadening is $v \sin i$ instead of v.

References

Alibert, Y. et al. (2005). "Models of giant planet formation with migration and disc evolution". In: *A&A* 434, pp. 343–353. DOI: 10.1051/0004-6361:20042032. eprint: astro-ph/0412444.

Baraffe, I. et al. (2003). "Evolutionary models for cool brown dwarfs and extrasolar giant planets. The case of HD 209458". In: *A&A* 402, pp. 701–712. DOI: 10.1051/0004-6361:20030252. eprint: astro-ph/0302293.

Barman, T. S. et al. (2011). "Clouds and Chemistry in the Atmosphere of Extrasolar Planet HR8799b". In: *ApJ* 733, 65, p. 65. DOI: 10.1088/0004-637X/733/1/65. arXiv: 1103.3895 [astro-ph.EP].

Batygin, K., P. H. Bodenheimer, and G. P. Laughlin (2016). "In Situ Formation and Dynamical Evolution of Hot Jupiter Systems". In: *ApJ* 829, 114, p. 114. DOI: 10.3847/0004-637X/829/2/114. arXiv: 1511.09157 [astro-ph.EP].

Batygin, K. and G. Laughlin (2015). "Jupiter's decisive role in the inner Solar System's early evolution". In: *Proceedings of the National Academy of Science* 112, pp. 4214–4217. DOI: 10.1073/pnas.1423252112. arXiv: 1503.06945 [astro-ph.EP].

Beaugé, C. and D. Nesvorný (2012). "Multiple-planet Scattering and the Origin of Hot Jupiters". In: *ApJ* 751, 119, p. 119. DOI: 10.1088/0004-637X/751/2/119. arXiv: 1110.4392 [astro-ph.EP].

Boley, A. C. (2009). "The Two Modes of Gas Giant Planet Formation". In: *ApJL* 695, pp. L53–L57. DOI: 10.1088/0004-637X/695/1/L53. arXiv: 0902.3999 [astro-ph.EP].

Bowler, B. P. (2016). "Imaging Extrasolar Giant Planets". In: *PASP* 128.10, p. 102001. DOI: 10.1088/1538-3873/128/968/102001. arXiv: 1605.02731 [astro-ph.EP].

Bowler, B. P. and L. A. Hillenbrand (2015). "Near-infrared Spectroscopy of 2M0441+2301 AabBab: A Quadruple System Spanning the Stellar to Planetary Mass Regimes". In: *ApJL* 811, L30, p. L30. DOI: 10.1088/2041-8205/811/2/L30. arXiv: 1509.01658 [astro-ph.EP].

Bowler, B. P., M. C. Liu, et al. (2010). "Near-infrared Spectroscopy of the Extrasolar Planet HR 8799 b". In: *ApJ* 723, pp. 850–868. DOI: 10.1088/0004-637X/723/1/850. arXiv: 1008.4582 [astro-ph.EP].

Chabrier, G. et al. (2014). "Giant Planet and Brown Dwarf Formation". In: *Protostars and Planets VI*, pp. 619–642. DOI: 10.2458/azu_uapress_9780816531240-ch027. arXiv: 1401.7559 [astro-ph.SR].

Chatterjee, S. et al. (2008). "Dynamical Outcomes of Planet-Planet Scattering". In: *ApJ* 686, 580-602, pp. 580–602. DOI: 10.1086/590227. eprint: astro-ph/0703166.

Desch, S. J., A. Kalyaan, and C. M. O. Alexander (2017). "The Effect of Jupiter's Formation on the Distribution of Refractory Elements and Inclusions in Meteorites". In: *ArXiv e-prints*. arXiv: 1710.03809 [astro-ph.EP].

Dressing, C. D. and D. Charbonneau (2015). "The Occurrence of Potentially Habitable Planets Orbiting M Dwarfs Estimated from the Full Kepler Dataset and an Empirical Measurement of the Detection Sensitivity". In: *ApJ* 807, 45, p. 45. DOI: 10.1088/0004-637X/807/1/45. arXiv: 1501.01623 [astro-ph.EP].

Fischer, D. A. et al. (2014). "Exoplanet Detection Techniques". In: *Protostars and Planets VI*, pp. 715–737. DOI: 10.2458/azu_uapress_9780816531240-ch031. arXiv: 1505.06869 [astro-ph.EP].

Fressin, F. et al. (2013). "The False Positive Rate of Kepler and the Occurrence of Planets". In: *ApJ* 766, 81, p. 81. DOI: 10.1088/0004-637X/766/2/81. arXiv: 1301.0842 [astro-ph.EP].

Goldreich, P. and S. Tremaine (1980). "Disk-satellite interactions". In: *ApJ* 241, pp. 425–441. DOI: 10.1086/158356.

Helled, R. et al. (2014). "Giant Planet Formation, Evolution, and Internal Structure". In: *Protostars and Planets VI*, pp. 643–665. DOI: 10.2458/azu_uapress_9780816531240-ch028. arXiv: 1311.1142 [astro-ph.EP].

Howard, A. W. et al. (2012). "Planet Occurrence within 0.25 AU of Solar-type Stars from Kepler". In: *ApJS* 201, 15, p. 15. DOI: 10.1088/0067-0049/201/2/15. arXiv: 1103.2541 [astro-ph.EP].

Knutson, H. A. et al. (2014). "Friends of Hot Jupiters. I. A Radial Velocity Search for Massive, Long-period Companions to Close-in Gas Giant Planets". In: *ApJ* 785, 126, p. 126. DOI: 10.1088/0004-637X/785/2/126. arXiv: 1312.2954 [astro-ph.EP].

Konopacky, Q. M. et al. (2013). "Detection of Carbon Monoxide and Water Absorption Lines in an Exoplanet Atmosphere". In: *Science* 339, pp. 1398–1401. DOI: 10.1126/science.1232003. arXiv: 1303.3280 [astro-ph.EP].

Kraus, A. L. et al. (2014). "Three Wide Planetary-mass Companions to FW Tau, ROXs 12, and ROXs 42B". In: *ApJ* 781, 20, p. 20. DOI: 10.1088/0004-637X/781/1/20. arXiv: 1311.7664 [astro-ph.EP].

Lambrechts, M. and A. Johansen (2012). "Rapid growth of gas-giant cores by pebble accretion". In: *A&A* 544, A32, A32. DOI: 10.1051/0004-6361/201219127. arXiv: 1205.3030 [astro-ph.EP].

Levison, H. F., E. Thommes, and M. J. Duncan (2010). "Modeling the Formation of Giant Planet Cores. I. Evaluating Key Processes". In: *AJ* 139, pp. 1297–1314. DOI: 10.1088/0004-6256/139/4/1297. arXiv: 0912.3144 [astro-ph.EP].

Lin, D. N. C., P. Bodenheimer, and D. C. Richardson (1996). "Orbital migration of the planetary companion of 51 Pegasi to its present location". In: *Nature* 380, pp. 606–607. DOI: 10.1038/380606a0.

Lin, D. N. C. and J. Papaloizou (1986). "On the tidal interaction between protoplanets and the protoplanetary disk. III - Orbital migration of protoplanets". In: *ApJ* 309, pp. 846–857. DOI: 10.1086/164653.

Marley, M. S. and T. D. Robinson (2015). "On the Cool Side: Modeling the Atmospheres of Brown Dwarfs and Giant Planets". In: *ARA&A* 53, pp. 279–323. DOI: 10.1146/annurev-astro-082214-122522. arXiv: 1410.6512 [astro-ph.EP].

Marois, C., D. Lafrenière, et al. (2006). "Angular Differential Imaging: A Powerful High-Contrast Imaging Technique". In: *ApJ* 641, pp. 556–564. DOI: 10.1086/500401. eprint: astro-ph/0512335.

Marois, C., B. Macintosh, and J.-P. Véran (2010). "Exoplanet imaging with LOCI processing: photometry and astrometry with the new SOSIE pipeline". In: *Adaptive Optics Systems II*. Vol. 7736. Proc. SPIE, 77361J. DOI: 10.1117/12.857225.

Mayer, L. et al. (2002). "Formation of Giant Planets by Fragmentation of Protoplanetary Disks". In: *Science* 298, pp. 1756–1759. DOI: 10.1126/science.1077635. eprint: astro-ph/0301088.

Morbidelli, A., B. Bitsch, et al. (2016). "Fossilized condensation lines in the Solar System protoplanetary disk". In: *Icarus* 267, pp. 368–376. DOI: 10.1016/j.icarus.2015.11.027. arXiv: 1511.06556 [astro-ph.EP].

Morbidelli, A., J. I. Lunine, et al. (2012). "Building Terrestrial Planets". In: *Annual Review of Earth and Planetary Sciences* 40, pp. 251–275. DOI: 10.1146/annurev-earth-042711-105319. arXiv: 1208.4694 [astro-ph.EP].

Nagasawa, M., S. Ida, and T. Bessho (2008). "Formation of Hot Planets by a Combination of Planet Scattering, Tidal Circularization, and the Kozai Mechanism". In: *ApJ* 678, 498-508, pp. 498–508. DOI: 10.1086/529369. arXiv: 0801.1368.

Naud, M.-E. et al. (2014). "Discovery of a Wide Planetary-mass Companion to the Young M3 Star GU Psc". In: *ApJ* 787, 5, p. 5. DOI: 10.1088/0004-637X/787/1/5. arXiv: 1405.2932 [astro-ph.EP].

Nelson, A. F. et al. (1998). "Dynamics of Circumstellar Disks". In: *ApJ* 502, pp. 342–371. DOI: 10.1086/305869. eprint: astro-ph/9802191.

Oppenheimer, B. R. et al. (2013). "Reconnaissance of the HR 8799 Exosolar System. I. Near-infrared Spectroscopy". In: *ApJ* 768, 24, p. 24. DOI: 10.1088/0004-637X/768/1/24. arXiv: 1303.2627 [astro-ph.EP].

Pollack, J. B. et al. (1996). "Formation of the Giant Planets by Concurrent Accretion of Solids and Gas". In: *Icarus* 124, pp. 62–85. DOI: 10.1006/icar.1996.0190.

Rafikov, R. R. (2006). "Atmospheres of Protoplanetary Cores: Critical Mass for Nucleated Instability". In: *ApJ* 648, pp. 666–682. DOI: 10.1086/505695. eprint: astro-ph/0405507.

Seager, S. (2010). *Exoplanets*.

Snellen, I. A. G. et al. (2014). "Fast spin of the young extrasolar planet β Pictoris b". In: *Nature* 509, pp. 63–65. DOI: 10.1038/nature13253.

Soummer, R., L. Pueyo, and J. Larkin (2012). "Detection and Characterization of Exoplanets and Disks Using Projections on Karhunen-Loève Eigenimages". In: *ApJL* 755, L28, p. L28. DOI: 10.1088/2041-8205/755/2/L28. arXiv: 1207.4197 [astro-ph.IM].

Tanaka, H., T. Takeuchi, and W. R. Ward (2002). "Three-Dimensional Interaction between a Planet and an Isothermal Gaseous Disk. I. Corotation and Lindblad Torques and Planet Migration". In: *ApJ* 565, pp. 1257–1274. DOI: 10.1086/324713.

Tsiganis, K. et al. (2005). "Origin of the orbital architecture of the giant planets of the Solar System". In: *Nature* 435, pp. 459–461. DOI: 10.1038/nature03539.

Vazan, A. and R. Helled (2012). "On the Evolution and Survival of Protoplanets Embedded in a Protoplanetary Disk". In: *ApJ* 756, 90, p. 90. DOI: 10.1088/0004-637X/756/1/90. arXiv: 1206.5887 [astro-ph.EP].

Wu, Y. and Y. Lithwick (2011). "Secular Chaos and the Production of Hot Jupiters". In: *ApJ* 735, 109, p. 109. DOI: 10.1088/0004-637X/735/2/109. arXiv: 1012.3475 [astro-ph.EP].

Wu, Y. and N. Murray (2003). "Planet Migration and Binary Companions: The Case of HD 80606b". In: *ApJ* 589, pp. 605–614. DOI: 10.1086/374598. eprint: astro-ph/0303010.

Youdin, A. N. and J. Goodman (2005). "Streaming Instabilities in Protoplanetary Disks". In: *ApJ* 620, pp. 459–469. DOI: 10.1086/426895. eprint: astro-ph/0409263.

Youdin, A. and A. Johansen (2007). "Protoplanetary Disk Turbulence Driven by the Streaming Instability: Linear Evolution and Numerical Methods". In: *ApJ* 662, pp. 613–626. DOI: 10.1086/516729. eprint: astro-ph/0702625.

Zhou, Y. et al. (2016). "Discovery of Rotational Modulations in the Planetary-mass Companion 2M1207b: Intermediate Rotation Period and Heterogeneous Clouds in a Low Gravity Atmosphere". In: *ApJ* 818, 176, p. 176. DOI: 10.3847/0004-637X/818/2/176. arXiv: 1512.02706 [astro-ph.EP].

Chapter 2

STATISTICS OF LONG PERIOD GAS GIANT PLANETS IN KNOWN PLANETARY SYSTEMS

2.1 Abstract

We conducted a Doppler survey at Keck combined with NIRC2 K-band AO imaging to search for massive, long-period companions to 123 known exoplanet systems with one or two planets detected using the radial velocity (RV) method. Our survey is sensitive to Jupiter mass planets out to 20 AU for a majority of stars in our sample, and we report the discovery of eight new long-period planets, in addition to 20 systems with statistically significant RV trends indicating the presence of an outer companion beyond 5 AU. We combine our RV observations with AO imaging to determine the range of allowed masses and orbital separations for these companions, and account for variations in our sensitivity to companions among stars in our sample. We estimate the total occurrence rate of companions in our sample to be 52 ± 5% over the range 1 - 20 $M_{\rm Jup}$ and 5 - 20 AU. Our data also suggest a declining frequency for gas giant planets in these systems beyond 3-10 AU, in contrast to earlier studies that found a rising frequency for giant planets in the range 0.01-3 AU. This suggests either that the frequency of gas giant planets peaks between 3-10 AU, or that outer companions in these systems have a different semi-major axis distribution than the overall gas giant planet population. Our results also suggest that hot gas giants may be more likely to have an outer companion than cold gas giants. We find that planets with an outer companion have higher average eccentricities than their single counterparts, suggesting that dynamical interactions between planets may play an important role in these systems.

2.2 Introduction

The presence of a substantial population of gas giant planets on orbits interior to 1 AU poses a challenge to models of planet formation and migration. Standard core accretion models favor giant planet formation beyond the ice line, where core-nucleated accretion may proceed on a timescale substantially shorter than the lifetime of the disk (Pollack et al., 1996; Alibert et al., 2005; Rafikov, 2006). In this scenario, gas giant planets on short period orbits most likely migrated in from their original formation locations (Lin, Bodenheimer, and Richardson, 1996). Mi-

gration models for these planets can be divided into two broad categories. The first is smooth disk migration, in which exchanges of angular momentum with the disk causes the planet's orbit to gradually decay. This mechanism would be expected to produce close to, if not completely, circular orbits that are well aligned with the spin axis of the host star (Goldreich and Tremaine, 1980; Lin and Papaloizou, 1986; Tanaka, Takeuchi, and Ward, 2002). The second migration channel is three-body interactions. These include the Kozai mechanism, in which the presence of a stellar or planetary companion causes the argument of periastron to undergo resonant librations, allowing the planet's orbit to exchange between mutual inclination and eccentricity. Alternatively, planet-planet scattering or long term secular interactions between planets could impart a large orbital eccentricity to the inner planet (Chatterjee et al., 2008; Nagasawa, Ida, and Bessho, 2008; Wu and Lithwick, 2011). This highly eccentric orbit can then shrink and circularize at short periods via tidal dissipation.

High eccentricity migration channels and dynamical interactions between planets are thought to frequently produce planets whose orbits are misaligned with the rotation axes of their host stars[1]. Over the past decade, Rossiter-McLaughlin measurements of spin-orbit alignment have found a number of hot Jupiter systems that are misaligned (Torres, Winn, and Holman, 2008; Hébrard et al., 2011; Albrecht, Winn, Johnson, et al., 2012). However, previous studies demonstrated that there is no correlation between the presence of an outer planetary or stellar companion and the spin-orbit angle of hot Jupiters (Knutson et al., 2014; Ngo et al., 2015). Furthermore, Batygin (2012) and Batygin & Adams (2013) have suggested that a distant stellar companion could tilt the protoplanetary disk with respect to the star's spin axis, in which case disk migration could lead to a misaligned orbit (Spalding and Batygin, 2014). This scenario is supported by the discovery of apparently coplanar multi-planet systems with spin-orbit misalignments (Huber et al., 2013; Bourrier and Hébrard, 2014), although other surveys have suggested that such systems may be relatively rare (Albrecht, Winn, Marcy, et al., 2013; Morton and Winn, 2014). In either case, it appears that the cause of hot Jupiter misalignment is more complicated than the simple picture presented above.

Measurements of orbital eccentricities for a large sample of single and multi-planet systems provide a more direct diagnostic of the importance of dynamical interactions

[1]This assessment is however sensitive to the dynamical evolution of the stellar spin-axis itself, as spin-orbit misalignments may be suppressed by adiabatic coupling (Storch, Anderson, and Lai, 2014)

in shaping the observed architectures of planetary systems. We expect dynamical interactions between planets to pump up the eccentricities of their orbits, a process that could result in migration if the periapse of an orbit gets close enough to the star for tidal forces to become significant (Rasio and Ford, 1996; Jurić and Tremaine, 2008). However, previous radial velocity studies of gas giants indicate that high eccentricities are more common in apparently single systems (Howard, 2013). It has been suggested that this enhanced eccentricity may be due to planet-planet scattering, where one planet was ejected from the system (Chatterjee et al., 2008). This is consistent with the results of Dawson (2014), which suggest that higher eccentricities are more common when the star has a high metallicity, and infer that this is because higher metallicity stars are more likely to form multiple giant planets, which then interact and pump up planet eccentricities. Limbach and Turner (2015) also find a positive correlation between lower eccentricity and higher system multiplicity. Conversely, Dong, Katz, and Socrates (2014) finds that warm Jupiters with outer companions are more likely to have higher eccentricities than single warm Jupiters, albeit with a relatively small sample size of just 26 systems. We can test these trends by directly searching for outer companions at wide orbital separations in a large sample of known planetary systems, and checking to see if these companions are associated with a larger orbital eccentricity for the inner planet.

In order to understand whether or not dynamical interactions between planets are responsible for the inward migration of a subset of these planets, it is useful to study systems where we can obtain a complete census of gas giant planets across a broad range of orbital separations. While large surveys have made it possible to understand the statistical properties of exoplanet populations, recent studies have focused on determining mass distributions and occurrence rates of short period, low mass planets around apparently single main sequence FGK stars (e.g. Howard, Marcy, et al., 2012; Fressin et al., 2013; Howard, 2013; Petigura, Howard, and Marcy, 2013). Many of these surveys are primarily sensitive to short-period planets, making it difficult to evaluate the role that a massive distant planetary companion might have on the formation and orbital evolution of the inner planets. Early studies of hot Jupiters, which are among the best-studied exoplanet populations, indicated that they rarely contain nearby companions (Steffen et al. (2012), but see Becker et al. 2015 for a recent exception). In contrast, recent work by Knutson et al (2014) looked at 51 hot Jupiter systems and found that they are not lonely — the occurrence rate of massive, outer companions was 51 ± 10% for companions with masses of 1-13 M_{Jup} and separations of 1-20 AU. This implies that long period companions to hot

Jupiters are common, and thus might play an important role in the orbital evolution of these systems.

In this study we combine Keck HIRES radial velocity measurements with NIRC2 K band adaptive optics (AO) imaging to search for massive, long period companions to a sample of 123 known exoplanet systems detected using the radial velocity (RV) method. Unlike our previous survey, which focused exclusively on transiting hot Jupiter systems, our new sample includes planets with a wide range of masses and orbital separations (Fig. 2.1). We present results from this survey in two papers. In this paper, we focus on long-term RV monitoring of the confirmed exoplanet systems, probing planetary and brown dwarf mass companions out to ~100 AU. We test whether close-in gas giant planets are more likely to have outer companions than their long period counterparts, and whether planets in two-planet systems are more likely to have higher eccentricities than single planet systems. In the second paper, we will use our complementary K-band AO images to find and confirm low mass stellar companions in these systems in order to determine how stellar companions might influence the formation and evolution of the inner planets.

In section 2.3 we describe the selected sample of systems, as well as the methods for obtaining the RV and K-band AO imaging data. In section 2.4 we describe fits to the RV data, generation of contrast curves from the AO data, identification of significant RV accelerations, calculation of two-dimensional companion probability distributions, and the completeness analysis that was performed for each individual system. Finally, in section 2.5 we discuss our occurrence rate calculations and analysis of eccentricity distributions.

2.3 Observations

Radial velocity measurements were made at Keck Observatory as part of more than a dozen PI-led programs falling under the umbrella of the California Planet Survey (CPS; Howard, Johnson, Marcy, D. A. Fischer, Wright, Bernat, et al., 2010). We observed each target star using the High Resolution Echelle Spectrometer (HIRES) (Vogt, Allen, et al., 1994) following standard practices of CPS. Our selected sample includes all known one- and two-planet systems discovered via the radial velocity method with at least ten RV observations obtained using HIRES. We also excluded systems with a Keck baseline shorter than the published orbital period. The published planets in our resulting sample of 123 systems span a range of masses and semi-major axes, as shown in Figure 2.1. RV baselines for these targets range

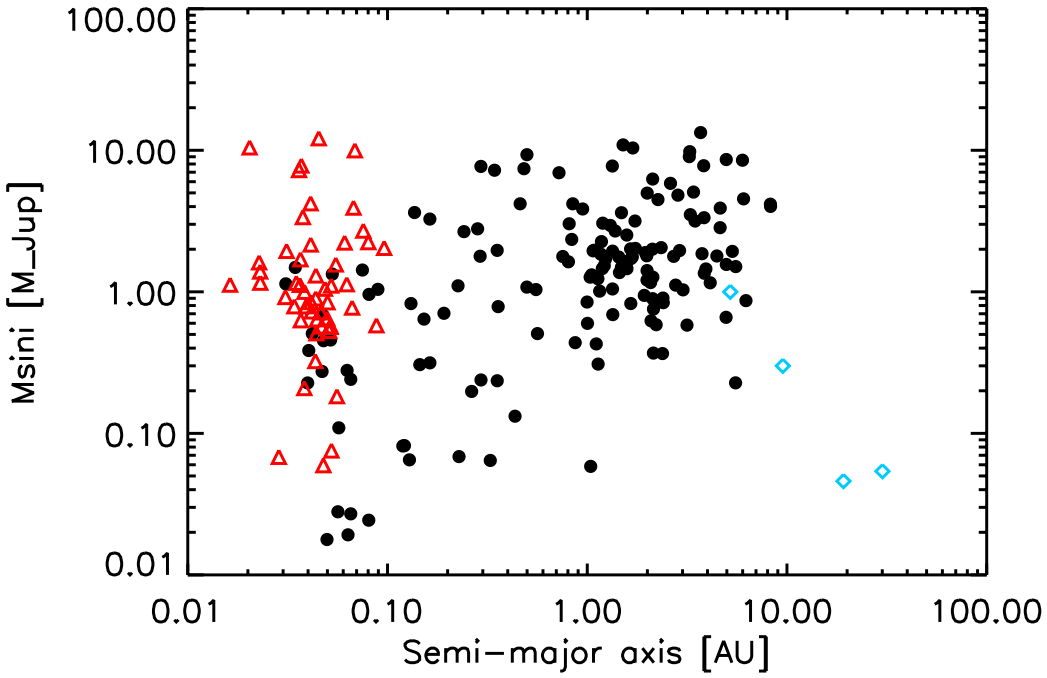

Figure 2.1: Transiting hot Jupiters from our previous radial velocity study (Knutson et al., 2014) are shown as red triangles, and the new sample of gas giant planets in this study are shown as black circles. The blue diamonds represent the gas and ice giant planets in the solar system for comparison.

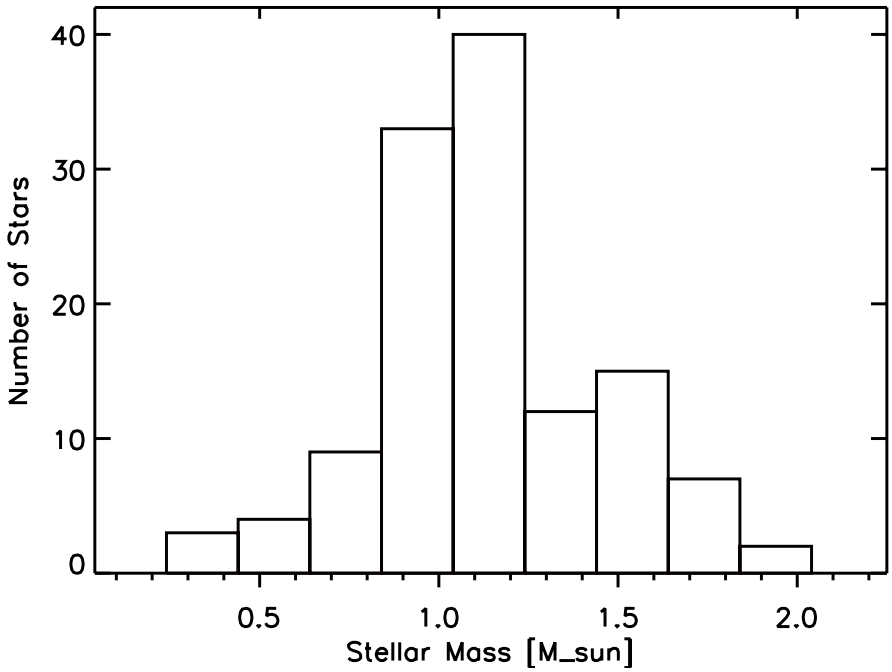

Figure 2.2: Distribution of masses for the stars in our sample.

from 5.02 to 18.18 years, making it possible to detect gas giant planets spanning a broad range of orbital semi-major axes. Properties of the target stars are described in Table 2.1. Figure 2.2 shows the distribution of stellar masses in our sample. While most stars are F and G stars, there are significant numbers of M, K, and A stars. The A stars in this sample are all moderately evolved, which facilitates precise radial velocity measurements (Johnson, Howard, Bowler, et al., 2010; Johnson, Clanton, et al., 2011).

Keck HIRES Radial Velocities

All of the target stars were observed using the High Resolution Echelle Spectrometer (HIRES) on Keck I (Vogt, Allen, et al., 1994). While the majority of the RV data used in this study was published in previous papers, we also obtained new observations that extend these published baselines by up to 12 years. To reduce the RV data, the standard CPS HIRES configuration and reduction pipeline were used (Wright et al 2004; Howard et al 2009; Johnson et al 2010). We measured Doppler shifts from the echelle spectra using an iodine absorption spectrum and a modeling procedure descended from Butler, Marcy, et al. (1996) and described in Howard et al. (2011b). The set of observations for each star comprise a "template spectrum" taken without iodine and de-convolved using a reference point spread function (PSF) inferred from near-in-time observations of B-stars through iodine, and a set of dozens to hundreds of observations through iodine that each yield an RV. We used one of the 0."86-wide slits ('B5' or 'C2') for the observations taken through iodine and a 0."57 ('B1' or 'B3') or 0."86-wide slit for the template observations. Using a real-time exposure meter, integration times of 1–8 minutes were chosen to achieve (in most cases) a signal-to-noise ratio of ~220 in the reduced spectrum at the peak of the blaze function near 550 nm. All Doppler observations were made with an iodine cell mounted directly in front of the spectrometer entrance slit. The dense set of molecular absorption lines imprinted on the stellar spectra provide a robust wavelength fiducial against which Doppler shifts are measured, as well as strong constraints on the shape of the spectrometer instrumental profile at the time of each observations (Marcy and Butler, 1992; Valenti, Butler, and Marcy, 1995). The velocity and corresponding uncertainty for each observation is based on separate measurements for ~700 spectral chunks each 2Å wide. The RVs are corrected for motion of Keck Observatory through the solar System (barycentric corrections). The measurements span 1996–2015 (see Table 2.2). Measurements made after the HIRES CCD upgrade in 2004 August have a different (arbitrary) velocity zero

point (not the star's systemic velocity) and suffer from somewhat smaller systematic errors. A summary of the radial velocity data used in this work is provided in Table 2.2. We include best-fit stellar jitter and RV acceleration "trend" values from our orbital solution fitting described in section 2.4.

NIRC2 AO Imaging

We observed K band images for all targets using the NIRC2 instrument (Instrument PI: Keith Matthews) on Keck II. We used natural guide star AO imaging and the narrow camera setting (10 mas pixel^{-1}) to achieve better contrast and spatial resolution. For most targets, we imaged using the full NIRC2 array (1024×1024 pixels) and used a 3-point dither pattern that avoids NIRC2's noisier quadrant. Because NIRC2 does not have neutral density filters, we used the subarray mode (2.5" or 5" field of view) to decrease readout time when it was necessary to avoid saturation. We typically obtained two minutes of on-target integration time per system in position angle mode.

We use dome flat fields and dark frames to calibrate the images. We identify image artifacts by searching for pixels that are 8σ outliers compared to the counts in the surrounding 5×5 box. We replace these pixels by the median value of the same 5×5 box. To compute contrast curves, we register all frames with the target star and then combine using a median stack. Table 2.3 summarizes the NIRC2 AO observations taken during this survey that were used in subsequent analysis.

Table 2.1: Stellar Parameters

Star	Mass [$M_\odot$]	[Fe/H]	$B-V$	S_{HK}	References
ρ CrB[1]	0.97	-0.20	0.61	0.15	Takeda et al. (2007)
16 Cyg B[2]	0.96	0.04	0.66	0.15	Takeda et al. (2007)
24 Sex[3]	1.54	-0.0	0.91	0.14	Mortier et al. (2013)
51 Peg[4]	1.05	0.20	0.67	0.15	Takeda et al. (2007)
70 Vir[5]	1.10	-0.012	0.69	0.14	Takeda et al. (2007)
GJ 176[6]	0.49	-0.10	1.5	1.5	Endl, Cochran, Wittenmyer, and Boss (2008)
GJ 179[7]	0.36	0.30	1.6	1.1	Howard et al (2009)
GJ 317	0.24	-0.23	1.6	1.2	Johnson, Butler, et al. (2007)
GJ 649[8]	0.54	0.08	1.6	1.6	Johnson, Aller, et al. (2010)
GJ 849[9]	0.49	0.16	1.5	1.0	Butler, Johnson, et al. (2006)
HD 1461	1.03	0.18	0.68	0.16	Takeda et al. (2007)
HD 1502	1.61	-0.04	0.92	0.10	Mortier et al. (2013)
HD 3651	0.88	0.16	0.92	0.17	Takeda et al. (2007)
HD 4203	1.13	0.45	0.73	0.14	Takeda et al. (2007)
HD 4208	0.88	-0.28	0.67	0.15	Takeda et al. (2007)
HD 4313	1.72	0.05	0.96	0.12	Mortier et al. (2013)

Continued on next page

Table 2.1 – continued from previous page

Star	Mass [$M_\odot$]	[Fe/H]	$B-V$	S_{HK}	References
HD 5319	1.56	0.02	0.98	12.	Mortier et al. (2013)
HD 5891	1.61	-0.38	0.99	0.12	Mortier et al. (2013)
HD 8574	1.12	-0.01	0.57	0.15	Takeda et al. (2007)
HD 10697	1.11	0.19	0.66	0.15	Takeda et al. (2007)
HD 11506	1.19	0.31	0.60	0.15	D. A. Fischer, Vogt, et al. (2007)
HD 11964A	1.11	0.14	0.83	0.13	Mortier et al. (2013)
HD 12661	1.14	0.36	0.72	0.15	Takeda et al. (2007)
HD 13931	1.02	0.03	0.64	0.15	Takeda et al. (2007)
HD 16141	1.05	0.17	0.71	0.15	Takeda et al. (2007)
HD 17156	1.29	0.24	0.64	0.15	Gilliland et al. (2011)
HD 24040	1.09	0.21	0.66	0.15	Boisse, Bonfils, and Santos (2012)
HD 28678	1.74	-0.21	1.0	0.13	Mortier et al. (2013)
HD 30856	1.35	-0.14	0.96	0.13	Mortier et al. (2013)
HD 33142	1.48	0.03	0.95	0.14	Mortier et al. (2013)
HD 33283	1.24	0.37	0.61	0.13	Johnson, Marcy, et al. (2006)
HD 33636	1.02	-0.13	0.58	0.17	Takeda et al. (2007)
HD 34445	1.07	0.14	0.62	0.16	Takeda et al. (2007)
HD 37605	1.00	0.34	0.82	0.16	Wang et al. (2012)
HD 38529	1.48	0.40	0.77	0.16	Mortier et al. (2013)
HD 38801	1.36	0.25	0.87	0.16	Mortier et al. (2013)
HD 40979	1.15	0.17	0.52	0.22	Takeda et al. (2007)
HD 43691	1.38	0.25	0.59	0.15	da Silva et al. (2007)
HD 45350	1.05	0.29	0.74	0.14	Takeda et al. (2007)
HD 46375	0.93	0.24	0.86	0.18	Takeda et al. (2007)
HD 49674	1.02	0.31	0.71	0.19	Takeda et al. (2007)
HD 50499	1.28	0.34	0.57	0.14	Takeda et al. (2007)
HD 50554	1.03	-0.07	0.53	0.16	Takeda et al. (2007)
HD 52265	1.17	0.19	0.53	0.14	Takeda et al. (2007)
HIP 57050	0.34	0.32	1.6	0.76	Haghighipour, Vogt, et al. (2010)
HD 66428	1.06	0.31	0.71	0.14	Takeda et al. (2007)
HD 68988	1.12	0.32	0.62	0.16	Takeda et al. (2007)
HD 72659	1.07	-0.0	0.57	0.15	Takeda et al. (2007)
HD 73534	1.23	0.16	0.95	0.12	Mortier et al. (2013)
HD 74156	1.24	0.13	0.54	0.14	Takeda et al. (2007)
HD 75898	1.28	0.27	0.59	0.14	Robinson et al. (2007)
HIP 79431	0.49	0.40	1.5	0.90	Delfosse et al. (2000)
HD 80606	1.06	0.34	0.71	0.15	Takeda et al. (2007)
HD 82886	1.06	-0.31	0.86	0.14	Johnson, Clanton, et al. (2011)
HD 83443	0.99	0.36	0.79	0.19	Takeda et al. (2007)
HD 86081	1.21	0.26	0.66	0.16	Johnson, Marcy, et al. (2006)
HD 88133	1.20	0.33	0.82	0.13	Mortier et al. (2013)
HD 92788	1.08	0.32	0.69	0.16	Takeda et al. (2007)
HD 96063	1.02	-0.20	0.85	0.14	Mortier et al. (2013)
HD 96167	1.31	0.34	0.68	0.13	Peek et al. (2009)
HD 97658	0.78	-0.30	0.80	0.17	Dragomir et al. (2013)
HD 99109	0.94	0.32	0.87	0.15	Takeda et al. (2007)
HD 99492	0.83	0.36	1.0	0.25	Takeda et al. (2007)

Continued on next page

Table 2.1 – continued from previous page

Star	Mass [$M_\odot$]	[Fe/H]	$B-V$	S_{HK}	References
HD 99706	1.72	0.14	0.99	0.12	Johnson, Clanton, et al. (2011)
HD 102195	0.87	0.05	0.90	0.35	Melo et al. (2007)
HD 102329	1.95	0.05	1.0	0.12	Mortier et al. (2013)
HD 102956	1.68	0.19	0.97	0.15	Johnson, Aller, et al. (2010)
HD 104067	0.79	-0.06	0.99	0.33	Ségransan et al. (2011)
HD 106270	1.32	0.06	0.74	0.21	Mortier et al. (2013)
HD 107148	1.14	0.31	0.66	0.15	Takeda et al. (2007)
HD 108863	1.85	0.20	0.99	0.13	Mortier et al. (2013)
HD 108874	0.95	0.18	0.71	0.15	Takeda et al. (2007)
HD 109749	1.21	0.25	0.70	0.16	D. A. Fischer, Laughlin, et al. (2006)
HD 114729	1.00	-0.26	0.62	0.15	Takeda et al. (2007)
HD 114783	0.85	0.12	0.90	0.18	Takeda et al. (2007)
HD 116029	1.58	0.08	1.0	0.12	Mortier et al. (2013)
HD 117207	1.03	0.27	0.72	0.15	Takeda et al. (2007)
HD 126614	1.15	0.56	1.2	0.14	Takeda et al. (2007)
HD 128311	0.83	0.21	0.99	0.57	Takeda et al. (2007)
HD 130322	0.84	0.01	0.75	0.23	Takeda et al. (2007)
HD 131496	1.61	0.25	1.0	0.13	Johnson, Clanton, et al. (2011)
HD 134987	1.05	0.28	0.70	0.14	Takeda et al. (2007)
HD 141937	1.05	0.13	0.60	0.20	Takeda et al. (2007)
HD 142245	1.69	0.23	1.0	0.14	Johnson, Clanton, et al. (2011)
HD 149143	1.20	0.26	0.68	0.16	D. A. Fischer, Laughlin, et al. (2006)
HD 152581	0.93	-0.46	0.90	0.14	Johnson, Clanton, et al. (2011)
HD 154345	0.89	-0.11	0.76	0.20	Takeda et al. (2007)
HD 156279	0.93	0.14	0.80	0.16	Diaz et al (2012)
HD 156668	0.77	0.05	1.0	0.23	Howard et al. (2011a)
HD 158038	1.65	0.28	1.0	0.13	Johnson, Clanton, et al. (2011)
HD 163607	1.09	0.21	0.77	0.16	Giguere et al. (2012)
HD 164509	1.13	0.21	0.66	0.18	Giguere et al. (2012)
HD 164922	0.93	0.17	0.80	0.15	Takeda et al. (2007)
HD 168443	1.00	0.04	0.70	0.14	Pilyavsky et al. (2011)
HD 168746	0.92	-0.08	0.69	0.15	Takeda et al. (2007)
HD 169830	1.41	0.15	0.47	0.14	Takeda et al. (2007)
HD 170469	1.14	0.30	0.62	0.15	Takeda et al. (2007)
HD 175541	1.52	-0.11	0.89	0.13	Mortier et al. (2013)
HD 177830	1.46	0.30	1.1	0.12	Mortier et al. (2013)
HD 178911B	1.06	0.29	0.73	0.18	Valenti and D. A. Fischer (2005)
HD 179079	1.09	0.29	0.74	0.16	Valenti, D. Fischer, et al. (2009)
HD 180902	1.52	0.0	0.93	0.15	Mortier et al. (2013)
HD 181342	1.58	0.15	1.0	0.12	Mortier et al. (2013)
HD 183263	1.12	0.30	0.63	0.15	Takeda et al. (2007)
HD 187123	1.04	0.12	0.61	0.15	Takeda et al. (2007)
HD 188015	1.06	0.29	0.70	0.16	Takeda et al. (2007)
HD 189733	0.81	-0.03	0.93	0.50	Torres, Winn, and Holman (2008)
HD 190228	1.82	-0.18	0.75	0.17	Takeda et al. (2007)
HD 190360	0.98	0.21	0.73	0.14	Takeda et al. (2007)
HD 192263	0.80	0.05	0.93	0.48	Takeda et al. (2007)

Continued on next page

Table 2.1 – continued from previous page

Star	Mass [$M_\odot$]	[Fe/H]	$B-V$	S_{HK}	References
HD 192310	0.85	-0.04	0.87	0.19	Pepe et al. (2011)
HD 195019	1.03	0.07	0.64	0.16	Takeda et al. (2007)
HD 200964	1.44	-0.15	0.88	0.14	Mortier et al. (2013)
HD 206610	1.56	0.10	1.0	0.14	Mortier et al. (2013)
HD 207832	0.94	0.06	0.69	0.24	Haghighipour, Butler, et al. (2012)
HD 209458	1.13	0.0	0.53	0.16	Takeda et al. (2007)
HD 210277	0.99	0.21	0.71	0.15	Takeda et al. (2007)
HD 212771	1.15	-0.14	0.88	0.14	Mortier et al. (2013)
HD 217107	1.11	0.39	0.72	0.14	Takeda et al. (2007)
HD 222582	0.97	-0.03	0.60	0.16	Takeda et al. (2007)
HD 224693	1.33	0.34	0.63	0.14	Johnson, Marcy, et al. (2006)
HD 231701	1.14	0.07	0.53	0.17	D. A. Fischer, Vogt, et al. (2007)

Notes. All of these systems are HD numbers except where otherwise specified.

[1]Alternate name HD 143761
[2]Alternate name HD 186427
[3]Alternate name HD 90043
[4]Alternate name HD 217014
[5]Alternate name HD 117176
[6]Alternate name HD 285968
[7]Alternate name HIP 22627
[8]Alternate name HIP 83043
[9]Alternate name HIP 109388

Table 2.2: Radial Velocity Observations

System	N_{obs}	Start Date	End Date	Duration [days]	Trend [m s^{-1} yr^{-1}]	Jitter [m s^{-1}]	Orbital Soln Ref
ρ CrB	210	1997 Jun 2	2015 Feb 8	6460	$0.16^{+0.13}_{-0.12}$	$1.1^{+0.0036}_{-0.0037}$	Butler, Wright, et al. (2006)
16 Cyg B	135	2006 Jul 11	2014 Dec 9	3073	$0.099^{+0.13}_{-0.13}$	$2.4^{+0.19}_{-0.18}$	Butler, Wright, et al. (2006)
24 Sex	44	2008 Dec 5	2013 Dec 12	1833	$-0.062^{+1.4}_{-1.5}$	$7.3^{+1.3}_{-0.96}$	Johnson, Clanton, et al. (2011)
51 Peg	43	2006 Jul 10	2014 Sep 13	2987	$-0.42^{+0.20}_{-0.20}$	$2.4^{+0.37}_{-0.31}$	Butler, Wright, et al. (2006)
70 Vir	56	2006 Jul 17	2015 Feb 4	3124	$0.14^{+0.25}_{-0.25}$	$3.5^{+0.44}_{-0.37}$	Kane et al. (2015)
GJ 176	71	1998 Jan 26	2014 Sep 6	6067	$0.33^{+0.35}_{-0.34}$	$4.9^{+0.61}_{-0.48}$	Forveille et al. (2009)
GJ 179	43	2000 Feb 6	2014 Aug 24	5313	$-0.62^{+0.55}_{-0.57}$	$5.8^{+1.1}_{-0.93}$	Howard, Johnson, Marcy, D. A. Fischer, Wright, Bernat, et al. (2010)
GJ 317	48	2000 Jan 7	2013 Dec 10	2535	$= 0 \pm 0$ [10]	$8.6^{+1.2}_{-1.0}$	Anglada-Escudé et al. (2012)
GJ 649	52	1999 Aug 19	2014 Feb 20	5299	$0.58^{+0.49}_{-0.48}$	$4.5^{+0.63}_{-0.51}$	Johnson, Howard, Marcy, et al. (2010)
GJ 849	87	1997 Jun 6	2014 Aug 14	6278	$0.32^{+2.5}_{-2.6}$	$3.5^{+0.41}_{-0.37}$	Bonfils et al. (2013)
HD 1461	218	1996 Oct 10	2015 Feb 7	6694	$-0.0064^{+0.87}_{-0.65}$	$3.8^{+0.14}_{-0.13}$	Rivera et al. (2010)
HD 1502	61	2007 Aug 27	2013 Dec 12	2299	$-0.46^{+1.1}_{-1.1}$	$11.^{+1.2}_{-1.0}$	Johnson, Clanton, et al. (2011)
HD 3651	91	1996 Oct 10	2015 Feb 7	6694	$0.50^{+0.14}_{-0.14}$	$3.1^{+0.30}_{-0.26}$	Wittenmyer et al. (2009)
HD 4203	46	2000 Jul 31	2014 Dec 11	5246	$= 0 \pm 0$ [10]	$3.4^{+0.54}_{-0.45}$	Butler, Wright, et al. (2006)
HD 4208	12	2005 Aug 21	2014 Sep 6	3303	$-1.2^{+0.30}_{-0.30}$	$3.8^{+0.51}_{-0.44}$	Butler, Wright, et al. (2006)
HD 4313	43	2007 Aug 27	2014 Aug 4	2534	$-1.1^{+0.42}_{-0.42}$	$4.2^{+0.65}_{-0.54}$	Johnson, Howard, Marcy, et al. (2010)
HD 5319	87	2004 Jan 10	2014 Dec 11	3988	$0.50^{+0.31}_{-0.31}$	$6.7^{+0.61}_{-0.55}$	Robinson et al. (2007)
HD 5891	63	2007 Aug 27	2013 Dec 14	2301	$0.86^{+4.2}_{-4.2}$	$33.^{+3.4}_{-2.9}$	Johnson, Clanton, et al. (2011)
HD 8574	25	1999 Feb 17	2014 Aug 12	5655	$0.31^{+0.96}_{-1.0}$	$-7.2^{+15.}_{-2.1}$	Wittenmyer et al. (2009)
HD 10697	77	1996 Oct 10	2014 Jul 8	6480	$0.17^{+0.36}_{-0.35}$	$6.0^{+0.59}_{-0.51}$	Wittenmyer et al. (2009)
HD 11506	125	2004 Jan 10	2015 Feb 7	4046	$-7.4^{+0.47}_{-0.47}$	$9.9^{+0.71}_{-0.63}$	D. A. Fischer, Vogt, et al. (2007)
HD 11964A	149	1996 Oct 9	2014 Aug 4	6508	$-0.22^{+0.13}_{-0.13}$	$3.2^{+0.23}_{-0.21}$	Wright, Upadhyay, et al. (2009)
HD 12661	98	1998 Dec 23	2014 Aug 12	5711	$-0.11^{+0.19}_{-0.18}$	$2.7^{+0.28}_{-0.25}$	Wright, Upadhyay, et al. (2009)
HD 13931	57	1998 Jan 24	2014 Jul 27	6028	$-0.14^{+0.37}_{-0.39}$	$2.8^{+0.39}_{-0.32}$	Howard, Johnson, Marcy, D. A. Fischer, Wright, Bernat, et al. (2010)
HD 16141	90	1996 Oct 9	2014 Aug 11	6515	$-0.37^{+0.19}_{-0.19}$	$3.3^{+0.33}_{-0.30}$	Butler, Wright, et al. (2006)
HD 17156	48	2006 Jan 11	2014 Sep 10	3164	$-0.13^{+0.41}_{-0.41}$	$3.2^{+0.85}_{-0.96}$	Barbieri et al. (2009)
HD 24040	60	1998 Jan 25	2014 Aug 5	6036	$2.0^{+0.34}_{-0.35}$	$4.7^{+0.54}_{-0.47}$	Boisse, Bonfils, and Santos (2012)
HD 28678	39	2007 Aug 27	2014 Aug 25	2555	$3.9^{+0.99}_{-1.0}$	$6.4^{+0.99}_{-0.82}$	Johnson, Clanton, et al. (2011)

Continued on next page

Table 2.2 – continued from previous page

System	N_{obs}	Start Date	End Date	Duration [days]	Trend [m s^{-1} yr^{-1}]	Jitter [m s^{-1}]	Orbital Soln Ref
HD 30856	22	2007 Aug 27	2013 Dec 14	2301	$-2.4^{+1.4}_{-1.5}$	$6.1^{+1.5}_{-1.1}$	Johnson, Clanton, et al. (2011)
HD 33142	40	2007 Aug 27	2014 Sep 12	2573	$-1.3^{+0.97}_{-1.0}$	$1.4^{+0.079}_{-0.074}$	Johnson, Clanton, et al. (2011)
HD 33283	42	2004 Jan 10	2014 Sep 7	3893	$-0.18^{+0.27}_{-0.26}$	$3.3^{+0.55}_{-0.46}$	Johnson, Marcy, et al. (2006)
HD 33636	48	1998 Jan 25	2014 Sep 7	6069	$-0.56^{+0.35}_{-0.34}$	$4.2^{+0.59}_{-0.50}$	Butler, Wright, et al. (2006)
HD 34445	117	1998 Jan 25	2015 Feb 4	6219	$-0.93^{+0.32}_{-0.32}$	$6.7^{+0.51}_{-0.45}$	Howard, Johnson, Marcy, D. A. Fischer, Wright, Bernat, et al. (2010)
HD 37605	41	2006 Sep 3	2014 Sep 7	2926	$3.8^{+1.7}_{-5.3}$	$2.3^{+0.41}_{-0.35}$	Wang et al. (2012)
HD 38529	96	1996 Dec 1	2014 Aug 19	6470	$0.65^{+0.57}_{-0.55}$	$8.9^{+0.76}_{-0.67}$	Wright, Upadhyay, et al. (2009)
HD 38801	17	2006 Sep 3	2014 Sep 7	2926	$4.1^{+1.2}_{-1.3}$	$10.^{+3.3}_{-2.2}$	Harakawa et al. (2010)
HD 40979	35	2001 Nov 6	2014 Sep 8	4689	$-0.99^{+1.6}_{-1.6}$	$19.^{+3.1}_{-2.4}$	Wittenmyer et al. (2009)
HD 43691	19	2004 Jan 10	2014 Sep 6	3892	$-0.51^{+0.63}_{-0.60}$	$4.8^{+1.7}_{-1.1}$	da Silva et al. (2007)
HD 45350	58	1999 Dec 31	2014 Sep 10	5367	$-0.29^{+0.21}_{-0.20}$	$3.7^{+0.46}_{-0.39}$	Endl, Cochran, Wittenmyer, and Hatzes (2006)
HD 46375	57	1998 Sep 13	2014 Sep 10	5841	$-0.29^{+0.31}_{-0.30}$	$3.8^{+0.55}_{-0.46}$	Butler, Wright, et al. (2006)
HD 49674	79	2000 Dec 4	2014 Sep 8	5026	$-0.21^{+0.34}_{-0.33}$	$5.2^{+0.50}_{-0.44}$	Butler, Wright, et al. (2006)
HD 50499	61	1996 Dec 1	2013 Dec 14	6222	$= 0 \pm 0$ [11]	$4.6^{+0.60}_{-0.53}$	Vogt, Butler, et al. (2005)
HD 50554	41	1998 Dec 23	2015 Feb 4	5887	$-1.2^{+0.39}_{-0.37}$	$4.8^{+0.77}_{-0.64}$	Butler, Wright, et al. (2006)
HD 52265	65	1998 Jan 25	2014 Sep 7	6069	$0.63^{+0.25}_{-0.24}$	$4.4^{+0.51}_{-0.43}$	Butler, Wright, et al. (2006)
HIP 57050	43	2000 Feb 6	2013 Dec 14	5060	$0.88^{+0.85}_{-0.85}$	$8.1^{+1.3}_{-1.0}$	Haghighipour, Vogt, et al. (2010)
HD 66428	57	2000 Dec 4	2015 Feb 4	5175	$-3.1^{+0.23}_{-0.23}$	$3.5^{+0.45}_{-0.38}$	Butler, Wright, et al. (2006)
HD 68988	48	2000 Jan 8	2013 Dec 13	5088	$= 0 \pm 0$ [11]	$1.8^{+0.036}_{-0.042}$	Butler, Wright, et al. (2006)
HD 73534	46	2004 Jan 10	2015 Feb 8	4047	$0.62^{+0.29}_{-0.29}$	$3.8^{+0.53}_{-0.44}$	Valenti, D. Fischer, et al. (2009)
HD 74156	53	2001 Apr 8	2013 Dec 12	4631	$1.9^{+0.73}_{-0.74}$	$6.9^{+0.99}_{-0.85}$	Meschiari et al. (2011)
HD 75898	54	2004 Jan 10	2015 Feb 5	4044	$= 0 \pm 0$ [11]	$2.7^{+0.074}_{-0.076}$	Robinson et al. (2007)
HIP 79431	31	2009 Apr 6	2014 Aug 23	1965	$1.8^{+1.9}_{-2.0}$	$6.0^{+1.1}_{-0.88}$	Apps et al. (2010)
HD 80606	79	2001 Apr 8	2013 Dec 13	4632	$0.23^{+0.27}_{-0.28}$	$3.8^{+0.40}_{-0.35}$	Moutou et al. (2009)
HD 82886	35	2007 Apr 26	2013 Dec 12	2422	$-1.2^{+1.4}_{-1.5}$	$9.6^{+1.6}_{-1.3}$	Johnson, Clanton, et al. (2011)
HD 83443	37	2000 Dec 19	2015 Feb 8	5164	$-0.081^{+0.64}_{-0.64}$	$5.8^{+1.0}_{-0.82}$	Butler, Wright, et al. (2006)
HD 86081	41	2005 Nov 19	2013 Dec 14	2947	$-1.3^{+0.25}_{-0.25}$	$4.2^{+0.66}_{-0.55}$	Johnson, Marcy, et al. (2006)
HD 88133	53	2004 Jan 10	2013 Dec 11	3623	$-0.48^{+0.36}_{-0.35}$	$4.7^{+0.61}_{-0.51}$	Butler, Wright, et al. (2006)
HD 92788	37	2000 Jan 8	2014 Feb 20	5157	$= 0 \pm 0$ [11]	$3.7^{+0.069}_{-0.065}$	Butler, Wright, et al. (2006)

Continued on next page

Table 2.2 – continued from previous page

System	N_{obs}	Start Date	End Date	Duration [days]	Trend [m s^{-1} yr^{-1}]	Jitter [m s^{-1}]	Orbital Soln Ref
HD 95089	37	2007 Apr 26	2013 Dec 12	2422	$= 0 \pm 0$ [11]	$7.6^{+1.3}_{-1.1}$	Johnson, Howard, Marcy, et al. (2010)
HD 96063	22	2007 Apr 26	2013 Dec 11	2421	$-0.69^{+0.10}_{-1.0}$	$6.0^{+1.5}_{-1.1}$	Johnson, Clanton, et al. (2011)
HD 96167	59	2004 Jan 10	2013 Dec 14	3626	$-0.047^{+0.29}_{-0.29}$	$4.3^{+0.51}_{-0.44}$	Peek et al. (2009)
HD 97658	209	1997 Jan 14	2015 Feb 11	6602	$0.39^{+0.11}_{-0.12}$	$2.9^{+0.16}_{-0.15}$	Dragomir et al. (2013)
HD 99109	54	1998 Dec 24	2013 Dec 11	5466	$-0.73^{+0.56}_{-0.53}$	$7.0^{+0.10}_{-0.84}$	Butler, Wright, et al. (2006)
HD 99492	104	1997 Jan 13	2015 Feb 11	6603	$0.42^{+0.19}_{-0.19}$	$4.1^{+0.35}_{-0.31}$	Butler, Wright, et al. (2006)
HD 99706	33	2007 Nov 23	2014 Jul 7	2418	$-2.5^{+1.2}_{-1.1}$	$1.7^{+2.5}_{-0.57}$	Johnson, Clanton, et al. (2011)
HD 102195	31	2006 Jan 11	2013 Dec 11	2891	$1.3^{+0.69}_{-0.69}$	$10.^{+1.8}_{-1.4}$	Melo et al. (2007)
HD 102329	27	2007 Apr 26	2013 Dec 11	2421	$3.5^{+1.7}_{-1.8}$	$3.7^{+0.31}_{-0.35}$	Johnson, Clanton, et al. (2011)
HD 102956	31	2007 Apr 26	2013 Aug 9	2297	$0.39^{+1.3}_{-1.3}$	$7.3^{+1.2}_{-1.0}$	Johnson, Howard, Marcy, et al. (2010)
HD 104067	61	1997 Jan 13	2013 Dec 14	6179	$-0.16^{+0.43}_{-0.42}$	$6.0^{+0.71}_{-0.60}$	Ségransan et al. (2011)
HD 106270	27	2007 Apr 26	2014 Jul 13	2635	$1.9^{+1.7}_{-1.6}$	$12.^{+2.4}_{-1.8}$	Johnson, Clanton, et al. (2011)
HD 107148	57	2000 Jan 9	2013 Dec 11	5085	$0.20^{+0.44}_{-0.50}$	$5.0^{+0.64}_{-0.54}$	Butler, Wright, et al. (2006)
HD 108863	41	2007 Apr 26	2013 Dec 10	2420	$-1.2^{+0.98}_{-0.93}$	$6.5^{+0.91}_{-0.75}$	Johnson, Clanton, et al. (2011)
HD 108874	89	1999 Jun 11	2014 Aug 19	5548	$-0.30^{+0.23}_{-0.23}$	$3.4^{+0.36}_{-0.32}$	Wright, Upadhyay, et al. (2009)
HD 109749	28	2004 Jan 10	2013 Dec 14	3626	$0.75^{+0.19}_{-0.20}$	$1.9^{+0.48}_{-0.39}$	D. A. Fischer, Laughlin, et al. (2006)
HD 114729	48	1997 Jan 14	2013 Dec 12	6176	$0.16^{+0.35}_{-0.37}$	$4.2^{+0.61}_{-0.52}$	Butler, Wright, et al. (2006)
HD 114783	119	1998 Jun 19	2015 Feb 4	6074	$-0.18^{+0.34}_{-0.34}$	$3.8^{+0.30}_{-0.28}$	Wittenmyer et al. (2009)
HD 116029	28	2007 Apr 26	2014 Aug 25	2678	$0.83^{+1.0}_{-1.0}$	$6.2^{+1.5}_{-1.1}$	Johnson, Clanton, et al. (2011)
HD 117207	52	1997 Jan 14	2014 Jun 18	6364	$-0.074^{+0.33}_{-0.32}$	$3.2^{+0.47}_{-0.41}$	Butler, Wright, et al. (2006)
HD 126614	81	1999 Jan 21	2015 Feb 7	5861	$87.^{+1.2}_{-1.6}$	$3.1^{+0.33}_{-0.29}$	Howard, Johnson, Marcy, D. A. Fischer, Wright, Bernat, et al. (2010)
HD 128311	118	1998 Jun 19	2015 Feb 11	6081	$-0.18^{+0.70}_{-0.69}$	$16.^{+1.2}_{-1.1}$	Wittenmyer et al. (2009)
HD 130322	25	2000 Jul 30	2014 Jun 18	5071	$0.36^{+1.1}_{-1.1}$	$7.0^{+1.5}_{-1.1}$	Wittenmyer et al. (2009)
HD 131496	48	2007 Jun 6	2014 Jul 7	2588	$-1.5^{+1.1}_{-0.99}$	$7.6^{+1.0}_{-0.82}$	Johnson, Clanton, et al. (2011)
HD 134987	103	1996 Jul 12	2015 Feb 11	6788	$-0.32^{+0.68}_{-0.69}$	$3.1^{+0.29}_{-0.26}$	Jones et al. (2010)
HD 141937	33	2002 Aug 29	2014 Jul 9	4332	$-0.61^{+0.52}_{-0.53}$	$6.3^{+1.1}_{-0.86}$	Udry et al. (2002)
HD 142245	26	2007 Jun 6	2014 Jul 7	2588	$0.82^{+0.76}_{-0.74}$	$6.0^{+1.2}_{-0.91}$	Johnson, Clanton, et al. (2011)
HD 149143	48	2004 Jul 11	2014 Aug 13	3685	$0.12^{+0.40}_{-0.40}$	$6.7^{+0.88}_{-0.75}$	D. A. Fischer, Laughlin, et al. (2006)
HD 152581	30	2007 Jun 6	2014 Jul 24	2605	$0.22^{+0.71}_{-0.71}$	$5.1^{+0.93}_{-0.75}$	Johnson, Clanton, et al. (2011)

Continued on next page

Table 2.2 – continued from previous page

System	N_{obs}	Start Date	End Date	Duration [days]	Trend [m s^{-1} yr^{-1}]	Jitter [m s^{-1}]	Orbital Soln Ref
HD 154345	113	1997 Apr 8	2015 Feb 4	6511	$0.053^{+0.19}_{-0.19}$	$2.8^{+0.25}_{-0.22}$	Wright, Marcy, Butler, Vogt, et al. (2008)
HD 156279	73	2003 Jul 12	2015 Feb 4	4225	$-5.1^{+6.0}_{-2.8}$	$2.2^{+0.27}_{-0.23}$	Diaz et al (2012)
HD 156668	219	2003 Jul 12	2015 Feb 5	4226	$-0.24^{+0.080}_{-0.085}$	$2.060^{+0.092}_{-0.085}$	Howard et al. (2011b)
HD 158038	33	2007 Jun 6	2015 Feb 4	2800	$= 0 \pm 0$ [11]	$12.^{+4.4}_{-2.0}$	Johnson, Clanton, et al. (2011)
HD 163607	66	2005 Jul 19	2015 Feb 4	3487	$2.3^{+0.37}_{-0.39}$	$4.4^{+0.50}_{-0.43}$	Giguere et al. (2012)
HD 164509	57	2005 Jul 19	2014 Sep 8	3338	$-3.3^{+0.56}_{-0.53}$	$6.2^{+0.76}_{-0.64}$	Giguere et al. (2012)
HD 164922	166	1996 Jul 11	2015 Feb 8	6786	$-0.030^{+0.10}_{-0.10}$	$3.0^{+0.20}_{-0.18}$	Butler, Wright, et al. (2006)
HD 168443	139	1996 Jul 12	2014 Aug 11	6604	$-3.0^{+0.16}_{-0.16}$	$3.6^{+0.27}_{-0.25}$	Pilyavsky et al. (2011)
HD 168746	27	2000 Jul 30	2014 Jul 26	5109	$-0.24^{+0.30}_{-0.30}$	$2.6^{+0.77}_{-0.61}$	Butler, Wright, et al. (2006)
HD 169830	52	2000 Jul 30	2014 Sep 10	5155	$-0.30^{+0.30}_{-0.29}$	$4.5^{+0.64}_{-0.53}$	Mayor et al. (2004)
HD 170469	42	2000 Jun 10	2014 Jun 22	5125	$0.93^{+0.50}_{-0.52}$	$4.5^{+0.69}_{-0.56}$	D. A. Fischer, Vogt, et al. (2007)
HD 175541	81	1996 Jul 19	2014 Jul 25	6580	$0.66^{+0.40}_{-0.41}$	$6.4^{+0.61}_{-0.53}$	Johnson, Butler, et al. (2007)
HD 177830	121	1996 Jul 11	2014 Sep 6	6631	$0.097^{+0.27}_{-0.27}$	$4.7^{+0.36}_{-0.33}$	Butler, Wright, et al. (2006)
HD 178911b	41	1999 Jun 12	2014 Aug 11	5539	$-0.070^{+0.47}_{-0.47}$	$5.5^{+0.82}_{-0.66}$	Wittenmyer et al. (2009)
HD 179079	84	2004 Jul 11	2014 Sep 8	3711	$0.15^{+0.33}_{-0.33}$	$3.9^{+0.38}_{-0.33}$	Valenti, D. Fischer, et al. (2009)
HD 180902	26	2007 Aug 27	2014 Aug 11	2541	$470^{+5.7}_{-6.0}$	$4.4^{+1.0}_{-0.77}$	Johnson, Howard, Marcy, et al. (2010)
HD 181342	30	2007 Aug 27	2014 Aug 11	2541	$-0.43^{+1.5}_{-1.5}$	$12.^{+2.0}_{-1.6}$	Johnson, Howard, Marcy, et al. (2010)
HD 183263	73	2001 Jul 4	2014 Dec 11	4908	$-2.5^{+4.6}_{-2.6}$	$3.4^{+0.39}_{-0.34}$	Wright, Upadhyay, et al. (2009)
HD 187123	113	1997 Dec 23	2014 Sep 6	6101	$-0.22^{+0.24}_{-0.22}$	$2.4^{+0.23}_{-0.21}$	Wright, Upadhyay, et al. (2009)
HD 188015	63	2000 Jul 29	2014 Sep 6	5152	$-0.21^{+0.33}_{-0.33}$	$4.7^{+0.54}_{-0.47}$	Butler, Wright, et al. (2006)
HD 189733	28	2003 Jul 12	2014 Aug 24	4061	$-0.63^{+1.0}_{-1.0}$	$14.^{+2.6}_{-2.0}$	Bouchy et al. (2005)
HD 190228	31	2002 Aug 28	2013 Dec 11	4123	$-0.36^{+0.61}_{-0.61}$	$4.7^{+0.90}_{-0.70}$	Wittenmyer et al. (2009)
HD 190360	150	1996 Oct 9	2014 Jun 22	6465	$-0.32^{+0.15}_{-0.15}$	$2.8^{+0.21}_{-0.20}$	Wright, Upadhyay, et al. (2009)
HD 192263	39	1998 Jun 19	2014 Sep 7	5924	$-0.38^{+0.69}_{-0.66}$	$8.1^{+1.2}_{-0.97}$	Butler, Wright, et al. (2006)
HD 192310	112	2004 Aug 20	2014 Sep 10	3673	$0.26^{+0.14}_{-0.14}$	$2.1^{+0.19}_{-0.17}$	Pepe et al. (2011)
HD 195019	57	1998 Sep 12	2014 Sep 11	5843	$1.1^{+0.37}_{-0.36}$	$4.7^{+0.58}_{-0.50}$	Butler, Wright, et al. (2006)
HD 200964	58	2007 Oct 26	2014 Sep 11	2512	$-0.38^{+0.55}_{-0.53}$	$5.1^{+0.65}_{-0.54}$	Johnson, Clanton, et al. (2011)
HD 206610	38	2007 Aug 1	2014 Aug 9	2565	$-8.8^{+0.68}_{-0.63}$	$4.9^{+0.80}_{-0.65}$	Johnson, Howard, Marcy, et al. (2010)
HD 207832	63	2004 Jul 4	2013 Oct 20	3395	$-2.3^{+1.3}_{-0.89}$	$7.7^{+0.99}_{-0.82}$	Haghighipour, Butler, et al. (2012)

Continued on next page

Table 2.2 – continued from previous page

System	N_{obs}	Start Date	End Date	Duration [days]	Trend [m s^{-1} yr^{-1}]	Jitter [m s^{-1}]	Orbital Soln Ref
HD 209458	81	1999 Jun 11	2014 Aug 19	5548	$0.10^{+0.32}_{-0.33}$	$5.9^{+0.56}_{-0.49}$	Torres, Winn, and Holman (2008)
HD 210277	139	1996 Jul 12	2014 Jul 22	6584	$0.36^{+0.16}_{-0.16}$	$3.6^{+0.26}_{-0.24}$	Butler, Wright, et al. (2006)
HD 212771	30	2007 Aug 27	2014 Aug 14	2544	$2.1^{+1.1}_{-1.2}$	$8.3^{+1.5}_{-1.2}$	Johnson, Howard, Marcy, et al. (2010)
HD 217107	123	1998 Sep 12	2014 Sep 8	5840	$-0.36^{+0.50}_{-0.47}$	$3.6^{+0.40}_{-0.30}$	Wright, Upadhyay, et al. (2009)
HD 222582	51	1997 Dec 23	2014 Aug 4	6068	$-0.21^{+0.32}_{-0.32}$	$3.3^{+0.47}_{-0.40}$	Butler, Wright, et al. (2006)
HD 224693	38	2004 Jul 4	2014 Aug 14	3693	$0.66^{+0.47}_{-0.47}$	$6.1^{+1.1}_{-0.85}$	Johnson, Marcy, et al. (2006)
HD 231701	28	2004 Jul 4	2014 Aug 11	3690	$0.067^{+0.79}_{-0.80}$	$6.4^{+1.5}_{-1.1}$	D. A. Fischer, Vogt, et al. (2007)

Notes. Systems with 3σ trends and above are listed in bold.

[10] Because this system has a new outer planet whose period is just covered by the RV baseline, we fix the trend to zero.

[11] Because the RV accelerations in systems HD 50499, HD 68988, HD 72659, HD 75898, HD 92788, and HD 158038 have some curvature, we fit them with a two planet solution. Since the partially resolved orbit and linear trend are degenerate, we fix the slope to zero in these fits. During these fits, we also fix the poorly constrained eccentricity of the outer planet to zero. One caveat is that we assume that the residual RV signals are due to a single body, even though they could be the sum of multiple bodies.

2.4 Analysis

Radial Velocity Fitting

The presence of a distant, massive companion manifests as a long-term acceleration for observations with baselines significantly shorter than the companion's orbital period (e.g. Crepp et al 2012). To detect and quantify the significance of these "trends", we performed a uniform analysis of these systems using a Markov Chain Monte Carlo technique.

The initial set of parameter values for the MCMC run were determined using a χ^2 minimization fitting procedure. For a single-planet system, the MCMC algorithm simultaneously fit eight free parameters to the RV data - six orbital parameters (the velocity semi-amplitude, the period of the orbit, the eccentricity of the orbit, the argument of periastron, the true anomaly of the planet at a given time, and the arbitrary RV zero point), a linear velocity trend, and a stellar jitter term (Isaacson and D. Fischer, 2010). This additional error term is added to the internal uncertainty of each radial velocity measurement in quadrature. All parameters had uniform priors. While it is formally correct to use log priors for parameters such as the velocity semi-amplitude, jitter term, and linear trend, we find that our use of uniform priors has a negligible effect on our posterior PDFs. We initialize our MCMC chains using the published parameters for the inner planets in these systems, which are typically quite close to our final best-fit parameters. Furthermore, we note that the choice of prior should only affect the posterior probability distributions in the data-poor regime; in this case the data provide good constraints on the parameters in question, and as a result the posterior PDF is effectively independent of our choice of prior. The likelihood function used in this analysis is given in Equation 2.1, where σ_i is the instrumental error, σ_{jit} is the stellar jitter, v are the data, and m is the model.

$$\mathscr{L} = \frac{1}{\sqrt{2\pi}\sqrt{\sigma_i^2 + \sigma_{jit}^2}} \exp\left(-0.5\left(\frac{(v-m)^2}{\sigma_i^2 + \sigma_{jit}^2}\right)\right) \tag{2.1}$$

The confidence intervals on each parameter were obtained from their posterior distribution functions.

On August 19 2004, the HIRES CCD was upgraded, leading to a different RV zero point for data taken before and after this date. For systems with Keck HIRES RVs obtained prior to 2004, we include an offset parameter between the two datasets as an additional free parameter. Although there is some evidence that the post-upgrade jitter is lower than the pre-upgrade jitter by approximately 1 m/s (e.g.

Table 2.3: Summary of AO Observations

Target	UT Obs. Date	Filter	Array	$T_{\rm int}$ [s]	$N_{\rm exp}$
HD 3651	2013 Aug 19	K_{cont}	256	9.0	12
HD 4208	2013 Nov 17	K_{cont}	1024	10.0	15
HD 11506	2013 Nov 17	K_{cont}	1024	10.0	15
HD 24040	2015 Jan 10	K_{cont}	1024	13.6	12
HD 28678	2014 Oct 04	K_{cont}	1024	13.6	12
HD 38801	2014 Dec 7	K_{cont}	1024	12.5	12
HD 38801	2014 Jan 12	K_p	1024	9.0	9
HD 50499	2014 Nov 07	K_{cont}	1024	13.6	12
HD 50554	2013 Dec 18	K_{cont}	1024	10.0	12
HD 66428	2013 Dec 18	K_{cont}	1024	10.0	12
HD 68988	2013 Dec 18	K_{cont}	1024	10.0	12
HD 72659	2014 Jan 12	K_{cont}	1024	9.0	15
HD 72659	2014 Nov 10	K_{cont}	1024	13.6	12
HD 75898	2014 May 21	Kc	1024	12.5	12
HD 75898	2014 May 21	Jc	1024	12.5	12
HD 86081	2013 Dec 18	K_{cont}	1024	10.0	12
HD 86081	2014 Dec 5	K_{cont}	1024	12.0	12
HD 92788	2014 Dec 5	K_{cont}	1024	13.6	12
HD 109749	2014 Jun 09	K_{cont}	1024	12.5	12
HD 158038	2013 Jul 17	BrG	1024	2.8	25
HD 163607	2013 Aug 19	K_{cont}	1024	9.0	12
HD 168443	2013 Aug 19	K_{cont}	512	10.0	12
HD 180902	2014 Jul 12	K_{cont}	1024	13.6	12
HD 206610	2013 Aug 19	K_{cont}	1024	9.0	12

Notes. The "Array" column denotes the horizontal width, in pixels, of the section of the detector used to capture the image. All PHARO images are taken in the full 1024×1024 array. The NIRC2 array dimensions used in this survey were 1024×1024 (the full array), 512×512, or 256×264. These dimensions are constrained by NIRC2's readout software. The $T_{\rm int}$ column indicates the total integration time of a single exposure, in seconds, and the $N_{\rm exp}$ column indicates the number of exposures used in the final stacked image. System HD158038 was imaged using PHARO; the rest were imaged using NIRC2.

Howard et al. 2014), we find that this change is much smaller than the average jitter level for the majority of our targets, and our decision to fit a single jitter term across both epochs is therefore unlikely to have a significant effect on our conclusions. Approximately 30% of our targets have no pre-upgrade data at all, while an additional 50% have fewer than ten data points pre- or post-upgrade, making it difficult to obtain meaningful constraints on the change in jitter between these two epochs (e.g., Fulton et al. 2015). We therefore conclude that a uniform approach to these fits is preferable to a more customized approach in which we include two separate jitter terms for the approximately 20% of systems where such an approach is feasible.

In addition to reproducing the published solutions of confirmed exoplanets, we detected eight new long-period planets with fully resolved orbits in systems GJ 317, HD 4203, HD 33142, HD 95089, HD 99706, HD 102329, HD 116029, and HD 156279. Trends were previously mentioned for GJ 317 (Anglada-Escudé et al., 2012), HD 4203 (Butler, Wright, et al., 2006), HD 95089 (Johnson, Aller, et

al., 2010), HD 99706 (Johnson, Clanton, et al., 2011), and HD 116029 (Johnson, Clanton, et al., 2011).

We note that the two planets in HD 116029 are in 3:2 period commensurability. To assess whether a dynamical model fit was needed, we used the Mercury integrator to numerically integrate the orbits of both planets in HD 116029 in order to determine the magnitude of the change in orbital parameters. We found that over the observational window of $\sim$ 8 years, the orbital elements of both planets varied by less than a fraction of a percent. Thus we conclude that a Keplerian model fit is sufficient to characterize the planets in HD 116029. Relevant characteristics of the new outer planets are listed in Table 2.5, and the corresponding RV solutions are plotted in Figures 2.3 through 2.10. RV measurements for these eight systems are listed in Table 2.4.

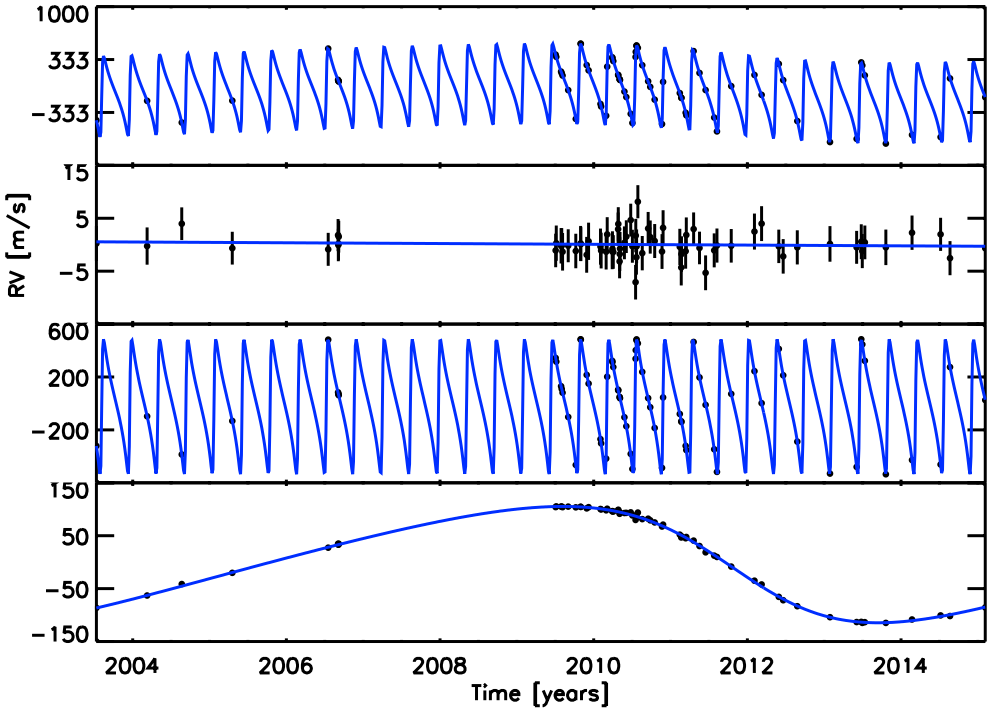

Figure 2.3: RV measurements and best fit models for HD 156279. The first and second panels show the combined two planet orbital solution and the residuals of that fit, respectively. The third plot shows the orbital solution for the inner planet after the outer planet solution and trend were subtracted, while the fourth plot shows the outer planet orbital solution with the inner planet and trend subtracted.

We considered a linear trend detection to be statistically significant if the best-fit slope differed from zero by more than 3σ, and report best-fit trend slopes and stellar

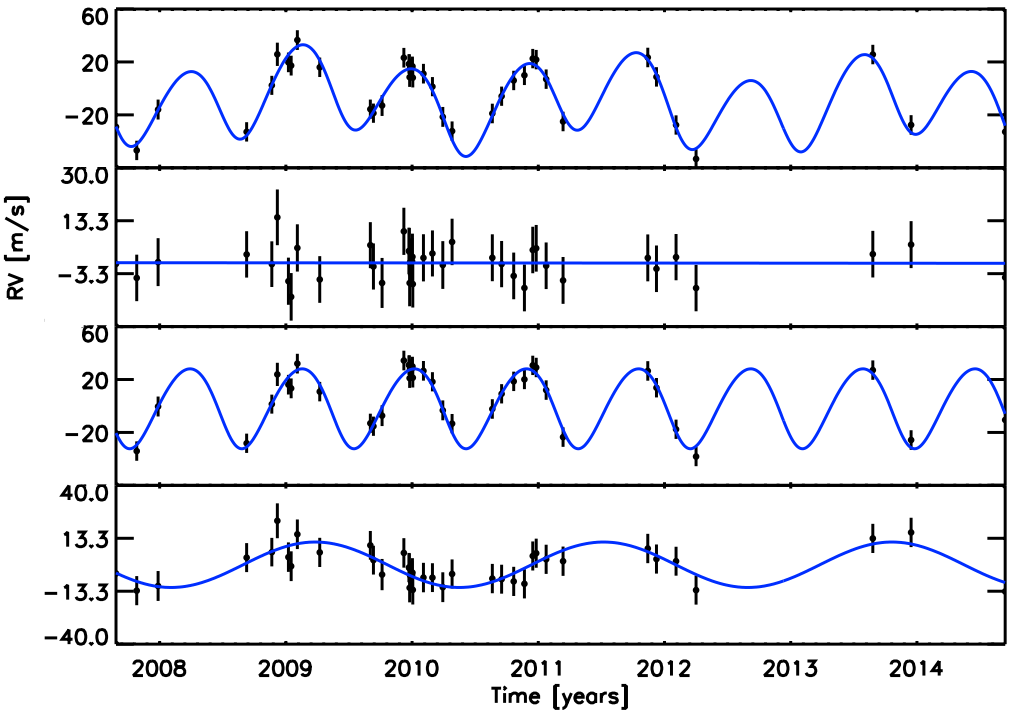

Figure 2.4: RV measurements and best fit models for the systems HD 33142. See caption to Figure 2.3 for more information.

jitter values for all systems in Table 2.2. The nominal values quoted in this table are taken from the χ^2 fits, and the errors come from the MCMC analysis. We detected 20 statistically significant trends due to the presence of an outer companion. We find that all but 16 of our orbital solutions for the known inner planets in these systems were consistent with the published orbits at the 2σ level or better.

Of the solutions that changed, the majority were systems with long-period planets for which our newly extended baseline provided a more tightly constrained orbital solution. This longer baseline was particularly important for systems with both long-period planets and RV accelerations, such as HD 190360. We present updated orbital solutions for all of the planets outside 3 AU in Table 2.5. We defer the publication of updated orbits for planets inside 3 AU and individual radial velocities for all systems to future publications, as these systems are the subject of other research projects currently in progress.

Table 2.4: RVs for Systems With New Planets: HD 156279, HD 33142, GJ 317, HD 90589, HD 4203, HD 99706, HD 102329, HD 116029

System	JD - 2,440,000	RV [m s^{-1}]	σ_{RV} [m s^{-1}]
HD 156279	12832.9	-436.3	1.084
HD 156279	13074.1	-191.6	1.302
HD 156279	13238.8	-465.2	0.870
HD 156279	13479.0	-184.7	0.874
HD 156279	13934.9	471.5	0.896
HD 156279	13981.8	77.0	0.814
HD 156279	13982.9	67.7	0.843
HD 156279	13983.8	61.7	0.845
HD 156279	13984.9	55.8	0.785
HD 156279	15016.0	395.2	0.951

Notes. The full set of RVs for each of these systems are available as electronic tables online.

Table 2.5: Updated Orbital Solutions for Planets Outside 3 AU and 8 New Planets

Planet	Period [days]	T_P -2,440,000 [days]	Eccentricity	ω [deg]	K [m s^{-1}]	Mass [M_{Jup}]	Stellar Mass [$M_\odot$]
HD 13931 b	4460^{+77}_{-67}	13359^{+1592}_{-826}	$0.033^{+0.030}_{-0.017}$	18^{+123}_{-67}	$23.92^{+0.90}_{-0.85}$	$1.92^{+0.08}_{-0.07}$	$1.022^{+0.020}_{-0.022}$
HD 24040 b	3498^{+23}_{-23}	12264^{+467}_{-348}	$0.010^{+0.015}_{-0.009}$	332^{+48}_{-36}	$51.4^{+1.4}_{-1.4}$	$4.08^{+0.11}_{-0.11}$	$1.18^{+0.10}_{-0.10}$
HD 33636 b	$2112.6^{+1.6}_{-1.6}$	$13305.9^{+3.5}_{-3.4}$	$0.488^{+0.005}_{-0.005}$	$336.18^{+0.90}_{-0.88}$	$160.9^{+1.0}_{-1.1}$	$8.98^{+0.06}_{-0.06}$	$1.017^{+0.032}_{-0.032}$
HD 50499 b	2453^{+27}_{-27}	13612^{+65}_{-67}	$0.334^{+0.059}_{-0.059}$	241^{+15}_{-14}	$18.4^{+1.6}_{-1.3}$	$1.36^{+0.12}_{-0.10}$	$1.280^{+0.034}_{-0.080}$
HD 66428 b	$2280.4^{+6.6}_{-6.6}$	12277^{+20}_{-20}	$0.448^{+0.016}_{-0.015}$	$179.7^{+3.1}_{-3.1}$	$51.4^{+1.5}_{-1.4}$	$3.09^{+0.07}_{-0.07}$	$1.061^{+0.070}_{-0.056}$
HD 72659 b	3506^{+40}_{-38}	15301^{+54}_{-59}	$0.249^{+0.028}_{-0.027}$	$272.7^{+8.4}_{-6.9}$	$39.0^{+2.4}_{-2.1}$	$2.99^{+0.19}_{-0.17}$	$1.068^{+0.022}_{-0.022}$
HD 73534 b	1707^{+37}_{-35}	14981^{+808}_{-280}	$0.022^{+0.058}_{-0.037}$	83^{+171}_{-60}	$15.2^{+1.1}_{-1.0}$	$1.02^{+0.07}_{-0.07}$	$1.170^{+0.070}_{-0.070}$
HD 106270 b	1872^{+20}_{-19}	14774^{+32}_{-28}	$0.197^{+0.035}_{-0.035}$	$7.5^{+6.1}_{-5.2}$	$137.3^{+4.4}_{-4.3}$	$9.78^{+0.28}_{-0.28}$	$1.330^{+0.050}_{-0.050}$
HD 117207 b	2628^{+21}_{-20}	13325^{+83}_{-83}	$0.150^{+0.026}_{-0.027}$	85^{+12}_{-12}	$27.8^{+0.95}_{-0.94}$	$1.90^{+0.07}_{-0.06}$	$1.031^{+0.046}_{-0.040}$
HD 154345 b	3267^{+33}_{-33}	15278^{+197}_{-359}	$0.038^{+0.027}_{-0.021}$	341^{+22}_{-40}	$17.05^{+0.48}_{-0.49}$	$1.15^{+0.03}_{-0.03}$	$0.893^{+0.038}_{-0.038}$
GJ 317 c	5312^{+758}_{-1248}	17424^{+1913}_{-3660}	$0.308^{+0.065}_{-0.079}$	194^{+27}_{-31}	30^{+36}_{-14}	$1.54^{+1.26}_{-0.57}$	$0.240^{+0.040}_{-0.040}$
HD 4203 c	7053^{+1624}_{-2324}	16179^{+1365}_{-1733}	$0.182^{+0.124}_{-0.172}$	$232.2^{+30.7}_{-32.5}$	$12.5^{+11.0}_{-5.0}$	$1.51^{+0.98}_{-0.57}$	$1.130^{+0.028}_{-0.100}$
HD 11964A c	1956^{+26}_{-25}	14189^{+682}_{-341}	$0.073^{+0.051}_{-0.037}$	158^{+125}_{-64}	$9.00^{+0.45}_{-0.45}$	$0.583^{+0.029}_{-0.029}$	$1.080^{+0.028}_{-0.012}$
HD 33142 c	834^{+29}_{-24}	15664^{+326}_{-117}	$0.05^{+0.172}_{-0.114}$	322^{+139}_{-53}	$11.4^{+2.0}_{-1.9}$	$5.97^{+1.04}_{-0.80}$	$1.620^{+0.090}_{-0.090}$
HD 37605 c	2455^{+468}_{-148}	14285^{+151}_{-213}	$0.^{+0.055}_{-0.029}$	136^{+18}_{-28}	$426^{+9.1}_{-3.1}$	$3.37^{+0.83}_{-0.26}$	$1.00^{+0.50}_{-0.50}$
HD 38529 c	$2132.4^{+3.2}_{-3.2}$	$14398.1^{+8.0}_{-8.0}$	$0.342^{+0.007}_{-0.007}$	$19.9^{+1.5}_{-1.5}$	$171.1^{+1.5}_{-1.5}$	$13.23^{+0.11}_{-0.12}$	$1.340^{+0.020}_{-0.020}$
HD 74156 c	2460^{+14}_{-15}	13440^{+16}_{-16}	$0.370^{+0.016}_{-0.016}$	$267.1^{+3.3}_{-3.2}$	$109.4^{+2.4}_{-2.3}$	$7.77^{+0.16}_{-0.16}$	$1.238^{+0.040}_{-0.044}$
HD 95089 c	1860^{+370}_{-570}	15492^{+43}_{-50}	$0.294^{+0.070}_{-0.067}$	$74.6^{+8.1}_{-9.8}$	$46.1^{+3.4}_{-4.7}$	$3.97^{+0.33}_{-0.59}$	$1.38^{+0.12}_{-0.12}$
HD 99706 c	1278^{+151}_{-198}	15383^{+249}_{-140}	$0.411^{+0.231}_{-0.178}$	136^{+64}_{-64}	$13.8^{+2.9}_{-2.5}$	$5.69^{+1.43}_{-0.96}$	$1.72^{+0.12}_{-0.12}$
HD 102329 c	1123^{+79}_{-53}	14736^{+569}_{-200}	$0.209^{+0.231}_{-0.202}$	21^{+165}_{-74}	$27.4^{+6.8}_{-4.5}$	$1.52^{+0.30}_{-0.25}$	$1.30^{+0.15}_{-0.15}$
HD 114783 c	4319^{+151}_{-130}	18112^{+422}_{-537}	$0.^{+0.091}_{-0.085}$	$6.5^{+37.9}_{-44.4}$	$9.21^{+0.71}_{-0.68}$	$0.611^{+0.056}_{-0.053}$	$0.853^{+0.034}_{-0.038}$
HD 116029 c	$907^{+30.}_{-29.}$	15291^{+134}_{-86}	$0.038^{+0.127}_{-0.075}$	$17.3^{+167.0}_{-49.7}$	$20.7^{+2.2}_{-2.2}$	$1.27^{+0.15}_{-0.15}$	$1.33^{+0.11}_{-0.11}$
HD 156279 c	4191^{+270}_{-310}	15912^{+17}_{-17}	$0.231^{+0.018}_{-0.021}$	$101.0^{+2.3}_{-1.9}$	$110.2^{+4.8}_{-5.3}$	$8.60^{+0.50}_{-0.55}$	$0.930^{+0.040}_{-0.040}$
HD 169830 c	$1834.3^{+8.3}_{-8.2}$	15350^{+40}_{-39}	$0^{+0.018}_{-0.019}$	$95.7^{+8.2}_{-7.9}$	$39.7^{+1.3}_{-1.3}$	$3.54^{+0.10}_{-0.10}$	$1.410^{+0.028}_{-0.112}$
HD 183263 c	5048^{+433}_{-701}	14952^{+77}_{-74}	$0.073^{+0.025}_{-0.034}$	$284.9^{+6.1}_{-5.4}$	$85.2^{+9.1}_{-14.5}$	$9.0^{+1.1}_{-1.7}$	$1.121^{+0.064}_{-0.040}$
HD 187123 c	3380^{+41}_{-40}	13649^{+42}_{-44}	$0.295^{+0.026}_{-0.025}$	$260.4^{+3.7}_{-3.7}$	$24.97^{+0.76}_{-0.70}$	$1.80^{+0.06}_{-0.06}$	$1.037^{+0.026}_{-0.024}$
HD 190360 c	2889^{+14}_{-14}	13548^{+32}_{-25}	$0.301^{+0.020}_{-0.020}$	$17.9^{+4.7}_{-3.8}$	$21.95^{+0.50}_{-0.49}$	$1.45^{+0.03}_{-0.03}$	$0.983^{+0.026}_{-0.048}$
HD 217107 c	5178^{+74}_{-67}	15951^{+49}_{-59}	$0.376^{+0.014}_{-0.014}$	$206.2^{+2.7}_{-2.7}$	$53.2^{+1.9}_{-1.7}$	$4.48^{+0.20}_{-0.18}$	$1.108^{+0.034}_{-0.052}$

Notes. New planet names are in bold.

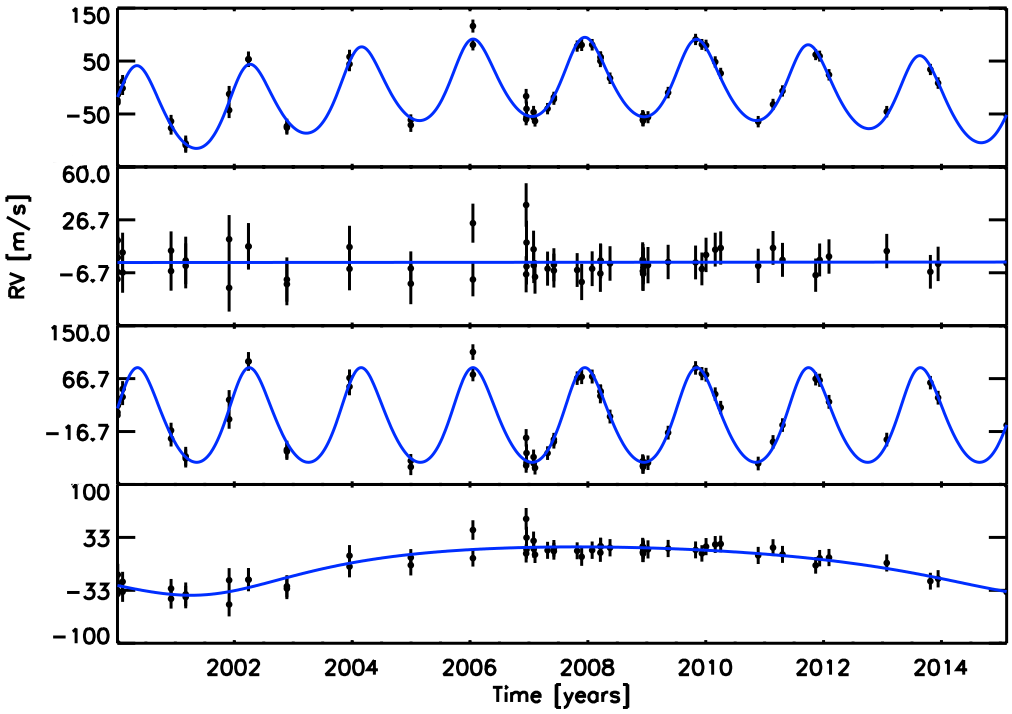

Figure 2.5: RV measurements and best fit models for GJ 317. See caption to Figure 2.3 for more information.

Non-Planetary Sources of RV Trends

There were two scenarios in which systems with statistically significant trend detections were excluded from further analysis. In two systems, we found that the observed accelerations were correlated with stellar activity. We compared the RV trends in each system to the measured emission in the Ca II H&K lines, quantified by the $S_{\rm HK}$ index (Wright, Marcy, Butler, and Vogt, 2004; Isaacson and D. Fischer, 2010), to determine if the RV trends were caused by stellar activity instead of an outer companion (Santos et al., 2010). Both HD 97658 and HD 1461 showed a clear correlation between the observed RV trend and the measured $S_{\rm HK}$ values, and we therefore excluded them from subsequent analysis.

We also excluded systems with a linear acceleration that could have been caused by a nearby directly imaged stellar companion. We first examined our K band AO images for all stars with statistically significant radial velocity trends in order to determine which systems contained a directly imaged stellar companion. HD 164509 has a companion 0.75" away, and HD 195109 has a companion 3.4" away. To determine whether these companions could have caused the RV trends in these systems, we

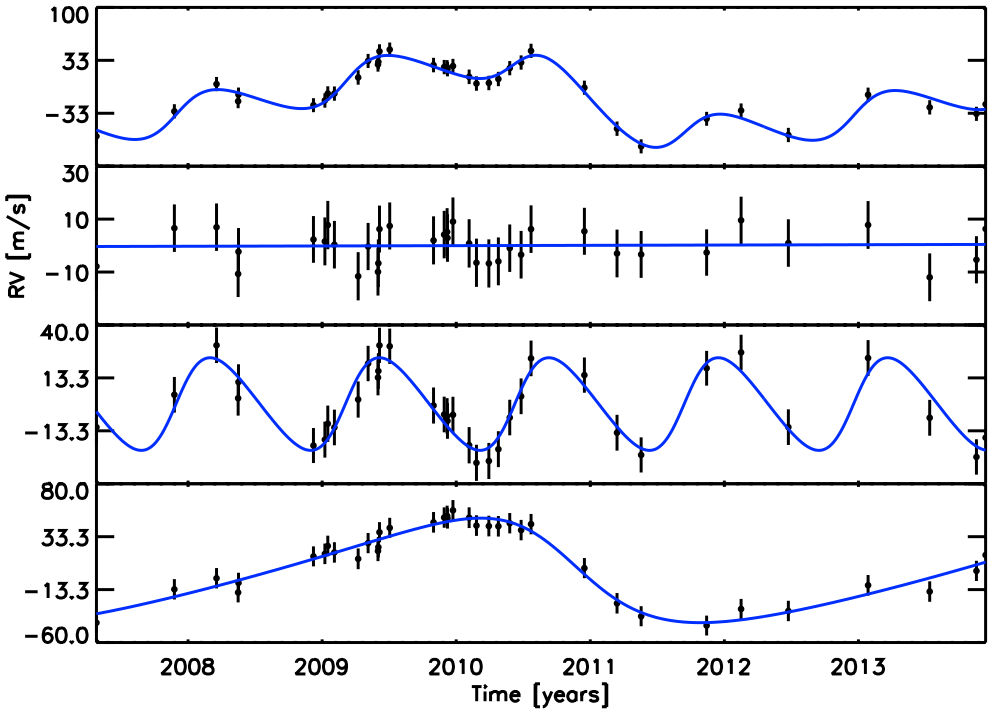

Figure 2.6: RV measurements and best fit models for HD 95089. See caption to Figure 2.3 for more information.

compared the minimum mass estimate from the RV trend to the companion mass estimate from the AO image. We calculated the minimum companion mass using the equation from Torres (1999):

$$M_{\rm comp} = 5.34 \times 10^{-6} M_{\odot} \left(\frac{d}{pc} \frac{\rho}{arcsec} \right)^2 \times \left| \frac{\dot{v}}{ms^{-1} yr^{-1}} \right| F(i, e, \omega, \phi) \qquad (2.2)$$

In this equation, d is the distance to the star, ρ is the projected separation of the companion and the star on the sky, $\dot{v}$ is the radial velocity trend, and $F(i, e, \omega, \phi)$ is a variable that depends on the orbital parameters of the companion that are currently unconstrained. We use a value of $\sqrt{27}/2$ for F, which is the minimum value of this function calculated in Liu et al (2002).

HD 164509 is 52 pc away and has a companion located at a separation of 0.75". With a radial velocity trend of 3.4 m s^{-1} yr^{-1}, this trend corresponds to a minimum companion mass of 0.072 $M_{\odot}$. To estimate the mass of the companion from the AO image, the brightness of the companion in K band relative to the primary is used, as described in subsection “Contrast Curves”. With a relative K band magnitude

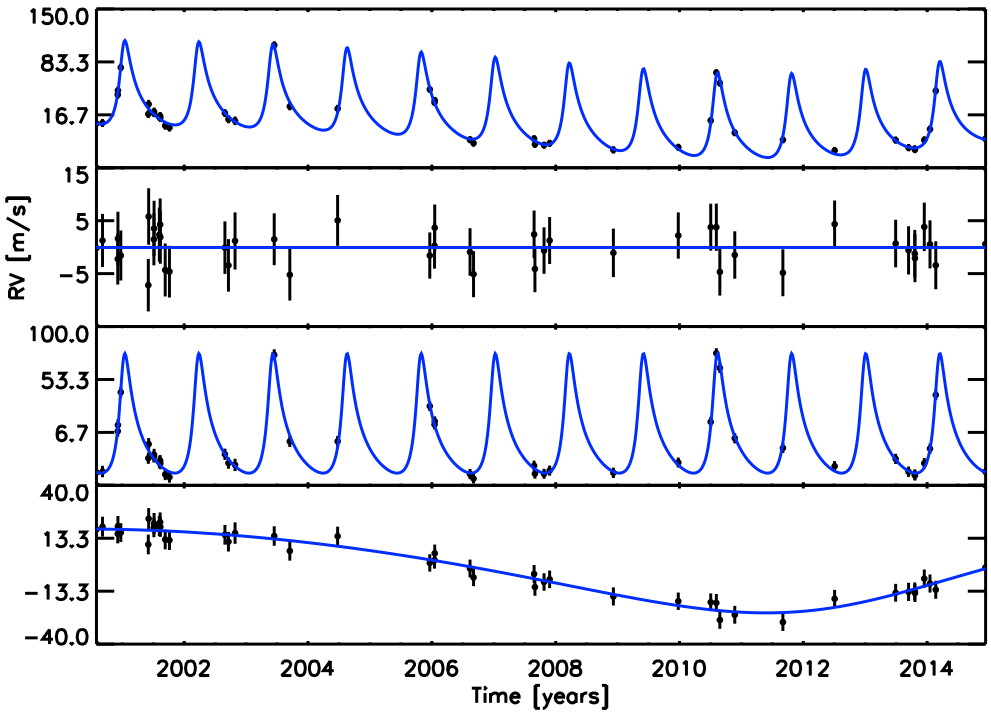

Figure 2.7: RV measurements and best fit models for HD 4203. See caption to Figure 2.3 for more information.

of 3.59, we find that the estimated mass from the AO data is 0.33 $M_{\odot}$. Since the companion mass calculated from the AO data is greater than the minimum mass needed to explain the RV trend, we therefore conclude that this companion may indeed be responsible for the observed trend and exclude this system from subsequent analysis.

HD 195109 is 38.5 pc away and has a companion located at a separation of 2.4". With a radial velocity acceleration of 1.9 m s^{-1} yr^{-1}, a stellar companion at the observed AO separation must have a mass of at least 0.44 $M_{\odot}$ in order to cause the observed trend. With a relative K-band magnitude of 2.66, we find that the estimated mass from the AO data is 0.58 $M_{\odot}$. We conclude that the imaged companion could have caused the RV acceleration, and thus removed this system from future analyses. We note that this companion was previously reported in Mugrauer et al. (2007).

Howard et al (2010) imaged a faint M-dwarf companion located 489.0 ± 1.9 mas from the primary star HD 126614. With an absolute K-band magnitude of 6.72, the authors estimated the mass of this companion to be 0.324 ± 0.004 $M_{\odot}$. From Equation 2.2, the estimated minimum mass of the companion inducing the RV trend,

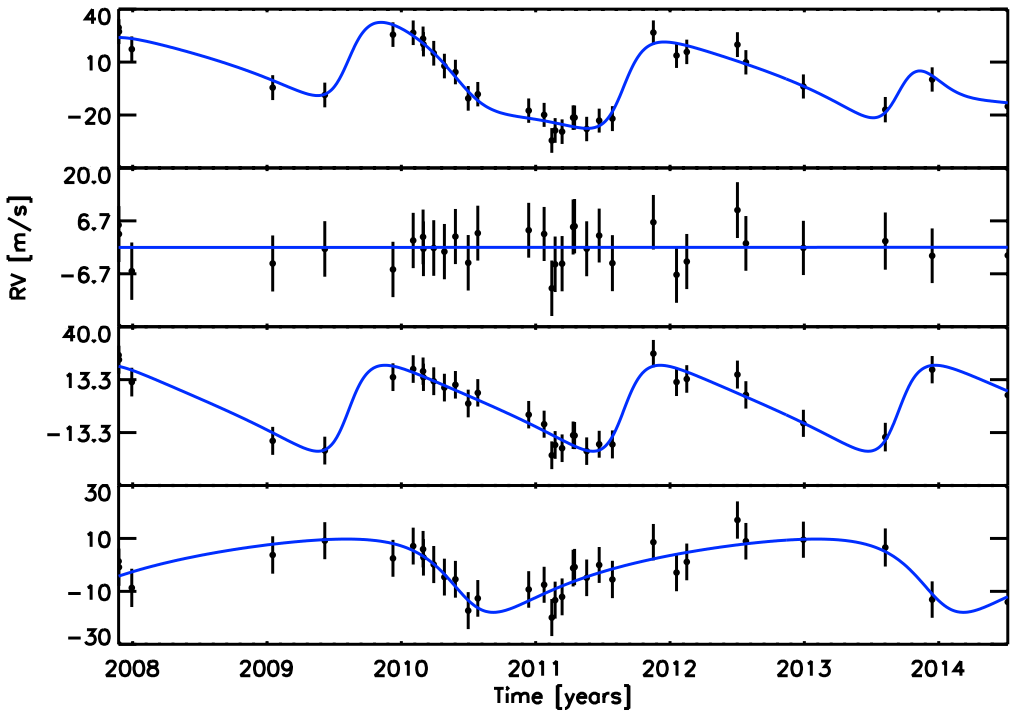

Figure 2.8: RV measurements and best fit models for HD 99706. See caption to Figure 2.3 for more information.

given a distance of 72.6 pc and a trend of 14.6 $ms^{-1}yr^{-1}$, is 0.26 $M_{\odot}$. Since the minimum estimated RV mass is lower than the estimated AO mass, we conclude that the imaged AO companion could cause the RV trend, and thus remove this system from subsequent analyses. Note that none of these AO companions have second epoch data, and thus have not been confirmed as bound to their respective primaries. However, at these projected separations and contrast ratios the probability that the companion is a background star is relatively low, and we therefore proceed under the assumption that they are bound.

We also carried out a literature search to determine whether any of the remaining trend systems had additional stellar or substellar companions. We found that HD 109749 has a known binary companion described in the published literature. HD 109749 has a companion with K-band magnitude of 8.123 separated by 8.35" (Desidera and Barbieri, 2007). This visual binary lies outside the field of view for our AO observations. After calculating the minimum companion mass from the measured RV trend and comparing this value to the estimated mass from the AO data found in the literature, we found that this companions cannot explain the

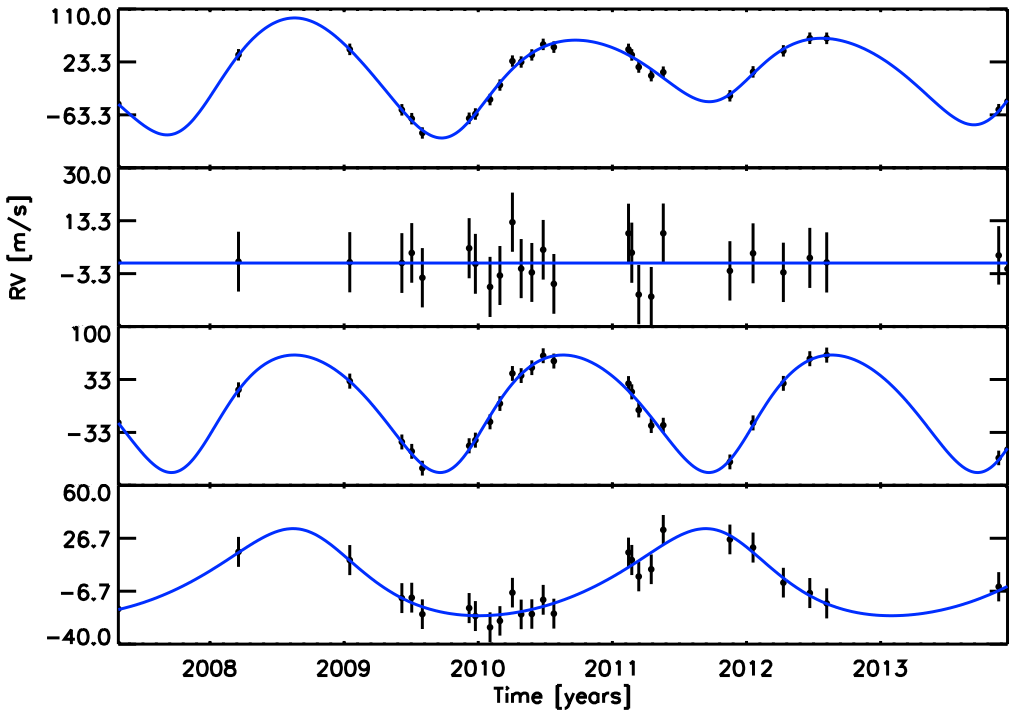

Figure 2.9: RV measurements and best fit models for HD 102329. See caption to Figure 2.3 for more information.

accelerations observed in these systems.

After removing stellar sources of RV trends, we find 20 systems with accelerations that have slopes at least 3σ away from zero. The RV data and best-fit accelerations for each of these systems are plotted in Figures 2.11, 2.12, and 2.13. Six of these trends were previously reported in the published literature: HD 24040 (Boisse, Bonfils, and Santos, 2012), HD 168443 (Pilyavsky et al., 2011), HD 180902 (Johnson, Aller, et al., 2010), HD 68988 (Butler, Wright, et al., 2006), HD 158038 (Johnson, Clanton, et al., 2011), and HD 50499 (Vogt, Butler, et al., 2005).

Contrast Curves

We used contrast curves from our AO observations to put limits on the masses and separations that a companion in each system could have. We calculate contrast curves for our target stars as follows. First, we measure the full width at half max (FWHM) of the central star's point spread function in the stacked and combined image, taking the average of the FWHM in the x and y directions as our reference value. We then create a box with dimensions equal to the FWHM and step it

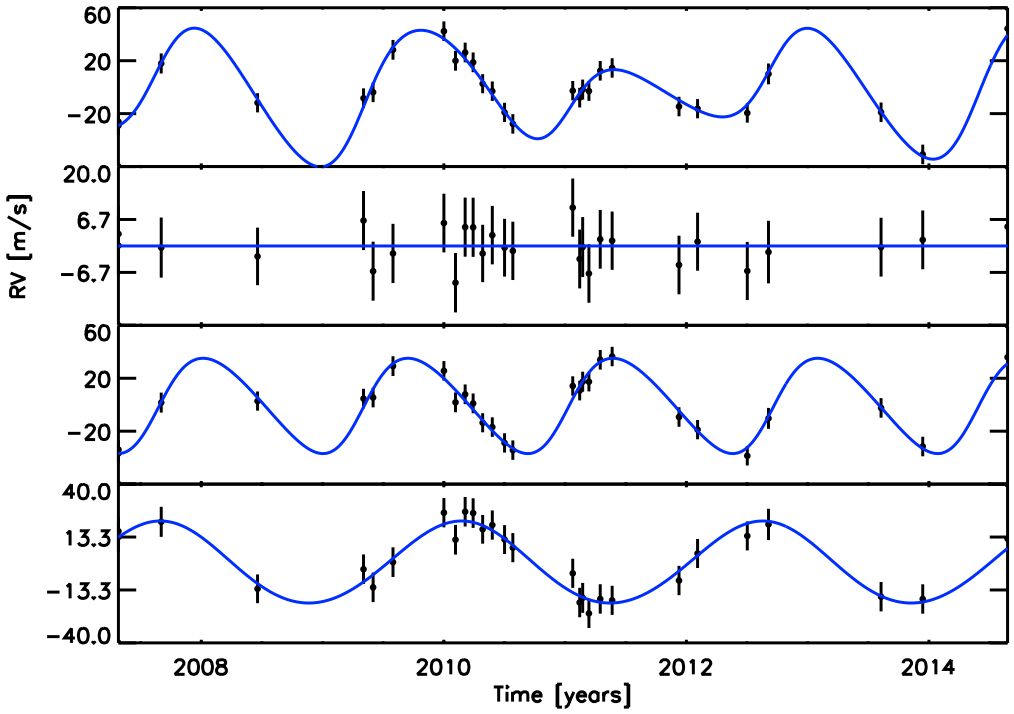

Figure 2.10: RV measurements and best fit models for HD 116029. See caption to Figure 2.3 for more information.

across the array, calculating the total flux from the pixels within the box at a given position. The 1σ contrast limit is then defined as the standard deviation of the total flux values for boxes located within an annulus with a width equal to twice the FWHM centered at the desired radial separation. We convert absolute flux limits to differential magnitude units by taking the total flux in a box of the same size centered on the peak of the stellar point spread function and calculating the corresponding differential magnitude at each radial distance. We show the resulting 5σ average contrast curve for these observations in Figure 2.14; although our field of view extends farther in some directions than the maximum separations shown here, we have limited our calculations to radial separations with data available at all position angles.

We next use our contrast curves to place limits on the allowed masses of stellar companions as a function of projected separation. We interpolate the PHOENIX stellar atmosphere models (Husser et al., 2013) in the available grid of solar metallicity models to produce a model that matches the effective temperatures and surface gravities of the primary star. For the proposed low-mass main sequence compan-

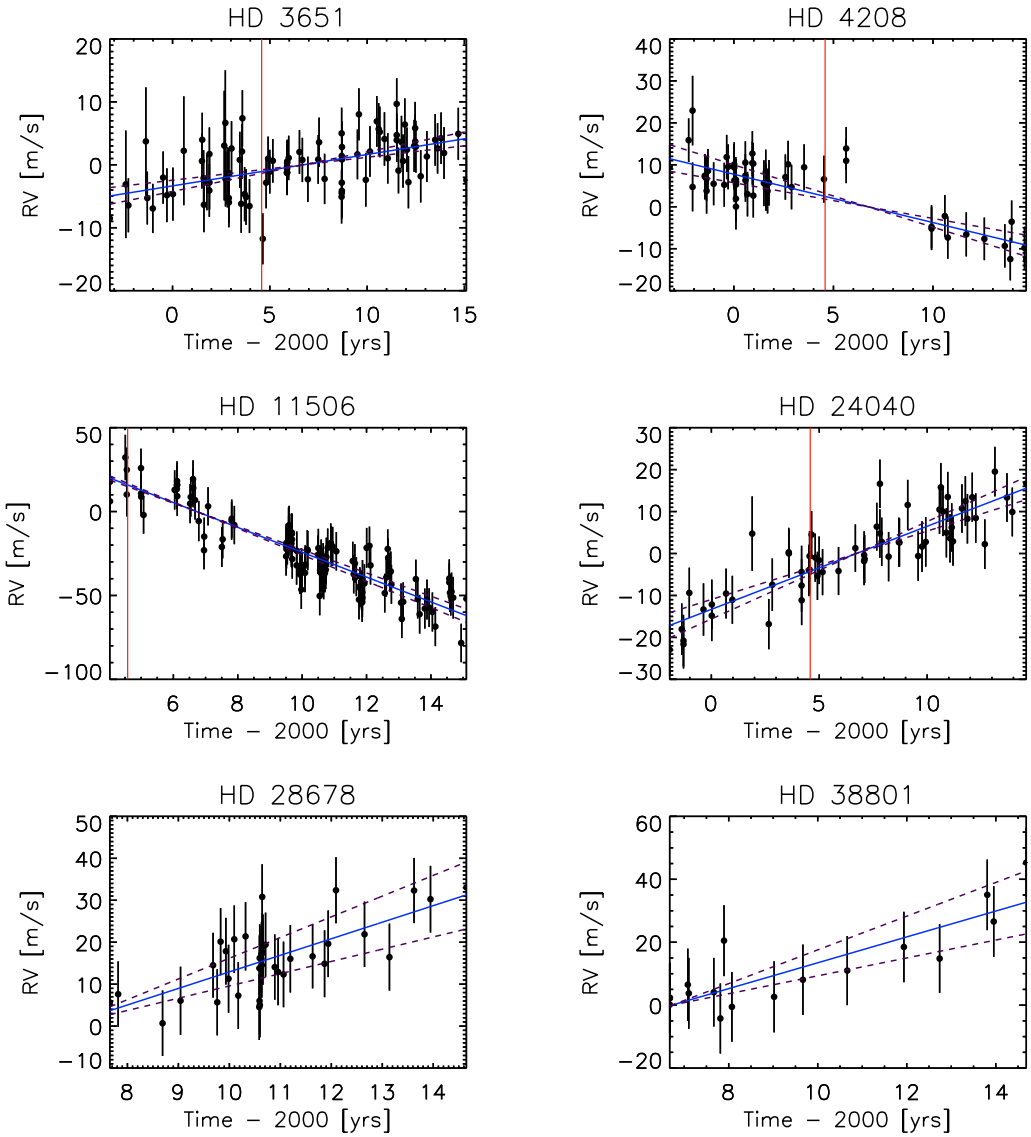

Figure 2.11: Best fit accelerations to the radial velocity data with a 3σ trend. The best fit trend is shown as a solid blue line, the errors on the slope are presented as dashed purple lines. The solid red line marks the date when the HIRES detector was replaced, which caused an offset in the measured RVs for the stars in our sample. The confirmed planet orbital solutions have been subtracted from both the RV data and from the best fit orbital solution to yield the trends. Systems with curved trends include HD 50499, HD 68988, HD 72659, HD 75898, HD 92788, and HD 158038. The plots with the curved trends show the best fit one planet orbital solution to the data after the inner planet solution was subtracted.

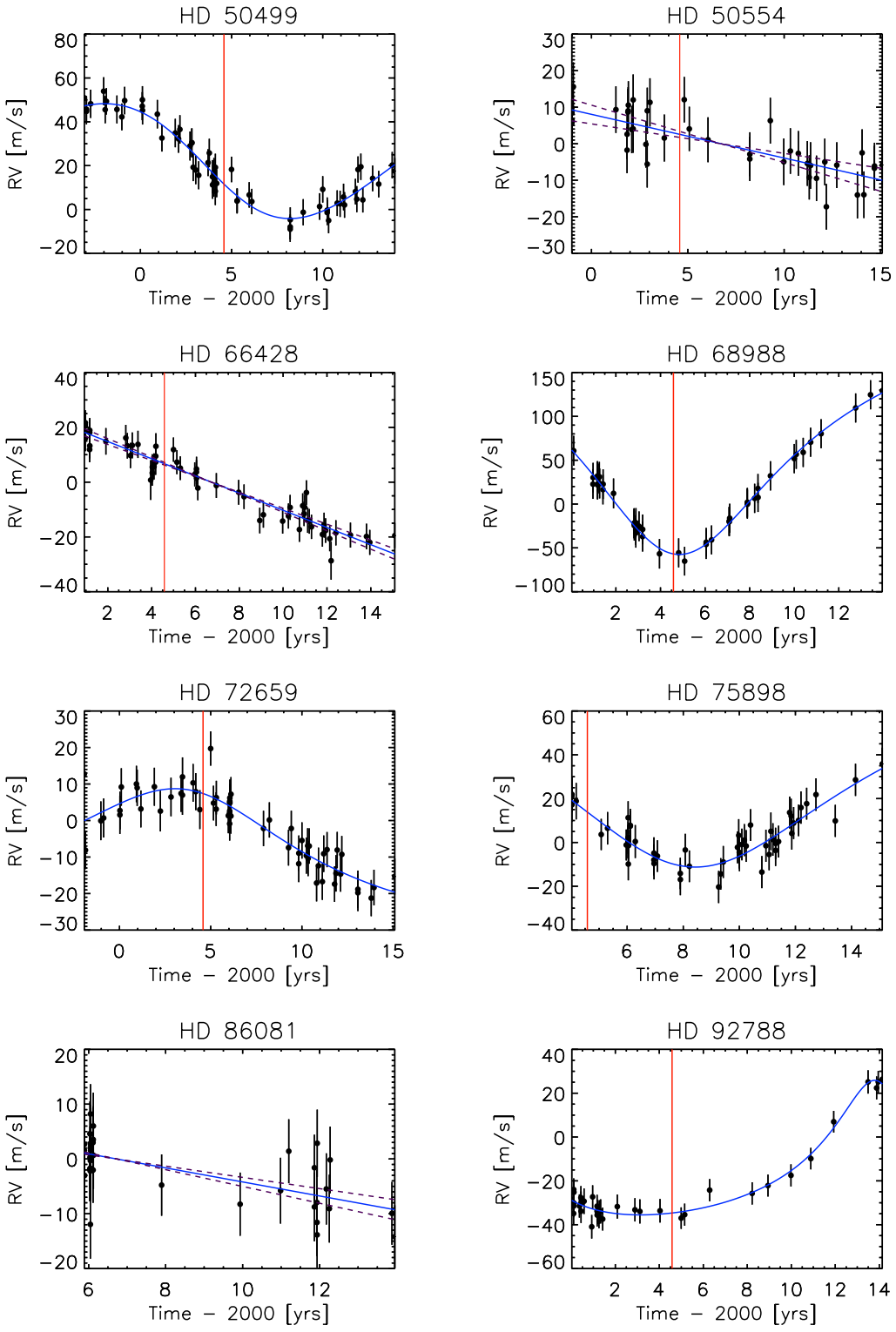

Figure 2.12: Best fit accelerations to the radial velocity data with a 3σ trend. See Figure 2.11 caption for more details.

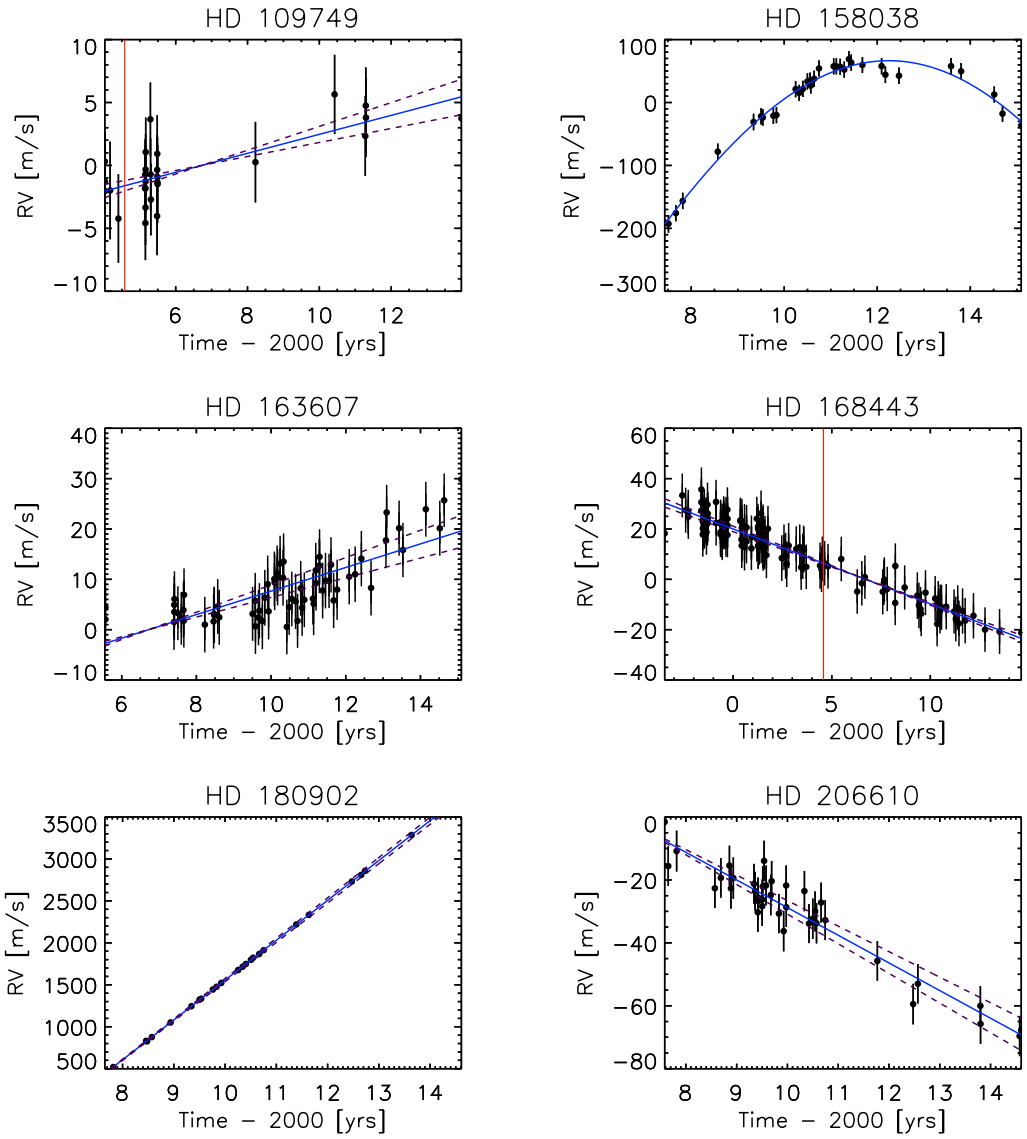

Figure 2.13: Remaining best fit accelerations to the radial velocity data with a 3σ trend. See Figure 2.11 caption for more details.

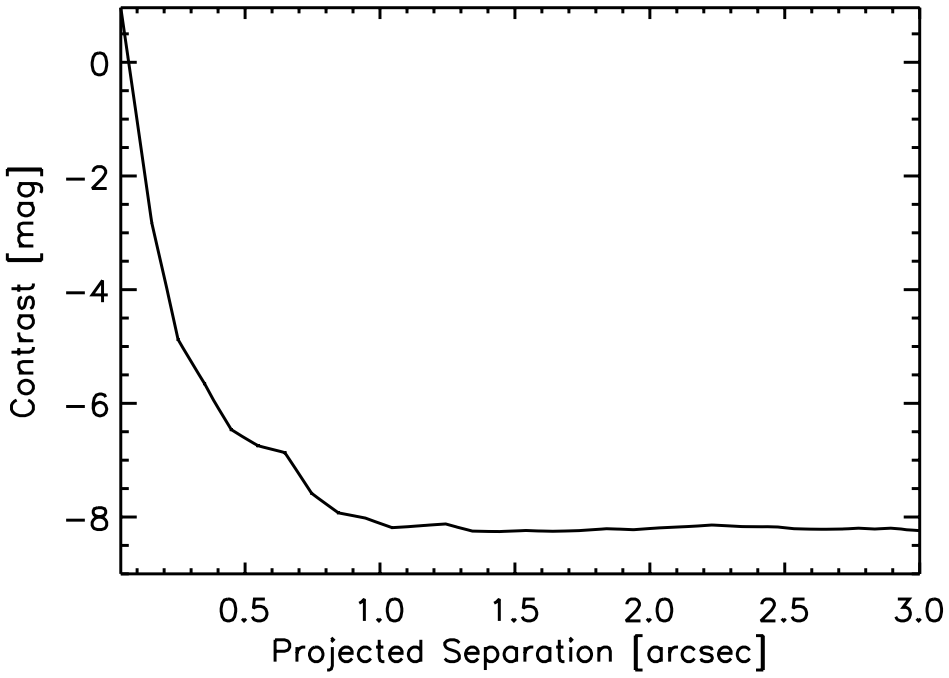

Figure 2.14: Mean contrast curve from the K-band AO observations described in this study.

ions, we create PHOENIX models with radii and effective temperatures drawn from Baraffe et al. (1998). We then calculate the corresponding contrast ratio between the primary and secondary by integrating over the appropriate bandpass (either K_p or K_s), adjusting the mass of the secondary downward until we match the 5σ limit from our contrast curve. We discuss the merits of this approach as compared to other methods commonly utilized in AO imaging searches in Knutson et al. (2014).

Companion Probability Distributions

We combine our AO and RV observations in order to constrain the allowed range of masses and semi-major axes for the observed companions. The duration and shape of the RV trend places a lower limit on the mass and semi-major axis of the companions. Similarly, a non-detection in AO gives a complementary upper limit on these quantities. We create a two dimensional probability distribution for each companion, by defining an equally spaced 50×50 grid of logarithmic companion mass (true mass) and semi-major axis ranging from 1-500 AU and $0.05 - 1000\ M_{\rm Jup}$. We then subtract off the orbital solutions of the confirmed inner planets, leaving only the trends due to the companions. At each grid point in mass and semi-major axis, we inject 500 simulated companions. While the semi-major axis and mass of

the companion remain fixed at each point, we drew a new inclination of the orbit each time from a uniform distribution in $cos(i)$, and a new eccentricity each time from the beta distribution (Kipping, 2013). This distribution is defined in Equation 2.3, where P_β is the probability of a given eccentricity, Γ is the gamma function, and $a' = 1.12$ and $b' = 3.09$ are constants calculated from the known population of long period giant planets.

$$P_\beta(e; a', b') = \frac{\Gamma(a' + b')}{\Gamma(a')\Gamma(b')} e^{a'-1}(1 - e)^{b'-1}. \tag{2.3}$$

Given this fixed mass, semi-major axis, and eccentricity for each simulated companion, we fit the remaining orbital parameters to the RVs using a least squares algorithm, and we calculate a corresponding χ^2 value. We note that the probability distribution calculations are not particularly sensitive to the assumed eccentricity distribution. We recalculate the probability distributions for 30 random systems within our sample assuming a uniform eccentricity distribution, and found that the 1σ semi-major axis and mass ranges, as presented in Table 2.6 for the 3σ trend systems, are generally consistent with each other to a couple of grid points.

We incorporate the constraints on potential companions from our AO observations using a method identical to the one described above. Within each mass and semi-major axis box we first generate a set of 500 companions with randomly selected masses, semi-major axes, and an eccentricity drawn from Eq. 2.3. We then fit for the remaining orbital parameters using the RV data, and use this best-fit orbit to calculate a set of 1000 projected separations for the companion sampled uniformly across the orbit. We then use our AO contrast curve to determine whether or not a companion of that mass and projected separation could have been detected in our AO image for each of the 1000 time steps considered. If the companion lies above our contrast curve we assume that it would have been detected, and if it lies below the curve we count it as a non-detection. For companions with large enough projected separations our images do not span all position angles, and we therefore assume that companions that lie above our contrast curve would be detected with a probability equal to the fractional position angle coverage of our image at that separation. We can then calculate the probability that a given companion would have been detected by determining the fraction of our 1000 time steps in which the companion lies above the contrast curve for that star.

The lower and upper limits on the mass/semi-major axis parameter space occupied by each companion can be combined to form a two dimensional probability distribution.

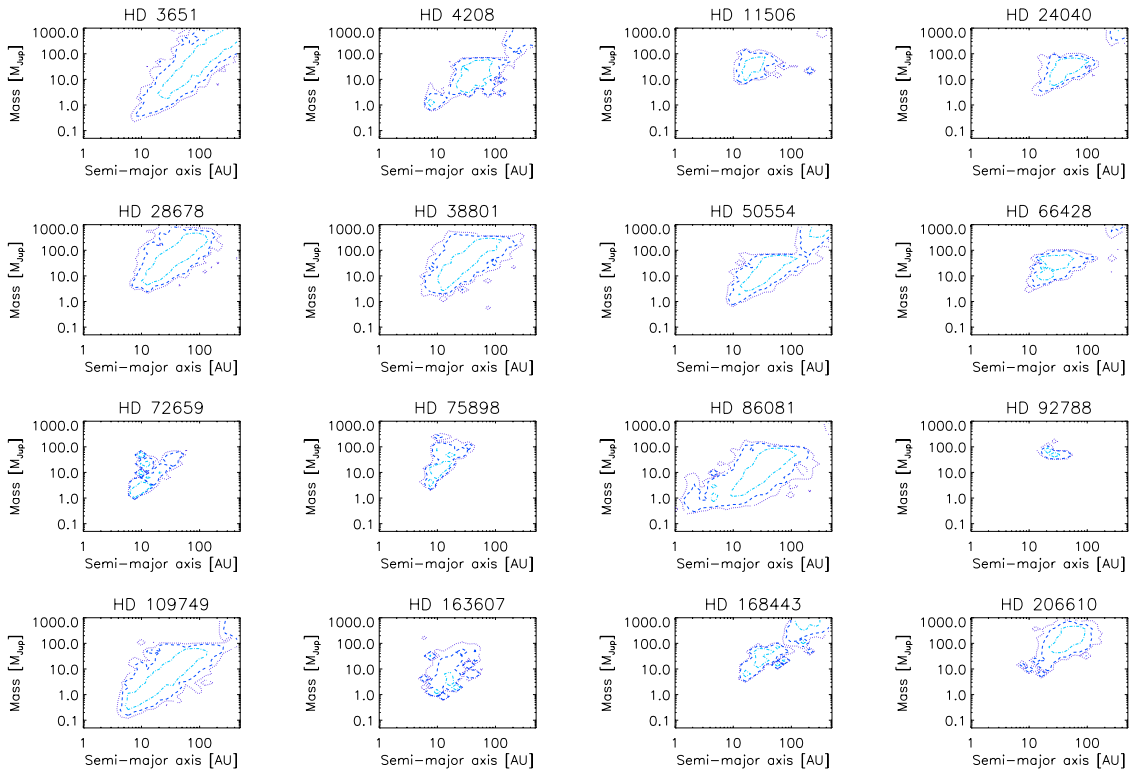

Figure 2.15: Companion probability distributions. The three contours define the 1σ, 2σ, and 3σ levels moving outward. While the radial velocity trends constrain these distributions on the low mass, low semi-major axis end, AO imaging constrains the high mass, high semi-major axis parameter space. Note that the masses in these plots are true masses, not $M \sin i$. Also note that the probability contours for HD 50499, HD 68988, HD 158038, and HD 180902 are not shown here. This is due to the fact that the grid is too coarse to resolve the contours of these well-constrained systems (the probability density is concentrated in only a couple of grid points). Finally, in some of these plots there is an apparent splitting of the contours at high mass and separation (e.g. HD 4208, HD 168443). This is due to the fact that the constraints from the AO images were modified by the percentage of position angles covered at wide separations.

After multiplying the χ^2 cube in mass, semi-major axis, and eccentricity from the RV trends by the detection probability cube from the AO contrast curves, we marginalize this new cube over eccentricity to yield a two dimensional probability distribution. Figure 2.15 shows the posterior distributions for the companions in each of the 20 systems with statistically significant RV trends. Table 2.6 lists the 1σ mass and semi-major axis ranges derived for each companion from this analysis. As expected, systems with strong curvature in the observed radial velocity accelerations have tighter constraints on the allowed mass and semi-major axis of the companion than those with linear trends.

Based on the probability contours in Figure 2.15 and corresponding table of allowed companion masses, we conclude that the majority of companions are most likely gas

Table 2.6: Constraints on Companion Properties

Companion	Mass [M_{Jup}]	Semi-major axis [AU]
HD 3651	0.84 – 817	14 – 440
HD 4208	0.84 – 668	7.6 – 342
HD 11506	9.6 – 72	14 – 40
HD 24040	6.4 – 817	24 – 342
HD 28678	5.2 – 446	11 – 124
HD 38801	2.8 – 297	8.6 – 124
HD 50554	1.9 – 817	13 – 440
HD 50499	2.8 – 12	7.6 – 8.6
HD 66428	4.3 – 72	11 – 66
HD 68988	9.6 – 59	6.7 – 7.6
HD 72659	1.3 – 133	7.6 – 35
HD 75898	2.8 – 199	6.7 – 21
HD 86081	0.69 – 72	4.6 – 124
HD 92788	48 – 88	14 – 40
HD 109749	0.25 – 59	5.9 – 160
HD 163607	1.3 – 39	7.6 – 24
HD 168443	4.3 – 817	14 – 388
HD 180902	162 – 446	8.6 – 18
HD 206610	7.8 – 446	13 – 85

Notes. The masses in this table are true masses, not $M \sin i$.

giant planets, as field surveys indicate that the occurrence rate of brown dwarfs (13 - 80 M_{Jup}) around sun-like stars is $3.2^{+3.1}_{-2.7}$% (Metchev and Hillenbrand, 2009). We note that while the Metchev and Hillenbrand result is for brown dwarf companions to sun-like stars between 28-1590 AU, the brown dwarf parts of parameter space for our companions are typically outside of 28 AU. Therefore, the comparison to the Metchev and Hillenbrand occurrence rate is appropriate. For comparison, Cumming et al. (2008) states that 17% – 20% of solar type stars host a giant planet (0.3 - 10 M_{Jup}) within 20 AU.

Completeness Maps

We quantified the sensitivity of this survey to companions over a range of masses and semi-major axes by determining the completeness of each system given the system's radial velocity baseline. Once again, we defined a 50×50 grid in log mass/semi-major axis space from 1-500 AU and 0.05-1000 M_{Jup}. In each defined grid box, we injected 500 simulated planets, each with a random mass and semi-major axis uniformly drawn from the grid box. We draw the inclination of the orbit from a uniform distribution in $\cos i$, the eccentricity from the beta distribution, and the remaining orbital elements from a uniform distribution. At each epoch that the star was observed, we calculated the expected RV signal caused by the injected companion. We generated errors for these simulated data by drawing randomly from a normal distribution of width $\sqrt{\sigma_i^2 + \sigma_{jitter}^2}$, where σ_i are the randomly shuffled

measurement errors from the original radial velocities and σ_{jitter} is the best-fit jitter value.

To determine if a simulated companion would be detectable, we fit either a one planet orbital solution, a linear trend, or a flat line to the simulated RV observations over the observed baseline. To determine which was the best fit, we used the Bayesian information criterion (BIC). This is defined as: BIC $= -2L + k \ln n$, where L is the likelihood of the model, k is the number of free parameters in the model, and n is the number of data points in the observed data set. While the likelihood can be increased by simply fitting models with more free parameters, BIC selects against these with a penalty term. The lower the BIC value the better the model fit. Comparing two models, if $\Delta BIC > 10$, this is very strong evidence for the model with the lower BIC (Kass et al 1995). Thus if the BIC values for the trend or the one-planet models were less than ten compared to the BIC value for the flat line, the simulated companion was “detected", whereas if the flat line was the best fit, that companion was “not detected". This process was repeated for 500 simulated companions injected into each grid box, producing a completeness map of detection probability as a function of mass and semi-major axis. Figure 2.16 shows the average completeness map of all of the systems.

Figure 2.17 shows the 50% contour for the average of all the systems, for the least sensitive system, and for the most sensitive system. The sensitivity of each system to planets with varying masses and semi-major axes depends on the length of the RV baseline, the magnitude of the measurement errors, and the number of data points for the system. The longer the baseline, the smaller the errors, and the greater the number of data points, the more sensitive the system. The least sensitive system is HD 5891, while the most sensitive system is HD 156668.

2.5 Discussion

The distribution of wide companions

Now that we have determined the parameter space where each detected companion is most likely to reside, we can determine the most likely underlying distribution for these massive, long-period companions in confirmed exoplanet systems. We assume that the companions are distributed in mass and semi-major axis space according to a double power law (e.g. Tabachnik & Tremaine 2002, Cumming et al 2008):

$$f(m, a) = C m^{\alpha} a^{\beta} \tag{2.4}$$

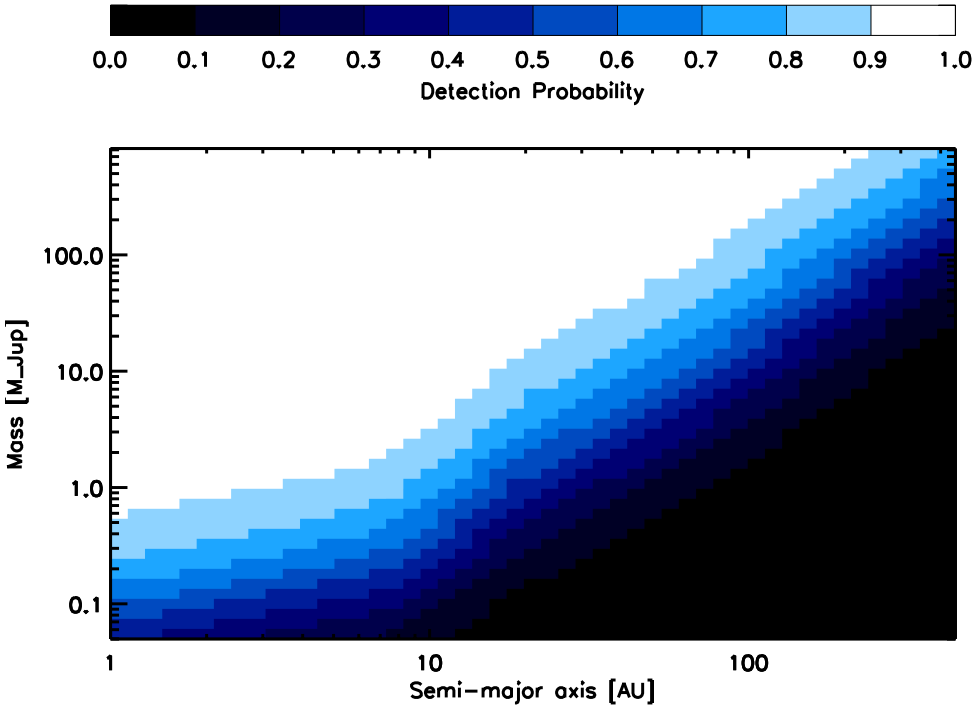

Figure 2.16: Average completeness map for all systems. Each color corresponds to a detection probability. For example, companions occupying parameter space in the white areas of the map had a 90% to a 100% chance of being detected by this survey.

The total likelihood for a set of N exoplanet systems is given by:

$$\mathscr{L} = \Pi_{i=1}^{N} p(d_i|C, \alpha, \beta) \tag{2.5}$$

where the expression on the right is the probability of obtaining the set of data d for a system i given values for C, α, and β. We assume that each system can have at most one companion, and that the probability of obtaining the measured RV dataset for an individual star is therefore the sum of the probability that the system does contain a planet and the probability that the system does not contain a planet for each set of C, alpha, and beta values considered. The probability of a system having zero planets is given by:

$$p(d_i, 0|C, \alpha, \beta) = p(d_i|0)[1 - Z] \tag{2.6}$$

The quantity $p(d_i|0)$ is the probability of obtaining the measured RV dataset given that there are no planets in the system. Z is the probability that the system contains

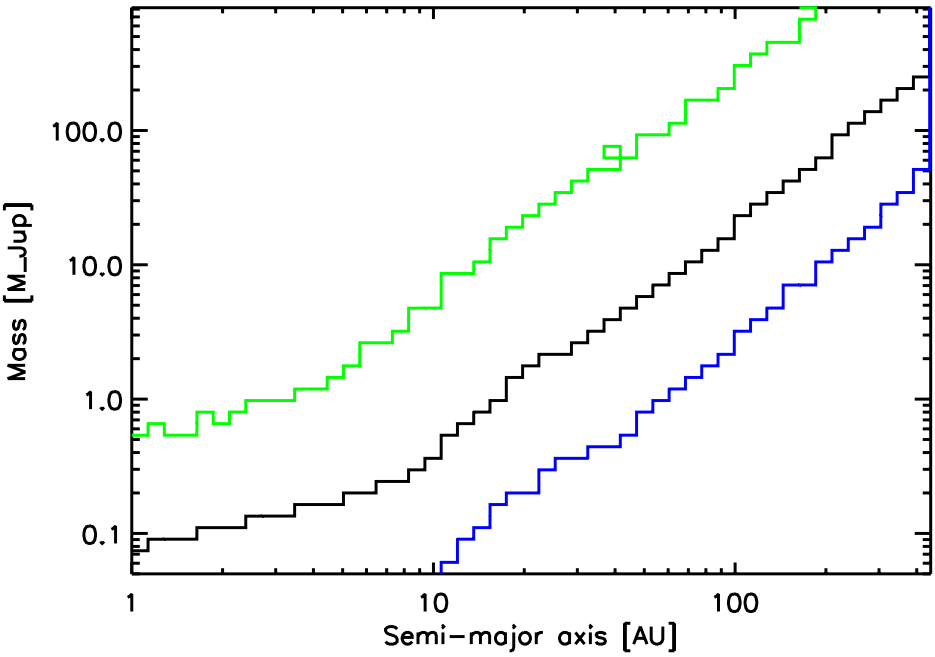

Figure 2.17: Completeness contours corresponding to 50% probability of detection. The black contour corresponds to the average sensitivity for all the systems, the blue contour corresponds to HD 156668, the system with the greatest sensitivity, and the green contour corresponds to HD 5891, the system with the least sensitivity.

a planet within the specified range in mass and semi-major axis space. Here, $p(d_i|0)$ and Z are given by the following equations.

$$p(d_i|0) = \Pi_j \frac{1}{\sqrt{2\pi}\sigma_j} exp\left[\frac{-1}{2}\left(\frac{d_j - m_j}{\sigma_j}\right)^2\right] \tag{2.7}$$

$$Z = \int_{m_1}^{m_2} d\ln m \int_{a_1}^{a_2} d\ln a\, C m^{\alpha} a^{\beta} \tag{2.8}$$

In Eq 2.7, d_j is the jth datapoint in the dataset d for system i, m_j is the corresponding model point, and σ_j is the error on the jth datapoint.

The probability of a system having one planet given values C, α, and β is:

$$p(d_i, 1|C, \alpha, \beta) = \int_{a_1}^{a_2} d\ln a \int_{m_1}^{m_2} d\ln m\; p(d_i|a, m) C m^{\alpha} a^{\beta} \tag{2.9}$$

where $p(d_i|a, m)$ is the probability of a companion at a given mass and semi-major axis, which we know from the previously calculated two dimensional probability

distributions. We then combine these expressions in order to calculate the likelihood of a given set of C, α, and β values given the measured RV data for all the stars in our sample:

$$\mathscr{L} = \Pi_{i=1}^{N} \left[p_i(d_i, 0|C, \alpha, \beta) + p_i(d_i, 1|C, \alpha, \beta) \right] \tag{2.10}$$

Note that for this calculation we use the probability distributions for all systems, not just those with 3σ trends. To maximize $\mathscr{L}$, we varied the values of C, α, and β using a grid search. The 16% - 84% confidence intervals on these parameters were then obtained using the MCMC technique.

Occurrence Rates

The overall occurrence rate for the population of companions can be estimated by integrating $f(m, a)$ over a range of masses and semi-major axes. In addition to the population of exoplanet systems described previously, we also included the 51 hot Jupiter systems published in Knutson et al. (2014). While we adopted the published RV model fits for each of the hot Jupiter systems, we recalculated probability distributions with the same grid spacing used for the 123 new systems described in this study for consistency.

In Knutson et al. (2014), we utilized a conservative approach in which we defined a given planet as a non-detection with 100% probability whenever the measured trend slope was less than 3σ away from zero. Instead of using a binary picture of planet occurrence, our revised likelihood function is more statistically correct, as it considers the probability of hosting a planet in all of our systems. We note that integrated companion occurrence rates calculated using this approach are particularly sensitive to the estimated jitter levels in our fits, where an underestimate of the true stellar jitter levels could result in an over-estimate of the corresponding companion occurrence rates. As a test of this new method we re-calculate the companion occurrence rate for the sample of 51 transiting hot Jupiters presented in Knutson et al. (2014) and find a value of 70 ± 8% for companions between 1 - 13 M_{Jup} and 1 - 20 AU. This is approximately 2σ higher than the value of 51 ± 10% obtained for this sample of stars using our older, more conservative likelihood function.

We calculate the overall frequency of companions beyond 5 AU in our new expanded system of 174 planetary systems by integrating over our best-fit probability distributions. We evaluate the companion frequency using a variety of different mass

Table 2.7: Total Occurrence Rates for Companions Beyond 5 AU

	5 - 20 AU	5 - 50 AU	5 - 100 AU
0.5 - 20 $M_{\rm Jup}$	$59.2^{+5.1}_{-5.2}$	$66.5^{+5.6}_{-5.8}$	$62.1^{+5.4}_{-5.7}$
0.5 - 13 $M_{\rm Jup}$	$56.9^{+5.2}_{-5.3}$	$62.3^{+5.7}_{-5.8}$	$61.0^{+5.5}_{-5.8}$
1 - 20 $M_{\rm Jup}$	$52.4^{+4.5}_{-4.7}$	$59.6^{+5.4}_{-5.5}$	$60.9^{+5.2}_{-5.6}$

Table 2.8: Power Law Coefficients for Companions Beyond 5 AU

	5 - 20 AU	5 - 50 AU	5 - 100 AU
0.5 - 20 $M_{\rm Jup}$	$C = 0.0036^{+0.0047}_{-0.0018}$	$C = 0.0174^{+0.0174}_{-0.0085}$	$C = 0.023^{+0.026}_{-0.012}$
	$\alpha = -0.04^{+0.13}_{-0.12}$	$\alpha = 0.29^{+0.18}_{-0.16}$	$\alpha = 0.53^{+0.25}_{-0.22}$
	$\beta = 1.46^{+0.47}_{-0.37}$	$\beta = 0.38^{+0.22}_{-0.22}$	$\beta = 0.05^{+0.18}_{-0.19}$
0.5 - 13 $M_{\rm Jup}$	$C = 0.0063^{+0.0076}_{-0.0029}$	$C = 0.015^{+0.031}_{-0.014}$	$C = 0.019^{+0.039}_{-0.016}$
	$\alpha = 0.08^{+0.15}_{-0.14}$	$\alpha = 0.56^{+0.22}_{-0.19}$	$\alpha = 0.86^{+0.28}_{-0.26}$
	$\beta = 1.22^{+0.33}_{-0.35}$	$\beta = 0.38^{+0.21}_{-0.22}$	$\beta = 0.02^{+0.17}_{-0.20}$
1 - 20 $M_{\rm Jup}$	$C = 0.0020^{+0.0062}_{-0.0029}$	$C = 0.0083^{+0.0084}_{-0.0038}$	$C = 0.0063^{+0.0072}_{-0.0029}$
	$\alpha = -0.22^{+0.15}_{-0.15}$	$\alpha = 0.44^{+0.22}_{-0.23}$	$\alpha = 0.86^{+0.26}_{-0.23}$
	$\beta = 1.82^{+0.25}_{-0.27}$	$\beta = 0.56^{+0.22}_{-0.22}$	$\beta = 0.26^{+0.14}_{-0.15}$

Notes. We note that the α and β values presented here are strongly influenced by the slope of the probability distributions for companions with partially resolved orbits, and therefore should not be taken as reliable estimates of the actual companion distribution. Please see the discussion below for further explanation.

and period ranges in order to determine how sensitively this result is to the specific limits of integration selected. The resulting total occurrence rates are presented in Table 2.7, and the corresponding values of C, α, and β are shown in Table 2.8.

We find that our values of α and β vary significantly depending on the integration range chosen, and are therefore not accurate estimates of the power law coefficients for this population of long-period companions. This dependence on integration range is due to the fact that many of the companions detected in our study have poorly constrained masses and orbits. When we vary the range of masses and semi-major axes used in our fits we truncate the probability distributions for these companions at different points, therefore biasing our corresponding estimates of α and β.

Although it is difficult to obtain reliable estimates for the values of α and β for long-period companions, we can nonetheless investigate whether or not this population increases in frequency as a function of increasing mass and semi-major axis by calculating the occurrence rate of this sample of systems using equal steps in log space to increase the semi-major axis and mass integration ranges. When stepping in semi-major axis, we keep the mass range constant, 1 - 20 $M_{\rm Jup}$, and when

stepping in mass, we keep the semi-major axis range constant, 5 - 20 AU. We then compare the observed changes in companion frequency per step in log mass or log semi-major axis in order to determine empirically how the overall distribution of companions compares to predictions from various power law models. For example, if the increase in frequency per log semi-major axis declines at larger separations this would imply a negative value for β, whereas the opposite would be true for a positive β. We calculate the uncertainties on the changes in occurrence rates by adding the individual uncertainties on the occurrence rates in quadrature.

We calculate the change in the integrated occurrence rate as a function of increasing semi-major axis (Figure 2.18) using a lower integration limit of 1 AU and including all planets in these systems, not just the outer companions. We find that for small separations these rates increase relatively quickly as compared to the predictions of a power law model with $\beta = 0$ (i.e. a uniform distribution in semi-major axis), whereas for large separations these rates increase relatively slowly. This suggests a positive β value for giant planets at smaller separations and a negative β value for outer companions at larger separations, with a broad peak in the distribution between 3 - 10 AU. When we examine the corresponding change in occurrence rate for companions beyond 5 AU as a function of planets mass (Figure 2.19), we find that these rates also increase slowly as compared to the predictions of a power law model with $\alpha = 0$. This implies a negative α value.

We next compare our constraints on the mass and semi-major axis distribution of long-period companions to predictions based on studies of short-period planets around FGK stars. Since values of α and β are broadly consistent among these studies (e.g. Bowler et al 2010), the results from Cumming et al. (2008) will be taken as representative: $\alpha = -0.31 \pm 0.2$ and $\beta = 0.26 \pm 0.1$. These values were derived for planet masses between $0.3 - 10\ M_{\rm Jup}$ and periods less than 2000 days (approximately 3 AU). We would like to know whether or not the population of companions beyond 5 AU is consistent with predictions based on the power law coefficients from this study. We answer this question by repeating our previous calculation using the Cumming et al power law, where we determine the change in the integrated occurrence rate per log mass and semi-major axis steps over the parameter range of interest. We calculate the uncertainties on these changes in occurrence rate by assuming Gaussian distributions for α and β and using a Monte Carlo method to get a distribution of occurrence rates for each semi-major axis and mass integration range. We then determine the uncertainties on the changes in

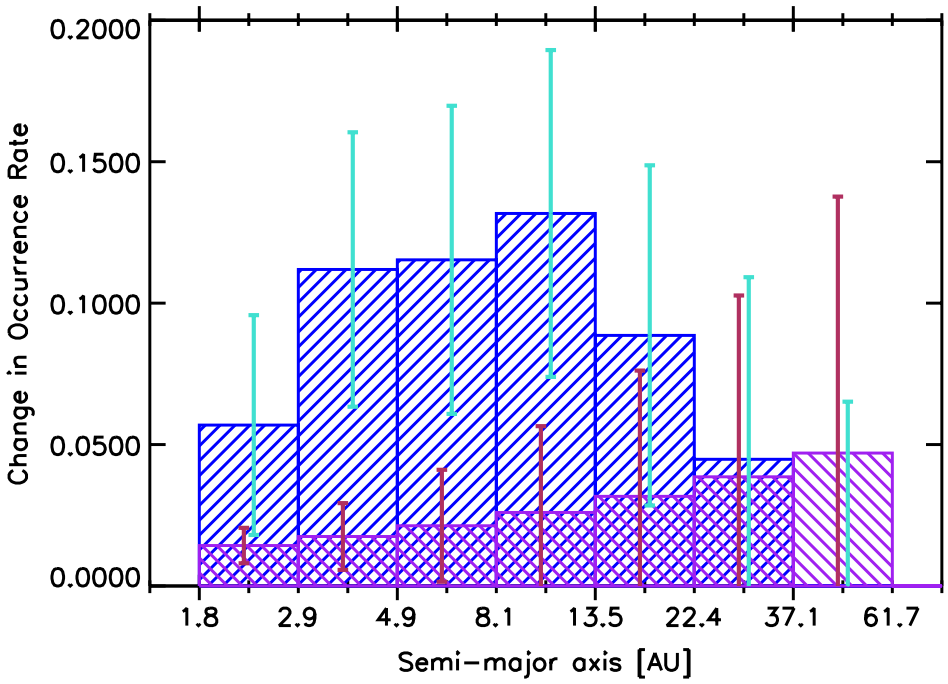

Figure 2.18: This plot shows the change in occurrence rate between adjoining semi-major axis steps as a function of the upper semi-major axis integration limit. The results for the Cumming et al power law distribution are plotted in purple, while the results from this survey are plotted in blue. For the fits for our survey we include all planets in these systems outside 1 AU, not just outer companions as in the rest of our analysis. This allows us to study the relative distribution of planets in these systems across a broad range of semi-major axes. The sensitivity limit of the Cumming et al survey is ~3 AU. For our survey, we are ~50% complete between 1 - 20 $M_{\rm Jup}$ and 5 - 100 AU. We note that the slight upward trend of the purple histogram bins corresponds to a β value that is 2.6σ away from zero.

occurrence rates by adding the uncertainties on the occurrence rates in quadrature. We note that due to correlations between α and β these uncertainties are slightly overestimated. We then compare these results to those obtained by fitting to our sample of long-period planets in Figures 2.18 and 2.19.

As shown in Figure 2.18, the Cumming et al. power law predicts an increase in the frequency of planets as a function of increasing semi-major axis, whereas our fits suggest a declining frequency for gas giant companions beyond the conservative 3 - 10 AU range. This implied disagreement between the integrated occurrence rates for our sample as compared to the extrapolated occurrence rates of Cumming et al is not surprising, as Cumming et al. (2008) only fits gas giant planets interior to 3 AU. We speculate that this difference may indicate either a peak in the frequency of gas giant planets in the 3-10 AU range, or a difference between the population of outer giant planet companions in these systems and the overall giant planet population.

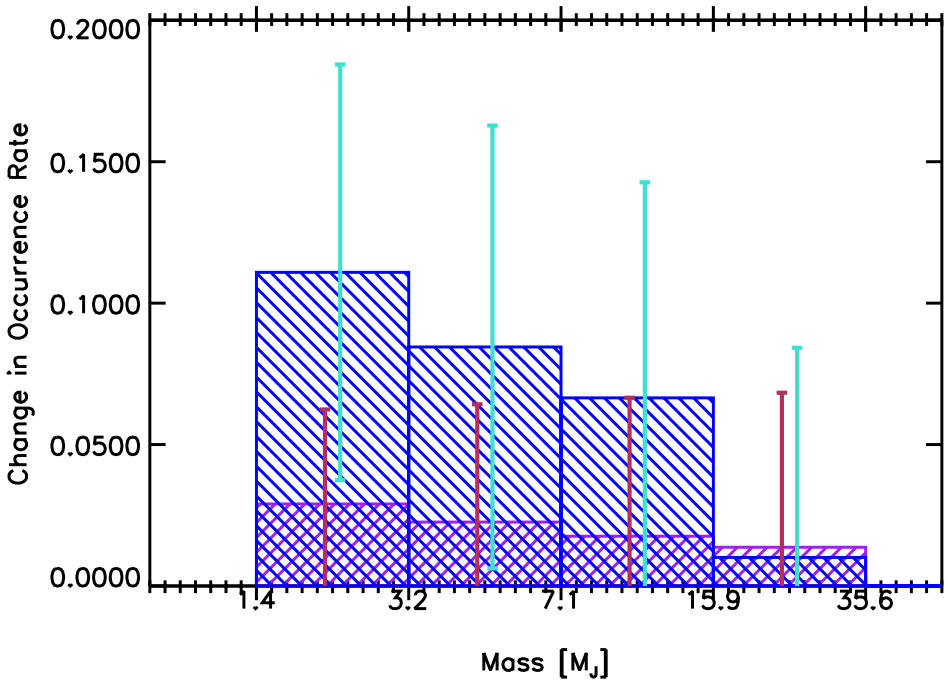

Figure 2.19: This plot shows the change in occurrence rate between adjoining mass steps as a function of the upper mass integration limit. The results from the Cumming et al power law distribution are plotted in purple, while the results from this survey are plotted in blue. We note that Cumming et al only includes planets with masses below 10 $M_{\rm Jup}$ in their survey, whereas we include companions with masses up to 20 $M_{\rm Jup}$. The occurrence rates for larger masses shown in this plot are therefore an extrapolation based on our best-fit power law models. The slight downward trend in the purple histograms corresponds to an α value that is 1.6σ away from zero.

In contrast to this result, Figure 2.19 indicates that the mass distribution of the long-period companions in our study is consistent with the negative α value (i.e. increasing frequency with decreasing planet mass) reported by Cumming et al. for the population of planets interior to 3 AU.

We next consider how the frequency of companions in these systems varies as a function of other parameters, including the inner planet mass, semi-major axis, and stellar mass. We select an integration range of 1 – 20 $M_{\rm Jup}$ and 5 - 20 AU for these companions; this range is large enough to include all known companions detected by our survey, while still remaining small enough to ensure that we do not extrapolate too far beyond the region in which we are sensitive to companions. We find that within this integration range, the total occurrence rate for massive, long-period companions is $52.4^{+4.5}_{-4.7}$%.

Johnson, Aller, et al. (2010) showed that planet occurrence rates and system archi-

tecture vary as a function of stellar mass. The A and M star systems are the high and low extremes of the sample's stellar mass range. To address the concern that including A and M star systems would influence our final results, we ran the entire grid search and MCMC analyses again excluding the 29 A and M star systems in the sample. The occurrence rate for this FGK-only sample is $54.6^{+4.8}_{-4.8}$%. We therefore conclude that the occurrence rates for the sample with and without the A and M stars are consistent with each other at the 0.4σ level.

Following the total occurrence rate calculation, we calculated the occurrence rate of massive, long-period companions as a function of inner-planet semi-major axis. We divided the total sample up into three bins - systems with planets interior to 0.1 AU (hot gas giants), systems with planets between 0.1 and 1 AU (warm gas giants), and systems with planets between 1 and 5 AU (cold gas giants). For each bin, we repeated our fits to derive new values of C, α, and β, which we integrated over a range of $1 - 20$ M_{Jup} and 5 - 20 AU. Our results are presented in Figure 2.20. The hot gas giant companion frequency is 2.4σ higher than that of the warm gas giants, and 2.3σ higher than that of the cold gas giants. This suggests that gas giants with orbital semi-major axes interior to 0.1 AU may have a higher companion fraction than their long-period counterparts, albeit with the caveat that this short-period bin is dominated by our transiting hot Jupiter sample. These planets typically have fewer radial velocity measurements than planets detected using the radial velocity technique, which could result in an underestimate of the stellar jitter for these stars.

If this enhanced companion fraction for short-period planets is confirmed by future studies, it would suggest that three body interactions may be an important mechanism for hot Jupiter migration. Alternatively, this trend might also result from differences in the properties of the protoplanetary disks in these systems. If we suppose that each disk that successfully generates gas giant planets produces them at some characteristic radius (e.g. the ice line — see Bitsch et al. (2013)) separated by some time span, and these planets subsequently migrate inwards via type II migration. Gas giants that migrate early in the disk's lifetime will reach the inner magnetospheric cavity of the disk, and due to eccentricity excitation mechanisms (Rice, Armitage, and Hogg, 2008), will rapidly accrete onto the host star over a timescale that is short compared to the lifetime of the disk. As the disk ages however, photoevaporation will grow the radius of the inner disk cavity. Accordingly, for those gas giants that arrive later in the lifetime of the disk, the inner disk edge will have been eaten away to the point that the eccentricity excitation mechanisms are no longer effective at

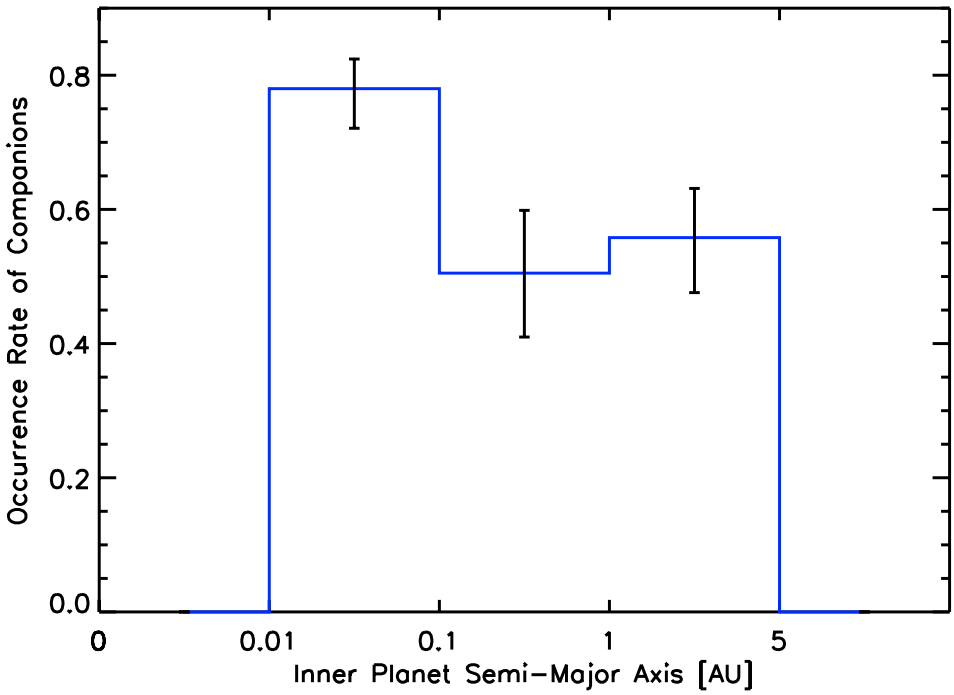

Figure 2.20: Occurrence rate as a function of inner planet semi-major axis. The values for each histogram starting at the leftmost bin are $75.1^{+4.4}_{-5.9}$%, $48.8^{+9.4}_{-9.5}$%, and $53.7^{+7.3}_{-8.2}$%.

shepherding the planets into the host stars, allowing migration to halt. We note that there is a very narrow window of time where the aforementioned processes allow for a successful formation of a hot Jupiter (which may self-consistently explain their inherent rarity — see Rice, Armitage, and Hogg (2008)). We would thus expect hot Jupiters to form primarily around stars that hosted disks that were especially efficient at giant planet formation, thus increasing the chances of having a planet reach the inner disk edge during the small window of time where hot Jupiter formation is possible. These highly efficient disks would also be expected to produce more than one gas giant planet, which leads to the expectation that hot Jupiters would be more likely to have companions.

We also calculated the occurrence rate of companions as a function of inner planet mass. We divided the sample up into three bins, corresponding to planets with masses between 0.05 and 0.5 M_{Jup}, 0.5 – 5 M_{Jup}, and 5 – 15 M_{Jup}. Our results are plotted in Figure 2.21. We find that intermediate mass planets may be more likely to have a massive, long-period companion, although all three bins are consistent at the 2σ level. We note that our ability to discern trends in companion rate as a function of planet mass is limited by the relatively small sample sizes in the lowest

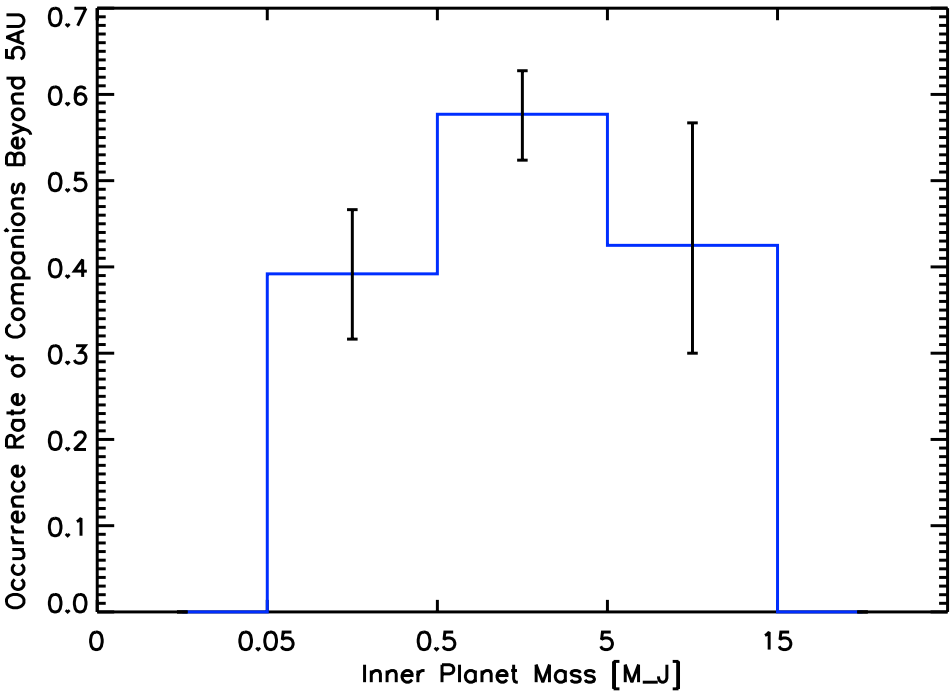

Figure 2.21: Occurrence rate as a function of inner planet mass. The values for each histogram starting at the leftmost bin are $39.2^{+7.4}_{-7.6}$%, $57.7^{+5.1}_{-5.3}$%, and $42.5^{+14.2}_{-12.5}$%.

and highest mass bins, which result in correspondingly large uncertainties on their companion rates.

Finally, we calculated the occurrence rate of companions outside of 5 AU as a function of stellar mass. Once again, we divided the sample up into three bins - systems with stellar masses from 0.08 - 0.8 $M_\odot$ (M and K stars), 0.8 - 1.4 $M_\odot$ (G and F stars), and 1.4 - 2.1 $M_\odot$ (A stars). Our results are plotted in Figure 2.22. We find that the occurrence rates for each stellar mass bin are consistent with each other at the 0.2σ level. Earlier studies indicated that the occurrence rate for gas giant planets interior to 3 AU is higher around A stars than F and G stars (Johnson, Aller, et al., 2010); our results for companions beyond 5 AU suggest that these differences may be reduced at large orbital separations, albeit with large uncertainties due to the small number of A stars included in our sample. We note that while mass estimates for the evolved A stars have been debated in the literature (Schlaufman and Winn, 2013; Johnson and Wright, 2013; Johnson, Morton, and Wright, 2013; Lloyd, 2011; Lloyd, 2013), this has a minimal impact on our conclusions in this study as we find that these evolved stars have the same frequency of companions as the main sequence FGKM stars in our sample.

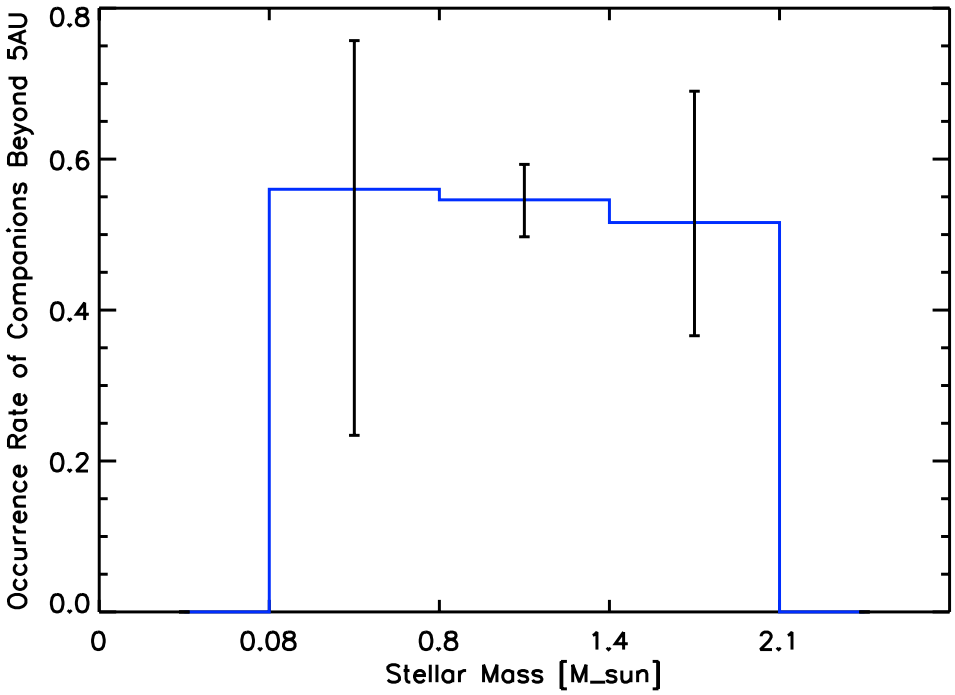

Figure 2.22: Occurrence rate of massive outer companions as a function of stellar mass. The values for each histogram starting at the leftmost bin are $56.0^{+19.7}_{-32.6}$%, $54.6^{+4.7}_{-4.9}$%, and $51.6^{+17.4}_{-15.0}$%.

Eccentricity Distribution

In addition to the results described above, we also seek to quantify how the eccentricity distribution of exoplanets in single planet systems might differ from that of exoplanets in two planet systems or systems with an outer body, as indicated by a radial velocity trend. We quantify these differences by fitting the set of inner planet eccentricities for each sample using the beta distribution (Kipping, 2013):

$$P_\beta(e; a, b) = \frac{\Gamma(a+b)}{\Gamma(a)\Gamma(b)} e^{a-1}(1-e)^{b-1}. \tag{2.11}$$

We account for the uncertainties in the measured eccentricities for each planet by repeating our beta distribution fit 10,000 times, where each time we draw a random eccentricity from the MCMC posterior probability distribution for each individual planet. The resulting distributions of best-fit a and b values therefore reflect both the measured eccentricities and their uncertainties. Figure 2.23 plots the distribution of best-fit eccentricities for the two groups of planets. We excluded planets interior to 0.1 AU whose eccentricities might be circularized due to tidal forces from the primary star from this plot as well as the beta distribution fits. Figure 2.24 compares

the two-dimensional posterior probability distributions in a and b for each of the two groups, taking into account the uncertainties on each planet eccentricity. We find that the two-planet systems appear to have systematically higher eccentricities than their single planet counterparts, with a significance greater than 3σ.

This result appears to contradict previous studies, which found that multi-planet systems have lower eccentricities (Chatterjee et al., 2008; Howard, 2013; Limbach and Turner, 2015; Wright, Upadhyay, et al., 2009). This difference may be explained if the separation between inner and outer planets is larger for cases where the inner planet has a large orbital eccentricity. Previous surveys were typically only sensitive to a 1 $M_{\rm Jup}$ planet out to 3 - 5 AU, suggesting that many of the multi-planet systems detected by our survey would have been misclassified as single planet systems.

The most detailed study of this correlation to date was presented in Limbach and Turner (2015). This study used 403 cataloged RV exoplanets from exoplanet.org (Han et al., 2014) to determine a relationship between eccentricity and system multiplicity. 127 of these planets were members of known multi-planet systems, with up to six planets in each system. When the authors calculated the mean eccentricity as a function of the number of planets in each system, they found that systems with more planets had lower eccentricities. We note that the difference between our new study and this one may be due to the fact that the majority of their planets have relatively short orbital periods. For systems with three or more planets, this means that the spacing between planets is typically small enough to require less eccentric orbits in order to ensure that the system remains stable over the lifetime of the system. Furthermore, their analysis did not take into account the uncertainties on individual exoplanet eccentricities, which can be substantial. Howard (2013) reaches a similar conclusion in their simpler analysis of published RV planets. This study compared eccentricity distributions of single giant planets to giant planets in multi-planet systems, and found that eccentricities of planets in multi-planet systems are lower on average.

Because Limbach and Turner (2015) did not carry out their own fits to the radial velocity data, they did not consistently allow for the possibility of long-term radial velocity accelerations due to unresolved outer companions. Previous studies by D. A. Fischer, Marcy, et al. (2001) and Rodigas and Hinz (2009) demonstrate that undetected outer planets can systematically bias eccentricity estimates for the inner planet to larger values. This is also a problem for systems where the signal to noise of the planet detection is low or the data are sparsely sampled (Shen and Turner,

2008). Although we use a smaller sample of planets for our study than Limbach and Turner (2015), our systems all have high signal to noise detections and long radial velocity baselines, which we use to fit and remove long-term accelerations that might otherwise bias our eccentricity estimates.

In contrast to these other studies, Dong et al (2014) found that warm Jupiters with companions have higher eccentricities than single warm Jupiters. However, we note that this study relied on a relatively small sample of planets (9 systems with $e > 0.4$ and 17 with $e < 0.2$), and the authors did not report uncertainties on their estimated occurrence rates for either sample. In this study the authors also point out that in order to migrate a warm Jupiter inwards via dynamical interactions with an outer body, the perturber in question must be close enough to overcome GR precession of the inner planet. We use this constraint, presented in their Equation 4, to test this formation scenario for the warm Jupiter population in our sample. Of the 42 warm Jupiter systems in our sample, 15 have resolved companions and 4 have statistically significant linear trends. We find that for the resolved companions, 13 out of the 15 companions satisfy the criterion for high-eccentricity migration (namely that warm Jupiters must reach a critical periastron distance of 0.1 AU within a Kozai-Lidov oscillation). We take the best fit masses and semi-major axes for the companions causing the trends from their probability distributions, and use these values to calculate the upper limit on the separation ratio between the warm Jupiter and the companion. We find that zero out of the four systems satisfy the criterion for high-e migration. Combining the resolved and trend systems, 13 out of 19 warm Jupiter systems with companions satisfy the criterion. However, we note that the criterion presented in Dong et al (2014) is necessary but insufficient for high-eccentricity migration. While our observations in principle do not rule out Kozai-Lidov migration for the warm Jupiter population, in order to decide if migration is relevant the character of the angular-momentum exchange cycle must be understood. In order to do this to lowest order, the mass and semi-major axis of the perturbing orbit, as well as the mutual inclination, must be known.

2.6 Conclusions

We conducted a Doppler survey at Keck combined with NIRC2 K-band AO imaging to search for massive, long period companions to a sample of 123 known one and two planet systems detected using the radial velocity method. These companions manifest as long term radial velocity trends in systems where the RV baseline is not long enough to resolve a full orbit. We extended archival RV baselines by up

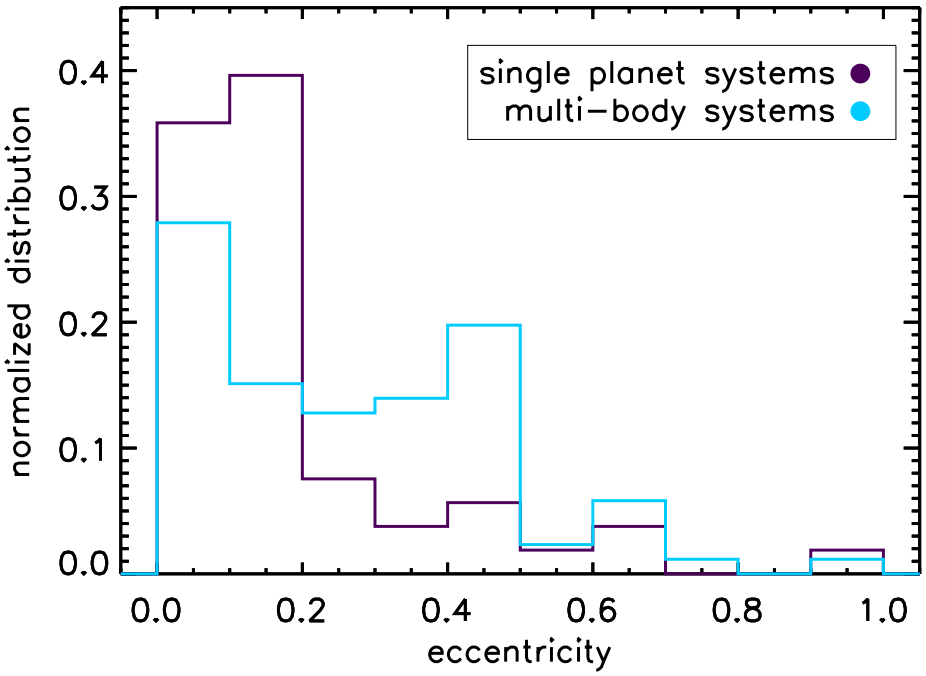

Figure 2.23: Eccentricity distributions of the planets in the full sample. The purple line shows this histogram for all single planets without outer planets or RV trends, while the blue histogram shows the distribution for planets in two planet systems and single planets with trends.

to 12 years for the stars in our sample, and found that 25 systems had statistically significant radial velocity trends, six of which displayed significant curvature (HD 68988, HD 50499, HD 72659, HD 92788, HD 75898, and HD 158038). We found that trends detected in HD 1461 and HD 97658 correlxated with the Ca II H&K line strengths, indicating that these trends were likely due to stellar activity and not due to a wide-separation companion. These systems were removed from further analysis. We also checked each system for stellar companions, and found that HD 164509, HD 126614, and HD 195109 had stellar companions that could account for the linear RV accelerations. These systems were also removed from further analysis.

For the remaining 20 trend systems, we placed lower limits on companion masses and semi-major axes from the RV trends, and upper limits from the AO contrast curves of the corresponding systems. We quantified the sensitivity of our survey and found that on average we were able to detect a 1 M_{Jup} planet out to 20 AU, and a Saturn mass planet out to 8 AU with 50% completeness. We fit the companion probability distributions with a double power law in mass and semi-major axis, and integrated this power law to determine the giant planet companion occurrence rate.

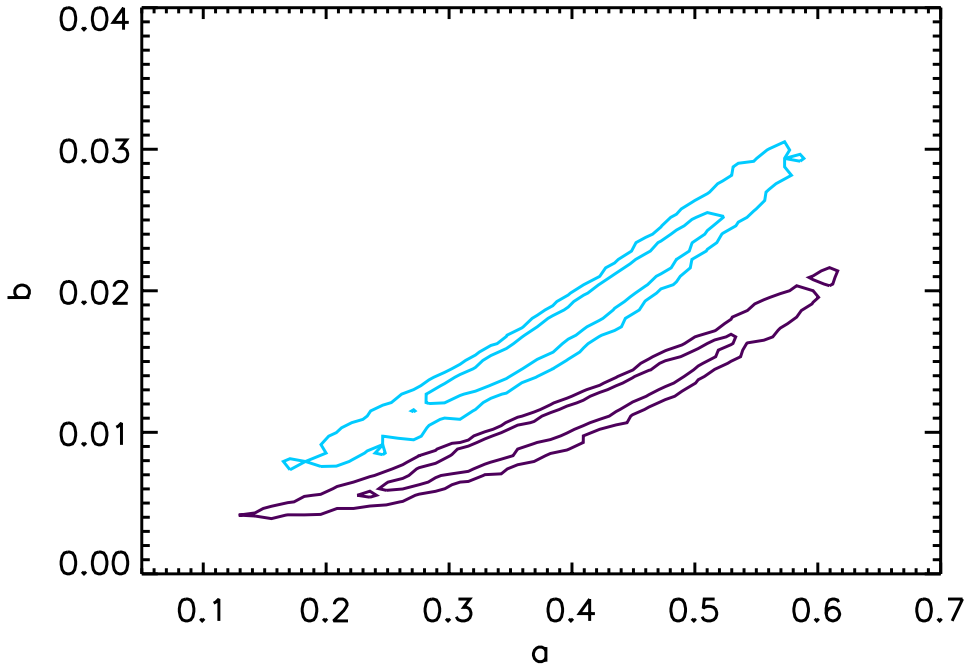

Figure 2.24: Two dimensional likelihood distributions of a and b. The purple contours represent the 1σ and 2σ contours of the two planet systems and single planets with positive trend detections. The blue contours represent the 1σ and 2σ contours of the single planet systems with no outer bodies.

We found the total occurrence rate of companions over a mass range of 1 - 20 M_{Jup} and semi-major axis range of 5-20 AU to be $52.4^{+4.5}_{-4.7}$%, and obtained a comparable occurrence rate when the A and M star systems were removed from the calculation. The distribution of these long-period companions is best matched by models with a declining frequency as a function of increasing semi-major axis, and appears to be inconsistent with an extrapolation from fits to the population of gas giant planets interior to 3 AU described in Cumming et al. (2008). This suggests that either the radial distribution of gas giants peaks between 3 - 10 AU, or that the distribution of outer gas giant companions differs from that of the overall gas giant population.

When calculating the occurrence rate as a function of inner planet semi-major axis, we found that the hot gas giants were more likely to have a massive outer companion as compared to their cold gas giant counterparts. This result suggests that dynamical interactions between planets may be an important migration mechanism for gas giant planets.

When we compared the eccentricity distributions of single planets in this sample with no outer bodies to planets in two-planet systems and single planets with a positive

trend detection, we found that in multi-body systems, the eccentricity distribution was significantly higher than that of single planet systems with no outer bodies. The higher average eccentricities in these systems suggest that dynamical interactions between gas giant planets play a significant role in the evolution of these systems.

If we wish to better understand the role that dynamical evolution plays in these systems, there are several possible approaches to consider. First, continued RV monitoring would help to better constrain companion orbits and masses. Second, deep imaging of the trend systems could probe down to brown dwarf masses and determine whether any of the observed trends could be caused by stellar instead of planetary mass companions. If any brown dwarf companions are detected via direct imaging, the existence of complementary radial velocity data would allow us to dynamically measure their masses, which would provide a valuable test of stellar evolution models in the low mass regime (Crepp et al., 2012). Finally, long term RV monitoring of systems with lower mass planets and/or systems with three or more short period planets detected by transit surveys such as Kepler could allow us to determine if the companion occurrence rate of these systems differs from that of their gas giant counterparts. A significant limitation of this last suggestion is the need to detect low mass planetary systems orbiting bright, nearby stars — most Kepler stars are time consuming to observe with RVs, but K2, and later TESS, should provide a good sample of low mass planets orbiting nearby stars.

2.7 Acknowledgements

We thank David Hogg and Ben Montet for helpful conversations. This work was supported by NASA grant NNX14AD24G, and was based on observations at the W. M. Keck Observatory granted by the University of Hawaii, the University of California, the California Institute of Technology, Yale University, and NASA. We thank the observers who contributed to the measurements reported here and acknowledge the efforts of the Keck Observatory staff. We extend special thanks to those of Hawaiian ancestry on whose sacred mountain of Mauna Kea we are privileged to be guests.

References

Albrecht, S., J. N. Winn, J. A. Johnson, et al. (2012). “Obliquities of Hot Jupiter Host Stars: Evidence for Tidal Interactions and Primordial Misalignments”. In: *ApJ* 757, 18, p. 18. DOI: 10.1088/0004-637X/757/1/18. arXiv: 1206.6105 [astro-ph.SR].

Albrecht, S., J. N. Winn, G. W. Marcy, et al. (2013). "Low Stellar Obliquities in Compact Multiplanet Systems". In: *ApJ* 771, 11, p. 11. DOI: 10.1088/0004-637X/771/1/11. arXiv: 1302.4443 [astro-ph.SR].

Alibert, Y. et al. (2005). "Models of giant planet formation with migration and disc evolution". In: *A&A* 434, pp. 343–353. DOI: 10.1051/0004-6361:20042032. eprint: astro-ph/0412444.

Anglada-Escudé, G. et al. (2012). "Astrometry and Radial Velocities of the Planet Host M Dwarf GJ 317: New Trigonometric Distance, Metallicity, and Upper Limit to the Mass of GJ 317b". In: *ApJ* 746, 37, p. 37. DOI: 10.1088/0004-637X/746/1/37. arXiv: 1111.2623 [astro-ph.EP].

Apps, K. et al. (2010). "M2K: I. A Jupiter-Mass Planet Orbiting the M3V Star HIP 79431". In: *PASP* 122, p. 156. DOI: 10.1086/651058. arXiv: 1001.1174 [astro-ph.EP].

Baraffe, I. et al. (1998). "Evolutionary models for solar metallicity low-mass stars: mass-magnitude relationships and color-magnitude diagrams". In: *A&A* 337, pp. 403–412. eprint: astro-ph/9805009.

Barbieri, M. et al. (2009). "Characterization of the HD 17156 planetary system". In: *A&A* 503, pp. 601–612. DOI: 10.1051/0004-6361/200811466. eprint: 0812.0785.

Bitsch, B. et al. (2013). "Highly inclined and eccentric massive planets. I. Planet-disc interactions". In: *A&A* 555, A124, A124. DOI: 10.1051/0004-6361/201220310. arXiv: 1305.7330 [astro-ph.EP].

Boisse, I., X. Bonfils, and N. C. Santos (2012). "SOAP. A tool for the fast computation of photometry and radial velocity induced by stellar spots". In: *A&A* 545, A109, A109. DOI: 10.1051/0004-6361/201219115. arXiv: 1206.5493 [astro-ph.IM].

Bonfils, X. et al. (2013). "The HARPS search for southern extra-solar planets. XXXI. The M-dwarf sample". In: *A&A* 549, A109, A109. DOI: 10.1051/0004-6361/201014704. arXiv: 1111.5019 [astro-ph.EP].

Bouchy, F. et al. (2005). "ELODIE metallicity-biased search for transiting Hot Jupiters. II. A very hot Jupiter transiting the bright K star HD 189733". In: *A&A* 444, pp. L15–L19. DOI: 10.1051/0004-6361:200500201. eprint: astro-ph/0510119.

Bourrier, V. and G. Hébrard (2014). "Detecting the spin-orbit misalignment of the super-Earth 55 Cancri e". In: *A&A* 569, A65, A65. DOI: 10.1051/0004-6361/201424266. arXiv: 1406.6813 [astro-ph.EP].

Butler, R. P., J. A. Johnson, et al. (2006). "A Long-Period Jupiter-Mass Planet Orbiting the Nearby M Dwarf GJ 849". In: *PASP* 118, pp. 1685–1689. DOI: 10.1086/510500. eprint: astro-ph/0610179.

Butler, R. P., G. W. Marcy, et al. (1996). "Attaining Doppler Precision of 3 M s-1". In: *PASP* 108, p. 500. DOI: 10.1086/133755.

Butler, R. P., J. T. Wright, et al. (2006). "Catalog of Nearby Exoplanets". In: *ApJ* 646, pp. 505–522. DOI: 10.1086/504701. eprint: astro-ph/0607493.

Chatterjee, S. et al. (2008). "Dynamical Outcomes of Planet-Planet Scattering". In: *ApJ* 686, 580-602, pp. 580–602. DOI: 10.1086/590227. eprint: astro-ph/0703166.

Crepp, J. R. et al. (2012). "The Dynamical Mass and Three-dimensional Orbit of HR7672B: A Benchmark Brown Dwarf with High Eccentricity". In: *ApJ* 751, 97, p. 97. DOI: 10.1088/0004-637X/751/2/97. arXiv: 1112.1725 [astro-ph.EP].

Cumming, A. et al. (2008). "The Keck Planet Search: Detectability and the Minimum Mass and Orbital Period Distribution of Extrasolar Planets". In: *PASP* 120, p. 531. DOI: 10.1086/588487. arXiv: 0803.3357.

da Silva, R. et al. (2007). "ELODIE metallicity-biased search for transiting Hot Jupiters. IV. Intermediate period planets orbiting the stars HD 43691 and HD 132406". In: *A&A* 473, pp. 323–328. DOI: 10.1051/0004-6361:20077314. arXiv: 0707.0958.

Dawson, R. I. (2014). "On the Tidal Origin of Hot Jupiter Stellar Obliquity Trends". In: *ApJL* 790, L31, p. L31. DOI: 10.1088/2041-8205/790/2/L31. arXiv: 1405.1735 [astro-ph.EP].

Delfosse, X. et al. (2000). "Accurate masses of very low mass stars. IV. Improved mass-luminosity relations". In: *A&A* 364, pp. 217–224. eprint: astro-ph/0010586.

Desidera, S. and M. Barbieri (2007). "Properties of planets in binary systems. The role of binary separation". In: *A&A* 462, pp. 345–353. DOI: 10.1051/0004-6361:20066319. eprint: astro-ph/0610623.

Dong, S., B. Katz, and A. Socrates (2014). "Warm Jupiters Need Close "Friends" for High-eccentricity Migration-a Stringent Upper Limit on the Perturber's Separation". In: *ApJL* 781, L5, p. L5. DOI: 10.1088/2041-8205/781/1/L5. arXiv: 1309.0011 [astro-ph.EP].

Dragomir, D. et al. (2013). "MOST Detects Transits of HD 97658b, a Warm, Likely Volatile-rich Super-Earth". In: *ApJL* 772, L2, p. L2. DOI: 10.1088/2041-8205/772/1/L2. arXiv: 1305.7260 [astro-ph.EP].

Endl, M., W. D. Cochran, R. A. Wittenmyer, and A. P. Boss (2008). "An m sin i = 24 M_{Earth} Planetary Companion to the Nearby M Dwarf GJ 176". In: *ApJ* 673, 1165-1168, pp. 1165–1168. DOI: 10.1086/524703. arXiv: 0709.0944.

Endl, M., W. D. Cochran, R. A. Wittenmyer, and A. P. Hatzes (2006). "Determination of the Orbit of the Planetary Companion to the Metal-Rich Star HD 45350". In: *AJ* 131, pp. 3131–3134. DOI: 10.1086/503746. eprint: astro-ph/0603007.

Fischer, D. A., G. Laughlin, et al. (2006). "The N2K Consortium. III. Short-Period Planets Orbiting HD 149143 and HD 109749". In: *ApJ* 637, pp. 1094–1101. DOI: 10.1086/498557.

Fischer, D. A., G. W. Marcy, et al. (2001). "Planetary Companions to HD 12661, HD 92788, and HD 38529 and Variations in Keplerian Residuals of Extrasolar Planets". In: *ApJ* 551, pp. 1107–1118. DOI: 10.1086/320224.

Fischer, D. A., S. S. Vogt, et al. (2007). "Five Intermediate-Period Planets from the N2K Sample". In: *ApJ* 669, pp. 1336–1344. DOI: 10.1086/521869. arXiv: 0704.1191.

Forveille, T. et al. (2009). "The HARPS search for southern extra-solar planets. XIV. Gl 176b, a super-Earth rather than a Neptune, and at a different period". In: *A&A* 493, pp. 645–650. DOI: 10.1051/0004-6361:200810557. arXiv: 0809.0750.

Fressin, F. et al. (2013). "The False Positive Rate of Kepler and the Occurrence of Planets". In: *ApJ* 766, 81, p. 81. DOI: 10.1088/0004-637X/766/2/81. arXiv: 1301.0842 [astro-ph.EP].

Giguere, M. J. et al. (2012). "A High-eccentricity Component in the Double-planet System around HD 163607 and a Planet around HD 164509". In: *ApJ* 744, 4, p. 4. DOI: 10.1088/0004-637X/744/1/4. arXiv: 1109.2955 [astro-ph.EP].

Gilliland, R. L. et al. (2011). "Asteroseismology of the Transiting Exoplanet Host HD 17156 with Hubble Space Telescope Fine Guidance Sensor". In: *ApJ* 726, 2, p. 2. DOI: 10.1088/0004-637X/726/1/2. arXiv: 1011.0435 [astro-ph.SR].

Goldreich, P. and S. Tremaine (1980). "Disk-satellite interactions". In: *ApJ* 241, pp. 425–441. DOI: 10.1086/158356.

Haghighipour, N., R. P. Butler, et al. (2012). "The Lick-Carnegie Survey: A New Two-planet System around the Star HD 207832". In: *ApJ* 756, 91, p. 91. DOI: 10.1088/0004-637X/756/1/91. arXiv: 1207.2806 [astro-ph.EP].

Haghighipour, N., S. S. Vogt, et al. (2010). "The Lick-Carnegie Exoplanet Survey: A Saturn-Mass Planet in the Habitable Zone of the Nearby M4V Star HIP 57050". In: *ApJ* 715, pp. 271–276. DOI: 10.1088/0004-637X/715/1/271. arXiv: 1004.4608 [astro-ph.EP].

Han, E. et al. (2014). "Exoplanet Orbit Database. II. Updates to Exoplanets.org". In: *PASP* 126, p. 827. DOI: 10.1086/678447. arXiv: 1409.7709 [astro-ph.EP].

Harakawa, H. et al. (2010). "Detection of a Low-eccentricity and Super-massive Planet to the Subgiant HD 38801". In: *ApJ* 715, pp. 550–553. DOI: 10.1088/0004-637X/715/1/550. arXiv: 1004.1779 [astro-ph.EP].

Hébrard, G. et al. (2011). "The retrograde orbit of the HAT-P-6b exoplanet". In: *A&A* 527, L11, p. L11. DOI: 10.1051/0004-6361/201016331. arXiv: 1101.5009 [astro-ph.EP].

Howard, A. W. (2013). "Observed Properties of Extrasolar Planets". In: *Science* 340, pp. 572–576. DOI: 10.1126/science.1233545. arXiv: 1305.0542 [astro-ph.EP].

Howard, A. W., J. A. Johnson, G. W. Marcy, D. A. Fischer, J. T. Wright, D. Bernat, et al. (2010). "The California Planet Survey. I. Four New Giant Exoplanets". In: *ApJ* 721, pp. 1467–1481. DOI: 10.1088/0004-637X/721/2/1467. arXiv: 1003.3488 [astro-ph.EP].

Howard, A. W., G. W. Marcy, et al. (2012). "Planet Occurrence within 0.25 AU of Solar-type Stars from Kepler". In: *ApJS* 201, 15, p. 15. DOI: 10.1088/0067-0049/201/2/15. arXiv: 1103.2541 [astro-ph.EP].

Howard, A. W. et al. (2011a). "The NASA-UC Eta-Earth Program. II. A Planet Orbiting HD 156668 with a Minimum Mass of Four Earth Masses". In: *ApJ* 726, 73, p. 73. DOI: 10.1088/0004-637X/726/2/73. arXiv: 1003.3444 [astro-ph.EP].

– (2011b). "The NASA-UC Eta-Earth Program. III. A Super-Earth Orbiting HD 97658 and a Neptune-mass Planet Orbiting Gl 785". In: *ApJ* 730, 10, p. 10. DOI: 10.1088/0004-637X/730/1/10. arXiv: 1011.0414 [astro-ph.EP].

Huber, D. et al. (2013). "Stellar Spin-Orbit Misalignment in a Multiplanet System". In: *Science* 342, pp. 331–334. DOI: 10.1126/science.1242066. arXiv: 1310.4503 [astro-ph.EP].

Husser, T.-O. et al. (2013). "A new extensive library of PHOENIX stellar atmospheres and synthetic spectra". In: *A&A* 553, A6, A6. DOI: 10.1051/0004-6361/201219058. arXiv: 1303.5632 [astro-ph.SR].

Isaacson, H. and D. Fischer (2010). "Chromospheric Activity and Jitter Measurements for 2630 Stars on the California Planet Search". In: *ApJ* 725, pp. 875–885. DOI: 10.1088/0004-637X/725/1/875. arXiv: 1009.2301 [astro-ph.EP].

Johnson, J. A., K. M. Aller, et al. (2010). "Giant Planet Occurrence in the Stellar Mass-Metallicity Plane". In: *PASP* 122, p. 905. DOI: 10.1086/655775. arXiv: 1005.3084 [astro-ph.EP].

Johnson, J. A., R. P. Butler, et al. (2007). "A New Planet around an M Dwarf: Revealing a Correlation between Exoplanets and Stellar Mass". In: *ApJ* 670, pp. 833–840. DOI: 10.1086/521720. arXiv: 0707.2409.

Johnson, J. A., C. Clanton, et al. (2011). "Retired A Stars and Their Companions. VII. 18 New Jovian Planets". In: *ApJS* 197, 26, p. 26. DOI: 10.1088/0067-0049/197/2/26. arXiv: 1108.4205 [astro-ph.EP].

Johnson, J. A., A. W. Howard, B. P. Bowler, et al. (2010). "Retired A Stars and Their Companions. IV. Seven Jovian Exoplanets from Keck Observatory". In: *PASP* 122, p. 701. DOI: 10.1086/653809. arXiv: 1003.3445 [astro-ph.EP].

Johnson, J. A., A. W. Howard, G. W. Marcy, et al. (2010). "The California Planet Survey. II. A Saturn-Mass Planet Orbiting the M Dwarf Gl 649". In: *PASP* 122, p. 149. DOI: 10.1086/651007. arXiv: 0912.2730 [astro-ph.EP].

Johnson, J. A., G. W. Marcy, et al. (2006). "The N2K Consortium. VI. Doppler Shifts without Templates and Three New Short-Period Planets". In: *ApJ* 647, pp. 600–611. DOI: 10.1086/505173. eprint: astro-ph/0604348.

Johnson, J. A., T. D. Morton, and J. T. Wright (2013). "Retired A Stars: The Effect of Stellar Evolution on the Mass Estimates of Subgiants". In: *ApJ* 763, 53, p. 53. DOI: 10.1088/0004-637X/763/1/53. arXiv: 1208.4377 [astro-ph.SR].

Johnson, J. A. and J. T. Wright (2013). "On Lloyd's "The Mass Distribution of Subgiant Planet Hosts" (arXiv:1306.6627v1)". In: *ArXiv e-prints*. arXiv: 1307.3441 [astro-ph.EP].

Jones, H. R. A. et al. (2010). "A long-period planet orbiting a nearby Sun-like star". In: *MNRAS* 403, pp. 1703–1713. DOI: 10.1111/j.1365-2966.2009.16232.x. arXiv: 0912.2716 [astro-ph.SR].

Jurić, M. and S. Tremaine (2008). "Dynamical Origin of Extrasolar Planet Eccentricity Distribution". In: *ApJ* 686, 603-620, pp. 603–620. DOI: 10.1086/590047. eprint: astro-ph/0703160.

Kane, S. R. et al. (2015). "A Comprehensive Characterization of the 70 Virginis Planetary System". In: *ApJ* 806, 60, p. 60. DOI: 10.1088/0004-637X/806/1/60. arXiv: 1504.04066 [astro-ph.EP].

Kipping, D. M. (2013). "Parametrizing the exoplanet eccentricity distribution with the Beta distribution". In: *MNRAS* 434, pp. L51–L55. DOI: 10.1093/mnrasl/slt075. arXiv: 1306.4982 [astro-ph.EP].

Knutson, H. A. et al. (2014). "Friends of Hot Jupiters. I. A Radial Velocity Search for Massive, Long-period Companions to Close-in Gas Giant Planets". In: *ApJ* 785, 126, p. 126. DOI: 10.1088/0004-637X/785/2/126. arXiv: 1312.2954 [astro-ph.EP].

Limbach, M. A. and E. L. Turner (2015). "Exoplanet orbital eccentricity: Multiplicity relation and the Solar System". In: *Proceedings of the National Academy of Science* 112, pp. 20–24. DOI: 10.1073/pnas.1406545111. arXiv: 1404.2552 [astro-ph.EP].

Lin, D. N. C., P. Bodenheimer, and D. C. Richardson (1996). "Orbital migration of the planetary companion of 51 Pegasi to its present location". In: *Nature* 380, pp. 606–607. DOI: 10.1038/380606a0.

Lin, D. N. C. and J. Papaloizou (1986). "On the tidal interaction between protoplanets and the protoplanetary disk. III - Orbital migration of protoplanets". In: *ApJ* 309, pp. 846–857. DOI: 10.1086/164653.

Lloyd, J. P. (2011). ""Retired" Planet Hosts: Not So Massive, Maybe Just Portly After Lunch". In: *ApJL* 739, L49, p. L49. DOI: 10.1088/2041-8205/739/2/L49. arXiv: 1108.1190 [astro-ph.EP].

– (2013). "The Mass Distribution of Subgiant Planet Hosts". In: *ApJL* 774, L2, p. L2. DOI: 10.1088/2041-8205/774/1/L2. arXiv: 1306.6627 [astro-ph.EP].

Marcy, G. W. and R. P. Butler (1992). "Precision radial velocities with an iodine absorption cell". In: *PASP* 104, pp. 270–277. DOI: 10.1086/132989.

Mayor, M. et al. (2004). "The CORALIE survey for southern extra-solar planets. XII. Orbital solutions for 16 extra-solar planets discovered with CORALIE". In: *A&A* 415, pp. 391–402. DOI: 10.1051/0004-6361:20034250. eprint: astro-ph/0310316.

Melo, C. et al. (2007). "A new Neptune-mass planet orbiting HD 219828". In: *A&A* 467, pp. 721–727. DOI: 10.1051/0004-6361:20066845. eprint: astro-ph/0702459.

Meschiari, S. et al. (2011). "The Lick-Carnegie Survey: Four New Exoplanet Candidates". In: *ApJ* 727, 117, p. 117. DOI: 10.1088/0004-637X/727/2/117. arXiv: 1011.4068 [astro-ph.EP].

Metchev, S. A. and L. A. Hillenbrand (2009). "The Palomar/Keck Adaptive Optics Survey of Young Solar Analogs: Evidence for a Universal Companion Mass Function". In: *ApJS* 181, pp. 62–109. DOI: 10.1088/0067-0049/181/1/62. arXiv: 0808.2982.

Mortier, A. et al. (2013). "New and updated stellar parameters for 90 transit hosts. The effect of the surface gravity". In: *A&A* 558, A106, A106. DOI: 10.1051/0004-6361/201322240. arXiv: 1309.1998 [astro-ph.EP].

Morton, T. D. and J. N. Winn (2014). "Obliquities of Kepler Stars: Comparison of Single- and Multiple-transit Systems". In: *ApJ* 796, 47, p. 47. DOI: 10.1088/0004-637X/796/1/47. arXiv: 1408.6606 [astro-ph.EP].

Moutou, C. et al. (2009). "Photometric and spectroscopic detection of the primary transit of the 111-day-period planet HD 80 606 b". In: *A&A* 498, pp. L5–L8. DOI: 10.1051/0004-6361/200911954. arXiv: 0902.4457 [astro-ph.EP].

Mugrauer, M. et al. (2007). "Multiplicity study of Exoplanet host Stars". In: *Binary Stars as Critical Tools and Tests in Contemporary Astrophysics*. Ed. by W. I. Hartkopf, P. Harmanec, and E. F. Guinan. Vol. 240. IAU Symposium, p. 329.

Nagasawa, M., S. Ida, and T. Bessho (2008). "Formation of Hot Planets by a Combination of Planet Scattering, Tidal Circularization, and the Kozai Mechanism". In: *ApJ* 678, 498-508, pp. 498–508. DOI: 10.1086/529369. arXiv: 0801.1368.

Ngo, H. et al. (2015). "Friends of Hot Jupiters. II. No Correspondence between Hot-jupiter Spin-Orbit Misalignment and the Incidence of Directly Imaged Stellar Companions". In: *ApJ* 800, 138, p. 138. DOI: 10.1088/0004-637X/800/2/138. arXiv: 1501.00013 [astro-ph.EP].

Peek, K. M. G. et al. (2009). "Old, Rich, and Eccentric: Two Jovian Planets Orbiting Evolved Metal-Rich Stars". In: *PASP* 121, p. 613. DOI: 10.1086/599862. arXiv: 0904.2786 [astro-ph.EP].

Pepe, F. et al. (2011). "The HARPS search for Earth-like planets in the habitable zone. I. Very low-mass planets around HD 20794, HD 85512, and HD 192310". In: *A&A* 534, A58, A58. DOI: 10.1051/0004-6361/201117055. arXiv: 1108.3447 [astro-ph.EP].

Petigura, E. A., A. W. Howard, and G. W. Marcy (2013). "Prevalence of Earth-size planets orbiting Sun-like stars". In: *Proceedings of the National Academy of Science* 110, pp. 19273–19278. DOI: 10.1073/pnas.1319909110. arXiv: 1311.6806 [astro-ph.EP].

Pilyavsky, G. et al. (2011). "A Search for the Transit of HD 168443b: Improved Orbital Parameters and Photometry". In: *ApJ* 743, 162, p. 162. DOI: 10.1088/0004-637X/743/2/162. arXiv: 1109.5166 [astro-ph.EP].

Pollack, J. B. et al. (1996). "Formation of the Giant Planets by Concurrent Accretion of Solids and Gas". In: *Icarus* 124, pp. 62–85. DOI: 10.1006/icar.1996.0190.

Rafikov, R. R. (2006). "Atmospheres of Protoplanetary Cores: Critical Mass for Nucleated Instability". In: *ApJ* 648, pp. 666–682. DOI: 10.1086/505695. eprint: astro-ph/0405507.

Rasio, F. A. and E. B. Ford (1996). "Dynamical instabilities and the formation of extrasolar planetary systems". In: *Science* 274, pp. 954–956. DOI: 10.1126/science.274.5289.954.

Rice, W. K. M., P. J. Armitage, and D. F. Hogg (2008). "Why are there so few hot Jupiters?" In: *MNRAS* 384, pp. 1242–1248. DOI: 10.1111/j.1365-2966.2007.12817.x. arXiv: 0712.0823.

Rivera, E. J. et al. (2010). "A Super-Earth Orbiting the Nearby Sun-like Star HD 1461". In: *ApJ* 708, pp. 1492–1499. DOI: 10.1088/0004-637X/708/2/1492. arXiv: 0912.2566 [astro-ph.EP].

Robinson, S. E. et al. (2007). "Two Jovian-Mass Planets in Earthlike Orbits". In: *ApJ* 670, pp. 1391–1400. DOI: 10.1086/522106. arXiv: 0708.0832.

Rodigas, T. J. and P. M. Hinz (2009). "Which Radial Velocity Exoplanets Have Undetected Outer Companions?" In: *ApJ* 702, pp. 716–723. DOI: 10.1088/0004-637X/702/1/716. arXiv: 0907.0020 [astro-ph.EP].

Santos, N. C. et al. (2010). "Do stellar magnetic cycles influence the measurement of precise radial velocities?" In: *A&A* 511, A54, A54. DOI: 10.1051/0004-6361/200913433. arXiv: 0912.2901 [astro-ph.EP].

Schlaufman, K. C. and J. N. Winn (2013). "Evidence for the Tidal Destruction of Hot Jupiters by Subgiant Stars". In: *ApJ* 772, 143, p. 143. DOI: 10.1088/0004-637X/772/2/143. arXiv: 1306.0567 [astro-ph.EP].

Ségransan, D. et al. (2011). "The HARPS search for southern extra-solar planets. XXIX. Four new planets in orbit around the moderatly active dwarfs <ASTROBJ>HD 63765</ASTROBJ>, <ASTROBJ>HD 104067</ASTROBJ>, <ASTROBJ>HD 125595</ASTROBJ>, and <ASTROBJ>HIP 70849</ASTROBJ>". In: *A&A* 535, A54, A54. DOI: 10.1051/0004-6361/200913580. arXiv: 1107.0339 [astro-ph.SR].

Shen, Y. and E. L. Turner (2008). "On the Eccentricity Distribution of Exoplanets from Radial Velocity Surveys". In: *ApJ* 685, 553-559, pp. 553–559. DOI: 10.1086/590548. arXiv: 0806.0032.

Spalding, C. and K. Batygin (2014). "Early Excitation of Spin-Orbit Misalignments in Close-in Planetary Systems". In: *ApJ* 790, 42, p. 42. DOI: 10.1088/0004-637X/790/1/42. arXiv: 1406.4183 [astro-ph.EP].

Steffen, J. H. et al. (2012). "Kepler constraints on planets near hot Jupiters". In: *Proceedings of the National Academy of Science* 109, pp. 7982–7987. DOI: 10.1073/pnas.1120970109. arXiv: 1205.2309 [astro-ph.EP].

Storch, N. I., K. R. Anderson, and D. Lai (2014). "Chaotic dynamics of stellar spin in binaries and the production of misaligned hot Jupiters". In: *Science* 345, pp. 1317–1321. DOI: 10.1126/science.1254358. arXiv: 1409.3247 [astro-ph.EP].

Takeda, G. et al. (2007). "Structure and Evolution of Nearby Stars with Planets. II. Physical Properties of ˜1000 Cool Stars from the SPOCS Catalog". In: *ApJS* 168, pp. 297–318. DOI: 10.1086/509763. eprint: astro-ph/0607235.

Tanaka, H., T. Takeuchi, and W. R. Ward (2002). "Three-Dimensional Interaction between a Planet and an Isothermal Gaseous Disk. I. Corotation and Lindblad Torques and Planet Migration". In: *ApJ* 565, pp. 1257–1274. DOI: 10.1086/324713.

Torres, G., J. N. Winn, and M. J. Holman (2008). "Improved Parameters for Extrasolar Transiting Planets". In: *ApJ* 677, 1324-1342, pp. 1324–1342. DOI: 10.1086/529429. arXiv: 0801.1841.

Udry, S. et al. (2002). "The CORALIE survey for southern extra-solar planets. VIII. The very low-mass companions of <ASTROBJ>HD 141937</ASTROBJ>, <ASTROBJ>HD 162020</ASTROBJ>, <ASTROBJ>HD 168443</ASTROBJ> and <ASTROBJ>HD 202206</ASTROBJ>: Brown dwarfs or "superplanets"?" In: *A&A* 390, pp. 267–279. DOI: 10.1051/0004-6361:20020685. eprint: astro-ph/0202458.

Valenti, J. A., R. P. Butler, and G. W. Marcy (1995). "Determining Spectrometer Instrumental Profiles Using FTS Reference Spectra". In: *PASP* 107, p. 966. DOI: 10.1086/133645.

Valenti, J. A. and D. A. Fischer (2005). "Spectroscopic Properties of Cool Stars (SPOCS). I. 1040 F, G, and K Dwarfs from Keck, Lick, and AAT Planet Search Programs". In: *ApJS* 159, pp. 141–166. DOI: 10.1086/430500.

Valenti, J. A., D. Fischer, et al. (2009). "Two Exoplanets Discovered at Keck Observatory". In: *ApJ* 702, pp. 989–997. DOI: 10.1088/0004-637X/702/2/989. arXiv: 0908.1612 [astro-ph.EP].

Vogt, S. S., S. L. Allen, et al. (1994). "HIRES: the high-resolution echelle spectrometer on the Keck 10-m Telescope". In: *Instrumentation in Astronomy VIII*. Ed. by D. L. Crawford and E. R. Craine. Vol. 2198. Proc. SPIE, p. 362. DOI: 10.1117/12.176725.

Vogt, S. S., R. P. Butler, et al. (2005). "Five New Multicomponent Planetary Systems". In: *ApJ* 632, pp. 638–658. DOI: 10.1086/432901.

Wang Sharon, X. et al. (2012). "The Discovery of HD 37605c and a Dispositive Null Detection of Transits of HD 37605b". In: *ApJ* 761, 46, p. 46. DOI: 10.1088/0004-637X/761/1/46. arXiv: 1210.6985 [astro-ph.EP].

Wittenmyer, R. A. et al. (2009). "A Search for Multi-Planet Systems Using the Hobby-Eberly Telescope". In: *ApJS* 182, pp. 97–119. DOI: 10.1088/0067-0049/182/1/97. arXiv: 0903.0652 [astro-ph.EP].

Wright, J. T., G. W. Marcy, R. P. Butler, and S. S. Vogt (2004). "Chromospheric Ca II Emission in Nearby F, G, K, and M Stars". In: *ApJS* 152, pp. 261–295. DOI: 10.1086/386283. eprint: astro-ph/0402582.

Wright, J. T., G. W. Marcy, R. P. Butler, S. S. Vogt, et al. (2008). "The Jupiter Twin HD 154345b". In: *ApJL* 683, L63, p. L63. DOI: 10.1086/587461. arXiv: 0802.1731.

Wright, J. T., S. Upadhyay, et al. (2009). "Ten New and Updated Multiplanet Systems and a Survey of Exoplanetary Systems". In: *ApJ* 693, pp. 1084–1099. DOI: 10.1088/0004-637X/693/2/1084. arXiv: 0812.1582.

Wu, Y. and Y. Lithwick (2011). "Secular Chaos and the Production of Hot Jupiters". In: *ApJ* 735, 109, p. 109. DOI: 10.1088/0004-637X/735/2/109. arXiv: 1012.3475 [astro-ph.EP].

Chapter 3

SEARCHING FOR SCATTERERS: HIGH-CONTRAST IMAGING OF YOUNG STARS HOSTING WIDE-SEPARATION PLANETARY-MASS COMPANIONS

3.1 Abstract

We have conducted an angular differential imaging survey with NIRC2 at Keck in search of close-in substellar companions to a sample of seven systems with confirmed planetary-mass companions (PMCs) on wide orbits (>50 AU). These wide-separation PMCs pose significant challenges to all three possible formation mechanisms: core accretion plus scattering, disk instability, and turbulent fragmentation. We explore the possibility that these companions formed closer in and were scattered out to their present-day locations by searching for other massive bodies at smaller separations. The typical sensitivity for this survey is $\Delta K \sim 12.5$ at 1". We identify eight candidate companions, whose masses would reach as low as one Jupiter mass if gravitationally bound. From our multi-epoch astrometry we determine that seven of these are conclusively background objects, while the eighth near DH Tau is ambiguous and requires additional monitoring. We rule out the presence of >7 M_{Jup} bodies in these systems down to 15 – 50 AU that could be responsible for scattering. This result combined with the totality of evidence suggests that dynamical scattering is unlikely to have produced this population of PMCs. We detect orbital motion from the companions ROXs 42B b and ROXs 12 b, and from this determine 95% upper limits on the companions' eccentricities of 0.58 and 0.83 respectively. Finally, we find that the 95% upper limit on the occurrence rate of additional planets with masses between 5 – 15 M_{Jup} outside of 40 AU in systems with PMCs is 54%.

3.2 Introduction

Observational studies of exoplanet systems present a unique opportunity to probe the mechanisms behind planet formation. Over the past decade, surveys using a variety of techniques (radial velocity, transit, microlensing, direct imaging) have revealed a multitude of new systems with astoundingly diverse properties. Many of these systems are difficult to explain within the framework of standard planet formation theories (e.g. Pollack et al., 1996; Boss, 2006), and have forced theorists

and observers alike to re-evaluate their narratives for planet formation and migration. Perhaps one of the biggest challenges for planet formation models comes from direct imaging surveys, which have uncovered of a new population of young planetary-mass companions (PMCs) (< 15 M_{Jup}) located beyond 50 AU.

In 2004 Chauvin et al. discovered a 5 M_{Jup} companion 2M1207 b orbiting 55 AU away from a 25 M_{Jup} brown dwarf. Shortly afterwards, additional discoveries of other wide-separation PMCs such as AB Pic b (Chauvin et al., 2005), DH Tau b (Itoh et al., 2005), and CHXR 73 b (Luhman, Wilson, et al., 2006) drove observers and theorists to question how this growing population of objects formed (Lodato, Delgado-Donate, and Clarke, 2005; Boss, 2006). To date, fifteen PMCs at large orbital distances have been confirmed, most of which are extremely young, <10 Myr old (Bowler, Liu, Kraus, and Mann, 2014). Three possible formation routes have been proposed for these wide-separation planets, including direct collapse from molecular cloud fragmentation, disk instability, and core accretion plus gas capture, but all three have significant problems explaining this population of PMCs.

In the process of turbulent fragmentation, all stellar and substellar objects begin as opacity-limited fragments with masses of a few Jupiter masses and subsequently begin to accrete gas from the molecular cloud (Low and Lynden-Bell, 1976). Hydrodynamical star formation simulations have shown that in order to stop accretion at brown dwarf or planetary masses, PMCs must either form at nearly the same time that the circumstellar envelope is exhausted, or else they must be dynamically ejected from the densest regions of gas before they are able to accrete much additional mass (Bate, Bonnell, and Bromm, 2002; Bate, 2009; Bate, 2012). This mechanism has a very difficult time producing binaries with the high mass ratios needed to match the observed wide-separation planetary systems.

In models of disk instability, gas giant planets form rapidly via fragmentation of a gravitationally unstable disk. For this model to work, the disk needs to be massive enough and cold enough to gravitationally collapse. In the majority of scenarios, the disk surface densities beyond 100 AU are too low for gravitational instability to operate. While some models show that disk fragmentation can occur outside 100 AU (Dodson-Robinson et al., 2009; Boss, 2006; Vorobyov, 2013), the fragments rarely survive to become full-fledged planetary embryos. This low survival probability is due to processes such as inward migration and accretion onto the host star, or ejection from the system due to dynamical interactions. While it has been suggested that disk instability could be effective for exceptionally massive disks, this is an

extremely limited region of disk parameter space (Vorobyov, 2013).

Finally, in the core accretion model, cores grow via successions of two-body collisions between solids until they are massive enough to start runaway gas accretion (Pollack et al., 1996; Alibert et al., 2005). In situ formation of massive wide-separation planets through core accretion is unlikely since the timescale to grow massive cores at these separations is longer than the observed lifetimes of proto-planetary disks. However, recent simulations of core formation via pebble accretion have shown that gas giant cores can form at separations out to 50 AU comfortably before the gas in the disk dissipates (Lambrechts and Johansen, 2012). Furthermore, it might be possible for these giant planets to form closer to the star and be subsequently scattered out beyond 100 AU by another planet in the system. One potential scenario is that if multiple planet-planet scatterings occur, these giant planets could permanently end up in stable, wide-separation orbits (Scharf and Menou, 2009). Simulations have shown that in this case, these wide-separation planets have high eccentricities of >0.5 (Scharf and Menou, 2009; Nagasawa and Ida, 2011). While planet-planet scattering seems to be a potential solution, it requires another body in the system at least as massive as the wide separation planets.

Thus far, despite hundreds of hours of AO imaging, only one multi-planet system has been confirmed with this technique, HR 8799 (Marois, Macintosh, T. Barman, et al., 2008; Marois, Macintosh, and Véran, 2010). Recently, two surveys have found evidence of additional planets in two more systems: LkCa 15 and HD 100546 (Kraus and Ireland, 2012; Quanz et al., 2015; Sallum et al., 2015; Currie, Cloutier, et al., 2015). Searching for additional planets in these directly imaged systems is critical to understanding the formation and orbital evolution of planets at wide separations, a parameter space currently explored solely by the direct imaging technique.

In this study, we explore the possibility that the observed wide-separation PMCs formed closer in to their host stars, and were scattered out to their present day locations by another massive companion within the system. We conducted an angular differential imaging (ADI) survey with NIRC2 at Keck in search of close-in substellar companions to a sample of seven systems with confirmed PMCs on extremely wide orbits. Our observations are sensitive to companions at significantly lower masses and smaller separations than previous studies of these systems, and allow us to place much stronger constraints on the presence of inner companions. We also use these same systems to calculate the first estimate of the multiplicity of directly imaged planetary systems.

This paper is structured in the following manner. In Section 3.3 we describe the selected sample of systems and the methods for obtaining the ADI imaging data. In Section 3.4 we describe the PCA reduction of the images as well as a new method to simultaneously calculate astrometry and relative photometry of candidate companions. Finally, in Section 3.5 we discuss our results and their implications for the formation mechanisms of this population of wide-separation PMCs.

3.3 Observations

Target Selection

We selected our targets from the sample of 15 systems with confirmed companions beyond 50 AU with mass ranges that are either below or straddle the deuterium burning limit (< 15 M_{Jup}). These systems are as a whole extremely young, which translates into higher sensitivity to lower mass planets at smaller separations. From this larger sample, we selected targets that were observable from Keck and that had previously been imaged only with short integrations. This would allow our deeper follow-up imaging to achieve unprecedented levels of sensitivity in these systems. Altogether, we targeted seven systems: ROXs 42B, ROXs 12, HN Peg, HD 203030, DH Tau, LP 261–75, and 2MASS J012250–243950. Table 3.1 summarizes the properties of this sample. In addition, we targeted 2MASS J162627744–2527247, which does not have a previously confirmed wide-separation PMC. This star is a wide separation stellar companion to ROXs 12, located ~40" away.[1] Not only do the two stars show identical proper motion, but 2M1626–2527 and ROXs 12 also exhibit WISE excesses, indicating that these objects form a wide binary, are disk-bearing, and are young.

[1]There was some confusion with regards to follow-up observations of ROXs 12. The coordinates for ROXs 12 listed in Simbad and in both the discovery and confirmation papers of the PMC ROXs 12b (Ratzka, Köhler, and Leinert, 2005; Kraus, Ireland, Cieza, et al., 2014) are for 2M1626-2527, which does not have a confirmed PMC. The correct coordinates for ROXs 12 are listed in Table 3.1.

Table 3.1: Target Sample

System	RA (J2000)	Dec (J2000)	Pri. SpT	m_K (mag)	m_R (mag)	Dist. (pc)	M_{comp} (M_{Jup})	Age (Myr)	Ref.
2M0122–2439	01 22 50.94	–24 39 50.6	M3.5	9.20 ± 0.03	13.6	36 ± 4	12 – 25	120 ± 10	1, 2, 3
DH Tau	04 29 41.56	+26 32 58.3	M1	8.18 ± 0.03	12.1	145 ± 15	12^{+10}_{-4}	1 – 2	4, 6, 10, 13
LP 261–75	09 51 04.60	+35 58 09.8	M4.5	9.69 ± 0.02	14.4	32.9^{+3}_{-2}	20^{+10}_{-5}	100 – 200	1, 6, 7, 10
2M1626–2527	16 26 27.75	–25 27 24.7	M0	9.21 ± 0.03	15.8	120 ± 10	···	8^{+4}_{-3}	2, 4, 6
ROXs 12	16 26 28.10	–25 26 47.1	M0	9.10 ± 0.03	13.5	120 ± 10	12 – 20	8^{+4}_{-3}	2, 4, 6, 12
ROXs 42B	16 31 15.02	–24 32 43.7	M1	8.67 ± 0.02	13.4	120 ± 10	6 – 14	7^{+3}_{-2}	2, 4, 5, 6, 8
HD 203030	21 18 58.22	+26 13 49.9	G8	6.65 ± 0.02	7.9	40.9 ± 1.2	23^{+8}_{-11}	130 – 400	6, 9, 10
HN Peg	21 44 31.33	+14 46 19.0	G0	4.56 ± 0.04	5.6	18.4 ± 0.3	21 ± 9	300 – 400	6, 10, 11

Notes. References: (1) Bowler, Liu, Shkolnik, et al. (2013), (2) **CMC2011** (3) Cutri and et al. (2013), (4) Kraus, Ireland, Cieza, et al. (2014), (5) Currie, Daemgen, et al. (2014), (6) Cutri, Skrutskie, et al. (2003), (7) Reid and Walkowicz (2006), (8) Zacharias, Finch, et al. (2012), (9) Metchev and Hillenbrand (2006), (10) Zacharias, Monet, et al. (2005), (11) Luhman, Patten, et al. (2007), (12) Skiff (2013), (13) Currie, Daemgen, et al. (2014)

Table 3.2: Keck/NIRC2 Observations of PMC Systems

System	UT Date	Filter	Coronagraph Diam. (mas)	No. of Exp.	Tot. Exp. Time (min)	Rot. (deg)	Airmass [1]	FWHM ,2[1] (mas)
2M0122-2439	2014 Nov 9	K_S	600	30	30	11.0	1.44	46.5 ± 0.6
DH Tau	2014 Dec 7	K_S	600	25	25	57.6	1.07	45.9 ± 1.9
DH Tau	2015 Nov 04	K_S	600	25	25	36.7	1.01	46.3 ± 1.2
2M1626–2527	2014 May 13	K_S	600	28	28	11.3	1.44	73.6 ± 11.6
2M1626–2527	2015 Jun 23	K_S	600	25	25	9.5	1.48	45.8 ± 1.5
ROXs 12	2011 Jun 23	K_P	300	27	13.5	5.4	1.56	47.7 ± 1.6
ROXs 12	2015 Aug 27	K_S	600	20	20	6.4	1.54	53.0 ± 9.3
ROXs 42B	2011 Jun 23	K_P	300	46	23	13.9	1.44	45.2 ± 4.9
ROXs 42B	2014 May 13	K_S	600	30	30	12.3	1.41	60.1 ± 10.1
HD 203030	2014 Nov 9	K_S	600	60	30	12.4	1.06	43.0 ± 0.3
HD 203030	2015 Jun 3	K_S	600	80	40	80.9	1.02	40.4 ± 1.6
HN Peg	2014 Aug 4	K_S	600	50	25	102.3	1.01	47.7 ± 0.7
HN Peg	2015 Jun 2	K_S	600	70	35	32.1	1.04	39.6 ± 1.2

[1] Values averaged over the total duration of the observations for each target, which typically spanned 20 - 30 minutes.

[2] The reported uncertainty on each FWHM value is the standard deviation of the PSF over the duration of the observations.

NIRC2 Imaging

We used the near-infrared imaging camera NIRC2 at the Keck II 10 m telescope for all of our observations. Adaptive optics imaging was carried out in natural guide star mode using the narrow camera. Due to the realignment of the Keck II AO and NIRC2 system in April 2015, for epochs taken prior to this date we used a plate scale of 0.009952 ± 0.000002 arcsec/pixel (Yelda et al., 2010), and for epochs taken after this date we used a plate scale of 0.009971 ± 0.000004 arcsec/pixel (Service et al., 2016). The field of view of the 1024×1024 array is 10.2"×10.2". For each system we obtained a total integration time of ∼ 30 minutes in ADI mode with an average of ∼ 30 degrees of sky rotation. For each image, the star was centered behind a coronagraph, which for nearly all images was the 600 mas diameter coronagraph. This coronagraph is partially transparent with 6.65 +/- 0.10 magnitudes of attenuation in Ks band (Bowler, Shkolnik, et al., 2015). Due to high noise levels in the lower left quadrant of the detector, we positioned the occulting spot (already fixed at row 430) at column 616. When possible, we observed these systems as they were transiting to maximize the rotation achieved during the observation, which makes post-processing PSF subtraction more effective. The inner working angle achieved for these observations is 300 mas, while the outer working angle for complete FOV coverage is ∼ 4”. All observations were taken with the Ks filter, which maximizes the Strehl ratio while avoiding the high sky backgrounds encountered in L band. We took second epoch data for the systems where we identified a candidate companion.

3.4 Analysis

PCA Image Reduction

After removing bad pixels and cosmic rays and flat-fielding, we applied the Yelda et al. (2010) distortion correction to raw images taken before April 2015, and applied the updated Service et al. (2016) distortion solution to later epochs. We then used principle component analysis (PCA) to further reduce these images. PCA is an algorithm that has recently been applied to high contrast imaging for increasing the contrast achievable next to a bright star. In short, PCA is a mathematical technique that relies on the assumption that every image in a stack can be represented as a linear combination of its principle orthogonal components, selecting structures that are present in most of the images. The stellar PSF, composed of a sum or orthogonal components, is subtracted from each image, thereby providing access to faint companions at contrasts below the speckle noise. We used a PCA routine

Table 3.3: Contrast Curves

System	0.5"	1"	1.5"	2"	2.5"	3"	3.5"
2M0122-2439	1.4×10^{-3}	2.5×10^{-5}	1.0×10^{-5}	5.9×10^{-6}	5.6×10^{-6}	5.1×10^{-6}	4.8×10^{-6}
DH Tau	2.7×10^{-4}	3.2×10^{-5}	9.1×10^{-6}	7.4×10^{-6}	6.9×10^{-6}	5.2×10^{-6}	5.1×10^{-6}
LP261-75	$1.6 \times 10^{-}4$	2.2×10^{-5}	1.5×10^{-5}	1.6×10^{-5}	1.5×10^{-5}	1.4×10^{-5}	1.5×10^{-5}
2M1626–2527	1.6×10^{-3}	8.4×10^{-5}	2.7×10^{-5}	1.6×10^{-5}	1.7×10^{-5}	1.5×10^{-5}	1.5×10^{-5}
ROXs 12	2.7×10^{-2}	3.0×10^{-4}	2.9×10^{-5}	2.0×10^{-5}	1.5×10^{-5}	1.2×10^{-5}	1.3×10^{-5}
ROXs 42B	5.1×10^{-4}	3.6×10^{-5}	1.1×10^{-5}	5.8×10^{-6}	5.1×10^{-6}	4.7×10^{-6}	4.8×10^{-6}
HD 203030	1.2×10^{-4}	1.0×10^{-5}	2.4×10^{-6}	9.7×10^{-7}	6.8×10^{-7}	6.2×10^{-7}	4.9×10^{-7}
HN Peg	3.4×10^{-4}	1.4×10^{-5}	2.4×10^{-6}	8.2×10^{-7}	4.2×10^{-7}	3.5×10^{-7}	2.9×10^{-7}

Notes. All of these contrasts correspond to images taken using the K_S filter.

following the method presented in Soummer, Pueyo, and Larkin (2012) which uses the KLIP algorithm.

The optimal number of principle components to use in a reduction is set by the trade-off between speckle noise and self-attenuation of the signal of interest. Too few components might not subtract enough speckle noise near the star, and too many may lead to self-subtraction of the planetary signal, reducing the achievable contrasts. In our analysis, we optimized the number of components used for each individual system empirically. We reduced the data for each system with different numbers of principle components, then compared resulting contrast curves that were calibrated for self-attenuation by injecting fake companions. For each system we adopted the number of principle components that corresponded to the most favorable contrast as the optimal number. These ranged from 5 – 20 principle components for systems in our sample.

We found a total of nine candidate companions at a wide variety of separations in the eight systems that we observed. These candidate companions are shown in Figure 3.1, and the contrast curves for all systems observed are shown in Figure 3.2. We determine our contrast curves by calculating the noise level in our images as a function of radial distance using the standard deviation on concentric annuli of width FWHM of the stellar PSF. The noise level at each radius is corrected for self-subtraction by dividing by the self-attenuation at that radius. This self-attenuation factor is calculated by injection and recovery of sources with known magnitudes at different radii. We present the 5σ contrast curves in Figure 3.2, which are simply our noise levels divided by the self-attenuation factor multiplied by a factor of 5. We list 5σ contrast values for a range of angular separations for each target in Table 3.3. We note that these contrasts are often limited by small PA rotation and subsequent ADI self-subtraction.

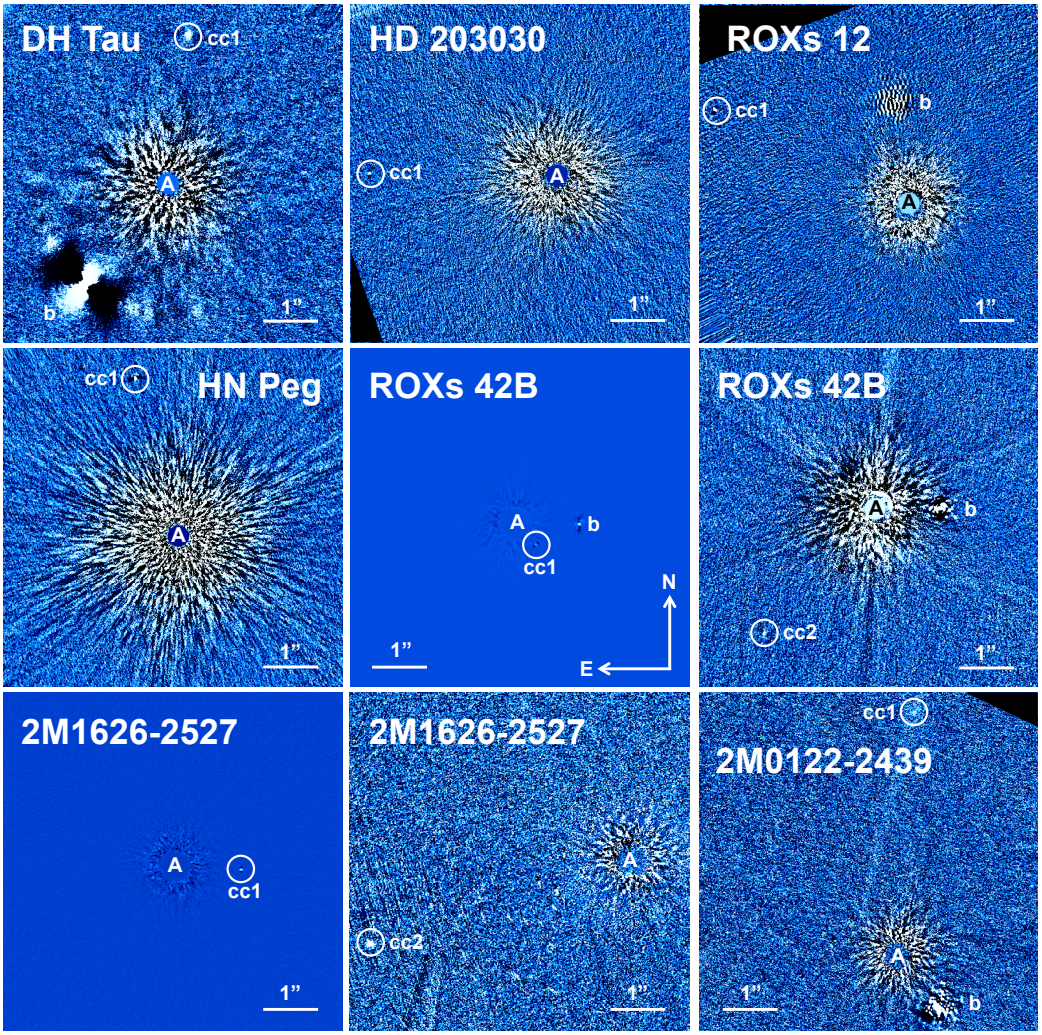

Figure 3.1: Candidate companions in our sample. All images are north-aligned. ROXs 42B and 2M1626-2527 are shown twice with different stretches to accommodate candidate companions with significantly different flux ratios. Some of the known companions exhibit speckle-like features in these images. This is due to the fact that these bright companions were not masked during the PCA reduction, so some of the PCA components were structured to subtract away the signal of the confirmed companions. The PCA algorithm was able to more successfully subtract away companions with small amounts of rotation (i.e. ROXs 12 b) in comparison to companions with large amounts of rotation (i.e. DH Tau b).

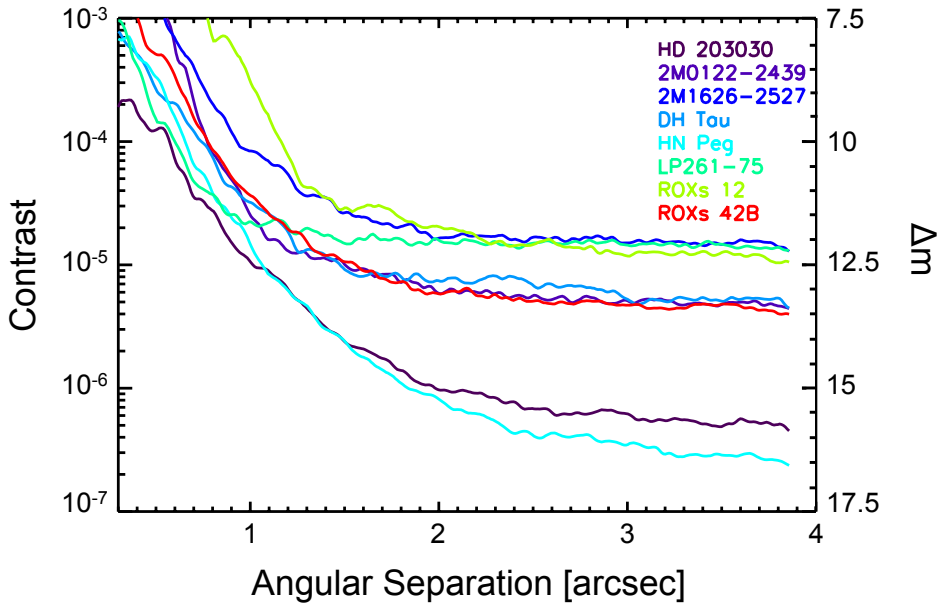

Figure 3.2: 5σ contrast curves for systems in our sample. The stellar flux was modified by a throughput correction (Bowler, Liu, Shkolnik, et al., 2013) due to attenuation from the coronagraph spot. The curves have been corrected for self-attenuation of the target of interest using a robust injection and recovery technique. Note that the flattening of the contrast curves indicates a background-limited regime, as opposed to speckle limitations.

Simultaneous Astrometry and Relative Photometry

Using second epoch data, we can determine whether or not these candidate companions are co-moving. Typical methods for determining the astrometry and photometry of candidate companions use the final post-processed images for these calculations. However, we note that because of self-subtraction, using the final LOCI or PCA images to calculate separations, position angles, and their uncertainties can lead to significant biases in the corresponding photometry and astrometry (e.g. Marois, Macintosh, and Véran, 2010). To avoid this, we developed an MCMC algorithm that simultaneously calculates the astrometry and relative photometry of these candidate companions. For each iteration in the MCMC process, we injected a negative PSF into each individual science image in the vicinity of the companion of interest prior to de-rotation, where we modeled these negative PSFs as Moffat distributions. There were three parameters that we varied with each step during the MCMC routine, namely the negative PSF amplitude, separation, and position angle. We fixed all other free parameters to the values determined from fitting the Moffat distribution to the stellar PSF. The science images with injected negative PSFs were then run

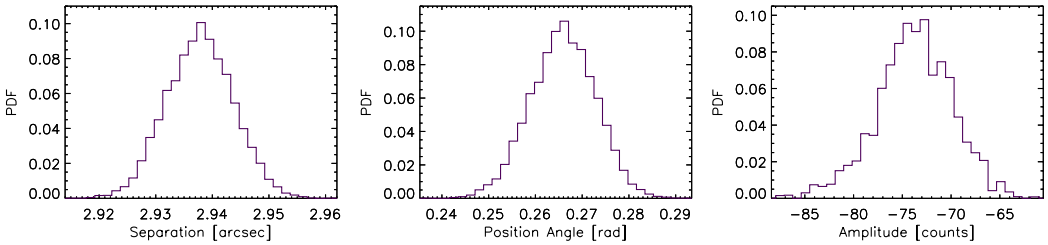

Figure 3.3: Example posterior PDFs from the MCMC astrometry calculation for the candidate companion in our observations of HN Peg. Note that the amplitude PDF shows the amplitude of the negative PSF injected into the science images.

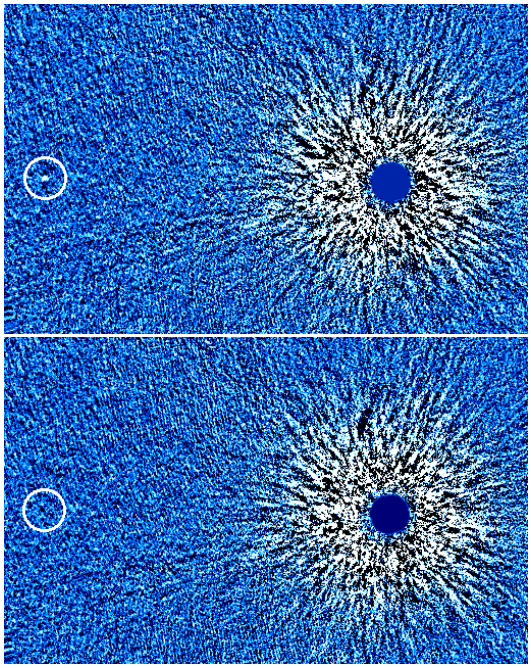

Figure 3.4: Comparison of PCA images of the HD 203030 candidate companion without (top) and with (bottom) the best fit negative PSF injected.

through the PCA reduction routine. The smaller the RMS noise at the location of the candidate companion, the better the fit of the negative PSF. The result of this MCMC analysis is a posterior distribution for the amplitude, separation, and position angle of the candidate companions, an example of which is shown in Figure 3.3. Figure 3.4 compares a reduced image with and without the best-fit negative PSF injected at the best fit separation and position angle of the candidate companion.

In addition to the errors from the candidate companion PDFs for the separation and position angle, after the MCMC program is finished we also account for uncertainties from the registration of the stellar position in each science image, uncertainties

from the distortion correction, and uncertainties associated with the plate scale. We also include the +0.252 degree correction for north alignment to the NIRC2 header position angles (Yelda et al., 2010) for epochs taken before April 2015, and for subsequent epochs include the +0.262 degree correction for north alignment (Service et al., 2016). This MCMC technique calculates robust uncertainties from the posterior distributions, without the systematic uncertainties that occur when the reduced LOCI or PCA images are used. The best-fit separations and position angles for each candidate companion, as well as confirmed companions in these systems, are presented in Table 3.4.

While the separation, position angle, and amplitude are the three parameters that were actively varied with each step in the MCMC program, we also track the total flux of the candidate companion. For each link in the chain, we place an aperture at the separation and position angle of that step and sum the number of counts in the aperture. While the size of the aperture for a given companion remains fixed, the aperture size ranged from 4 – 6 pixels depending on the candidate companion FWHM. The aperture moves with the changes in position angle and separation as the MCMC program progresses, producing a posterior distribution of counts for the candidate companion. We note that since we calculate the astrometry and relative photometry simultaneously using this MCMC program, we use the same aperture sizes for both of these steps for a given candidate companion.

We next calculate the contrast relative to the host star, Δm, for each candidate companion. To determine the flux from the star, the throughput of the occulting spot (0.0022 ± 0.0002, Bowler et al 2015), and the sky noise need to be accounted for. The measured counts are a combination of the flux from the star plus the flux from the sky, both attenuated by the throughput of the mask. We denote this combined and attenuated star plus sky flux as $F_{b,\star}$. The corrected flux for the star is shown in Equation 1. T is the throughput (0.0022) of the mask in K_S, F_{sky} is the sky flux, and $F_\star$ is the flux from the star corrected for both throughput losses and sky noise.

$$F_\star = \frac{F_{\star,b}}{T} - F_{sky}. \tag{3.1}$$

This calculation is performed for each image in the stack; for a stack of N images, there are N values of $F_\star$. The error on this flux value is:

$$\sigma_{F,\star} = \sqrt{\left(\frac{F_{b,\star}}{T}\right)^2 \times \left[\left(\frac{\sigma_{\star,b}}{F_{\star,b}}\right)^2 + \left(\frac{\sigma_T}{T}\right)^2\right] + \sigma_{sky}^2}. \tag{3.2}$$

Here, $\sigma_{\star,b}$ is the standard deviation of the $F_{\star,b}$ values for each image in the stack, σ_T is the measured error on the throughput, and σ_{sky} is the standard deviation of the sky values calculated for each image.

We obtain the companion flux and its uncertainty from the posterior distribution generated from the MCMC analysis, and subtract off sky noise. The flux ratio between the star and the companion is simply $F_{ratio} = \frac{F_\star}{F_{\rm comp}}$, and the error on this flux ratio can be propagated analytically:

$$\sigma_{fr} = F_{ratio} \times \sqrt{\left(\frac{\sigma_{F,\star}}{F_\star}\right)^2 + \left(\frac{\sigma_{comp}}{F_{comp}}\right)^2}. \tag{3.3}$$

The contrast ratio Δm in magnitudes is:

$$\Delta m = -2.5 \log_{10} F_{ratio}. \tag{3.4}$$

Finally, the error on Δm is given by:

$$\sigma_{\Delta m} = \frac{2.5}{\ln 10} \times \frac{\sigma_{fr}}{F_{ratio}}. \tag{3.5}$$

We present the Δm values for each candidate and confirmed companion in Table 3.4. We note that because 2M0122-2439 cc1 is so faint we were unable to use our MCMC analysis to calculate the astrometry of that companion (the MCMC chains failed to converge). Instead, we used centroiding on the final image to obtain the separation and position angle of the candidate companion, and adopted the robust errors calculated for the faint HD 203030 cc1. Furthermore, since the candidate companion near 2M0122-2439 appears to be extended (its FWHM is about twice that of the stellar PSF), we conclude that is likely a background galaxy, not a bound planet, and exclude it from the rest of the analysis.

Our astrometry conclusively shows that seven of the remaining eight candidate companions are background objects, while the nature of the candidate companion near DH Tau is ambiguous. Figures 3.5 and 3.6 show the relative astrometry of each candidate companion compared to the expected background track of a

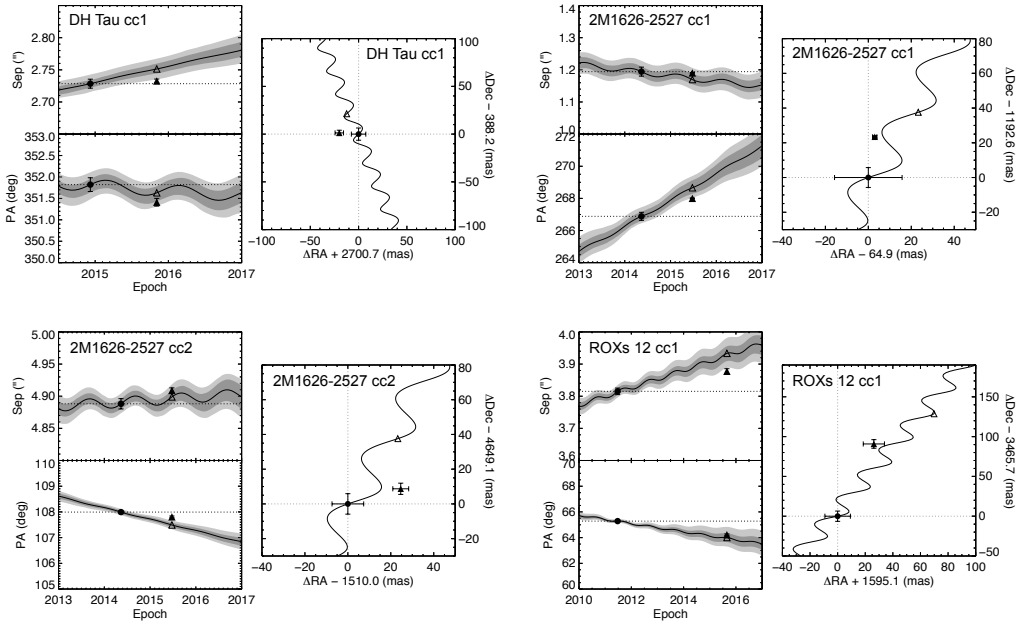

Figure 3.5: These plots show how the candidate companion's astrometry compares to expected trajectories of a co-moving object and a stationary background object. The first epoch of astrometry is denoted by a filled circle, and the second epoch is denoted by a filled triangle. The open triangles denote the expected astrometry of a stationary background object at the second epoch. The dark and light grey regions represent the one and two sigma errors on the predicted background tracks, respectively. These errors include uncertainties in the distance to the system, proper motion, and astrometry from the reference epoch. If the candidate companion was bound to the star, the second epoch triangles would fall on the horizontal dotted line (separation and position angle would not change as a function of time, except due to orbital motion). Top left: DH Tau candidate companion (cc) 1. Top right: 2M1626–2527 cc1. Bottom left: 2M1626–2527 cc2. Bottom right: ROXs 12 cc1.

stationary object. The candidate companion background track plots clearly show that the second epoch astrometry falls on or near the predicted track for a stationary background object. While some of the second epoch astrometry measurements don't fall precisely on the expected track of a stationary background object, we note that this could be due to small errors in proper motion or distance, which would affect the predicted trajectory of a distant stationary object. We note that ROXs 42B cc1 was previously identified as likely a background object in the literature (Kraus, Ireland, Cieza, et al., 2014; Currie, Daemgen, et al., 2014) but our astrometry conclusively shows that it is a background object. For DH Tau cc1, while the second epoch astrometry falls close to the co-moving line, uncertainties on the expected trajectory of a background object make comovement ambiguous. The separation of a stationary object at the second epoch differs by $\sim 2.9\sigma$ from the separation we find for DH Tau cc1. Zhou et al. (2014) published *HST* UVIS optical photometry for

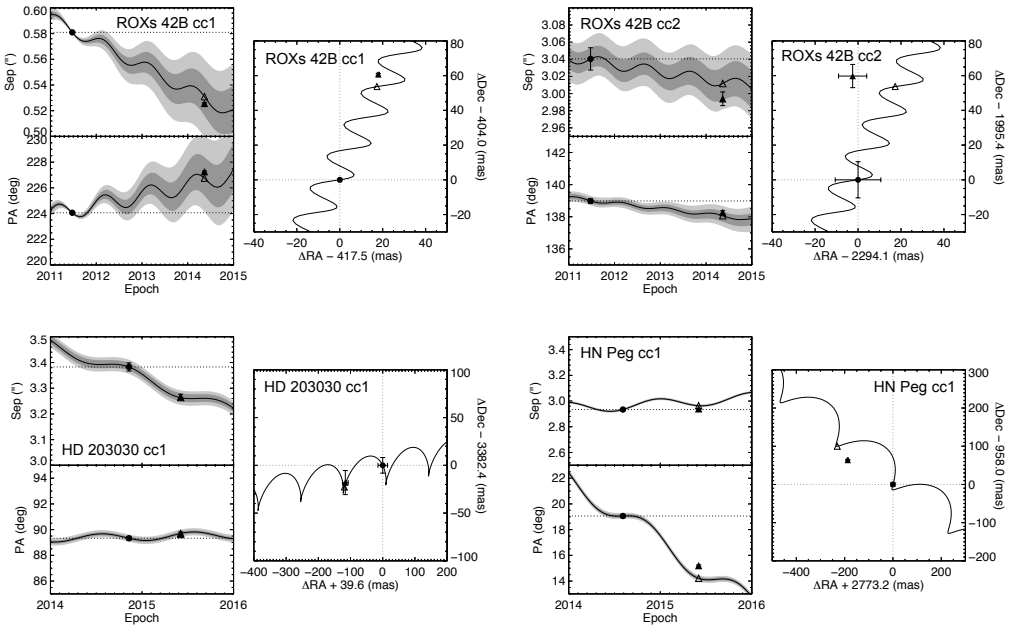

Figure 3.6: Background track plots for four of our candidate companions. See Figure 5 for more details. Top left: ROXs 42B cc1. Top right: ROXs 42B cc2. Bottom left: HD 203030 cc1. Bottom right: HN Peg cc1.

the DH Tau system but they did not report a detection of our candidate companion. They presented detection limits in both i and z filters, which we can use to place limits on the colors of DH Tau cc1. We find that the bluest DH Tau cc1 could be is $i - K = 7.8$ mag. Furthermore, line of sight visual extinction is low, 0.0 - 1.5 mag (Strom et al., 1989; White and Ghez, 2001). This apparently red color further motivates additional follow-up for the potentially bound DH Tau cc1. A third epoch taken when DH Tau is next observable end of 2016 would conclusively determine whether or not DH Tau cc1 is a bound object.

We also plot the relative astrometry for the previously confirmed companions to ROXs 12, ROXs 42B, and 2M0122-2439 in Figure 3.7. We have included astrometry from the literature in addition to the data presented in this paper. These plots show that follow-up astrometry generally fall near the dotted line denoting co-moving objects. We do not plot the relative astrometry for DH Tau b, since there are significant systematic offsets for measurements of the companion position angle and separation amongst previous epochs spanning 1999 through 2013. Table 3.5 lists literature astrometry measurements that we used for the confirmed companions in each of these three systems.

Table 3.4: Candidate PMC Astrometry and Photometry

System	Epoch	Filter	ρ (mas)	P.A. (deg)	Δm (mag)	Sep. (AU)
2M0122–2439 b	2014.8575	K_S	1450^{+1}_{-1}	$216.48^{+0.02}_{-0.02}$	4.79 ± 0.11	52
2M0122–2439 cc1	2014.8575	K_S	5238^{+12}_{-16}	$355.75^{+0.14}_{-0.14}$	9.60 ± 0.20	188
DH Tau cc1	2014.9342	K_S	2726^{+7}_{-7}	$351.82^{+0.16}_{-0.16}$	8.66 ± 0.25	395
DH Tau cc1	2015.8438	K_S	2734^{+4}_{-4}	$351.35^{+0.10}_{-0.10}$	8.45 ± 0.23	396
DH Tau b	2014.9342	K_S	2343^{+1}_{-1}	$140.25^{+0.02}_{-0.02}$	5.91 ± 0.20	340
DH Tau b	2015.8438	K_S	2339^{+1}_{-1}	$139.94^{+0.02}_{-0.02}$	5.72 ± 0.28	340
2M1626–2527 cc1	2014.3644	K_S	1193^{+11}_{-14}	$266.88^{+0.26}_{-0.21}$	7.36 ± 0.23	143
2M1626–2527 cc1	2015.4767	K_S	1189^{+2}_{-1}	$267.93^{+0.03}_{-0.02}$	6.93 ± 0.13	143
2M1626–2527 cc2	2014.3644	K_S	4883^{+8}_{-7}	$107.99^{+0.06}_{-0.06}$	7.62 ± 0.25	586
2M1626–2527 cc2	2015.4767	K_S	4901^{+4}_{-3}	$107.82^{+0.03}_{-0.03}$	7.11 ± 0.13	589
ROXs 12 cc1	2011.4767	K_P	3811^{+10}_{-10}	$65.29^{+0.08}_{-0.07}$	...	457
ROXs 12 cc1	2015.6548	K_S	3877^{+15}_{-14}	$64.12^{+0.09}_{-0.09}$	8.51 ± 0.13	465
ROXs 12 b	2011.4767	K_P	1778^{+1}_{-1}	$8.90^{+0.08}_{-0.08}$	...	213
ROXs 12 b	2015.6548	K_S	1786^{+1}_{-1}	$8.18^{+0.29}_{-0.30}$	4.30 ± 0.13	214
ROXs 42B cc1	2011.4767	K_P	580^{+1}_{-1}	$224.06^{+0.06}_{-0.06}$	...	70
ROXs 42B cc1	2014.3644	K_S	525^{+1}_{-1}	$227.27^{+0.06}_{-0.06}$	6.23 ± 0.27	63
ROXs 42B cc2	2011.4767	K_P	3037^{+14}_{-11}	$138.99^{+0.14}_{-0.15}$	...	365
ROXs 42B cc2	2014.3644	K_S	2991^{+8}_{-7}	$138.27^{+0.10}_{-0.12}$	8.37 ± 0.25	359
ROXs 42B b	2011.4767	K_P	1173^{+1}_{-1}	$270.06^{+0.01}_{-0.01}$	...	141
ROXs 42B b	2014.3644	K_S	1170^{+1}_{-1}	$270.55^{+0.01}_{-0.01}$	6.16 ± 0.35	140
HD 203030 cc1	2014.8575	K_S	3379^{+12}_{-16}	$89.33^{+0.14}_{-0.14}$	11.17 ± 0.15	139
HD 203030 cc1	2015.4219	K_S	3263^{+10}_{-7}	$89.76^{+0.16}_{-0.22}$	11.46 ± 0.20	134
HN Peg cc1	2014.5918	K_S	2931^{+4}_{-5}	$19.06^{+0.13}_{-0.11}$	12.63 ± 0.6	54
HN Peg cc1	2015.4192	K_S	2933^{+2}_{-2}	$15.22^{+0.05}_{-0.05}$	12.13 ± 0.48	54

Notes. We do not list Δm for the 2011 epochs because we did not have throughput measurements for the 300 mas coronagraph is K_P. Uncertainties in the astrometry and distance estimates to these systems typically lead to errors in separation in AU of 5 - 40 AU.

Table 3.5: Literature Measurements of Confirmed PMC Astrometry

Companion	Epoch	ρ (mas)	P.A. (deg)	ref
2M0122-2439 b	2012.7808	1444 ± 7	216.7 ± 0.2	3
2M0122-2439 b	2013.0493	1448.6 ± 0.6	216.4 ± 0.08	3
2M0122-2439 b	2013.4959	1448 ± 4	216.47 ± 0.07	3
2M0122-2439 b	2013.6258	1488 ± 3	216.52 ± 0.09	5
ROXs 12 b	2001.5014	1747 ± 30	10.3 ± 0.9	2
ROXs 12 b	2012.2575	1783.0 ± 1.8	8.85 ± 0.06	1
ROXs 42B b	2001.5014	1137 ± 30	268.0 ± 1.5	2
ROXs 42B b	2005.2904	1157 ± 10	268.8 ± 0.6	4
ROXs 42B b	2008.5479	1160 ± 10	269.7 ± 1.0	4
ROXs 42B b	2012.2575	1172.0 ± 1.2	270.03 ± 0.10	1
ROXs 42B b	2013.3233	1172.5 ± 1.2	270.25 ± 0.10	1

Notes. References: (1) Kraus, Ireland, Cieza, et al. (2014), (2) Ratzka, Köhler, and Leinert (2005), (3) Bowler, Liu, Shkolnik, et al. (2013), (4) Currie, Daemgen, et al. (2014), (5) Bowler, Shkolnik, et al. (2015)

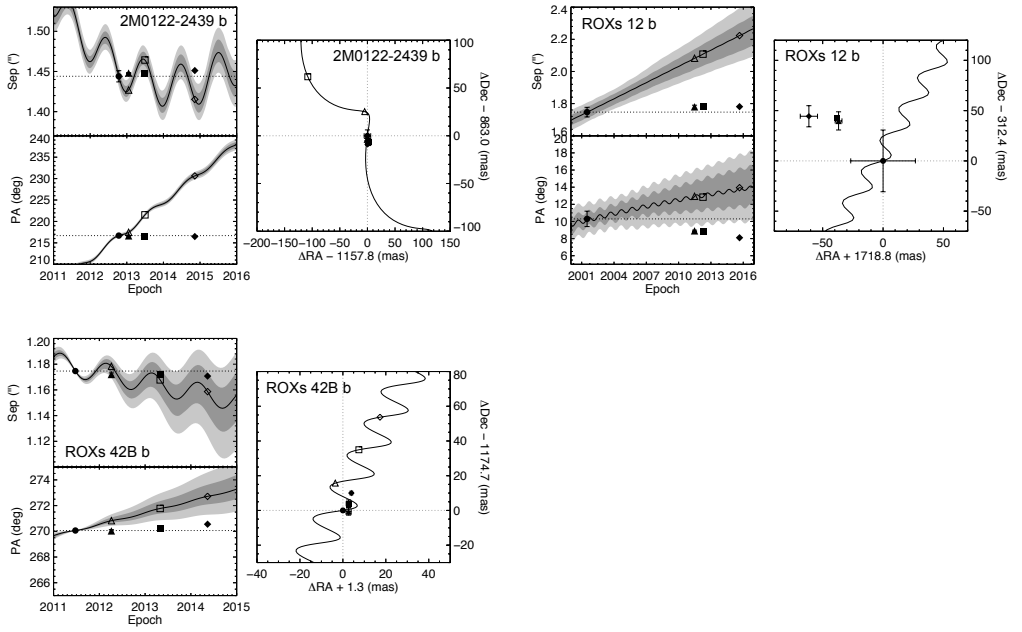

Figure 3.7: These background track plots show the astrometry of three previously confirmed companions in our sample. Top left: 2M0122–2439 b. Top right: ROXs 12 b. Bottom left: ROXs 42B b. In the 2M0122–2439 plot, we include two additional epochs of data in 2012 and 2013 from Bowler et al 2013. In the ROXs 12 plot, we include two additional epochs, in 2001 from Ratzka et al 2005, and in 2012 from Kraus et al 2014. In the ROXs 42B plot, we include two additional epochs, in 2001 from Ratzka et al 2005, and in 2012 from Kraus et al 2014. The plots for ROXs 12 b and ROXs 42B b show evidence of orbital motion. See subsection "Orbital Motion" for details.

Orbital Motion

We tested ROXs 42B b, 2M0122-2439 b, and ROXs 12b for evidence of orbital motion. Assuming a face on, circular orbit, we find that between the first and last epoch of ROXs 42B b, the maximum amount of change we would expect to see in position angle is 0.6 degrees. The actual change in PA between the first and last epochs is 0.49 ± 0.02 degrees. We performed a linear fit to all epochs with uncertainties in PA and in separation and compared these to the best-fit constants using evidence ratios. Evidence ratios use Akaike's information criterion (AIC) to quantitatively compare models. They are equal to the ratio of each model's Akaike weights, which are a measure of the strength of evidence for a model. An evidence ratio of 9 comparing model 1 to model 2 would mean that model 1 is 9 times more likely than model 2 given the data. We label linear fits as preferred if the slope of the line differs from zero by 2 - 4σ, and highly preferred if this slope is > 4σ away.

In PA we find the evidence ratio comparing a linear to constant fit for ROXs 42B b to be > 10^4, and in separation the evidence ratio is 62. The best fit slope of the

linear fit in PA is 0.1703 ± 0.0049 deg/yr, and in separation is -0.00132 ± 0.00029 arcsec/yr. We therefore conclude that the linear fits are highly preferred, suggesting that the displacements that we see in PA and separation over time are due to the orbital motion of ROXS 42B b.

For the confirmed companion orbiting 2M0122-2439, at a separation of only 52 AU we would expect this companion to have moved by 1.3 degrees in PA between the first and last epochs assuming a circular, face-on orbit. However, we only find a change in PA of 0.2 ± 0.2 degrees between the first and last epochs. Given that the change in PA is consistent with zero, and the evidence ratio for the separation of the companion favors a constant over a linear fit, we conclude that we do not find evidence of orbital motion for 2M0122-2439 b.

Finally, we assess whether orbital motion is evident for the confirmed companion ROXs 12 b. Between the first and last epochs, assuming a face-on circular orbit we would expect to see a change in PA of 1.6 degrees. We find a change of 2.1 ± 0.9 degrees. Evidence ratios comparing best linear fits to best fit constants through all four epochs including uncertainties are 4.5×10^3 in PA and 10^4 in separation. The best fit slope of the linear fit in PA is -0.164 ± 0.048 deg/yr and in separation is 0.00058 ± 0.00032 arcsec/yr. We conclude that linear fits are preferred, and that we likely see orbital motion from ROXs 12 b.

Using multiple epochs of astrometry allows us to constrain the orbits of ROXs 42B b and ROXs 12 b. To fit each orbit we use an updated implementation of the Rejection Sampling Monte Carlo method described in De Rosa et al. (2015), based on the method of Ghez et al. (2008). This technique generates an initial orbit with semi-major axis (a) of unity and position angle of nodes (Ω) of 0, with eccentricity (e), inclination angle (i), argument of periastron (ω), and epoch of periastron passage (T_0) drawn from the appropriate probability distribution: uniform for e, ω, T_0, and uniform in $\cos(i)$, and we use Kepler's third law to generate the period from a fixed system mass. We then scale a and rotate Ω to fit a single observational epoch, with observational errors included by adding Gaussian random noise to the observed separation and position angle for that epoch with σ equal to the observational errors. Stellar mass and distance for each trial are both drawn from Gaussian distributions with medians at the measurements and standard deviations of the measurement uncertainties. Unlike De Rosa et al. (2015) where all potential orbits where shifted and scaled to the earliest epoch, here we randomly select an epoch for each orbit, which avoids the fit being biased toward the first epoch.

The algorithm has also been modified at the rejection sampling step: previously we proceeded one epoch at a time, rejecting ill-fitting orbits at each epoch. In this version the chi-square for the newly-scaled orbit is calculated for all the remaining epochs, and then the orbit is accepted if a uniform random variable is less than $e^{-\frac{\chi^2}{2}}$ and rejected otherwise. Mathematically this is the same operation as we used previously, but it allows for higher computational efficiency in the face of outliers, since the rejection test can be scaled to the minimum value of χ^2 reached for the given astrometry, with orbits now accepted if the random variable is less than $e^{-\frac{\chi^2}{2}}$ / $e^{-\frac{\chi^2_{min}}{2}}$. This method is described in more detail in Blunt et al. (2017).

This rejection sampling technique produces identical posterior probability distributions to those generated by MCMC, but requires much less computational time for astrometry covering short arcs of an orbit, as demonstrated in De Rosa et al. (2015) for the exoplanet 51 Eri b. In the very long-period orbits presented here we find that even after 10^{10} steps of Metropolis Hastings MCMC the chains have not converged, though the posteriors are broadly similar to those generated by the Rejection Sampling method.

Figures 3.8 and 3.9 show the range of Keplerian orbits consistent with the available astrometry for ROXs 12 b and ROXs 42B b respectively, while Figures 3.10 and 3.11 show the posterior distributions for the orbital parameters that were fit for ROXs 12 b and ROXs 42B b, respectively. We note that even with a small fraction of orbital coverage, fitting orbits and obtaining marginal constraints on the corresponding parameters is useful. For example, several recent studies have fit the small orbital coverage observed for Fomalhaut b, and find that they can constrain the eccentricity of this object to high values (P. Kalas et al., 2013; Beust et al., 2016). Furthermore, detected orbital motion of the low mass brown dwarfs PZ Tel b and GQ Lup b appears to constrain their eccentricities to high values (Ginski et al., 2014).

While the eccentricities of these PMCs are poorly constrained, we do find that low to moderate eccentricities are favored. The 95% upper limits on the eccentricities of ROXs 42B b and ROXs 12 b are 0.58 and 0.83 respectively. Previous studies have run scattering simulations to test if these wide-separation (> 100 AU) PMCs can form via planet-planet scattering. These simulations showed that for giant planets that end up outside of 100 AU, their eccentricities are significantly pumped up to > 0.5 (Scharf and Menou, 2009; Nagasawa and Ida, 2011). The fact that the eccentricity distributions for ROXs 42B b and ROXs 12 b favor moderate to low eccentricities argues against the scattering hypothesis for these companions. Note

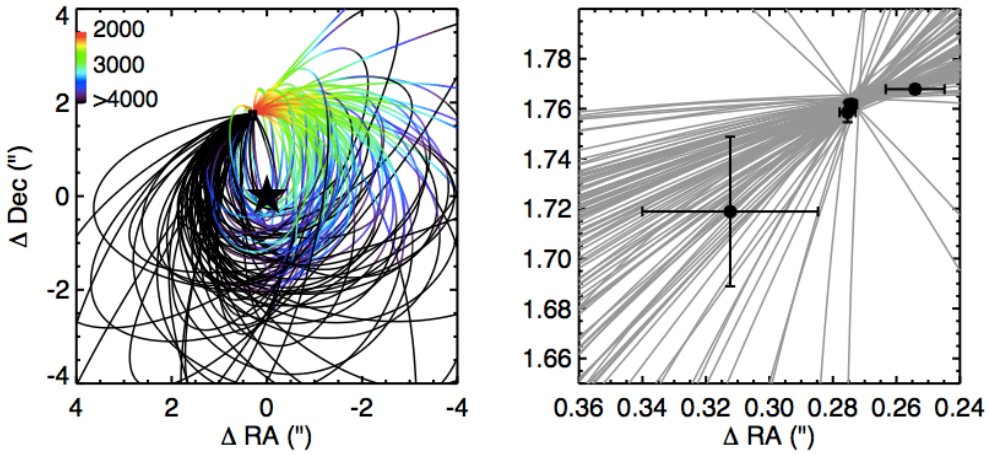

Figure 3.8: 100 randomly selected orbital tracks drawn from the posterior distribution for ROXs 12 b. (left) Colors correspond to elapsed time since 2000. A clockwise orbit ($i > 90$) is favored, though the astrometric errors allow for a counterclockwise orbit as well. (right) A zoom-in on the measured astrometry of the system and the same 100 orbital tracks. Future high-precision astrometric monitoring of the system should improve the constraints on allowable orbits.

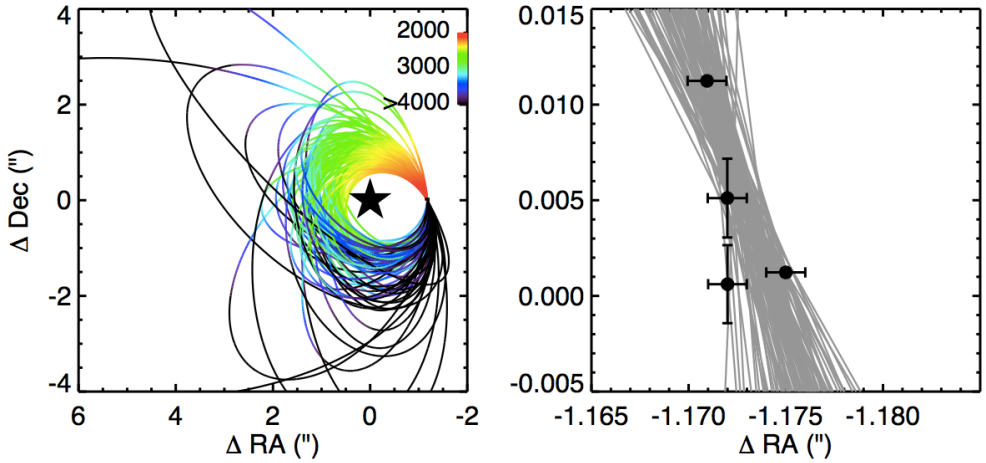

Figure 3.9: Orbital tracks for ROXs 42B b. See Figure 3.8 for details. Generally a face on ($i \lesssim 50$), circular ($e \lesssim 0.5$) orbit is preferred.

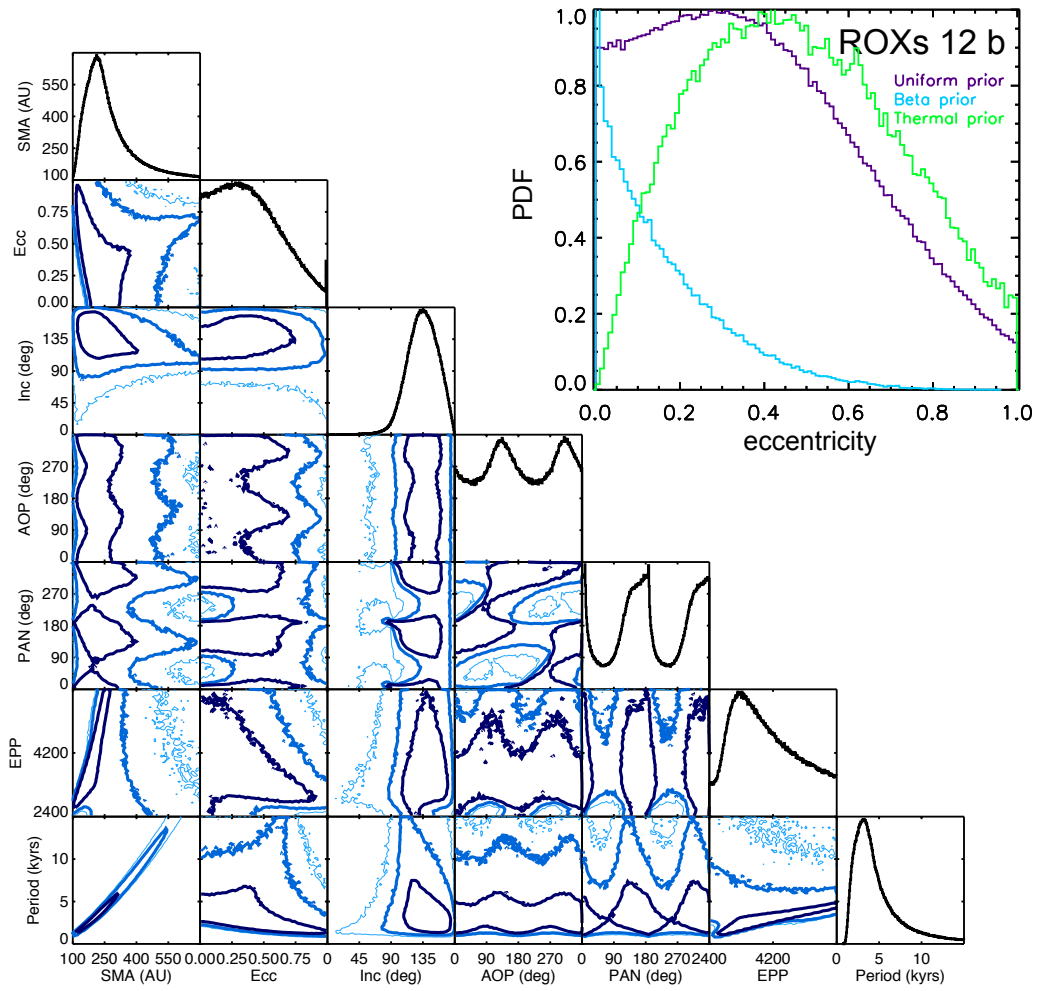

Figure 3.10: The marginalized one-dimensional posterior probability distributions of orbital parameters for ROXs 12 b along the diagonal, and two-dimensional covariances in off-diagonal elements. Parameters plotted are semi-major axis, eccentricity, inclination, argument of periastron, position angle of nodes, epoch of periastron passage, and period. In the covariance plots the dark to light blue contours denote locations with 68%, 95%, and 99.7% of the probability enclosed. The most likely orbits have a semi-major axis of ~200 AU, ~3000 year period, and generally circular ($e \lesssim 0.5$) and face on ($i \lesssim 70$ or $i \gtrsim 110$). In the inset on the upper right, three different eccentricity posteriors are plotted corresponding to three different priors. The purple, light blue, and dark blue posteriors correspond to a uniform, thermal, and β distribution respectively.

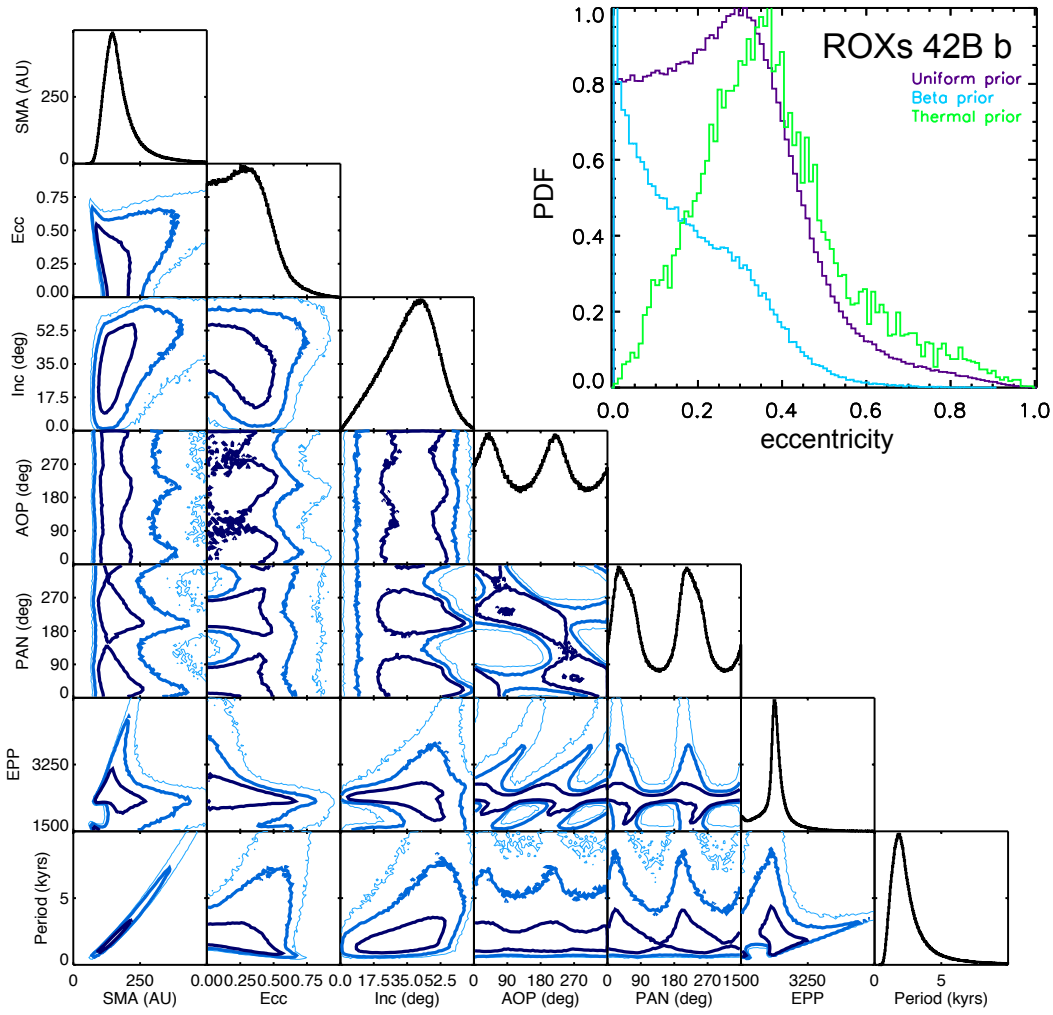

Figure 3.11: Orbital parameter posterior distributions for ROXs 42B. b The distributions peak for ~150 AU, ~2000 year orbits. More circular orbits are preferred, with higher inclinations corresponding to longer periods. As in Figure 3.10, in the inset on the upper right, three different eccentricity posteriors are plotted corresponding to three different priors. The purple, light blue, and dark blue posteriors correspond to a uniform, thermal, and β distribution respectively.

that while a uniform prior on the eccentricity is used in these fits, the eccentricity posterior is significantly different. We can conclude that the eccentricity posterior is a reflection of the underlying companion eccentricity and not of the prior chosen. To further test this, we ran these orbit fits with two additional eccentricity priors, the β distribution (Kipping, 2013) and the thermal distribution (Ambartsumian et al 1937). The thermal distribution of eccentricities, which is proportional to $2e\ \mathrm{d}e$, is the distribution that binary companions should follow if they are distributed solely as a function of energy. The eccentricity posteriors using these priors are overplotted with the eccentricity posterior found using a uniform prior in the top right plot in Figures 3.10 and 3.11. For both ROXs 12 b and ROXs 42B b, while the eccentricity posterior using the thermal distribution prior pushes to higher eccentricities, in general lower to moderate eccentricities are favored.

Detection Probability

We calculate the detection probability for additional companions in these eight systems over a range of masses and separations. Our contrast curves can be converted into sensitivity maps in mass and semi-major axis using evolutionary models, the age and distance of the system and the uncertainties on these values, and an underlying distribution of planet eccentricities. Following Bowler et al. (2015), we generate a population of artificial companions on random, circular Keplerian orbits with a given mass and semi-major axis. Each synthetic planet is assigned an apparent magnitude using an interpolated grid of the Cond hot-start evolutionary models (Baraffe et al., 2003), the distance and age of the host star, and the companion mass. We use the Cond evolutionary models because they extend down to planetary masses, although we note that different models can vary significantly in their predictions for the same planet mass. We do not explicitly account for this model-dependent error in our final analysis. The fraction of companions falling above a contrast curve compared to those falling below it yields the fractional sensitivity at that grid point. We further take into account the fractional field of view coverage for each target, which is uniformly complete out to 4" for our sample and drops to zero beyond that. Iterating over masses between 0.5–100 M_{Jup} and semi-major axes between 1–1000 AU yields sensitivity maps for each target, which are shown in Figure 3.12 for this sample. Depending on the distance and age of the target, our observations are generally sensitive to 1–10 M_{Jup} companions beyond about 30 AU.

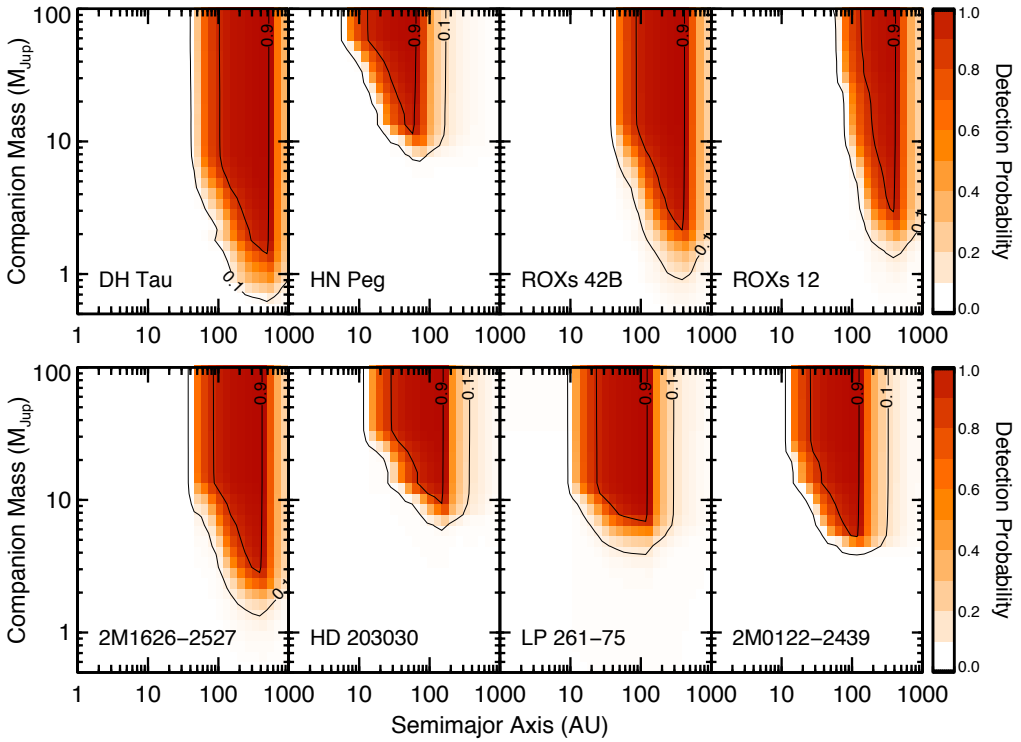

Figure 3.12: Detection probability maps for our sample. Contours denote the 90% and 10% sensitivity regions using the Baraffe et al. (2003) hot-start evolutionary models. No grid point is exactly 100% sensitive to companions because even brown dwarfs and low-mass stars at wide orbital distances could be temporarily located at close projected separations from their host star. The outer drop in sensitivity is caused by limited field of view coverage. These maps assume circular orbits, but adopting modest eccentricities does not qualitatively change these results.

3.5 Discussion

Can Dynamical Scattering Explain This Population?

Except for DH Tau cc1, which remains ambiguous, none of the new candidate companions detected in our sample are bound. While we can generally rule out the existence of massive scatterers above our detection limits (outside of 15-50 AU for massive planets), we cannot unambiguously rule out scattering as a formation mechanism based on our results alone, since the massive scatterers might be located closer in. However, our results combined with complementary lines of evidence suggest that formation close to the host star plus subsequent scattering is probably not the dominant formation mechanism for these wide-separation PMCs. Note that in order for the scattering scenario to operate, there must be a body that is often at least as massive as these already massive PMCs closer in to the host stars (Veras and Armitage, 2004). We present a comprehensive list of this evidence below.

- In this study, we do not find any potential scatterers down to ~ 15 - 50 AU in

this sample of seven systems which host wide-separation PMCs. Furthermore, other studies with comparably deep imaging of wide separation PMCs also did not find any potential scatterers in HD 106906 and 1 RXS 1609-2105 (e.g. Bailey et al., 2014; Lafrenière, Jayawardhana, and van Kerkwijk, 2010; Lagrange et al., 2016; P. G. Kalas et al., 2015). Efforts using non-redundant aperture masking techniques have probed higher masses (>15 M_{Jup}) down to smaller separations (> ∼ 5 AU), and have likewise found a dearth of inner companions (Cheetham et al., 2015; Kraus, Ireland, Martinache, et al., 2011). If additional inner gas giant planets or brown dwarfs are present, they must be located within a few tens of AU of their host stars.

- Moderate to low eccentricities are favored for ROXs 12 b and ROXs 42B b, which both exhibit orbital motion. This is in contrast to the predictions of scattering simulations, which show that giant planets that get scattered out to >100 AU typically have high eccentricities >0.5 (Nagasawa and Ida, 2011; Scharf and Menou, 2009).

- From RV studies, it is clear that high-mass planets are rare. This is evident from the significantly negative power law in mass found by Cumming et al. (2008) for a sample of giant planets 0.3 – 10 M_{Jup} out to 3 AU, where for a power law m^{α}, $\alpha = -0.31 \pm 0.2$. Within this semi-major axis range, this power law implies that the occurrence rate of giant planets in the range 5 - 10 M_{Jup} is 1.3%. Similarly, work by Bryan et al (2016) suggests that for a sample of gas giant planets outside 5 AU, lower-mass planets are more frequent than higher-mass planets. This implies that planets massive enough to be potential scatterers for the wide-separation directly imaged planets in this study (> 5 M_{Jup}) are intrinsically rare in RV surveys. However, even if massive planets are disfavored generally, this doesn't necessarily mean that there would only be one super-massive planet per system. For example, perhaps unusual disk properties are required to form a > 5 M_{Jup} planet, but once this kind of disk is formed it is easy to form multiple massive planets at a range of separations. Given the low estimated occurrence rate of wide-separation PMCs (less than a few percent), this might be consistent with the low occurrence rate of massive planets found in RV surveys.

- Dynamical interactions between planets preferentially scatter out lower-mass planets (Veras, Crepp, and Ford, 2009). However, lower-mass planets (< 5 M_{Jup}) have not been discovered at distances greater than 100 AU despite

the fact that many surveys were sensitive down to a few Jupiter masses (e.g. Bowler, Liu, Shkolnik, et al., 2013; Biller et al., 2013). This implies that the companion mass function truncates at ~5 M_{Jup}, inconsistent with scattering.

- Rough estimates of the occurrence rate of these massive (> 5 M_{Jup}) wide-separation PMCs yield at most a frequency of a few percent (Ireland et al., 2011; Aller et al., 2013). In contrast, scattering simulations, which began with 100 systems populated with 10 planets each with masses between 0.1 - 10 M_{Jup} drawn from a uniform distribution in logM and with separations < 30 AU drawn from a uniform distribution in semi-major axis, find that the occurrence rate of scattered planets from 1 – 10 M_{Jup} outside of 300 AU is ~0.2% at ~10 Myr (Scharf and Menou, 2009). Furthermore, of the 0.2% occurrence rate of all planets from 1 – 10 M_{Jup} that get scattered beyond 300 AU, only a few percent of that population are > 4 M_{Jup} (Veras, Crepp, and Ford, 2009). This implies that the occurrence rate of massive (> 5 M_{Jup}) scattered planets predicted by these simulations is of the order several hundredths of a percent, which is orders of magnitude smaller than any of the occurrence rate measurements from surveys thus far.

- Many of these widely-separation PMCs are actively accreting from a circum-planetary disk (Zhou et al., 2014; Bowler, Liu, Kraus, Mann, and Ireland, 2011). However, if these objects were dynamically scattered, we might expect the circumplanetary disk to be partially or completely stripped away (Bowler, Liu, Kraus, Mann, and Ireland, 2011). This implies that many if not all of the PMCs that we find did not undergo such a violent evolution and were thus able to keep their disks.

Taken together, these lines of evidence indicate that the most likely origin for these wide-separation PMCs is in situ formation. Evidence for in situ formation, by cloud fragmentation or disk instability, includes the fact that PMCs have been found orbiting low-mass brown dwarfs with decidedly non-planetary mass ratios, implying that the tail of the initial mass function appears to continue down to at least 5 –10 M_{Jup}. In addition, Brandt et al. (2014) found that a single power law distribution is consistent with a sample of 5 – 70 M_{Jup} objects from the SEEDS survey. Given that results from many other surveys are well fit by this same power law distribution, this suggests that this population immediately below the deuterium-burning threshold

are the end of a smooth mass function, sharing a common origin with more massive brown dwarfs.

Occurrence Rate

We now consider the multiplicity of directly imaged planetary systems. Although we did not find any new companions in our sample, we can place an upper limit on the occurrence rate of inner, massive planets in systems with previously known wide-separation PMCs. Since we have no detections, our occurrence rate is simply:

$$O = \frac{N_m}{N_{sys}}, \tag{3.6}$$

where N_m is the number of planets that we missed in our survey due to incompleteness, and N_{sys} is the number of systems in our sample.

The number of planets that we missed due to survey incompleteness can be expressed as:

$$N_m = \Sigma_{i=0}^{N_{sys}} \left[\int_{a_1}^{a_2} d\log a \int_{m_1}^{m_2} d\log m \; f(m,a)(1 - P_i(m,a)) \right]. \tag{3.7}$$

Here, $P_i(m,a)$ is the probability of detecting a planet of mass m at semi-major axis a for system i. We have these values for a grid of masses and semi-major axes from our detection probability calculations, described in section 3.4 and shown in Figure 3.12. The quantity $f(m,a)$ is the assumed distribution in mass and semi-major axis for the population of planets whose occurrence rate we wish to calculate. In our calculation we adopt the underlying distribution in Clanton and Gaudi (2016), which combines five different exoplanet surveys compiled using three different detection methods to derive a double power law distribution in mass and semi-major axis for giant planets. This power law takes the form:

$$f(m,a) = \frac{dN}{d\log m_p d\log a} = A\left(\frac{m_p}{M_{Sat}}\right)^{\alpha}\left(\frac{a}{2.5AU}\right)^{\beta}. \tag{3.8}$$

In this equation, $A = 0.21^{+0.20}_{-0.15}$, $\alpha = -0.86^{+0.21}_{-0.19}$, and $\beta = 1.1^{+1.9}_{-1.4}$. We note that this power law was derived specifically for M dwarf host stars. Out of our seven systems with previously confirmed PMCs, five of the host stars are M stars. We then create a 30×30 grid evenly spaced in logarithmic bins with masses from 1 –

100 M_{Jup} and semi-major axes ranging from 1 – 1000 AU, and determine the power law distribution values at each grid point.

Since we want to determine the probability of finding an inner planet given that an outer PMC has been detected, we calculated the occurrence rate of PMCs between 5 – 15 M_{Jup} and from 40 AU to the location of each PMC. The inner limit on the separation was chosen because we are reasonably complete for massive planets beyond 40 AU for most of our systems. In order to take into account the large uncertainties on the power law parameters, we calculated the occurrence rate using a Monte Carlo method with 10^6 trials, each time drawing a new A, α, and β value from a Gaussian distribution with widths equal to the parameter uncertainties. This yielded a distribution of missed planets, which we converted to a distribution in occurrence rate.

We found that the 95% confidence upper limit on the occurrence rate of planetary companions interior to our sample of previously known wide separation PMCs is 54%. This result assumes the companion distribution shown in equation 3.8 as well as hot start evolutionary models. This first estimate of the occurrence rate upper limit will be better constrained with the discovery and analysis of more PMC systems. Note that covariances between parameters have not been taken into account in this method, which inflates our upper limit.

3.6 Conclusions

We conducted a deep angular differential imaging (ADI) survey with NIRC2 at Keck in search of close-in substellar companions to a sample of seven systems with confirmed PMCs on extremely wide orbits (>100 AU). We explored the possibility that the wide-separation PMCs formed closer in to their host stars and were subsequently scattered out to their present day locations by a more massive body in the system. In this survey we obtained deep imaging for each target, for the first time probing significantly lower masses and smaller separations in all systems.

Within our sample we found eight candidate companions. Using second epoch data, we measured the astrometry for each candidate and determined whether or not they were co-moving by using an MCMC technique that calculates robust uncertainties from the posterior distributions, without the systematics that occur when the reduced images are used.

Seven candidate companions are unequivocally background objects, while the candidate companion near DH Tau remains ambiguous. Although our results alone do

not conclusively rule out formation closer in to the host star followed by scattering as a formation mechanism for these wide-separation PMCs, the totality of evidence suggests that scattering is not a dominant formation mechanism. Instead, formation of these objects in situ appears to be more likely.

If we wish to better understand how these wide separation PMCs formed, there are several possible approaches to consider. *Gaia* will allow us to carve out the immediate environment around these young stars, which has been extremely difficult with our current imaging capabilities (due to unfavorable contrasts close to the star), and radial velocity capabilities (due to high jitter values for young stars). Furthermore, studying the composition of these PMCs by obtaining high resolution spectra might allow us to distinguish amongst formation mechanisms (Konopacky et al., 2013; T. S. Barman et al., 2015). While the core accretion model predicts that planets should have enhanced metallicities relative to their host stars, formation via disk instability or turbulent fragmentation should result in compositions matching those of the host star. Finally, large high-contrast imaging surveys of young star forming regions conducted homogeneously would give us a more precise measurement of the occurrence rates and orbital architectures of this population of planetary-mass objects.

3.7 Acknowledgements

The data presented herein were obtained at the W.M. Keck Observatory, which is operated as a scientific partnership among the California Institute of Technology, the University of California and the National Aeronautics and Space Administration. The Observatory was made possible by the generous financial support of the W.M. Keck Foundation. We acknowledge the efforts of the Keck Observatory staff. The authors wish to recognize and acknowledge the very significant cultural role and reverence that the summit of Mauna Kea has always had within the indigenous Hawaiian community. We are most fortunate to have the opportunity to conduct observations from this mountain.

References

Alibert, Y. et al. (2005). "Models of giant planet formation with migration and disc evolution". In: *A&A* 434, pp. 343–353. DOI: 10.1051/0004-6361:20042032. eprint: astro-ph/0412444.

Aller, K. M. et al. (2013). "A Pan-STARRS + UKIDSS Search for Young, Wide Planetary-mass Companions in Upper Scorpius". In: *ApJ* 773, 63, p. 63. DOI: 10.1088/0004-637X/773/1/63. arXiv: 1307.0506 [astro-ph.SR].

Bailey, V. et al. (2014). "HD 106906 b: A Planetary-mass Companion Outside a Massive Debris Disk". In: *ApJL* 780, L4, p. L4. DOI: 10.1088/2041-8205/780/1/L4. arXiv: 1312.1265 [astro-ph.EP].

Baraffe, I. et al. (2003). "Evolutionary models for cool brown dwarfs and extrasolar giant planets. The case of HD 209458". In: *A&A* 402, pp. 701–712. DOI: 10.1051/0004-6361:20030252. eprint: astro-ph/0302293.

Barman, T. S. et al. (2015). "Simultaneous Detection of Water, Methane, and Carbon Monoxide in the Atmosphere of Exoplanet HR8799b". In: *ApJ* 804, 61, p. 61. DOI: 10.1088/0004-637X/804/1/61. arXiv: 1503.03539 [astro-ph.EP].

Bate, M. R. (2009). "Stellar, brown dwarf and multiple star properties from hydrodynamical simulations of star cluster formation". In: *MNRAS* 392, pp. 590–616. DOI: 10.1111/j.1365-2966.2008.14106.x. arXiv: 0811.0163.

– (2012). "Stellar, brown dwarf and multiple star properties from a radiation hydrodynamical simulation of star cluster formation". In: *MNRAS* 419, pp. 3115–3146. DOI: 10.1111/j.1365-2966.2011.19955.x. arXiv: 1110.1092 [astro-ph.SR].

Bate, M. R., I. A. Bonnell, and V. Bromm (2002). "The formation mechanism of brown dwarfs". In: *MNRAS* 332, pp. L65–L68. DOI: 10.1046/j.1365-8711.2002.05539.x. eprint: astro-ph/0206365.

Beust, H. et al. (2016). "Orbital fitting of imaged planetary companions with high eccentricities and unbound orbits. Their application to Fomalhaut b and PZ Telescopii B". In: *A&A* 587, A89, A89. DOI: 10.1051/0004-6361/201527388. arXiv: 1512.03596 [astro-ph.EP].

Biller, B. A. et al. (2013). "The Gemini/NICI Planet-Finding Campaign: The Frequency of Planets around Young Moving Group Stars". In: *ApJ* 777, 160, p. 160. DOI: 10.1088/0004-637X/777/2/160. arXiv: 1309.1462 [astro-ph.EP].

Blunt, S. et al. (2017). "Orbits for the Impatient: A Bayesian Rejection-sampling Method for Quickly Fitting the Orbits of Long-period Exoplanets". In: *AJ* 153, 229, p. 229. DOI: 10.3847/1538-3881/aa6930. arXiv: 1703.10653 [astro-ph.EP].

Boss, A. P. (2006). "On the Formation of Gas Giant Planets on Wide Orbits". In: *ApJL* 637, pp. L137–L140. DOI: 10.1086/500613. eprint: astro-ph/0601278.

Bowler, B. P., M. C. Liu, A. L. Kraus, and A. W. Mann (2014). "Spectroscopic Confirmation of Young Planetary-mass Companions on Wide Orbits". In: *ApJ* 784, 65, p. 65. DOI: 10.1088/0004-637X/784/1/65. arXiv: 1401.7668 [astro-ph.EP].

Bowler, B. P., M. C. Liu, A. L. Kraus, A. W. Mann, and M. J. Ireland (2011). "A Disk around the Planetary-mass Companion GSC 06214-00210 b: Clues about the Formation of Gas Giants on Wide Orbits". In: *ApJ* 743, 148, p. 148. DOI: 10.1088/0004-637X/743/2/148. arXiv: 1109.5693 [astro-ph.EP].

Bowler, B. P., M. C. Liu, E. L. Shkolnik, et al. (2013). "Planets around Low-mass Stars. III. A Young Dusty L Dwarf Companion at the Deuterium-burning Limit". In: *ApJ* 774, 55, p. 55. DOI: 10.1088/0004-637X/774/1/55. arXiv: 1307.2237 [astro-ph.SR].

Bowler, B. P., E. L. Shkolnik, et al. (2015). "Planets Around Low-mass Stars (PALMS). V. Age-dating Low-mass Companions to Members and Interlopers of Young Moving Groups". In: *ApJ* 806, 62, p. 62. DOI: 10.1088/0004-637X/806/1/62. arXiv: 1505.01494 [astro-ph.EP].

Brandt, T. D. et al. (2014). "A Statistical Analysis of SEEDS and Other High-contrast Exoplanet Surveys: Massive Planets or Low-mass Brown Dwarfs?" In: *ApJ* 794, 159, p. 159. DOI: 10.1088/0004-637X/794/2/159. arXiv: 1404.5335 [astro-ph.SR].

Chauvin, G. et al. (2005). "A companion to AB Pic at the planet/brown dwarf boundary". In: *A&A* 438, pp. L29–L32. DOI: 10.1051/0004-6361:200500111. eprint: astro-ph/0504658.

Cheetham, A. C. et al. (2015). "Mapping the Shores of the Brown Dwarf Desert. IV. Ophiuchus". In: *ApJ* 813, 83, p. 83. DOI: 10.1088/0004-637X/813/2/83. arXiv: 1509.05217 [astro-ph.SR].

Clanton, C. and B. S. Gaudi (2016). "Synthesizing Exoplanet Demographics: A Single Population of Long-period Planetary Companions to M Dwarfs Consistent with Microlensing, Radial Velocity, and Direct Imaging Surveys". In: *ApJ* 819, 125, p. 125. DOI: 10.3847/0004-637X/819/2/125. arXiv: 1508.04434 [astro-ph.EP].

Cumming, A. et al. (2008). "The Keck Planet Search: Detectability and the Minimum Mass and Orbital Period Distribution of Extrasolar Planets". In: *PASP* 120, p. 531. DOI: 10.1086/588487. arXiv: 0803.3357.

Currie, T., R. Cloutier, et al. (2015). "Resolving the HD 100546 Protoplanetary System with the Gemini Planet Imager: Evidence for Multiple Forming, Accreting Planets". In: *ApJL* 814, L27, p. L27. DOI: 10.1088/2041-8205/814/2/L27. arXiv: 1511.02526 [astro-ph.EP].

Currie, T., S. Daemgen, et al. (2014). "Direct Imaging and Spectroscopy of a Candidate Companion Below/Near the Deuterium-burning Limit in the Young Binary Star System, ROXs 42B". In: *ApJL* 780, L30, p. L30. DOI: 10.1088/2041-8205/780/2/L30. arXiv: 1310.4825 [astro-ph.SR].

Cutri, R. M. and et al. (2013). "VizieR Online Data Catalog: AllWISE Data Release (Cutri+ 2013)". In: *VizieR Online Data Catalog* 2328.

Cutri, R. M., M. F. Skrutskie, et al. (2003). "VizieR Online Data Catalog: 2MASS All-Sky Catalog of Point Sources (Cutri+ 2003)". In: *VizieR Online Data Catalog* 2246.

De Rosa, R. J. et al. (2015). "Astrometric Confirmation and Preliminary Orbital Parameters of the Young Exoplanet 51 Eridani b with the Gemini Planet Imager". In: *ApJL* 814, L3, p. L3. DOI: 10.1088/2041-8205/814/1/L3. arXiv: 1509.07514 [astro-ph.EP].

Dodson-Robinson, S. E. et al. (2009). "The Formation Mechanism of Gas Giants on Wide Orbits". In: *ApJ* 707, pp. 79–88. DOI: 10.1088/0004-637X/707/1/79. arXiv: 0909.2662 [astro-ph.EP].

Ginski, C. et al. (2014). "Astrometric follow-up observations of directly imaged substellar companions to young stars and brown dwarfs". In: *MNRAS* 444, pp. 2280–2302. DOI: 10.1093/mnras/stu1586. arXiv: 1409.1850 [astro-ph.EP].

Ireland, M. J. et al. (2011). "Two Wide Planetary-mass Companions to Solar-type Stars in Upper Scorpius". In: *ApJ* 726, 113, p. 113. DOI: 10.1088/0004-637X/726/2/113. arXiv: 1011.2201 [astro-ph.SR].

Itoh, Y. et al. (2005). "A Young Brown Dwarf Companion to DH Tauri". In: *ApJ* 620, pp. 984–993. DOI: 10.1086/427086. eprint: astro-ph/0411177.

Kalas, P. G. et al. (2015). "Direct Imaging of an Asymmetric Debris Disk in the HD 106906 Planetary System". In: *ApJ* 814, 32, p. 32. DOI: 10.1088/0004-637X/814/1/32. arXiv: 1510.02747 [astro-ph.EP].

Kalas, P. et al. (2013). "STIS Coronagraphic Imaging of Fomalhaut: Main Belt Structure and the Orbit of Fomalhaut b". In: *ApJ* 775, 56, p. 56. DOI: 10.1088/0004-637X/775/1/56. arXiv: 1305.2222 [astro-ph.EP].

Kipping, D. M. (2013). "Parametrizing the exoplanet eccentricity distribution with the Beta distribution". In: *MNRAS* 434, pp. L51–L55. DOI: 10.1093/mnrasl/slt075. arXiv: 1306.4982 [astro-ph.EP].

Konopacky, Q. M. et al. (2013). "Detection of Carbon Monoxide and Water Absorption Lines in an Exoplanet Atmosphere". In: *Science* 339, pp. 1398–1401. DOI: 10.1126/science.1232003. arXiv: 1303.3280 [astro-ph.EP].

Kraus, A. L. and M. J. Ireland (2012). "LkCa 15: A Young Exoplanet Caught at Formation?" In: *ApJ* 745, 5, p. 5. DOI: 10.1088/0004-637X/745/1/5. arXiv: 1110.3808 [astro-ph.EP].

Kraus, A. L., M. J. Ireland, L. A. Cieza, et al. (2014). "Three Wide Planetary-mass Companions to FW Tau, ROXs 12, and ROXs 42B". In: *ApJ* 781, 20, p. 20. DOI: 10.1088/0004-637X/781/1/20. arXiv: 1311.7664 [astro-ph.EP].

Kraus, A. L., M. J. Ireland, F. Martinache, et al. (2011). "Mapping the Shores of the Brown Dwarf Desert. II. Multiple Star Formation in Taurus-Auriga". In: *ApJ* 731, 8, p. 8. DOI: 10.1088/0004-637X/731/1/8. arXiv: 1101.4016 [astro-ph.SR].

Lafrenière, D., R. Jayawardhana, and M. H. van Kerkwijk (2010). "The Directly Imaged Planet Around the Young Solar Analog 1RXS J160929.1 - 210524: Confirmation of Common Proper Motion, Temperature, and Mass". In: *ApJ* 719, pp. 497–504. DOI: 10.1088/0004-637X/719/1/497. arXiv: 1006.3070 [astro-ph.EP].

Lagrange, A.-M. et al. (2016). "A narrow, edge-on disk resolved around HD 106906 with SPHERE". In: *A&A* 586, L8, p. L8. DOI: 10.1051/0004-6361/201527264. arXiv: 1510.02511 [astro-ph.SR].

Lambrechts, M. and A. Johansen (2012). "Rapid growth of gas-giant cores by pebble accretion". In: *A&A* 544, A32, A32. DOI: 10.1051/0004-6361/201219127. arXiv: 1205.3030 [astro-ph.EP].

Lodato, G., E. Delgado-Donate, and C. J. Clarke (2005). "Constraints on the formation mechanism of the planetary mass companion of 2MASS 1207334-393254". In: *MNRAS* 364, pp. L91–L95. DOI: 10.1111/j.1745-3933.2005.00112.x. eprint: astro-ph/0509754.

Low, C. and D. Lynden-Bell (1976). "The minimum Jeans mass or when fragmentation must stop". In: *MNRAS* 176, pp. 367–390. DOI: 10.1093/mnras/176.2.367.

Luhman, K. L., B. M. Patten, et al. (2007). "Discovery of Two T Dwarf Companions with the Spitzer Space Telescope". In: *ApJ* 654, pp. 570–579. DOI: 10.1086/509073. eprint: astro-ph/0609464.

Luhman, K. L., J. C. Wilson, et al. (2006). "Discovery of a Young Substellar Companion in Chamaeleon". In: *ApJ* 649, pp. 894–899. DOI: 10.1086/506517. eprint: astro-ph/0609187.

Marois, C., B. Macintosh, T. Barman, et al. (2008). "Direct Imaging of Multiple Planets Orbiting the Star HR 8799". In: *Science* 322, p. 1348. DOI: 10.1126/science.1166585. arXiv: 0811.2606.

Marois, C., B. Macintosh, and J.-P. Véran (2010). "Exoplanet imaging with LOCI processing: photometry and astrometry with the new SOSIE pipeline". In: *Adaptive Optics Systems II*. Vol. 7736. Proc. SPIE, 77361J. DOI: 10.1117/12.857225.

Metchev, S. A. and L. A. Hillenbrand (2006). "HD 203030B: An Unusually Cool Young Substellar Companion near the L/T Transition". In: *ApJ* 651, pp. 1166–1176. DOI: 10.1086/507836. eprint: astro-ph/0607514.

Nagasawa, M. and S. Ida (2011). "Orbital Distributions of Close-in Planets and Distant Planets Formed by Scattering and Dynamical Tides". In: *ApJ* 742, 72, p. 72. DOI: 10.1088/0004-637X/742/2/72.

Pollack, J. B. et al. (1996). "Formation of the Giant Planets by Concurrent Accretion of Solids and Gas". In: *Icarus* 124, pp. 62–85. DOI: 10.1006/icar.1996.0190.

Quanz, S. P. et al. (2015). "Confirmation and Characterization of the Protoplanet HD 100546 b - Direct Evidence for Gas Giant Planet Formation at 50 AU". In: *ApJ* 807, 64, p. 64. DOI: 10.1088/0004-637X/807/1/64. arXiv: 1412.5173 [astro-ph.SR].

Ratzka, T., R. Köhler, and C. Leinert (2005). "A multiplicity survey of the ρ Ophiuchi molecular clouds". In: *A&A* 437, pp. 611–626. DOI: 10.1051/0004-6361:20042107. eprint: astro-ph/0504593.

Reid, I. N. and L. M. Walkowicz (2006). "LP 261-75/2MASSW J09510549+3558021: A Young, Wide M4.5/L6 Binary". In: *PASP* 118, pp. 671–677. DOI: 10.1086/503446.

Sallum, S. et al. (2015). "Accreting protoplanets in the LkCa 15 transition disk". In: *Nature* 527, pp. 342–344. DOI: 10.1038/nature15761. arXiv: 1511.07456 [astro-ph.EP].

Scharf, C. and K. Menou (2009). "Long-Period Exoplanets From Dynamical Relaxation". In: *ApJL* 693, pp. L113–L117. DOI: 10.1088/0004-637X/693/2/L113. arXiv: 0811.1981.

Service, M. et al. (2016). "A New Distortion Solution for NIRC2 on the Keck II Telescope". In: *PASP* 128.9, p. 095004. DOI: 10.1088/1538-3873/128/967/095004.

Skiff, B. A. (2013). "VizieR Online Data Catalog: General Catalogue of Stellar Spectral Classifications." In: *VizieR Online Data Catalog* 1.

Soummer, R., L. Pueyo, and J. Larkin (2012). "Detection and Characterization of Exoplanets and Disks Using Projections on Karhunen-Loève Eigenimages". In: *ApJL* 755, L28, p. L28. DOI: 10.1088/2041-8205/755/2/L28. arXiv: 1207.4197 [astro-ph.IM].

Strom, K. M. et al. (1989). "Circumstellar material associated with solar-type pre-main-sequence stars - A possible constraint on the timescale for planet building". In: *AJ* 97, pp. 1451–1470. DOI: 10.1086/115085.

Veras, D. and P. J. Armitage (2004). "Outward migration of extrasolar planets to large orbital radii". In: *MNRAS* 347, pp. 613–624. DOI: 10.1111/j.1365-2966.2004.07239.x. eprint: astro-ph/0310161.

Veras, D., J. R. Crepp, and E. B. Ford (2009). "Formation, Survival, and Detectability of Planets Beyond 100 AU". In: *ApJ* 696, pp. 1600–1611. DOI: 10.1088/0004-637X/696/2/1600. arXiv: 0902.2779 [astro-ph.EP].

Vorobyov, E. I. (2013). "Formation of giant planets and brown dwarfs on wide orbits". In: *A&A* 552, A129, A129. DOI: 10.1051/0004-6361/201220601. arXiv: 1302.1892 [astro-ph.EP].

White, R. J. and A. M. Ghez (2001). "Observational Constraints on the Formation and Evolution of Binary Stars". In: *ApJ* 556, pp. 265–295. DOI: 10.1086/321542. eprint: astro-ph/0103098.

Yelda, S. et al. (2010). “Improving Galactic Center Astrometry by Reducing the Effects of Geometric Distortion”. In: *ApJ* 725, 331-352, pp. 331–352. DOI: 10.1088/0004-637X/725/1/331. arXiv: 1010.0064.

Zacharias, N., C. T. Finch, et al. (2012). “VizieR Online Data Catalog: UCAC4 Catalogue (Zacharias+, 2012)”. In: *VizieR Online Data Catalog* 1322.

Zacharias, N., D. G. Monet, et al. (2005). “VizieR Online Data : NOMAD Catalog (Zacharias+ 2005)”. In: *VizieR Online Data Catalog* 1297.

Zhou, Y. et al. (2014). “Accretion onto Planetary Mass Companions of Low-mass Young Stars”. In: *ApJL* 783, L17, p. L17. DOI: 10.1088/2041-8205/783/1/L17. arXiv: 1401.6545 [astro-ph.SR].

Chapter 4

CONSTRAINTS ON THE SPIN EVOLUTION OF YOUNG PLANETARY-MASS COMPANIONS

4.1 Abstract

Surveys of young star-forming regions have discovered a growing population of planetary-mass (<13 M_{Jup}) companions around young stars (Bowler, 2016). There is an ongoing debate as to whether these companions formed like planets (that is, from the circumstellar disk) (Helled et al., 2014), or if they represent the low-mass tail of the star formation process (Chabrier et al., 2014). In this study we utilize high-resolution spectroscopy to measure rotation rates of three young (2-300 Myr) planetary-mass companions and combine these measurements with published rotation rates for two additional companions (Snellen et al., 2014; Zhou et al., 2016) to provide a look at the spin distribution of these objects. We compare this distribution to complementary rotation rate measurements for six brown dwarfs with masses <20 M_{Jup}, and show that these distributions are indistinguishable. This suggests that either that these two populations formed via the same mechanism, or that processes regulating rotation rates are independent of formation mechanism. We find that rotation rates for both populations are well below their break-up velocities and do not evolve significantly during the first few hundred million years after the end of accretion. This suggests that rotation rates are set during late stages of accretion, possibly by interactions with a circumplanetary disk. This result has important implications for our understanding of the processes regulating the angular momentum evolution of young planetary-mass objects, and of the physics of gas accretion and disk coupling in the planetary-mass regime.

4.2 Main Body

Previous studies have sought to constrain the origin of planetary-mass companions around young stars by characterizing their mass and semi-major axis distributions, but this approach is limited by the relatively small size of the current sample (Brandt et al., 2014). Here we propose a different approach, in which we measure rotation rates for planetary-mass companions to probe their accretion histories and subsequent angular momentum evolution. In the absence of any braking mechanism, an actively accreting gas giant planet embedded in a circumstellar disk should spin up

to rotation rates approaching break-up (that is, the maximum physically allowed) velocity. However, observations of the solar system gas giants indicate that they are rotating 3-4 times more slowly than their primordial break-up velocities. This may be due to magnetic coupling with a circumplanetary gas accretion disk, which could provide a channel for young planets to shed their angular momentum (Takata and Stevenson, 1996). After the dispersal of the circumstellar and circumplanetary gas disks, late giant collisions or gravitational tides can further alter the rotation rates of some planets (Morbidelli et al., 2012; Correia and Laskar, 2001).

We currently have a much better understanding of the angular momentum evolution of stars, whose rotation rates have been well characterized by large surveys of star-forming regions (Herbst et al., 2002). Similar to the general picture for gas giant planets, stars spin up as they accrete material from a circumstellar gas disk. Unlike planets, stars have several known mechanisms for regulating this angular momentum, including interactions between the star and its gas disk and angular momentum loss via stellar winds (Gallet and Bouvier, 2013). Extending into the substellar mass regime, surveys of mid- to high-mass brown dwarfs ($\sim$30 – 80 M_{Jup}) have shown that these objects tend to rotate faster and spin down more gradually than stars, indicating that the processes that allow stars to shed angular momentum become less efficient in this mass range (Scholz, Kostov, et al., 2015) (Zapatero Osorio et al., 2006). However, these studies are generally limited to brown dwarfs in nearby young clusters and star-forming regions, as most field brown dwarfs with measured rotation rates have poorly constrained ages and correspondingly uncertain mass constraints. As a result, only a handful of rotation rates have been measured for brown dwarfs with well-constrained masses less than 20 M_{Jup} (Mohanty, Jayawardhana, and Basri, 2005; Rice et al., 2010; Kurosawa, Harries, and Littlefair, 2006), and there are no published studies of the rotation rate distribution and angular momentum evolution in this mass range.

Here, we use the near-infrared spectrograph NIRSPEC at the Keck II 10m telescope to measure rotational line broadening for three young planetary-mass companions with wide projected orbital separations: ROXs 42B b (Kraus et al., 2014), GSC 6214-210 b (Ireland et al., 2011), and VHS 1256-1257 b (Gauza et al., 2015). We also observe five isolated brown dwarfs that were chosen to have ages and spectral types comparable to those of the sample of planetary-mass companions: OPH 90 (Alves de Oliveira et al., 2012), USco J1608-2315 (Lodieu et al., 2008), PSO J318.5-22 (Liu, Dupuy, and Allers, 2016), 2M0355+1133 (Quanz et al., 2010), and KPNO

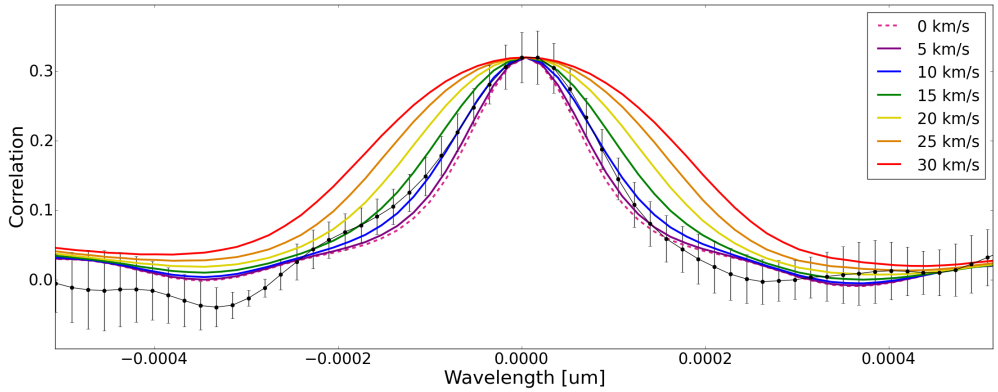

Figure 4.1: Rotational broadening in the ROXs 42B b spectrum. Cross correlation between the ROXs 42B b spectrum and a model atmosphere broadened to the instrumental resolution (black points) with 1σ uncertainties from a jackknife resampling technique (see Methods). The cross correlation functions between a model atmosphere broadened to the instrumental resolution and that same model additionally broadened by a range of rotation rates (5, 10, 15, 20, 25, 30 km/s) are overplotted in color. The autocorrelation for a model with no rotational line broadening is shown as a dashed pink line.

Tau 4 (Liu, Dupuy, and Allers, 2016). We reduce the data and measure rotation rates as described in the Methods section (Fig 4.1 and Table 4.1). We also search for brown dwarfs in the literature with spectral types later than M6, well-constrained ages typically less than 20 Myr, and measured rotation rates (Crossfield, 2014). We use the published magnitudes, spectral types, distances, and ages to derive new mass estimates for both these objects and the NIRSPEC sample of low-mass brown dwarfs in a uniform manner (see section 4.3), rather than relying on the relatively heterogeneous approaches from the literature. We select our comparison sample of low-mass brown dwarfs using a cutoff of 20 M_{Jup}, which yields six objects with measured rotation rates including three from our survey (OPH 90, USco J1608-2315, PSO J318.5-22), and three from the literature (2M1207-3932, GY 141, KPNO Tau 12) (Mohanty, Jayawardhana, and Basri, 2005; Rice et al., 2010; Kurosawa, Harries, and Littlefair, 2006). Although this mass range includes some objects above 13 M_{Jup}, we note that 1σ uncertainties on the mass estimates for some of the planetary-mass companions approach 20 M_{Jup}, and this mass distribution is therefore consistent with that of our bound companion sample.

We compare rotational velocities for our sample of planetary-mass companions to those of the low-mass brown dwarfs. Because these brown dwarfs likely formed via direct fragmentation of a molecular cloud, systematic differences in the observed rotation rates between the two populations would suggest differing formation

Table 4.1: Measured rotation rates for our sample of three new planetary-mass companions

Planetary-Mass Companion	Mass (M_{Jup})	Age (Myr)	Ref.	$v \sin i$ (km/s)
ROXs 42B b	10±4	3±2	(1),(2)	9.5 (+2.1 -2.3)
GSC 6215-210 b	12 – 15	11±2	(1),(3)	6.1 (+4.9 -3.8)
VHS 1256-1257 b	10 – 21	150 – 300	(1),(4)	13.5 (+3.6 -4.1)

Notes. References: (1) Bowler (2016), (2) Kraus et al. (2014), (3) Ireland et al. (2011), (4) Gauza et al. (2015)

histories. For this analysis we also include published spin measurements for two additional planetary-mass companions, β Pic b and 2M1207-3932 b (Snellen et al., 2014; Zhou et al., 2016), for a total sample size of five planetary-mass companions and six low-mass (<20 M_{Jup}) brown dwarfs. We note that the bound brown dwarf companions GQ Lup B and HN Peg B also have measured rotation rates (Schwarz et al., 2016; Metchev et al., 2015), but they were excluded from our sample because of their higher masses. For the objects in our observed sample we take the posterior distributions from the Markov chain Monte Carlo (MCMC) fits and divide by the probability distribution for sini, where we used an inclination distribution uniform in cosi. Here i is the inclination of the object's rotational axis with respect to our line of sight. For the objects observed by previous surveys, we produce a Gaussian distribution for each rotation rate centered on the measured vsini or veq values, and for those with measured vsini values divide that by the probability distribution for sini. This left us with a distribution of rotation rates for each object where we took into account the unknown inclination i. We then compare the resulting set of velocity distributions to models in which the rotational velocities of both populations are either drawn from a single Gaussian or from two distinct Gaussians using the Bayesian Information Criteria (BIC). The two Gaussian model BIC differs from the single Gaussian model BIC by $> 10^3$, indicating the single Gaussian model is strongly preferred. We also calculate the Akaike information criterion (AIC) and find that the single Gaussian model is also strongly preferred, with ΔAIC $> 10^3$. Finally, we calculate the evidence ratio of the two models, and again find that the single Gaussian model is favored by $> 10^4$.

We conclude that at the level of our observations, there is no evidence for a systematic difference in the measured rotation rates between the sample of planetary-mass companions and brown dwarfs with comparable masses. This suggests that either the planetary-mass companions formed via the same mechanism as the brown dwarfs (that is, turbulent fragmentation), or that the processes that regulate spin are inde-

pendent of formation mechanism at the level probed by our observations. This is consistent with a picture in which spin is regulated via interactions with the circumplanetary disk, as planetary-mass brown dwarfs should also host circumplanetary disks early in their lifetimes. However, it has been suggested that the properties of these disks might vary depending on the formation channel (Szulágyi, Mayer, and Quinn, 2017), and disks around isolated objects likely evolve differently than those embedded in a circumstellar disk. If spin is indeed regulated via interactions with a circumplanetary disk, our findings imply that both classes of objects should have broadly similar disk properties. We note that while there are other mechanisms such as planet-planet scattering, collisions, disk migration, and tides imposed by exomoons that could in theory alter the rotation rates of our bound companions, we do not expect any of these to affect the angular momentum evolution of these objects at the level measured by our observations.

We next compare the rotation rate for each object to its corresponding break-up velocity, taking into account uncertainties in the measured rotational line broadening, unknown inclination angles, estimated masses, radii, and ages for the objects in the sample (Fig 4.2). In the absence of any braking mechanism, we would expect actively accreting objects to spin up until they reach this critical rotation rate. The ratio of the observed rotation rate to the predicted break-up velocity therefore provides a useful measure of the relative efficiency of angular momentum loss mechanisms both during and after the end of accretion. Taking the error-weighted average over our sample, we find that the five planetary-mass companions that we observed are rotating at 0.137±0.058 of their break-up velocity. Our sample of low-mass brown dwarfs has a similar average rotation rate of 0.114±0.046 of their break-up velocity. If we combine both samples together, we find an average rotation rate of 0.126±0.036 times the break-up velocity, suggesting that both populations have shed an appreciable fraction of the angular momentum acquired during accretion.

Previous studies of young stars and higher mass brown dwarfs indicate that there is a correlation between their rotation rates and masses, with lower mass objects rotating faster on average (Scholz and Eislöffel, 2005). We next consider whether this correlation extends down into the planetary-mass regime, as has been suggested by previous studies (Zhou et al., 2016; Hughes, 2003). As before, we include published rotation rates for β Pic b and 2M1207-3932 b, and show Jupiter and Saturn for reference (Fig. 4.3). We exclude the terrestrial and ice giant solar system planets as their masses and spins are dominated by the accretion of solids rather than

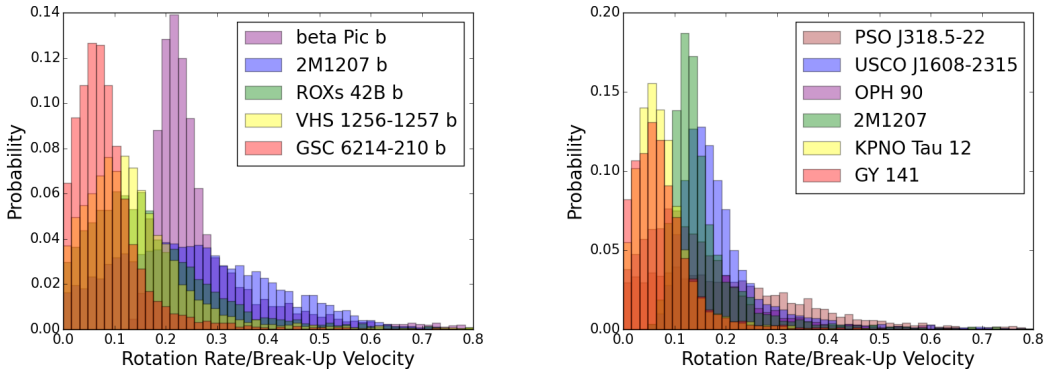

Figure 4.2: Distributions of observed rotation rates as a fraction of the corresponding break-up velocity for each object. The distributions for the planetary-mass companions are shown in the left panel and the distributions for brown dwarfs with masses less than 20 M_{Jup} are shown in the right panel. Note that these distributions take into account the uncertainties in the object's mass, age, and radius, as well as the unknown inclination of its rotation axis with respect to our line of sight. The uncertainties on the break-up velocities dominate the spread of these distributions.

hydrogen and helium, and in some cases have been further altered by giant impacts and/or tidal evolution (Morbidelli et al., 2012; Correia and Laskar, 2001). We find no evidence (Pearson correlation coefficient of -0.0788) for any correlation between rotation rate and mass for our sample of planetary-mass companions, brown dwarfs with masses below 20 M_{Jup}, and the solar system gas giants Jupiter and Saturn. This suggests that the mechanisms for shedding angular momentum are effectively independent of mass in the 1-20 M_{Jup} range.

We next investigate how the observed rotation rates for our sample of planetary-mass companions and brown dwarfs evolve during the first several hundred Myr (Fig. 4.4). We find that the rotation rates for both populations appear to remain constant with respect to their break-up velocities for ages between 2-300 Myr. Furthermore, the rotation rates for these objects are also similar to the present-day rotation rates of Jupiter and Saturn; given the lack of an observed correlation between planet mass and rotation rate, this suggests that there is also no significant spin evolution on timescales of billions of years. This suggests that the observed angular velocities of planetary-mass objects are set very early in their evolutionary lifetimes, perhaps through exchange of angular momentum between the object and its circumplanetary gas disk (Takata and Stevenson, 1996).

Although the mechanism that mediates angular momentum transfer in planetary-mass companions is currently unknown, we use the observations presented here to estimate its efficiency. In section 4.3, we present a calculation that approximates

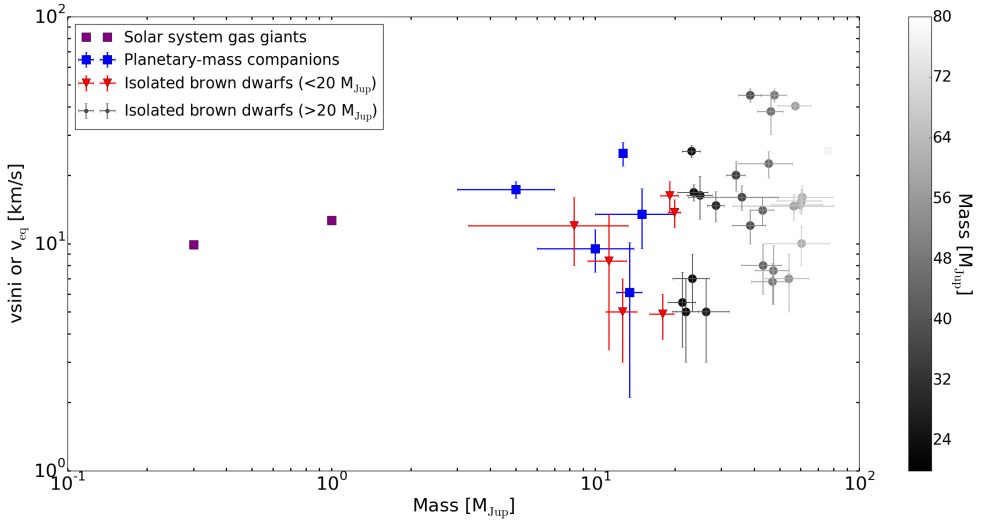

Figure 4.3: No correlation between mass and rotation rate for masses less than 20 M_{Jup}. Here we show rotation rate measurements and corresponding 1σ uncertainties for the bound planetary-mass companion sample in blue and the isolated brown dwarf (<20 M_{Jup}) sample in red. We include the gas giant solar system planets as purple squares for reference. The rates for the brown dwarfs and all planetary-mass companions except for 2M1207-3932 b are projected velocities, and the rotation rates for 2M1207-3932 b and the solar system gas giants are equatorial velocities. We also plot rotation rate measurements for more massive brown dwarfs (20-80 M_{Jup}) as filled grey circles, with the shading indicating the mass of each object. Five of these measurements are equatorial velocities derived from photometric rotation periods and the rest are projected rotation rates from measurements of rotational line broadening.

the angular momentum evolution of a newly formed 10 M_{Jup} object surrounded by a circumplanetary disk. Accounting for spin-up due to gravitational contraction and accretion of disk material, we find that the spin-down mechanism must extract angular momentum from the planetary-mass object at a characteristic rate of dL/dt$\sim 10^27$ kg m^2/s^2 during the disk-bearing epoch in order to reproduce the observed rotation rates in the sample. Understanding and modeling the physical nature of this mechanism represents an intriguing problem, worthy of future exploration.

The observations presented here provide constraints on the primordial rotation rates and angular momentum evolution of young planetary-mass companions and brown dwarfs with comparable masses. The degree of similarity between these two classes of objects suggests that irrespective of the formation mechanism, the physical processes that regulate angular momentum are likely to be the same for gas giant planets as they are for planetary-mass brown dwarfs. As a consequence, these observations lay the foundation for new theoretical investigations into the mechanisms that regulate gas accretion onto growing planetary-mass objects. Looking ahead, these results pave the way for future studies of gas giant planets using instruments on the

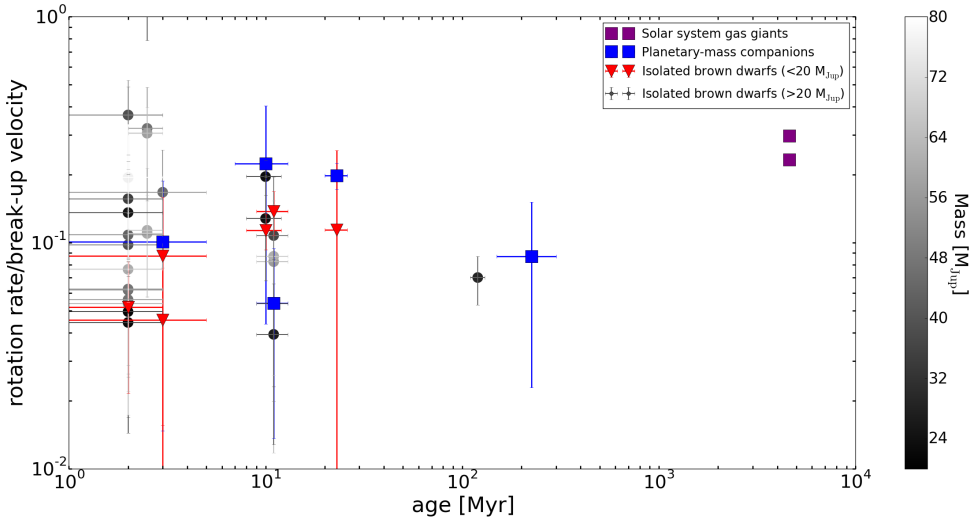

Figure 4.4: Angular momentum evolution of planetary-mass objects. Observed rotation rates as fractions of break-up velocities are plotted for our sample of five planetary-mass companions (blue squares), as well as a comparison sample of six isolated brown dwarfs with masses less than 20 M_{Jup} (red triangles), and Jupiter and Saturn (purple squares). For comparison we also plot published rotation rates for all brown dwarfs with well-constrained ages typically less than 20 Myr, and spectral types later than M6 (filled circles), where the shade of grey corresponds to our new estimates of the brown dwarf masses determined using the published magnitudes, spectral types, distances, and ages of these objects. We show 1σ uncertainties for all objects; these are dominated by uncertainties in the estimated break-up velocity for each object, with an additional contribution from the measured rotation rate and unknown inclination with respect to our line of sight.

upcoming generation of thirty-meter class telescopes such as the Giant Magellan Telescope's Near-IR Spectrometer.

4.3 Methods

NIRSPEC Observations

We observed our targets in K band (2.03 – 2.38 um) using the near-infrared spectrograph NIRSPEC at the Keck II 10 m telescope, which has a resolution of approximately 25,000. We used the 0.041x2.26 arcsec slit for our adaptive optics (AO) observations and the 0.432x24 arcsec slit for natural seeing observations, and obtained our data with a standard ABBA nod pattern. We observed the planetary-mass companions ROXs 42B b and GSC 6214-210 b (1.2" and 2.2" separations, respectively) in AO mode in order to minimize blending with their host stars; all other targets were observed in natural seeing mode, which has a much higher (10x greater) throughput. For ROXs 42B and VHS 1256-1257 we were able to observe both the host star and planetary-mass companion simultaneously, which made it easier to calculate a wavelength solution and telluric correction for the much fainter companions in these systems (see subsection "1D Wavelength Calibrated Spectrum

Extraction"). We could not do this for GSC 6214-210 b because the planetary-mass companion was located at a separation of 2.2", which was comparable to the slit length. For this object we obtained a separate spectrum for the star after completing our observations of the companion. See Table 4.2 for observation details.

Table 4.2: NIRSPEC K Band Observations

System	Pri. SpT	$m_{K,star}$ (mag)	$m_{K,pl}$ (mag)	Pl. SpT	Sep. (",AU)	M_{comp} (M_{Jup})	Age (Myr)	UT Date	AO?	No. Exp	To. Exp. (min)	Pl. S/N
ROXs 42B	M0	8.7	15.0	L1	1.2,140	10±4	3+/-2	2015/6/1	Yes	18	233	7.4
ROXs 42B	M0	8.7	15.0	L1	1.2,140	10±4	3+/-2	2015/6/2	Yes	6	80	4.4
GSC 6214-210	M1	9.2	14.4	L1	2.2,320	12-15	11+/-2	2015/6/3	Yes	16	240	6.0
VHS 1256-1257	M7.5	<10.4	14.7	L7	8.1,102	10-21	150-300	2015/5/7	No	14	93	11.1
OPH 90	...	...	14.9	L0	...	11±2	3±2	2015/6/4	No	8	52	16.6
USco J1608-2315	...	...	14.2	L1	...	19±1.5	11±2	2015/5/7	No	12	100	12.3
PSO J318.5-22	...	...	14.4	L7	...	8.3+/-0.5	21±4	2015/6/4	No	10	150	8.6
2M0355+1133	...	...	11.5	L3	...	29+/-2	120±10	2017/1/13	No	14	120	117.7
KPNO Tau 4	...	...	13.3	M9.5	...	25±2.5	2±1	2017/1/13	No	18	166	35.6

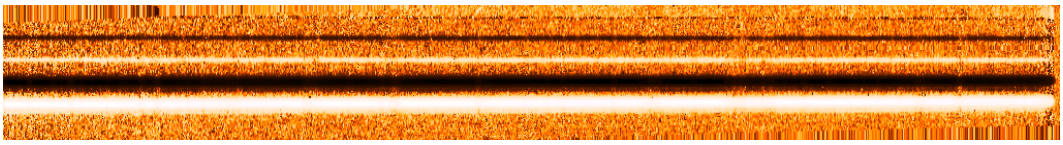

Figure 4.5: Representative 2D rectified spectrum. 2D rectified order 1 spectrum for the system VHS 1256-1257. Both the stellar and planetary traces are visible in this spectrum.

1D Wavelength Calibrated Spectrum Extraction

We extracted 1D spectra from our images using a Python pipeline modeled after Boogert, Hogerheijde, and G. A. Blake (2002). After flat-fielding, dark subtracting, and then differencing each nodded AB pair, we stacked and aligned the set of differenced images and combined them into a single image. We then fit the spectral trace for each order with a third order polynomial in order to align the modestly curved 2D spectrum along the x (dispersion) axis. For our sample of planetary-mass companions we fit the trace of the host star and used this fit to rectify the 2D spectra of both the star and the companion; this leveraged the high signal-to-noise of the stellar trace in order to provide better constraints on the shape of the fainter companion trace. Although we were not able to place GSC 6214-210 A and its companion in the slit simultaneously, we found that the shape of the spectral trace changed very little during our relatively modest 2.2" nod from the host star to the companion and therefore utilized the same approach with this data set. For both ROXs 42B b and GSC 6214-210 b, the initial solutions obtained from the stellar trace had a slope that differed by 2-3 pixels from beginning to end when applied to the companion trace. We corrected for this effect by rectifying the spectra of these two companions a second time using a linear function. Figure 4.5 shows an example 2D rectified spectrum for VHS 1256-1257 A and VHS 1256-1257 b.

We note that the NIRSPEC detector occasionally exhibits a behavior, likely due to variations in the bias voltages, in which one or more sets of every eight rows will be offset by a constant value for individual quadrants located on the left side of the detector. Our GSC 6214-210 b observations were the only ones that appeared to exhibit this effect, which produced a distinctive striped pattern in the two left-hand quadrants. We corrected for this effect by calculating the median value of the unaffected rows and then adding or subtracting a constant value from the bad rows in order to match this median pixel value. While the left side of the detector remained slightly noisier than the right in our GSC 6214-210 b data set, this noise was not high enough to preclude its use in our analysis.

After producing combined, rectified 2D spectra for each order, we extracted 1D spectra in pixel space for each positive and negative trace. We calculated an empirical PSF profile along the y (cross-dispersion) axis of the 2D rectified order, and used this profile to combine the flux along each column to produce a 1D spectrum. For the ROXs 42B and VHS 1256-1257 datasets, which include both the star and the planet in the slit simultaneously, we plotted this empirical PSF profile and confirmed that the stellar and companion traces were well-separated in the cross-dispersion direction. We identified the range of y (cross-dispersion) positions containing the stellar PSF and set these to zero before extracting the companion spectrum. When extracting the host star spectrum, we similarly set the region containing the companion trace to zero.

We next calculated a wavelength solution for each spectral order. Because we maintained the same instrument configuration (filter, rotator angle, etc.) throughout the night, the wavelength solution should remain effectively constant aside from a linear offset due to differences in the placement of the target within the slit. As with the 2D traces, we leverage the increased SNR of the host star spectra to obtain a more precise solution for our sample of planetary-mass companions. We fit the positions of telluric lines in each order with a third order polynomial wavelength solution of the form: $\lambda = ax^3 + bx^2 + cx + d$, where x is pixel number. We then apply this solution to the companion spectrum using a linear offset calculated by cross-correlating the companion spectrum with a telluric model spectrum. For our brown dwarf observations we found that the SNR of the spectra was typically not high enough to obtain a reliable wavelength solution using telluric lines, and therefore determined this solution by fitting higher SNR standard star observations obtained at a similar airmass immediately before or after each observation and applying a linear offset (i.e., the same approach as for the companion spectra).

We next remove telluric lines by simultaneously fitting a telluric model and an instrumental profile to each order in the extracted spectra. For the instrumental profile, we use a Gaussian function where we allow the width to vary as a free parameter. Although we also considered an instrumental profile with a central Gaussian and four satellite Gaussians on either side (Valenti, Butler, and Marcy, 1995), we found that our choice of instrumental profile had a negligible effect on our final rotational broadening measurement for ROXs 42B b and therefore elected to use the simpler single Gaussian model in our subsequent analyses. We determine the best-fit telluric models for our planetary-mass companion and low-mass brown

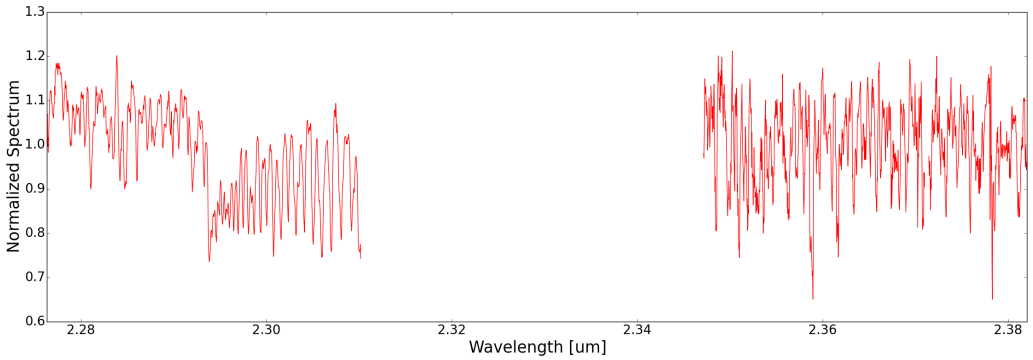

Figure 4.6: Representative wavelength calibrated and telluric corrected spectrum. Orders 1 and 2 of the telluric-corrected spectrum for 2M0355+1133 dataset. Note the start of the CO bandhead at ~2.29 um.

dwarf spectra by fitting the spectrum of either the host star or the standard star, respectively, and then applying a linear offset before dividing this model from the data. Figure 4.6 shows an example 1D wavelength calibrated and telluric corrected spectrum for 2M0355+1133.

MCMC Fits to Determine Rotational Line Broadening

We measure the rotational line broadening $v\sin i$, where v is the rotational velocity and i is the unknown inclination, and radial velocity offset for each object by calculating the cross-correlation function (CCF) between the first two orders of each object's spectrum (λ = 2.27 - 2.38 um) and a model atmosphere, where the model has first been broadened by the measured instrumental profile (R~25,000). We utilize these two orders because they contain absorption lines from both water and CO, including two strong CO bandheads, and because they have the most accurate telluric corrections and wavelength solutions. We generate atmospheric models for both our samples of planetary-mass companions and low-mass brown dwarfs using the SCARLET code (Benneke and Seager, 2012), with the parameters used for each object listed Table 4.3.

We next seek to match the shape of the measured CCF for each object by comparing it to the CCF between a model atmosphere with instrumental broadening and the same atmosphere model with both a radial velocity offset and additional rotational line broadening. We rotationally broaden the atmospheric model using a wavelength-dependent broadening kernel calculated using Equation 18.11 taken from Gray (2008) for a quadratic limb darkening law. The shape of the rotationally-broadened line profile depends on the planet's limb-darkening, which varies smoothly across

Table 4.3: Parameters Used to Generate Atmospheric Models and Best-Fit Rotation Rates, Barycentric Radial Velocity Offsets

System	T_{eff} (K)	log(g)	$v \sin i_{pl}$ (km/s)	RV_{pl} (km/s)
ROXs 42B	2100	3.81	9.5 (+2.1-2.3)	-2.3 ± 4.0
GSC 6214-210	2188	4.05	6.1 (+4.9 -3.8)	-7.3 ± 4.0
VHS 1256-1257	1280	4.5	13.5 (+3.6 -4.1)	2.1 (+1.6 -1.7)
OPH 90	2100	3.81	8.4 (+5.5 -5.0)	7.8 (+1.3 -1.2)
USco 1608-2315	2442	3.95	16.3 (+2.4 -2.5)	-4.0 (+1.1 -1.0)
PSO J318.5-22	1325	3.7	12.0 (+3.5 -4.4)	-6.8 ± 0.7
KPNO Tau 4	2477	3.74	16.3 (+3.2 -3.8)	17.9 (+0.7 -0.8)
2M0355+1133	1905	4.75	14.7 (+2.1 -2.3)	11.8 ± 0.5

Notes. For PSO J318.5-22 Teff and log(g) came from Allers et al. (2016). We note that the Teff determined by forward modeling the spectrum of PSO J318.5-22 is higher than that inferred from evolutionary models (Liu, Magnier, et al., 2013; Allers et al., 2016), suggesting that atmospheric models over-predict Teff. Similarly, we adopt a higher Teff for our atmospheric model for VHS 1256-1257 b than would be inferred from COND models using its mass and age, since the lower temperature models predict a significant abundance of methane that is not seen in our spectrum. All other Teff and log(g) listed in this table come from COND models, where we selected temperature and surface gravity values that corresponded to masses and ages closest to inferred masses and ages of each object (Table 4.2). We determined the barycentric velocity correction for each of our RV measurements using the program barycorr (Wright and Eastman, 2014). We note that since we only had two AB pairs for the host star GSC 6214-210, we were not able to obtain accurate uncertainty estimates for rotation rate and RV from the MCMC analysis. We therefore adopt more robust uncertainties from our analysis of VHS 1256-1257. Rotation rates have previously been measured for 2M0355+1133 (C. H. Blake, Charbonneau, and White, 2010), KPNO Tau 4 (Mohanty, Jayawardhana, and Basri, 2005), and PSO J318.5-22 (Allers et al., 2016) with published values of 12.31+/-0.15 km/s, 10+/-2 km/s, and 17.5 (+2.3 -2.8) km/s, consistent with the measured rotation rates in this paper at 1.0σ, 1.3σ, and 1.2σ respectively. We note that the previously published spin measurements for KPNO Tau 4 and 2M0355+1133 used models including pressure broadening while our models did not, and we would expect the inclusion of pressure broadening to reduce the reported rotation rates by several km/s (see subsection "MCMC Fits to Determine Rotational Line Broadening" for more details). RVs have previously been measured for 2M0355+1133 and PSO J318.5-22 with values of 11.92+/-0.22 km/s and -6.0 (+0.8 -1.1) km/s, consistent with our measured values at 0.2σ and 0.6σ. See subsection "MCMC Fits to Determine Rotational Line Broadening" for a discussion of the reported RV uncertainties for companions ROXs 42B b and GSC 6214-210 b.

the covered wavelength range and between line centers and line wings. We therefore calculate limb-darkening coefficients for each of the 2048 individual wavelength bins in our spectrum using the SCARLET model. We first compute the thermal emission intensity from the planet's atmosphere across a range of different zenith angles. From those intensities we then generate model intensity profiles at each wavelength, which we fit with quadratic limb-darkening coefficients. Finally, we use the resulting limb-darkening coefficients to calculate the appropriate rotational broadening kernel at that wavelength position.

We fit for the rotational line broadening $v \sin i$ and radial velocity offset of each object using a MCMC technique. We assume uniform priors on both parameters, and calculate the log likelihood function as $\sum_{i=1}^{n} \left[-0.5 \left(\frac{m_i - d_i}{\sigma_i} \right) \right]$, where d is the CCF between the data and the model spectrum with instrumental broadening only and m is the CCF of this model and the same model with additional rotational line broadening and a velocity offset applied. We calculate the uncertainties σ_i on the CCF of the model with the data using a jackknife resampling technique:

$$\sigma^2_{jackknife} = \frac{(n-1)}{n} \sum_{i=1}^{n} (x_i - x)^2 \tag{4.1}$$

where n is the total number of samples (defined here as the number of individual AB nod pairs), x_i is the cross-correlation function calculated utilizing all but the ith AB nod pair, and x is the cross-correlation function calculated using all AB nod pairs. The number of individual nod pairs for each target ranged between four and nine; see Table 4.2 for more details.

In addition to the measurement uncertainties on our extracted spectra, we also accounted for the uncertainty on the instrumental profile in our fits to the CCF. We did this by first fitting for the instrumental profiles in individual AB nod pairs using telluric lines in our high SNR stellar spectra (either host star or standard star). We then calculated the median resolution for each night and set the corresponding uncertainty on this value to the standard deviation of all resolution values divided by the square root of the number of AB nod pairs utilized. When fitting the CCF functions of the planetary-mass companions and brown dwarfs that we observed, we drew a new resolution from a Gaussian distribution with a peak located at the median resolution and width equal to the calculated uncertainty on that resolution at each step in the MCMC chain. We plot both the measured CCFs and the best-fit

model CCFs for each object in our sample in Figures 4.7, 4.8, and 4.9, and report the best-fit values and corresponding uncertainties in Table 4.1 and Table 4.3.

We next considered whether our measured rotational broadening values might be inflated by small offsets in the relative positions of individual spectra within our sequence of AB nod pairs. We tested for this by calculating a CCF for each individual AB nod pair in our ROXs 42B b observations, where we treat the positive and negative traces separately, and measuring the location of the CCF peak in wavelength space. We found that within the set of individual positive trace spectra (A nods) and negative trace spectra (B nods) the observed wavelength shifts were minimal, typically less than 1 km/s. However, the difference between the median positive and negative trace offsets could be as large as 5 km/s. As a result we opted to fit the positive and negative trace spectra separately, resulting in two independent estimates of the rotational broadening and velocity offset for each object. We find that in all cases these two values are consistent within the errors, and report their error-weighted average in Table 4.1 and Table 4.3. We also plot these values as a function of time in Figure 4.10. As an additional check, we also used the extracted spectra for the host star ROXs 42B, which have a much higher SNR in individual exposures, to determine the spin rate for each individual AB pair. We found that our measured rotational broadening also remained consistent across the full set of AB pairs, and agreed with the value calculated directly from the composite stellar spectrum (i.e., including all AB nod pairs) to $<0.5\sigma$.

We next compare the measured radial velocity offsets for our sample of bound planetary-mass companions to those of their host stars. For the host stars, we used Phoenix spectra (Husser et al., 2013) to model their spectra, where we select the model with log(g) and T_{eff} values closest to those reported in the literature for each system. We determined the rotation rates of ROXs 42B, GSC 6214-210A, and VHS 1256-1257A to be 43.6+/-0.2 km/s, 28.8+/-2.5 km/s, and 75.2 (+2.7 -2.3) km/s respectively, and measured velocity offsets of 1.8+/-0.2 km/s, -12.6 (+2.0 -2.2) km/s, and 1.5 (+2.0 -2.2) km/s respectively. We would expect both star and planetary-mass companion to share the same RV offset, as the predicted orbital velocities of these relatively wide separation companions should be much smaller than the precision of our measurements. For our lower S/N spectra (ROXs 42Bb and GSC 6214-210b), we find that the reported RV values for the planets differ from those of their host stars by 4.1 km/s and 5.3 km/s respectively. If we take the formal RV errors of 0.7 km/s and 1.3 km/s from our MCMC analysis at face value, this would correspond

to RV offsets of 7.7σ and 2.2σ respectively. However, we note that for these two relatively low SNR targets, the telluric lines we use for calibrating the linear offset in the planet's wavelength solution becomes the dominant source of uncertainty in our measurement of the planet's RV offset; this is not accounted for in our formal jackknife error analysis, which assumes an error-free wavelength solution. We therefore adopt a systematic noise floor of 4.0 km/s for the reported RV values for these two relatively low SNR targets. We also test the possible effects of 4-5 km/s errors in our wavelength solutions for these two planets by setting ROXs 42Bb's radial velocity equal to that of its host star (1.8 km/s vs -2.3 km/s) and re-running our MCMC analysis. We find that the measured rotation rate for the companion in this fit is 9.8 (+2.0 -2.1) km/s, consistent with our original measurement at 0.1σ.

We also investigate whether or not night-to-night variations in the instrumental broadening profile might affect our estimated values for rotational line broadening. We test this by fitting for the rotational line broadening of the host star ROXs 42B, which was observed along with its planetary-mass companion on two separate nights with an estimated instrumental resolution of R$\sim$30,000 and R$\sim$26,000, respectively. We found that the measured spins for the first and second night differed by $\sim$1σ, indicating that our method for determining the instrumental broadening profile using telluric lines is providing a reliable characterization of this parameter.

On the modeling side, we also check whether variations in the C/O ratio of the atmospheric model used in the cross-correlation might affect our measured spin rates. We test this by repeating our CCF analysis of the ROXs 42B b spectrum using models with C/O ratios of 0.8, 0.54 (solar), and 0.35. We find that the measured spin rates for the low and high C/O models are consistent with our solar C/O model at <0.5σ. We also consider the possibility that pressure broadening might cause us to over-estimate the amount of rotational line broadening in these objects. Our fiducial solar metallicity models were generated using opacities from the ExoMol database (Tennyson and Yurchenko, 2012), which does not include pressure broadening, but has line locations that better match our observed spectra. Alternative opacity tables such as HiTemp (Rothman and Gordon, 2010) do include pressure broadening, but do not match the line locations in our spectra as well as the ExoMol database.

We test the potential effects of pressure broadening on our estimate of the spin rate by generating a new version of our atmosphere model for ROXs 42B b using HiTemp molecular opacities and comparing the resulting vsini value to the one measured using our original ExoMol models. Depending on our choice of pressure-temperature

profile, we found that the measured rotation rate calculated using the HiTemp models was 2-5 km/s (0.7- 1.8σ) lower than the rotation rate using our original ExoMol models. We utilize the ExoMol opacities in our final rotation rate analysis for three reasons: (1) the pressure-temperature profiles for these young planetary-mass objects are poorly constrained by current observations, (2) the pressure-broadened profiles for many molecules at high temperatures are not currently well understood, and (3) the ExoMol line locations are a better match for our spectra than the HiTemp line locations. We note that including pressure-broadening in our models would likely decrease our estimated rotation rates by several km/s, corresponding to a change of approximately 1σ for most of the objects in our sample. However, this would not affect our conclusion that young planetary-mass objects appear to be rotating at much less than their break-up velocities, and that their rotation rates do not evolve significantly in time.

Finally, we test whether uncertainties in assumed effective temperatures and surface gravities could impact our measured rotation rates. We generate atmospheric models for PSO J318.5-22 using T_{eff} and log(g) values determined in the forward model analysis of Allers et al. (2016), T_{eff} = 1325 (+350 -12) K and log(g) = 3.7 (+1.1 -0.1). We recalculate rotation rates and velocity offsets using a model with T_{eff} = 1313 K and log(g) = 3.6, and another model with T_{eff} = 1675 K and log(g) = 4.8. We find that these parameters differ from the original values by less than 0.3σ.

Calculating the Break-up Velocity

To calculate break-up velocities, we need estimates of the masses and radii of the objects in our sample. For our sample of bound planetary-mass companions we utilize mass estimates from the literature. For our sample of low-mass brown dwarfs, we derive new mass estimates in a homogeneous manner rather than relying on the heterogeneous approaches from the literature (Table 4.4). We first calculate bolometric luminosities for these objects using the K-band bolometric correction for young ultracool dwarfs from Filippazzo et al. (2015) together with their distances and spectral types. We then calculate masses using their ages and luminosities together with a finely interpolated grid of hot-start evolutionary models from Burrows et al. (1997). We incorporate uncertainties in distance, spectral type, apparent K-band magnitude, and age in a Monte Carlo fashion by randomly drawing these values from normal distributions for a large number of trials. We note that estimating masses using the bolometric luminosity is more robust than using absolute magnitudes as the former is less reliant on the detailed accuracy of atmospheric models. This is

especially true in the optical where strong molecular opacities are generally more difficult to reproduce in synthetic spectra compared, for example, to near-infrared wavelengths.

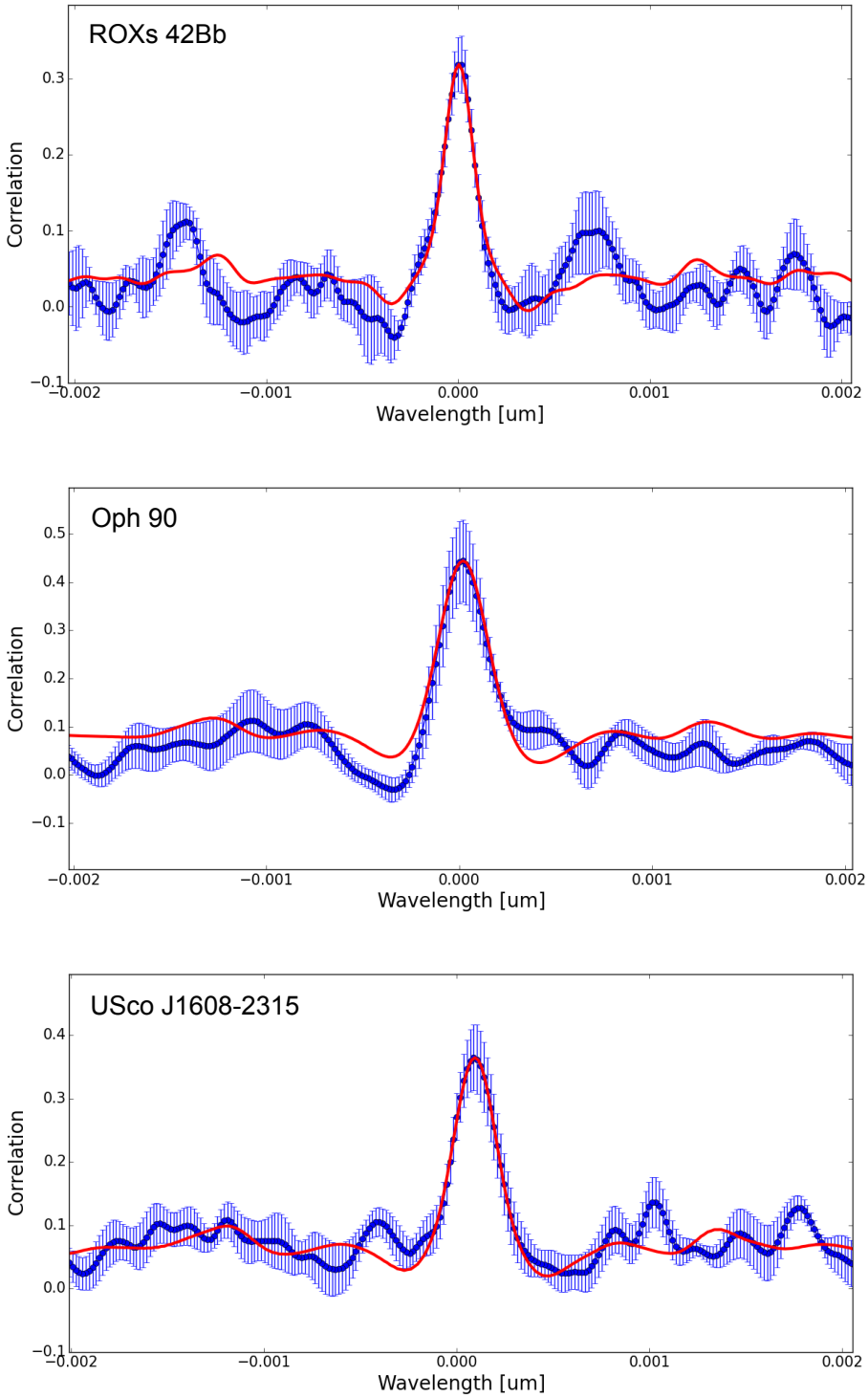

Figure 4.7: Cross correlation functions for planetary-mass companions and low-mass brown dwarfs obtained from our NIRSPEC observations. Cross correlation functions for each object are plotted in blue, with the best-fit model overplotted in red. 1σ uncertainties on these CCFs are calculated using the jackknife resampling technique (see subsection "MCMC Fits to Determine Rotational Line Broadening").

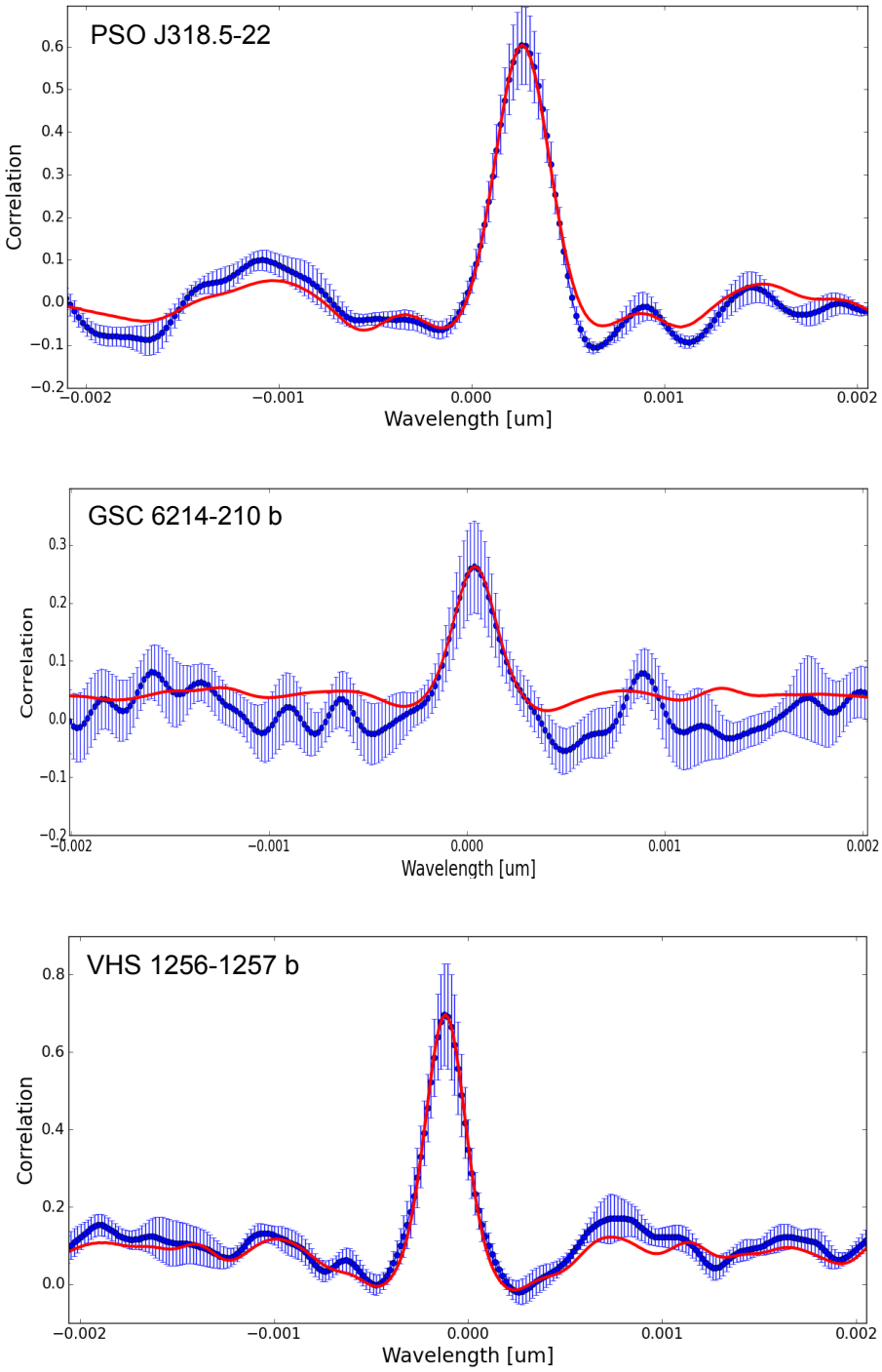

Figure 4.8: Cross correlation functions for planetary-mass companions and low-mass brown dwarfs obtained from our NIRSPEC observations. See Figure 4.7 for more details.

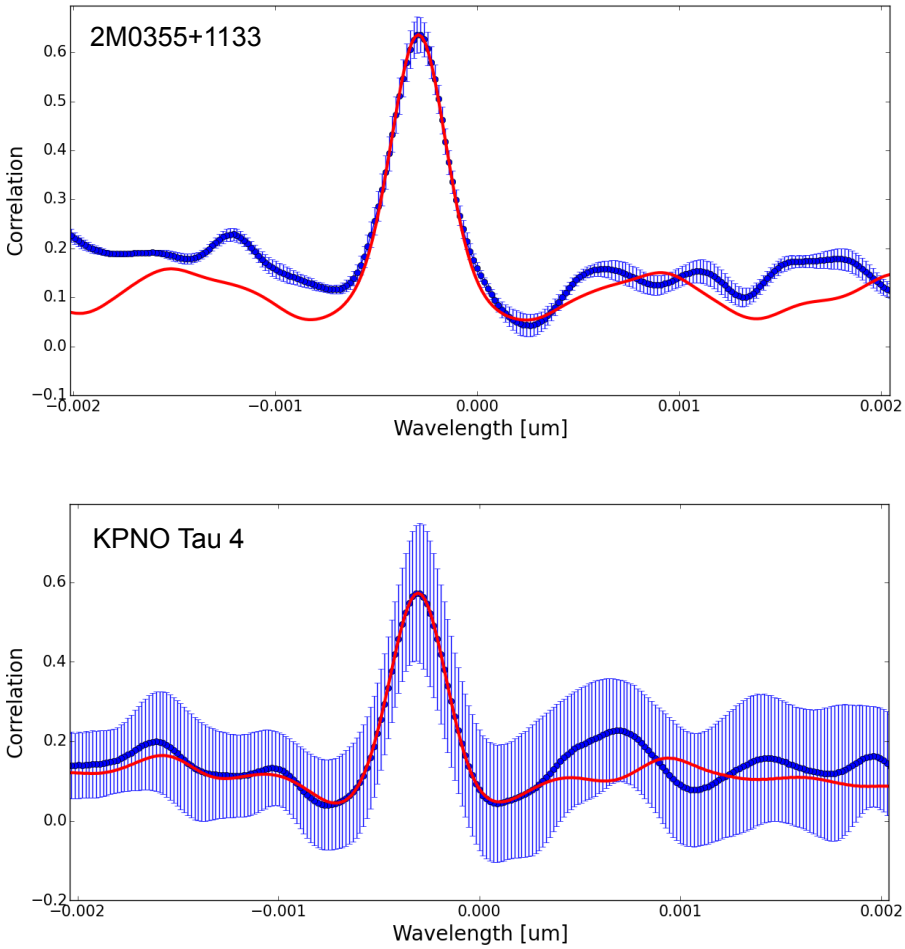

Figure 4.9: Cross correlation functions for planetary-mass companions and low-mass brown dwarfs obtained from our NIRSPEC observations. See Figure 4.7 for more details.

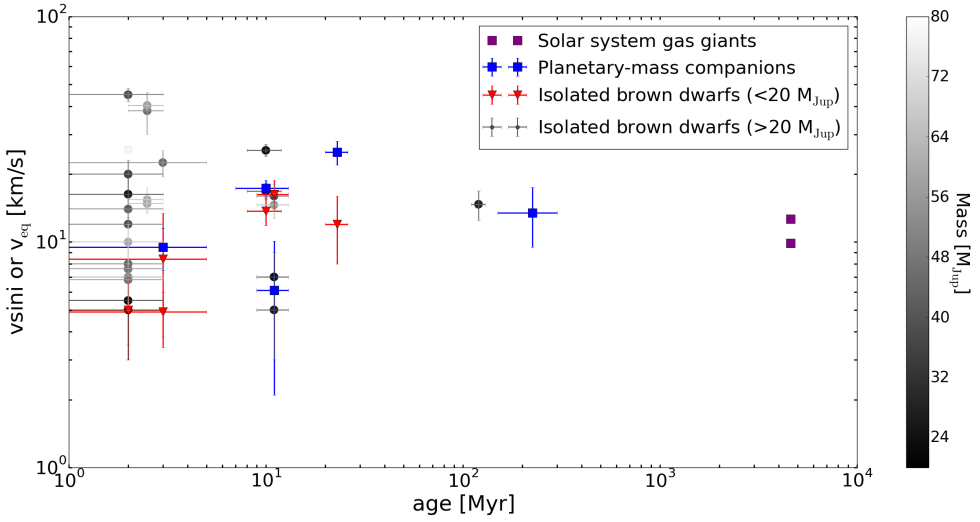

Figure 4.10: Rotation rate measurements versus age for planetary-mass companions (blue squares) and brown dwarfs with masses less than 20 M_{Jup} (red triangles). We include the gas giant solar system planets as purple squares and show more massive (20-80 MJup) brown dwarfs as filled circles, where color shade of grey indicates the mass. 1σ uncertainties are shown for each object.

Table 4.4: Brown Dwarf Properties, Including New Homogeneous Mass Estimates and Rotation Rates From the Literature

System	RA	Dec	SpT	Kmag (mag)	Dist. (pc)	Age (Myr)	Mass (M_{Jup})	$+1\sigma$ (M_{Jup})	-1σ (M_{Jup})	$v \sin i / v$ (km/s)	Ref.
2M1139-3159	11 39 51.140	-31 59 21.50	M8	11.503+/-0.023	50+/-1.8	10+/-2	23.174	1.409	1.854	25.5	Rice et al. (2010), Kurosawa, Harries, and Littlefair (2006)
2M1207-3932	12 07 33.500	-39 32 54.40	M8	11.945+/-0.026	50+/-1.8	10+/-2	19.916	0.925	1.187	13.7	Rice et al. (2010), Kurosawa, Harries, and Littlefair (2006)
2M 05373648-0241567	05 37 36.480	-02 41 56.70	M7	14.560+/-0.100	442+/-20	2-3	46.262	5.485	5.288	38.18	Cody and Hillenbrand (2010)
CFHT-BD-Tau 1	04 34 15.272	22 50 30.96	M7	11.849+/-0.018	145+/-15	2+/-1	54.128	6.362	10.249	7.0	Rice et al. (2010)
CFHT-BD-Tau 2	04 36 10.387	22 59 56.03	M7.5	12.169+/-0.019	145+/-15	2+/-1	43.240	4.477	7.502	8.0	Rice et al. (2010)
CFHT-BD-Tau 3	04 36 38.938	22 58 11.90	M7.75	12.367+/-0.025	145+/-15	2+/-1	38.652	3.544	5.619	12.0	Rice et al., 2010
Cha Ha 1	11 07 17.0	-77 35 54.00	M7.75	12.174+/-0.024	160	2	47.311	6.025	6.916	7.6	Joergens and Guenther (2001)
GG Tau Bb	04 32 30.25	17 31 30.90	M7.5	12.010+/-0.130	145+/-15	2+/-1	46.940	7.189	7.991	6.8	Rice et al. (2010) and White and Basri (2003)
IC 348 355	03 44 29.210	32 08 13.70	M8	13.499+/-0.035	300	1-3	47.717	4.030	5.540	45.0	Rice et al. (2010)
IC 348 363	03 44 17.265	32 00 15.23	M8	13.695+/-0.038	300	1-3	43.098	3.503	4.439	14.0	Rice et al. (2010)
IC 348 405	03 44 21.163	32 06 16.56	M8	13.910+/-0.100	300	1-3	38.659	3.186	3.820	45.0	Rice et al. (2010)
KPNO Tau 5	04 29 45.680	26 30 46.81	M7.5	11.536+/-0.018	145+/-15	2+/-1	60.490	17.359	16.611	10.0	Rice et al. (2010)
USco 130	15 59 43.665	-20 14 39.61	M7	13.075+/-0.034	145+/-15	11+/-2	56.487	16.303	23.397	14.6	Rice et al. (2010), Kurosawa, Harries, and Littlefair (2006)
USco 131	16 00 19.443	-22 56 28.77	M7	13.481+/-0.033	145+/-15	11+/-2	35.950	10.238	13.445	16.0	Rice et al. (2010)
USco DENIS 161916	16 19 16.463	-23 47 23.54	M8	13.596+/-0.050	145+/-15	11+/-2	26.305	3.760	5.949	5.0	Rice et al. (2010)
USco DENIS 162041	16 20 41.445	-24 25 49.17	M7.5	12.902+/-0.019	145+/-15	11+/-2	60.859	21.923	18.916	16.0	Rice et al. (2010)
2M 05375206-0236046	05 37 52.060	-02 36 04.60	M6.5	14.200+/-0.060	442+/-20	2-3	59.575	8.426	13.313	14.8	Cody and Hillenbrand (2010)
2M05391308-0237509	05 39 13.080	-02 37 50.90	M7	14.310+/-0.070	442+/-20	2-3	60.490	17.359	11.971	15.4	Cody and Hillenbrand (2010)
2M05400453-0236421	05 40 04.530	-02 36 42.10	M6.5	14.270+/-0.070	442+/-20	2-3 5	7.297	5.469	8.372	40.3	Cody and Hillenbrand (2010)
Cha Ha 12	11 05 37.5	-77 43 07.0	M6.5	11.811+/-0.019	160	2	76.412	17.581	24.264	25.7	Joergens and Guenther (2001)
GY 37	16 26 27.810	-24 26 41.82	M6	12.092+/-0.030	120+/-10	3+/-2	45.420	6.335	10.583	22.5	Rice et al. (2010)
IC 348 478	03 44 35.937	32 11 17.51	M6.25	14.574+/-0.073	300	1-3	34.119	2.550	2.885	20.0	Rice et al. (2010)
GY 141	16 26 51.284	-24 32 41.99	M8.5	13.889+/-0.057	120+/-10	3+/-2	17.953	1.877	1.961	4.9	Rice et al. (2010) and Kraus et al. (2014)
KPNO Tau 1	04 15 14.714	28 00 09.61	M8.5	13.772+/-0.035	145+/-15	2+/-1	21.394	1.867	2.558	5.5	Rice et al. (2010)
KPNO Tau 12	04 19 01.270	28 02 48.70	M9	14.927+/-0.092	145+/-15	2+/-1	12.664	1.632	1.769	5.0	Rice et al. (2010)
KPNO Tau 6	04 30 07.244	26 08 20.79	M8.5	13.689+/-0.037	145+/-15	2+/-1	22.047	2.023	2.4733.032	5.0	Rice et al. (2010)
S Ori 45	05 38 25.500	-02 48 36.00	M8.5	15.690+/-0.212	442+/-20	2-3	26.012	2.487	3.091	151	Zapatero Osorio et al (2003), Zapatero Osorio et al (2004)

Continued on next page

Table 4.4 – continued from previous page

System	RA	Dec	SpT	Kmag (mag)	Dist. (pc)	Age (Myr)	Mass (M_{Jup})	$+1\sigma$ (M_{Jup})	-1σ (M_{Jup})	$v \sin i / v$ (km/s)	Ref.
TWA 5B	11 31 55.400	-34 36 29.00	M8.5	11.400+/-0.200	50+/-1.8	10+/-2	23.615	2.134	3.692	16.8	Rice et al. (2010), Kurosawa, Harries, and Littlefair (2006)
USco DENIS 161006	16 10 06.082	-21 27 44.02	M8.5	13.768+/-0.056	145+/-15	11+/-2	23.328	2.153	2.244	7.0	Rice et al. (2010)
OPH 90	16 27 36.59	-24 51 36.1	L0	14.85+/-0.05	120+/-10	3+/-2	11.243	1.545	1.670	8.4	This paper
USco 1608	16 08 27.47	-23 15 10.4	L1	14.205+/-0.070	145+/-15	11+/-2	19.157	1.226	2.128	16.4	This paper
2M0355+1133	03 55 23.37	11 33 43.7	L3	11.526+-0.021	9.1+/-0.1	120+/-10	28.667	2.618	2.794	14.7	This paper
KPNO Tau 4	04 27 28.0	26 12 04.7	M9.5	13.281+/-0.032	145+/-15	2+/-1	24.970	2.794		16.3	This paper

Notes. We create this list by first identifying all brown dwarfs in the literature with spectral types later than M6, well-constrained ages typically less than 20 Myr, and measured rotation rates or rotation periods. We then deriv new mass estimates using published magnitudes, spectral types, distances, and ages. Here we list median masses as well as uncertainties corresponding to the highest prior density for objects with estimated masses less than 8 MJup. Objects in italics have new measured rotation rates from our NIRSPEC program. For objects 2M05373648-0241567, 2M05375206-0236046, 2M05391308-0237509, 2M05400453-0236421, and S Ori 45, the rotation rate presented here are equatorial rotation rates determined from published photometric rotation periods; all others are projected rotation rates from measurements of rotational line broadening. The "Ref." column cites the referenc where we obtained the rotation rates for each object.

Once we have a mass estimate, we used COND models (Baraffe et al., 2003) to estimate the radius of each object. We note that by using COND models, the radii we adopt assume a hot-start formation history. We calculate the 1σ minimum radius using the 1σ minimum age and mass, and the 1σ maximum radius using the 1σ maximum age and mass. Although we could have propagated the uncertainties in mass and age in quadrature, these are not independent quantities as the mass estimate depends directly on the age estimate, and we therefore opted for a more conservative approach. We calculate the best-fit break-up velocity for each object and the corresponding 1σ uncertainties on this parameter by propagating uncertainties from the mass, radius, and age of the object. Figures 4.11 and 4.12 compare the distributions of measured rotation rates and calculated break-up velocities for each object.

Angular Momentum Evolution Calculation

Here we seek to approximately characterize the angular momentum evolution of a giant planet or low-mass brown dwarf following the primary phase of assembly. In the absence of more stringent observational constraints we utilize a simple parameterized model to estimate the relevant timescale for angular momentum evolution. It is readily apparent that this timescale will be shorter than both the disk lifetime and the Kelvin-Helmholtz timescale, but such a parameterized model is nonetheless instructive for illustrating the relevant forces at work in this problem. We begin by discussing the consequences of gravitational contraction.

Gravitational Contraction

To approximate the interior structure of a newly-formed planetary mass object, we adopt a polytropic equation of state with index $\xi = 3/2$, characteristic of a fully-convective body. The binding energy of such an object is given by

$$\mathcal{E} = -b\frac{GM^2}{R}, \tag{4.2}$$

where $b = 3/(10 - 2\xi) = 3/7$, G is the gravitational constant, M is the mass of the object and R is the radius of the object. Equating the gravitational energy loss to the radiative flux at the surface, we have

$$\frac{d\mathcal{E}}{dt} = -4\pi R^2 \sigma T_{\rm eff}^4 = b\frac{GM^2}{R^2}\frac{dR}{dt}. \tag{4.3}$$

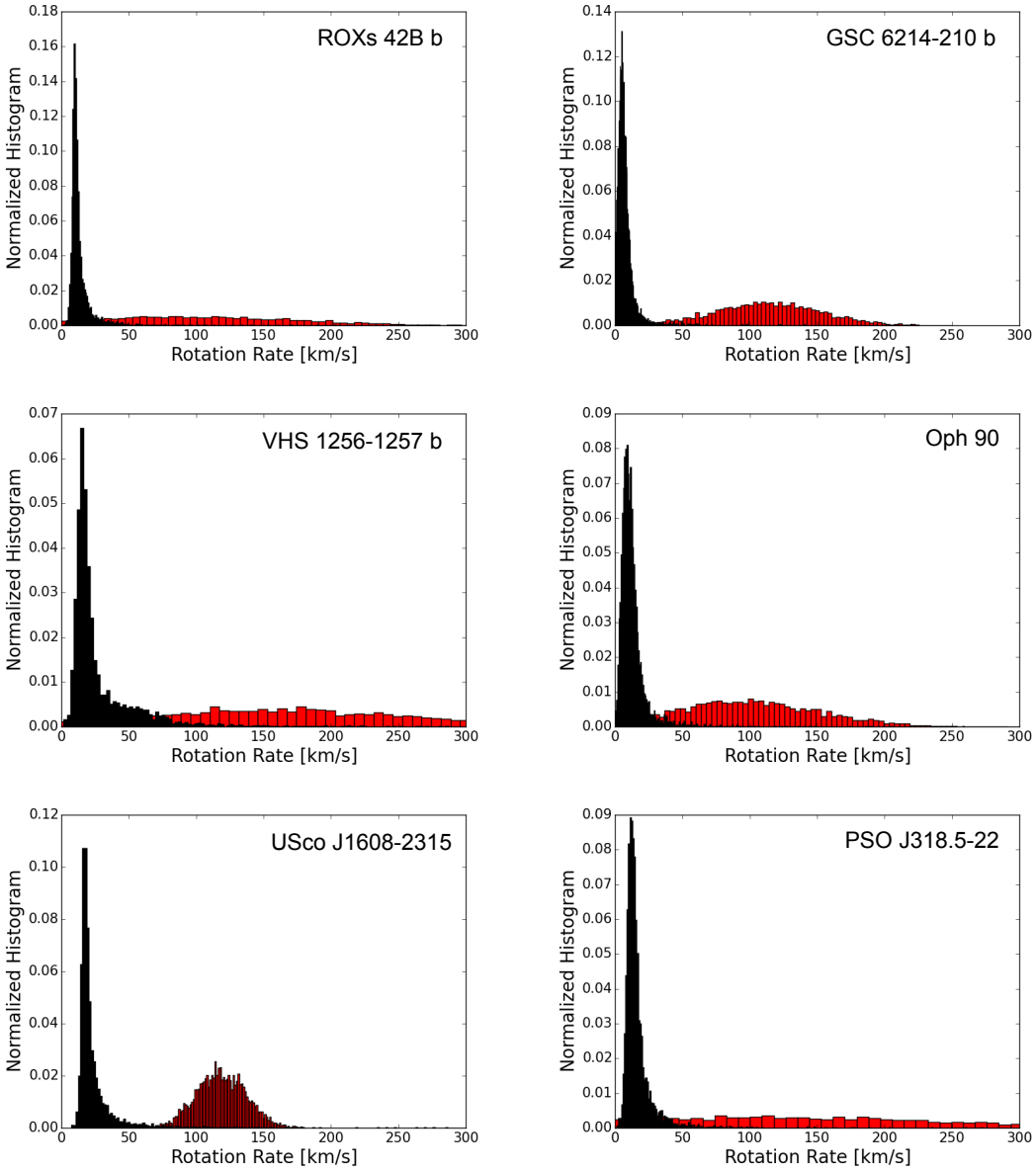

Figure 4.11: Distributions of measured rotation rates and calculated break-up velocities for each object. The rotation rate distributions (black) have widths that are set by the uncertainties in the measured rotational line broadening and unknown inclination, and the break-up velocity distributions (red) typically have larger uncertainties that are set by errors in the estimated masses, ages, and radii.

Adopting an initial condition $R|_{t=0} = R_0$, the above expression yields a differential equation for the evolution of the radius:

$$\frac{dR}{dt} = -R\left(\frac{R}{R_0}\right)^3\left(\frac{4\pi\sigma T_{\rm eff}^4 R_0^3}{bGM^2}\right) = -\frac{R}{\tau_{\rm KH}}\left(\frac{R}{R_0}\right)^3, \tag{4.4}$$

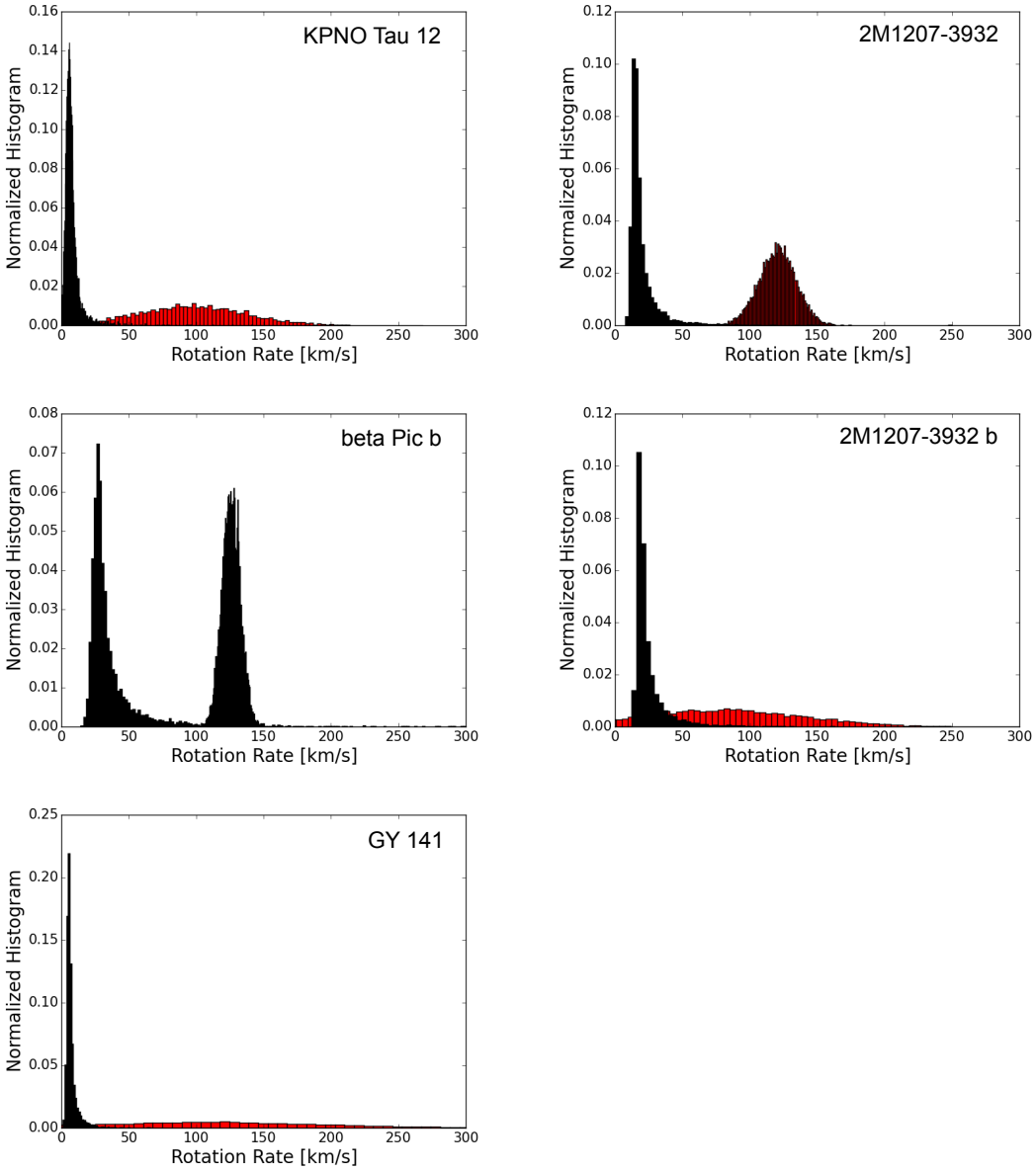

Figure 4.12: Distributions of measured rotation rates and calculated break-up velocities for each object. See Figure 4.11 for more details.

where τ_{KH} is the Kelvin-Helmholtz timescale. This equation admits the simple solution:

$$R = R_0 \left(\frac{\tau_{\rm KH}}{\tau_{\rm KH} + 3t} \right)^{1/3}. \tag{4.5}$$

Using the inferred masses, radii and effective temperatures of the young (age $\lesssim$ 10 Myr) objects within our sample, we estimate that the characteristic Kelvin-Helmholtz time for this subset of bodies is $\tau_{\rm KH} \sim 10$ Myr. This number has direct

consequences for the spin-evolution of these objects. In isolation, conservation of spin angular momentum, $\mathcal{L}$, yields

$$\frac{d\mathcal{L}}{dt} = 2IMR\omega\frac{dR}{dt} + IMR^2\frac{d\omega}{dt} = 0, \tag{4.6}$$

where $I \simeq 0.21$ is the reduced moment of inertia. Combined with equations (4.4) and (4.5), this expression governs the spin-up associated with gravitational contraction, and has the solution

$$\omega = \omega_0\left(\frac{3t + \tau_{\rm KH}}{\tau_{\rm KH}}\right)^{2/3}. \tag{4.7}$$

Importantly, expression (4.7) implies that in absence of external torques, the angular velocities of young planets will more than double on a timescale comparable to the Kelvin-Helmholtz time.

Accretion

A second process that is routinely envisioned to alter the spin evolution of young planetary mass objects is accretion of gaseous material from their circumplanetary disks. While we do not have observational constraints on circumplanetary disk lifetimes, we know that circumstellar disk dissipation timescales range from 1 – 10 Myr. It can be reasonably speculated that circumplanetary disks exist on a similar timescale. Without observations to suggest otherwise, we assume a similar disk dissipation timescale for circumplanetary disks as seen for circumstellar disks, i.e. $\tau_{\rm disk} \sim 3$ Myr (Canup and Ward, 2006). At the same time, gravitational stability requires that the ratio of the disk mass to central body's mass does not exceed the disk aspect ratio, h/r ~ 0.05. Accordingly, here we parameterize the disk mass in the following way:

$$M_{\rm disk} = M\left(\frac{h}{r}\right)\exp(-t/\tau_{\rm disk}). \tag{4.8}$$

Correspondingly, we interpret the derivative of the above expression as the accretion rate that the central body experiences:

$$\dot{M}_{\rm disk} = \frac{M}{\tau_{\rm disk}}\left(\frac{h}{r}\right)\exp(-t/\tau_{\rm disk}). \tag{4.9}$$

In the well-studied case of circumstellar disks that encircle T-Tauri stars, stellar magnetic fields act to carve out inner gaps with a characteristic radius of $\sim 10 R_{\rm Sun}$

(Mohanty and Shu, 2008). While strong (~kGauss) magnetic fields and sufficient levels of ionization are essentially guaranteed in the T-Tauri setting, it is unclear whether conditions required to clear out significant magnetospheric cavities are met in typical circumplanetary disks. Accordingly, here we ignore this possibility, and assume that the disk extends down to the planetary surface, for simplicity. Under this assumption, the rate at which angular momentum is deposited upon the planet by the accretionary flow can be expressed as follows:

$$2IMR\omega\frac{dR}{dt} + IMR^2\frac{d\omega}{dt} = \dot{M}_{\rm disk}\sqrt{GMR}. \tag{4.10}$$

Quantitatively, the spin-up due to gravitational contraction and that due to accretion operate on similar timescales, and have comparable magnitudes.

Spin-Down

While no observational constraints exist on the rotation rates of planets that are currently undergoing conglomeration, it is reasonable to anticipate that owing to accumulation of angular momentum stored in the source material, a planetary mass object should rotate at or near break-up towards the end of the phase of rapid of gas accretion (irrespective of whether the object formed through core accretion or via gravitational instability). In light of this expectation and the discussion presented above, another mechanism is needed to reduce the rotation rate to values well below break-up, and counteract spin-up due to gravitational contraction and accretion.

Because our observations do not show a statistically significant dependence of angular velocities on age, we speculate that the spin-down process (whatever it may be) operates exclusively during the disk-bearing stage of evolution. With this notion in mind, we scale this process according to the disk mass, planetary radius, and planetary spin, while parameterizing it in terms of a characteristic spin-down timescale τ_{spin}:

$$2IMR\omega\frac{dR}{dt} + IMR^2\frac{d\omega}{dt} = \dot{M}_{\rm disk}\sqrt{GMR} - M_{\rm disk}R^2\frac{\omega}{\tau_{\rm spin}}. \tag{4.11}$$

Although this equation admits no simple analytical solution, it is readily solvable numerically.

Retaining the same parameters as those quoted above, we have solved equation (4.11), adopting the initial conditions $R_0 = 3R_{\rm Jup}$ and $\omega_0 = \sqrt{GM/R_0^3}$ for a series

of spin-down timescales in the range $\tau_{\rm spin} = 2 \times 10^5 - 1.4 \times 10^6$ years, over a time interval of $3\tau_{\rm disk}$. Figure 4.13 shows a family of curves that denote the rotation rate of a $M = 10 M_{\rm Jup}$ planet, scaled by the breakup velocity, as a function of time. Qualitatively, these solutions exhibit the desired behavior, in that significant spin-down occurs over $\sim 1\tau_{\rm disk}$, and the spin subsequently equilibrates onto a quasi-stationary value. In particular, the evolutionary path with $\tau_{\rm spin} = 2 \times 10^5$ years equilibrates onto $\omega/\omega_{\rm breakup} \simeq 0.1$, similar to the observed values. Accordingly, we conclude that the spin-down mechanism must operate with an approximate efficiency of $d\mathcal{L}/dt = -M_{\rm disk} R^2 \omega / \tau_{\rm spin} \sim 10^{27}\,{\rm kg\,m^2/s^2}$ during the disk-bearing epoch, in order for sufficient spin-down to occur.

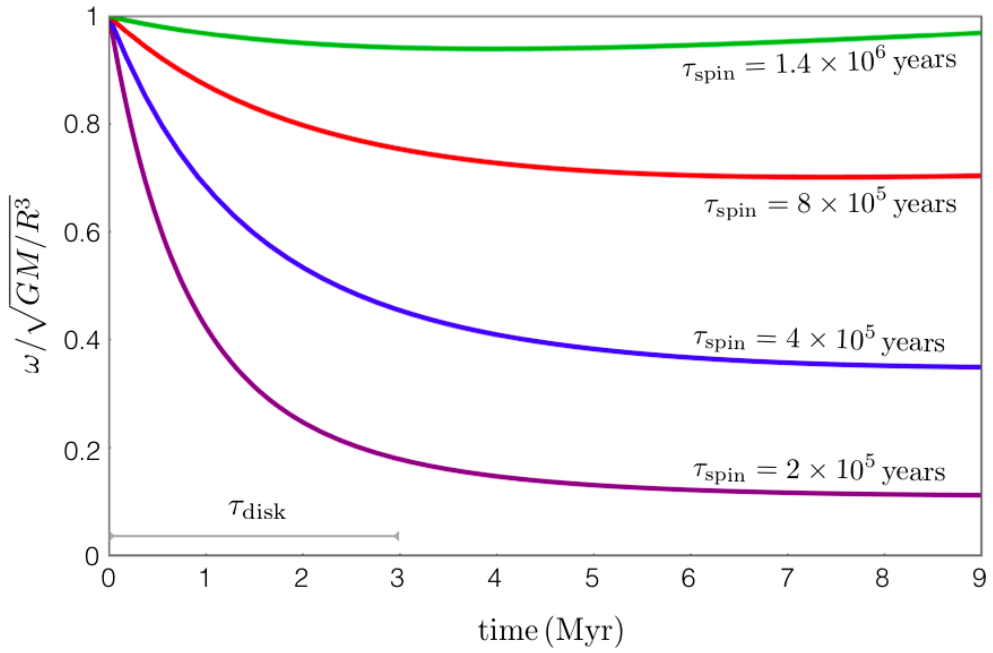

Figure 4.13: Numerical solution to equation (4.11). A 10 MJup planet is initialized at breakup rotation (qualitatively t=0 corresponds to the conclusion of rapid gas accretion), and subsequently experiences spin-up due to gravitational contraction and accretion, as well as spin-down due to a parameterized angular momentum exchange with the circumplanetary disk.

References

Allers, K. N. et al. (2016). "The Radial and Rotational Velocities of PSO J318.5338-22.8603, a Newly Confirmed Planetary-mass Member of the β Pictoris Moving Group". In: *ApJ* 819, 133, p. 133. DOI: 10.3847/0004-637X/819/2/133. arXiv: 1601.04717 [astro-ph.SR].

Alves de Oliveira, C. et al. (2012). "Spectroscopy of new brown dwarf members of ρ Ophiuchi and an updated initial mass function". In: *A&A* 539, A151, A151. DOI: 10.1051/0004-6361/201118230. arXiv: 1201.1912.

Baraffe, I. et al. (2003). "Evolutionary models for cool brown dwarfs and extrasolar giant planets. The case of HD 209458". In: *A&A* 402, pp. 701–712. DOI: 10.1051/0004-6361:20030252. eprint: astro-ph/0302293.

Benneke, B. and S. Seager (2012). "Atmospheric Retrieval for Super-Earths: Uniquely Constraining the Atmospheric Composition with Transmission Spectroscopy". In: *ApJ* 753, 100, p. 100. DOI: 10.1088/0004-637X/753/2/100. arXiv: 1203.4018 [astro-ph.EP].

Blake, C. H., D. Charbonneau, and R. J. White (2010). "The NIRSPEC Ultracool Dwarf Radial Velocity Survey". In: *ApJ* 723, pp. 684–706. DOI: 10.1088/0004-637X/723/1/684. arXiv: 1008.3874 [astro-ph.SR].

Boogert, A. C. A., M. R. Hogerheijde, and G. A. Blake (2002). "High-Resolution 4.7 micron Keck/NIRSPEC Spectra of Protostars. I. Ices and Infalling Gas in the Disk of L1489 IRS". In: *ApJ* 568, pp. 761–770. DOI: 10.1086/338969. eprint: astro-ph/0112163.

Bowler, B. P. (2016). "Imaging Extrasolar Giant Planets". In: *PASP* 128.10, p. 102001. DOI: 10.1088/1538-3873/128/968/102001. arXiv: 1605.02731 [astro-ph.EP].

Brandt, T. D. et al. (2014). "A Statistical Analysis of SEEDS and Other High-contrast Exoplanet Surveys: Massive Planets or Low-mass Brown Dwarfs?" In: *ApJ* 794, 159, p. 159. DOI: 10.1088/0004-637X/794/2/159. arXiv: 1404.5335 [astro-ph.SR].

Burrows, A. et al. (1997). "A Nongray Theory of Extrasolar Giant Planets and Brown Dwarfs". In: *ApJ* 491, pp. 856–875. DOI: 10.1086/305002. eprint: astro-ph/9705201.

Canup, R. M. and W. R. Ward (2006). "A common mass scaling for satellite systems of gaseous planets". In: *Nature* 441, pp. 834–839. DOI: 10.1038/nature04860.

Chabrier, G. et al. (2014). "Giant Planet and Brown Dwarf Formation". In: *Protostars and Planets VI*, pp. 619–642. DOI: 10.2458/azu_uapress_9780816531240-ch027. arXiv: 1401.7559 [astro-ph.SR].

Cody, A. M. and L. A. Hillenbrand (2010). "Precision Photometric Monitoring of Very Low Mass σ Orionis Cluster Members: Variability and Rotation at a Few Myr". In: *ApJS* 191, pp. 389–422. DOI: 10.1088/0067-0049/191/2/389. arXiv: 1011.3539 [astro-ph.SR].

Correia, A. C. M. and J. Laskar (2001). "The four final rotation states of Venus". In: *Nature* 411, pp. 767–770. DOI: 10.1038/35081000.

Crossfield, I. J. M. (2014). "Doppler imaging of exoplanets and brown dwarfs". In: *A&A* 566, A130, A130. DOI: 10.1051/0004-6361/201423750. arXiv: 1404.7853 [astro-ph.SR].

Filippazzo, J. C. et al. (2015). "Fundamental Parameters and Spectral Energy Distributions of Young and Field Age Objects with Masses Spanning the Stellar to Planetary Regime". In: *ApJ* 810, 158, p. 158. DOI: 10.1088/0004-637X/810/2/158. arXiv: 1508.01767 [astro-ph.SR].

Gallet, F. and J. Bouvier (2013). "Improved angular momentum evolution model for solar-like stars". In: *A&A* 556, A36, A36. DOI: 10.1051/0004-6361/201321302. arXiv: 1306.2130 [astro-ph.SR].

Gauza, B. et al. (2015). "Discovery of a Young Planetary Mass Companion to the Nearby M Dwarf VHS J125601.92-125723.9". In: *ApJ* 804, 96, p. 96. DOI: 10.1088/0004-637X/804/2/96. arXiv: 1505.00806 [astro-ph.EP].

Gray, D. F. (2008). *The Observation and Analysis of Stellar Photospheres*, pp. 464–465.

Helled, R. et al. (2014). "Giant Planet Formation, Evolution, and Internal Structure". In: *Protostars and Planets VI*, pp. 643–665. DOI: 10.2458/azu_uapress_9780816531240-ch028. arXiv: 1311.1142 [astro-ph.EP].

Herbst, W. et al. (2002). "Stellar rotation and variability in the Orion Nebula Cluster". In: *A&A* 396, pp. 513–532. DOI: 10.1051/0004-6361:20021362.

Hughes, D. W. (2003). "Planetary spin". In: *Planet. Space Sci.* 51, pp. 517–523. DOI: 10.1016/S0032-0633(03)00035-7.

Husser, T.-O. et al. (2013). "A new extensive library of PHOENIX stellar atmospheres and synthetic spectra". In: *A&A* 553, A6, A6. DOI: 10.1051/0004-6361/201219058. arXiv: 1303.5632 [astro-ph.SR].

Ireland, M. J. et al. (2011). "Two Wide Planetary-mass Companions to Solar-type Stars in Upper Scorpius". In: *ApJ* 726, 113, p. 113. DOI: 10.1088/0004-637X/726/2/113. arXiv: 1011.2201 [astro-ph.SR].

Joergens, V. and E. Guenther (2001). "UVES spectra of young brown dwarfs in Cha I: Radial and rotational velocities". In: *A&A* 379, pp. L9–L12. DOI: 10.1051/0004-6361:20011337. eprint: astro-ph/0110175.

Kraus, A. L. et al. (2014). "Three Wide Planetary-mass Companions to FW Tau, ROXs 12, and ROXs 42B". In: *ApJ* 781, 20, p. 20. DOI: 10.1088/0004-637X/781/1/20. arXiv: 1311.7664 [astro-ph.EP].

Kurosawa, R., T. J. Harries, and S. P. Littlefair (2006). "Radial and rotational velocities of young brown dwarfs and very low-mass stars in the Upper Scorpius OB association and the ρ Ophiuchi cloud core". In: *MNRAS* 372, pp. 1879–1887. DOI: 10.1111/j.1365-2966.2006.11005.x. eprint: astro-ph/0609053.

Liu, M. C., T. J. Dupuy, and K. N. Allers (2016). "The Hawaii Infrared Parallax Program. II. Young Ultracool Field Dwarfs". In: *ApJ* 833, 96, p. 96. DOI: 10.3847/1538-4357/833/1/96. arXiv: 1612.02426 [astro-ph.SR].

Liu, M. C., E. A. Magnier, et al. (2013). "The Extremely Red, Young L Dwarf PSO J318.5338-22.8603: A Free-floating Planetary-mass Analog to Directly Imaged Young Gas-giant Planets". In: *ApJL* 777, L20, p. L20. DOI: 10.1088/2041-8205/777/2/L20. arXiv: 1310.0457 [astro-ph.EP].

Lodieu, N. et al. (2008). "Near-infrared cross-dispersed spectroscopy of brown dwarf candidates in the UpperSco association". In: *MNRAS* 383, pp. 1385–1396. DOI: 10.1111/j.1365-2966.2007.12676.x. arXiv: 0711.1109.

Metchev, S. A. et al. (2015). "Weather on Other Worlds. II. Survey Results: Spots are Ubiquitous on L and T Dwarfs". In: *ApJ* 799, 154, p. 154. DOI: 10.1088/0004-637X/799/2/154. arXiv: 1411.3051 [astro-ph.SR].

Mohanty, S., R. Jayawardhana, and G. Basri (2005). "The T Tauri Phase Down to Nearly Planetary Masses: Echelle Spectra of 82 Very Low Mass Stars and Brown Dwarfs". In: *ApJ* 626, pp. 498–522. DOI: 10.1086/429794. eprint: astro-ph/0502155.

Mohanty, S. and F. H. Shu (2008). "Magnetocentrifugally Driven Flows from Young Stars and Disks. VI. Accretion with a Multipole Stellar Field". In: *ApJ* 687, 1323-1338, pp. 1323–1338. DOI: 10.1086/591924. arXiv: 0806.4769.

Morbidelli, A. et al. (2012). "Explaining why the uranian satellites have equatorial prograde orbits despite the large planetary obliquity". In: *Icarus* 219, pp. 737–740. DOI: 10.1016/j.icarus.2012.03.025. arXiv: 1208.4685 [astro-ph.EP].

Quanz, S. P. et al. (2010). "Search for Very Low-Mass Brown Dwarfs and Free-Floating Planetary-Mass Objects in Taurus". In: *ApJ* 708, pp. 770–784. DOI: 10.1088/0004-637X/708/1/770. arXiv: 0911.1925 [astro-ph.SR].

Rice, E. L. et al. (2010). "Physical Properties of Young Brown Dwarfs and Very Low Mass Stars Inferred from High-resolution Model Spectra". In: *ApJS* 186, pp. 63–84. DOI: 10.1088/0067-0049/186/1/63. arXiv: 0911.3844 [astro-ph.SR].

Rothman, L. and I. Gordon (2010). "PASCAL - Planetary Atmospheres Spectral Catalog". In: *EGU General Assembly Conference Abstracts*. Vol. 12. EGU General Assembly Conference Abstracts, p. 5561.

Scholz, A. and J. Eislöffel (2005). "Rotation and variability of very low mass stars and brown dwarfs near ϵ Ori". In: *A&A* 429, pp. 1007–1023. DOI: 10.1051/0004-6361:20041932. eprint: astro-ph/0410101.

Scholz, A., V. Kostov, et al. (2015). "Rotation Periods of Young Brown Dwarfs: K2 Survey in Upper Scorpius". In: *ApJL* 809, L29, p. L29. DOI: 10.1088/2041-8205/809/2/L29. arXiv: 1506.06771 [astro-ph.SR].

Schwarz, H. et al. (2016). "The slow spin of the young substellar companion GQ Lupi b and its orbital configuration". In: *A&A* 593, A74, A74. DOI: 10.1051/0004-6361/201628908. arXiv: 1607.00012 [astro-ph.EP].

Snellen, I. A. G. et al. (2014). "Fast spin of the young extrasolar planet β Pictoris b". In: *Nature* 509, pp. 63–65. DOI: 10.1038/nature13253.

Szulágyi, J., L. Mayer, and T. Quinn (2017). "Circumplanetary discs around young giant planets: a comparison between core-accretion and disc instability". In: *MNRAS* 464, pp. 3158–3168. DOI: 10.1093/mnras/stw2617. arXiv: 1610.01791 [astro-ph.EP].

Takata, T. and D. J. Stevenson (1996). "Despin Mechanism for Protogiant Planets and Ionization State of Protogiant Planetary Disks". In: *Icarus* 123, pp. 404–421. DOI: 10.1006/icar.1996.0167.

Tennyson, J. and S. N. Yurchenko (2012). "ExoMol: molecular line lists for exoplanet and other atmospheres". In: *MNRAS* 425, pp. 21–33. DOI: 10.1111/j.1365-2966.2012.21440.x. arXiv: 1204.0124 [astro-ph.EP].

Valenti, J. A., R. P. Butler, and G. W. Marcy (1995). "Determining Spectrometer Instrumental Profiles Using FTS Reference Spectra". In: *PASP* 107, p. 966. DOI: 10.1086/133645.

White, R. J. and G. Basri (2003). "Very Low Mass Stars and Brown Dwarfs in Taurus-Auriga". In: *ApJ* 582, pp. 1109–1122. DOI: 10.1086/344673. eprint: astro-ph/0209164.

Wright, J. T. and J. D. Eastman (2014). "Barycentric Corrections at 1 cm s^{-1} for Precise Doppler Velocities". In: *PASP* 126, p. 838. DOI: 10.1086/678541. arXiv: 1409.4774 [astro-ph.IM].

Zapatero Osorio, M. R. et al. (2006). "Spectroscopic Rotational Velocities of Brown Dwarfs". In: *ApJ* 647, pp. 1405–1412. DOI: 10.1086/505484. eprint: astro-ph/0603194.

Zhou, Y. et al. (2016). "Discovery of Rotational Modulations in the Planetary-mass Companion 2M1207b: Intermediate Rotation Period and Heterogeneous Clouds in a Low Gravity Atmosphere". In: *ApJ* 818, 176, p. 176. DOI: 10.3847/0004-637X/818/2/176. arXiv: 1512.02706 [astro-ph.EP].

Chapter 5

THE CORRELATION BETWEEN GAS GIANT PLANETS AND SUPER-EARTH FORMATION

5.1 Abstract

We use radial velocity observations to search for massive, long-period gas giant companions in 65 systems hosting inner super-Earth ($1-4$ $R_\oplus$, $1-10$ $M_\oplus$) planets in order to constrain formation and migration scenarios for this population. We consistently re-fit all published radial velocity datasets for these stars and find 10 systems with statistically significant trends indicating the presence of an outer companion. We combine these radial velocity data with AO images in order to constrain the allowed masses and semi-major axes of these companions. We quantify our sensitivity to the presence of long period companions in these system by fitting the sample with a power law distribution and find an estimated occurrence rate of $39\pm7\%$ for companions between $0.5-20$ $M_{\rm Jup}$ and $1-20$ AU. Half of our systems were discovered by the transit method and the other half were discovered by the RV method. While differences in RV baselines and number of data points between the two samples lead to different sensitivities to distant companions, we find that the occurrence rates of gas giant companions in each sample is consistent at the 0.5σ level. A quantitative comparison to previous determinations of the frequency of Jupiter analogs indicates that the occurrence rate of Jupiter analogs in super-Earth systems appears to be higher than the occurrence rate of gas giant planets around field stars. We conclude that the presence of outer gas giant planets does not suppress the formation of inner super-Earths, and may instead facilitate their formation. The presence of these outer companions also places an upper limit on the distance super-Earths in these systems might have migrated from their formation locations, as well as the range of migration the gas giant companions could have experienced.

5.2 Introduction

The presence or absence of outer gas giant planets can significantly influence the formation and evolution of planets on interior orbits. In our own solar system, Jupiter is thought to have played a key role in dynamically re-shaping the outer solar system architecture after the dissipation of the gas disk (Tsiganis et al., 2005),

driving volatile-rich planetesimals from beyond the ice line onto shorter-period orbits (Morbidelli, Lunine, et al., 2012; Raymond, 2006; O'Brien, Morbidelli, and Levison, 2006; Raymond and Izidoro, 2017). At earlier times, the gap in the gas disk created by Jupiter's presence would also have suppressed the flow of solid materials into the inner disk where the terrestrial planets subsequently formed affecting both the surface density of solids in the inner disk and also the compositions of those solids (Lambrechts, Johansen, and Morbidelli, 2014; Morbidelli, Bitsch, et al., 2016; Morbidelli, Lunine, et al., 2012; Desch, Kalyaan, and Alexander, 2017; Morbidelli and Crida, 2007). It has even been theorized that an in-and-then-out-again migration by Jupiter and Saturn (Walsh et al., 2011) might have disrupted planet formation in the inner several AU, therefore explaining why the solar system only hosts relatively small planets between $0.3 - 2$ AU and none interior to that (Batygin and Laughlin, 2015).

Given the dominant role that gas giant planets played in the early history of the solar system, it is natural to consider their possible influence in exoplanetary systems. Broadly speaking, there are several mechanisms by which outer gas giant planets can influence the formation and evolution of interior planets. Giant planets comparable to or larger than Saturn will open a gap in the gas disk (Lin and Papaloizou, 1986; Crida, Morbidelli, and F. Masset, 2006; Kley and Nelson, 2012), suppressing the flow of small solids ("pebbles") to the inner disk. Moriarty and D. Fischer (2015) find that the rate of planetesimal growth in the inner disk is sensitive to the rate at which pebbles drift radially inward, implying that systems with giant planets should have fewer and less massive planets in the inner region of the disk. However, the presence of a giant planet will also create local pressure maxima that collect solids, potentially sparking a secondary wave of planet formation (F. S. Masset et al., 2006; Hasegawa and Pudritz, 2011; Sato, Okuzumi, and Ida, 2016; Whipple, 1972; Morbidelli and Nesvorny, 2012; Rice et al., 2006).

Gas giants can also dynamically excite the population of planetesimals from which rocky planets are forming, increasing the likelihood that collisions will result in disruption rather than accretion (Walsh et al., 2011; Batygin and Laughlin, 2015). However, unless this process is followed by that material draining onto the host star, this dynamical excitation and disruption of material is not a barrier to rocky planet formation (Wallace, Tremaine, and Chambers, 2017). Dynamically hot outer gas giants can perturb inner planets onto eccentric and/or inclined orbits, reducing the multiplicity of planets in those systems (Pu and Lai, 2018; Hansen, 2017) or leading

to orbital instability within a few Myrs in some extreme cases (Huang, Petrovich, and Deibert, 2017).These same gas giants can also act as a barrier that prevents smaller planets formed in the outer disk (i.e., beyond the orbit of the gas giants) from migrating inward (Izidoro et al., 2015).

Even if they do not directly influence the formation or dynamical evolution of inner planetary systems, the presence of an outer gas giant planet is in and of itself a statement about the properties of the primordial disk. In the core accretion model (Pollack et al., 1996), cores must form before the disk gas dissipates in order to acquire massive envelopes. The well-established correlation between gas giant planet frequency and stellar metallicity for sun-like stars (D. A. Fischer and Valenti, 2005; Johnson et al., 2010) indicates that the core formation process occurs more readily in metal-rich disks (e.g. Dawson, E. Chiang, and Lee, 2015). The longer lifetime of disks around metal-rich stars also facilitates the formation of both gas giant planets (e.g. Yasui et al., 2010; Ercolano and Clarke, 2010) and those at lower masses (e.g. Buchhave, Bizzarro, et al., 2014; Petigura, Marcy, et al., 2018).

Despite the relative richness of theoretical work in this area, we currently have very few observational constraints on the role that outer gas giant planets play in determining the properties of inner planetary systems. This is largely due to the limited baselines of current surveys: both transit and radial velocity (RV) surveys typically require the observation of one or more complete orbits in order to count a given signal as a secure detection, but even the longest-running surveys have baselines that are shorter than the orbital periods of the solar system gas giants (Dressing and Charbonneau, 2015; Bryan et al., 2016; Rowan et al., 2016; Wittenmyer, Butler, et al., 2016; Cumming et al., 2008; Mayor, Marmier, et al., 2011; Howard, Marcy, Johnson, et al., 2010). Recently, several RV surveys (Wittenmyer, Butler, et al., 2016; Rowan et al., 2016) estimated the frequency of Jupiter analogs (defined as 0.3 - 13 M_{Jup} and 3 - 7 AU in Wittenmyer, Butler, et al. (2016) and 0.3 - 3 M_{Jup} and 3 - 6 AU in Rowan et al. (2016)), taking into account survey incompleteness at larger separations and smaller masses. Both surveys found the frequency of Jupiter analogs to be small; Wittenmyer, Butler, et al. (2016) found an occurrence rate of $6.2^{+2.8}_{-1.6}$%, while Rowan et al. (2016) found an occurrence rate of ~3%. However, neither of these surveys extended as far as Saturn's orbit, and relatively few of the stars in these two samples have known inner planets. Of the super-Earth systems examined in this study, we find that only three were included in the Wittenmyer, Butler, et al. (2016) sample, while Rowan et al. (2016) did not provide an explicit

list of the stars included in their survey.

If we are willing to consider planet candidates with partially observed orbits, we can extend the statistical reach of these surveys to larger orbital separations. This also allows us to consider systems with inner transiting planets, which typically have shorter photometric and radial velocity baselines (on the order of 1-5 years) (e.g. Marcy et al., 2014; Weiss and Marcy, 2014). While the Kepler mission is in principle sensitive to transiting gas giant planets in Jupiter-like orbits (Uehara et al., 2016; Foreman-Mackey et al., 2016), the transit probability for these planets is extremely low and a majority of the long period planet candidates reported to date do not have inner transiting companions. Alternatively, long-term radial velocity monitoring of systems with known inner planets can provide information on the frequency of outer companions regardless of whether or not they transit their host stars (e.g. Montet et al., 2014; Knutson et al., 2014; Bryan et al., 2016). Although our knowledge of the masses and orbital periods of these objects are incomplete, we can nonetheless search for correlations between inner planet properties and the presence or absence of an outer companion.

In previous studies we considered the frequency of outer companions in systems with transiting hot Jupiters (Knutson et al., 2014) and with inner gas giant planets spanning a range of orbital periods (Bryan et al., 2016). In this study we focus on stars known to host one or more super-Earth planets (defined as $1 - 4$ $R_\oplus$ or $1 - 10$ $M_\oplus$, depending on the detection method) located inside 0.5 AU. These planets dominate the observed population of planets orbiting nearby stars, with 30-50% of Sun-like stars hosting one or more super-Earths with orbital periods less than 100 days (Howard, Marcy, Johnson, et al., 2010; Fressin et al., 2013; Petigura, Howard, and Marcy, 2013; Zhu et al., 2018). We identify published RV data for a sample of 65 systems hosting inner super-Earths and use these data to search for long-period gas giant companions. In section 5.3 we describe our sample of systems. In section 5.4 we describe our fits to the RV data, identification of non-planetary sources of RV trends, our calculation of companion probability distributions, and our completeness estimations. Finally, in section 5.5 we discuss the occurrence rate of gas giant companions in our sample and implications of our results.

5.3 Observations

We collected published radial velocity (RV) data for systems with at least one confirmed super-Earth, where we define a super-Earth as a planet with either a

mass between $1 - 10$ $M_\oplus$ or a radius between $1 - 4$ $R_\oplus$, depending on the detection technique (Table 5.1). We exclude systems with fewer than ten data points and baselines shorter than 100 days, leaving us with 65 systems that meet these criteria (Figure 5.1). Of that sample, 33 systems host at least one super-Earth discovered using the transit method, and 32 systems host at least one super-Earth discovered using the RV method. 18 of these systems are single-planet systems, while the remaining 47 are multi-planet systems. 45 planets have both measured masses and radii, and thus measured densities. We provide a summary of the RV data used in this work in Table 5.1. We also include best-fit values for the RV acceleration from our orbital solution fitting as described in the following section.

Table 5.1: Sample of systems

Target	$M_\star$ ($M_\odot$)	[Fe/H]	N_{pl}	Disc. Method	N_{obs}	Baseline (days)	Trend (m s^{-1} yr^{-1})	RV Data Ref.
Kepler-93	0.91	-0.09	1	Transit	118	1892	**12.01±0.44**	1,2
Kepler-95	1.08	0.27	1	Transit	31	1078	$0.62^{+1.17}_{-1.13}$	2
Kepler-96	1.0	0.10	1	Transit	26	772	$-1.50^{+1.17}_{-1.10}$	2
Kepler-97	0.94	-0.16	1	Transit	20	789	$\mathbf{-4.49}^{+1.31}_{-1.35}$	2
Kepler-98	0.99	0.20	1	Transit	22	805	$2.34^{+2.15}_{-2.04}$	2
Kepler-99	0.79	0.18	1	Transit	21	792	$-2.96^{+1.35}_{-1.39}$	2
Kepler-21	1.41	-0.04	1	Transit	122	1756	0.73 ± 1.05	3,4
Kepler-22	0.97	-0.20	1	Transit	16	373	$0.84^{+3.13}_{-3.32}$	5
Kepler-407	1.0	0.41	1	Transit	17	750	**-156.59** ± 4.02	2
LHS 1140	0.15	-0.24	1	Transit	144	386	0.44 ± 1.68	6
Kepler-409	0.92	0.12	1	Transit	25	175	8.76 ± 6.21	2
Kepler-94	0.81	0.32	2	Transit	29	799	$28.11^{+18.62}_{-20.44}$	2
Kepler-103	1.09	0.13	2	Transit	19	736	2.70 ± 1.79	2
Kepler-109	1.04	-0.02	2	Transit	15	1092	$-2.59^{+2.48}_{-2.81}$	2
Kepler-113	0.75	0.13	2	Transit	24	833	0.15 ± 3.65	7
Kepler-131	1.02	0.19	2	Transit	20	742	$0.073^{+2.11}_{-2.19}$	2
Kepler-406	1.02	0.28	2	Transit	42	801	0.73 ± 1.10	2
Kepler-10	0.91	-0.11	2	Transit	148	510	$3.72^{+2.04}_{-1.97}$	8
Corot-7	0.91	0.03	2	Transit	109	357	10.95 ± 7.30	9
Corot-24	0.91	0.30	2	Transit	50	1154	**-10.95 ± 2.92**	10
Kepler-454	1.03	0.28	2	Transit	102	1901	$\mathbf{14.56}^{+0.58}_{-0.62}$	11
Kepler-100	1.08	0.10	3	Transit	49	1221	1.06 ± 0.80	2
Kepler-25	1.19	-0.05	3	Transit	62	828	$2.23^{+2.41}_{-2.30}$	2
Kepler-37	0.80	-0.25	3	Transit	33	862	0.26 ± 1.06	2
Kepler-68	1.08	0.14	3	Transit	64	1207	$1.68^{+0.77}_{0.803}$	2
K2-3	0.6	-0.32	3	Transit	72	103	$10.95^{+6.94}_{-7.67}$	12
Kepler-20	0.95	0.11	6	Transit	30	650	$-1.61^{+2.48}_{-2.56}$	13
K2-32	0.86	0.43	3	Transit	74	441	$2.41^{+2.04}_{-2.01}$	14
Kepler-106	1.0	-0.09	4	Transit	25	1074	-0.96 ± 1.3	2
Kepler-48	0.88	0.26	4	Transit	28	1135	$2.01^{+3.10}_{-3.32}$	2
Kepler-102	0.81	0.11	5	Transit	35	897	$1.06^{+1.13}_{-1.10}$	2
Kepler-62	0.69	-0.34	5	Transit	13	128	$60.2^{+42.0}_{-32.0}$	15
55 Cnc	0.91	0.31	5	RV	663	8476	$\mathbf{-0.42}^{+0.095}_{-0.099}$	16,17
61 Vir	0.94	-0.01	3	RV	643	3461	-0.27 ± 0.14	18, 19

Continued on next page

Table 5.1 – continued from previous page

Target	$M_\star$ ($M_\odot$)	[Fe/H]	$N_{planets}$	Discovery Method	N_{obs}	Baseline (days)	Trend (m s^{-1} yr^{-1})	RV Data Ref.
GJ 15A	0.38	-0.32	1	RV	349	6215	$-0.44^{+0.077}_{-73}$ 0.054	19, 20
GJ 176	0.45	-0.10	1	RV	167	5836	$-0.27^{+0.34}_{-0.35}$	19, 21
GJ 273	0.29	0.09	2	RV	354	6855	$\mathbf{1.2}^{+0.066}_{-0.062}$	19, 22
GJ 433	0.48	-0.22	1	RV	100	5476	$-0.22^{+0.22}_{-0.20}$	19,23
GJ 536	0.52	-0.08	1	RV	228	6128	-0.13 ± 0.10	19, 24
GJ 581	0.31	-0.25	3	RV	531	5139	$0.43^{+0.16}_{-0.15}$	19,25
GJ 667 C	0.33	-0.59	5	RV	238	4847	**1.79 ± 0.18**	19,26,27
GJ 3341	0.47	-0.09	1	RV	135	1456	0.27± 0.20	28
HD 215497	0.87	0.23	2	RV	99	1842	-0.24 ± 0.23	29
HD 156668	0.77	0.05	1	RV	527	4226	-0.15 ± 0.12	30
HD 20794	0.70	-0.40	4	RV	187	2610	$-0.044^{+0.047}_{-0.044}$	31
GJ 832	0.45	-0.30	2	RV	109	5569	$0.14^{+0.21}_{-0.22}$	32
HD 181433	0.78	0.33	3	RV	107	1757	$1.5^{+0.98}_{-2.9}$	33
HD 7924	0.83	-0.15	3	RV	906	4783	0.080 ± 0.051	34
GJ 3138	0.68	-0.30	3	RV	199	2932	$0.20^{+0.12}_{-0.13}$	22
GJ 3323	0.16	-0.27	2	RV	142	4333	0.12 ± 0.11	22
HD 1461	1.02	0.19	2	RV	921	6310	$-0.055^{+0.16}_{-0.15}$	19, 35
Proxima Cen	0.12	0.14	1	RV	144	4325	$-0.13^{+0.10}_{-0.095}$	36
HD 3167	0.86	0.04	3	Transit	251	152	$\mathbf{9.96}^{+1.97}_{-2.04}$	37
GJ 3998	0.50	-0.16	2	RV	136	869	$-0.66^{+0.55}_{-0.51}$	38
GJ 876	0.33	0.05	4	RV	389	6074	1.0 ± 0.38	19,39
GJ 3293	0.42	0.02	4	RV	205	2311	-0.11 ± 0.11	22
HD 40307	0.77	-0.31	5	RV	226	3811	0.55 ± 0.040	35
HD 175607	0.71	-0.62	1	RV	110	3390	$0.13^{+0.11}_{-0.12}$	40
GJ 163	0.4	-0.01	3	RV	153	3068	-0.12 ±0.16	41
HD 219134	0.81	0.11	6	RV	992	4096	-0.45 ± 0.084	19,42
GJ 3634	0.45	-0.10	1	RV	54	460	$9.6^{+0.95}_{-1.0}$	43
HD 85512	0.69	-0.33	1	RV	185	2745	0.32 ± 0.051	26
GJ 676	0.71	0.23	4	RV	127	3231	**21.72 ± 0.47**	44
WASP-47	1.11	0.36	4	Transit	146	2340	$-1.31^{+1.28}_{-2.26}$	45, 46, 47
Wolf 1061	0.29	-0.09	3	RV	187	4136	$0.037^{+0.058}_{-0.055}$	22

Notes. References: (1) Dressing, Charbonneau, et al. (2015), (2) Marcy et al. (2014), (3) López-Morales et al. (2016), (4) Howell et al. (2012), (5) Borucki, Koch, et al. (2012), (6) Dittmann et al. (2017), (7) Berta-Thompson et al. (2015), (8) Dumusque et al. (2014), (9) Queloz et al. (2009), (10) Alonso et al. (2014), (11) Gettel et al. (2016), (12) Almenara et al. (2015), (13) Gautier et al. (2012), (14) Petigura, Sinukoff, et al. (2017), (15) Borucki, Agol, et al. (2013), (16) Endl et al. (2012), (17) D. A. Fischer, Marcy, et al. (2008), (18) Vogt, Wittenmyer, et al. (2010), (19) Butler et al. (2017), (20) Howard, Marcy, D. A. Fischer, et al. (2014), (21) Forveille et al. (2009), (22) Astudillo-Defru, Forveille, et al. (2017), (23) Delfosse et al. (2013), (24) Suárez Mascareño et al. (2017), (25) Mayor, Bonfils, et al. (2009), (26) Anglada-Escudé, Tuomi, et al. (2013), (27) Anglada-Escudé, Arriagada, et al. (2012), (28) Astudillo-Defru, Bonfils, et al. (2015), (29) Lo Curto et al. (2010), (30) Bryan et al. (2016), (31) Pepe et al. (2011), (32) Wittenmyer, Tuomi, et al. (2014), (33) Bouchy et al. (2009), (34) Fulton, Weiss, et al. (2015), (35) Diaz et al. (2016), (36) Anglada-Escudé, Amado, et al. (2016), (37) Christiansen et al. (2017), (38) Affer et al. (2016), (39) Correia et al. (2010), (40) Mortier et al. (2016), (41) Bonfils, Lo Curto, et al. (2013), (42) Gillon et al. (2017), (43) Bonfils, Gillon, et al. (2011), (44) Anglada-Escudé and Tuomi (2012), (45) Sinukoff et al. (2017), (46) Neveu-VanMalle et al. (2016), (47) Dai et al. (2015). For all Kepler systems the stellar metallicities were taken from Petigura, Howard, Marcy, et al. (2017). For all other systems, listed metallicities were obtained from the RV references cited, except for systems: Corot-7, GJ 581, and Proxima Cen, whose metallicities were taken from Léger et al. (2009), Bonfils, Delfosse, et al. (2005), and Schlaufman and Laughlin (2010) respectively.

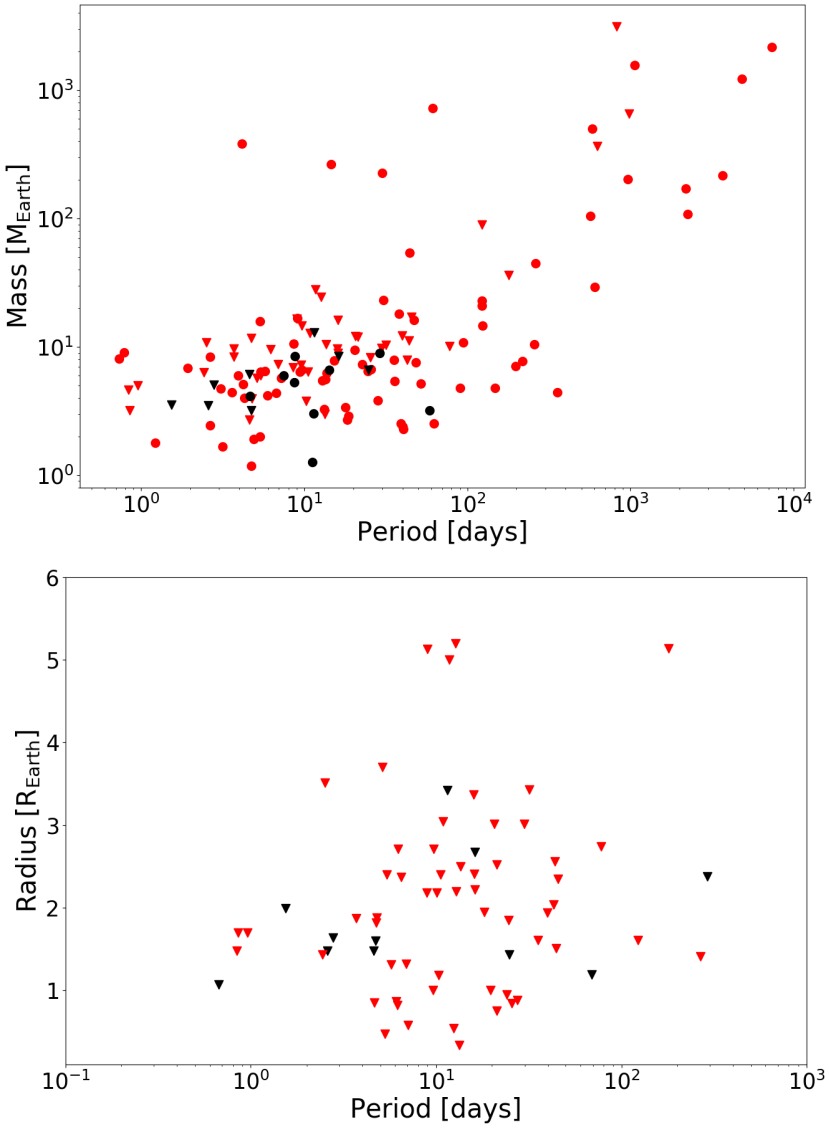

Figure 5.1: Confirmed resolved planets for our sample of 65 super-Earth systems. We show the planets with measured masses as a function of period on the top, and planets with measured radii on the bottom. Systems discovered using the transit method are shown as filled triangles, while systems discovered by the RV method are shown as filled circles. Planets in multi-planet systems are plotted in red, while single planets are plotted in black.

5.4 Analysis

RV Fitting

The presence of a distant companion manifests as a long term trend in the RV data when the orbital period of the companion is significantly longer than the RV baseline. In order to quantify the significance of these long-term trends, we simultaneously fit for the orbits of the known inner planets as well as a linear trend in each dataset using RadVel (Fulton, Petigura, et al., 2018). After identifying the best-fit solution for each data set, we next carry out a Markov Chain Monte Carlo (MCMC) exploration of the parameter space to determine the uncertainties on each model parameter. For a system with a single known planet, our model has eight free parameters including six orbital parameters (the planet's velocity semi-amplitude, orbital period, eccentricity, argument of periastron, true anomaly, and an RV zero point), a linear velocity trend, and stellar jitter.

We fit using the basis $[P, T_c, \sqrt{e}\sin\omega, \sqrt{e}\cos\omega, K]$ and impose flat priors on all of these orbital elements. For the planets that transit, we apply Gaussian priors centered on the orbital period and time of conjunction values derived from the transit data with a width equal to the measured uncertainties on these values. In cases where we include data from multiple telescopes or where the HIRES data include observations taken prior to the 2004 detector upgrade (Vogt, Butler, et al., 2005; Bryan et al., 2016), we fit a separate RV zero point and jitter value for each dataset. We also bin each set of radial velocity data in two-hour increments, binning datasets from different telescopes separately. We define our likelihood function in Equation 5.1, where σ_i is the instrumental error, σ_{jit} is the stellar jitter, v are the data, and m is the model.

$$\mathscr{L} = \prod_i \frac{1}{\sqrt{2\pi}\sqrt{\sigma_i^2 + \sigma_{jit}^2}} \exp\left(-0.5\left(\frac{(v_i - m_i)^2}{\sigma_i^2 + \sigma_{jit}^2}\right)\right) \tag{5.1}$$

We initialize each MCMC chain using the best-fit parameters from our fit. We note that for several systems we fit a different number of Keplerian orbits than the published number of planets (Table 5.1). Of the transiting planet systems, this includes Kepler-20 and Kepler-407. For Kepler-20 there are six published planets but we fit three Keplerian orbits, as three of the transiting planets did not yield statistically significant RV semi-amplitudes in previous studies (Gautier et al., 2012). For Kepler-407, there is one transiting planet and a long-term trend with curvature that was published as a planet detection, but we only fit a full Keplerian

orbit for the inner planet as the outer planet's orbital period is poorly constrained by the current RV data (Marcy et al., 2014).

For the RV-detected planetary systems, we search for periodic signals in the radial velocity datasets using the automated planet search pipeline described in Fulton, Weiss, et al. (2015). We fit Keplerian orbits to all signals with empirical false alarm probabilities (eFAP) less than or equal to 1% and K greater than or equal to 1.0 m/s in our final RV analysis. For systems GJ 667, GJ 876, HD 40307, and GJ 676, we find that we are only able to recover a subset of the previously published planets, and fit for 3, 3, 4, and 3 planetary orbits, respectively in these systems.

For GJ 3341, HD 156668, HD 175607, and GJ 163 we find additional periodic signals with eFAP$\leq$1% that do not correspond to the periods of the confirmed planets in these systems and may be due to either stellar activity or additional unconfirmed planetary companions. We determine whether to include these additional periodic signals by comparing model fits with and without these additional signals using the Bayesian Information Criterion (BIC). The BIC is defined as: $\mathrm{BIC} = -2L + k \ln n$, where L is the log likelihood of a model fit, k is the number of free parameters in the model, and n is the number of data points. In this case, the preferred model is the one with the lowest BIC value. If the BIC value for the model with additional periodic signals is smaller than the BIC value for the model without the additional periodic signals by at least 10 (a reasonable rule of thumb for statistically significant improvements in fit; Kass & Rafferty (1995)), we consider the model with additional period signals to be a better fit, and include these signals in subsequent analyses.

For GJ 3341, using the automated planet search pipeline we recover the known 14.2 day period planet and also detect a second signal with a period of 202 days and an amplitude of 2.0 m/s (eFAP = 1%). When we compare BIC values between model fits to the RV data with and without this 202 day signal, we find that the BIC value for the model with the additional periodic signal is not smaller than the BIC value for the model without the additional periodic signal by at least 10. We therefore do not include this additional periodic signal in the RV model fits to the data.

For HD 156668, the known planet with a period of 4.6 days is easily detected by our automated pipeline. We also detect a second signal at a period of 808 days with an amplitude of 2.9 m/s and a very low false alarm probability. This appears to be a promising planet candidate but will require additional vetting in order to assess its planetary nature. When comparing model fits, we find that $\Delta\mathrm{BIC} > 10$ between the model without the additional signal and the model with the additional signal, and

thus include this 808 day signal in our RV model fits.

For HD 175607, which has a known planet with an orbital period of 29 days, we detect a second signal with an eFAP of 0.5% and a period of 707 days. However, this period is very close to two years and has poor phase coverage as a result. We also see a third peak in the periodigram at double this period (~1400 days), indicating that there is some ambiguity in the true period of this signal. When comparing model fits, we find that ΔBIC > 10 between the model without the additional signal and the model with the additional signal, and thus include this 707 day signal in our RV model fits. We note however that this additional signal will likely require additional RV observations to confirm or disprove its planetary nature.

Finally, for GJ 163 we detect signals corresponding to the three previously confirmed planets as well as two additional signals at periods of 108 and 19 days. Previous studies of these systems (Bonfils, Lo Curto, et al., 2013) have identified these two signals as potential planet candidates. We find that a model including these additional signals is a significantly better fit to the RV data than a model that does not include these signals (ΔBIC > 10), so we include all five signals in our RV analysis.

After fitting our model to each data set, we search for systems with statistically significant linear trends (defined here as fits where the linear slope differs from zero by more than 3σ). We list the best-fit trend values from the maximum-likelihood fit for each system in Table 5.1, with corresponding uncertainties determined from the MCMC chains. We find that 15 of the 65 systems in our sample have statistically significant trends.

In addition to long term trends, we also find that nine systems have fully resolved outer gas giant companions (>0.5 M_{Jup}). We select this lower mass limit definition when considering gas giant companions because 0.5 M_{Jup} is approximately the minimum mass needed to open a gap in a protoplanetary disk. We include outer gas giant companions if they are outside other planets in the system that are below the 0.5 M_{Jup} threshold. All of the outer gas giant companions in these systems are outside 1 AU. We list the properties of these previously confirmed outer gas giant planets in Table 5.2.

AO Imaging

For the systems with statistically significant trends, we obtained AO imaging data to determine whether these systems had stellar companions that might have caused

Table 5.2: Resolved Outer Gas Giant Companion Properties

Companion	Mass (M_{Jup})	Semi-major Axis (AU)
Kepler 94 c	9.8	1.6
Kepler 454 c	4.5	1.2
Kepler 68 d	0.8	1.5
Kepler 48 e	2.1	1.9
55 Cnc d	3.9	5.5
GJ 832 b	0.7	3.6
HD 181433 c	0.6	1.8
HD 181433 d	0.5	3.0
GJ 676 c	6.8	6.6
GJ 676 b	5.0	1.8
WASP 47 c	1.6	1.4

the observed trend. We identified published AO images (Furlan et al., 2017; Alonso et al., 2014; Ngo, Knutson, Bryan, et al., 2017; Howard, Marcy, D. A. Fischer, et al., 2014; Rodriguez et al., 2015; Christiansen et al., 2017; Tanner, Gelino, and Law, 2010; Sahlmann et al., 2016) for all but three of these systems. Of the remaining three systems, two (HD 40307 and HD 85512) had unpublished archival data obtained with the NACO instrument (Lenzen et al., 2003; Rousset et al., 2003) on the Very Large Telescope (VLT). The HD 40307 data were taken in Ks-band with a total integration time of 1.1 hr (ID: 088.C-0832(A), PI: Loehne). The HD 85512 data were obtained in Ks-band with a total integration time of 9 minutes (ID: 090.C-0125(A), PI: Mugrauer). Both datasets were obtained without a coronagraph, using a 4-point dither pattern.

We downloaded the data for both stars from the ESO archive and processed them using the pipeline outlined in Meshkat et al. (2014). We did not detect any stellar companions in either of these datasets. We show 5σ Ks contrast values for both systems in Table 5.3.

For the remaining system (GJ 3634), we obtained K_c-band AO images using NIRC2 at Keck on UT Feb 5 2018 with an effective integration time of 9 seconds and a three-point dither pattern. We identified a close pair of candidate companions at a separation of $1''.8$ and used a multi-peak point spread function (PSF) to simultaneously fit GJ 3634 and the two candidate companions in each frame where the companion is resolved. We constructed the PSF as a sum of Moffat and Gaussian functions and fit over a circular aperture of 10 pixels in radius, corresponding to twice the full width at half maximum (FWHM) of the PSF as described in Ngo, Knutson, Hinkley, et al. (2015).

We next integrated the best-fit PSFs for GJ 3634 and its candidate companions

Table 5.3: 5σ Contrast Curves

System	Separation (arcsec)	5σ Contrast (mag)
	1.90	10.87
	2.99	11.72
	4.07	11.45
	5.16	11.91
	6.24	11.90
	7.33	12.06
	8.42	12.63
	9.50	12.66
HD 85512	0.79	4.41
	1.28	6.95
	1.76	7.40
	2.25	8.06
	2.74	8.68
	3.23	9.34
	3.69	9.95
	4.18	9.44
	4.67	10.07
GJ 3634	0.09	0.014
	0.22	3.92
	0.35	4.81
	0.49	5.24
	0.63	6.18
	0.77	6.71
	0.91	6.92
	1.05	7.15
	1.18	7.11
	1.32	7.18
	1.46	7.20
	1.60	7.11
	1.74	7.14
	1.88	7.05
	2.02	7.05
	2.16	7.05
	2.30	7.10
	2.43	7.05
	2.57	7.04
	2.71	7.11
	2.85	7.05
	2.99	7.13
	3.13	7.06
	3.26	7.01

over the same aperture to determine their flux ratios. We similarly measured the companion separation and position angle by calculating the difference between the centroids of each star. We then applied the NIRC2 astrometric corrections from Service et al. (2016) to compensate for the NIRC2 array's distortion and rotation. We find that the easternmost candidate companion (labeled as cc1 in Figure 5.2) has a flux ratio of 116, corresponding to $\Delta K_c = 5.16$. This companion is separated from GJ 3634 by $1''.778 \pm 0''.002$ at a position angle of $177.37° \pm 0.04°$ east of north. For the western candidate companion (cc2), we measure a flux ratio of 75 ± 8, corresponding to $\Delta K_c = 4.7 \pm 0.1$. This companion is separated from GJ 3634 by $1''.860 \pm 0.''002$ at a position angle of $203.40° \pm 0.05°$ east of north. We calculate our uncertainties as the quadrature sum of measurement uncertainties and the uncertainty in the distortion solution. However, for cc1 in one of the three frames the companion did not have a regular PSF shape and as a result we were unable to fit for its peak and location. Since we do not have enough frames for cc1 to calculate a measurement uncertainty, we only report the astrometric distortion solution uncertainties.

For each companion in GJ 3634, we determine stellar masses using PHOENIX spectral models and the Baraffe et al. (1998) zero age main sequence models. We first select a PHOENIX model for the primary star based on the published stellar properties and then determine the companion's effective temperature by identifying the PHOENIX model that most closely matches the observed flux ratio. For each PHOENIX model, we determine the corresponding stellar mass and radius using the Baraffe et al. models. For both companions, we find best-fit masses of 0.08 $M_\odot$. However, as we only have one epoch of data for this system, we are unable to determine whether or not these companions are bound to the primary. We note, however, that this is a high proper motion target (-582.8, -92.1 mas/yr) and follow-up astrometric measurements with just a one year baseline would easily determine whether these companions are bound.

We next consider whether or not the RV trends in these systems might plausibly be explained by the presence of a nearby stellar companion. Kepler-93, Kepler-97, Kepler-407, and GJ 3634 each have candidate stellar companions, meaning that these systems have one epoch of data showing nearby stars that could be either bound companions or distant background stars. GJ 15A and GJ 676 have confirmed stellar companions that have been shown to have the same proper motion as the primary. We calculate the minimum companion mass in each system needed to

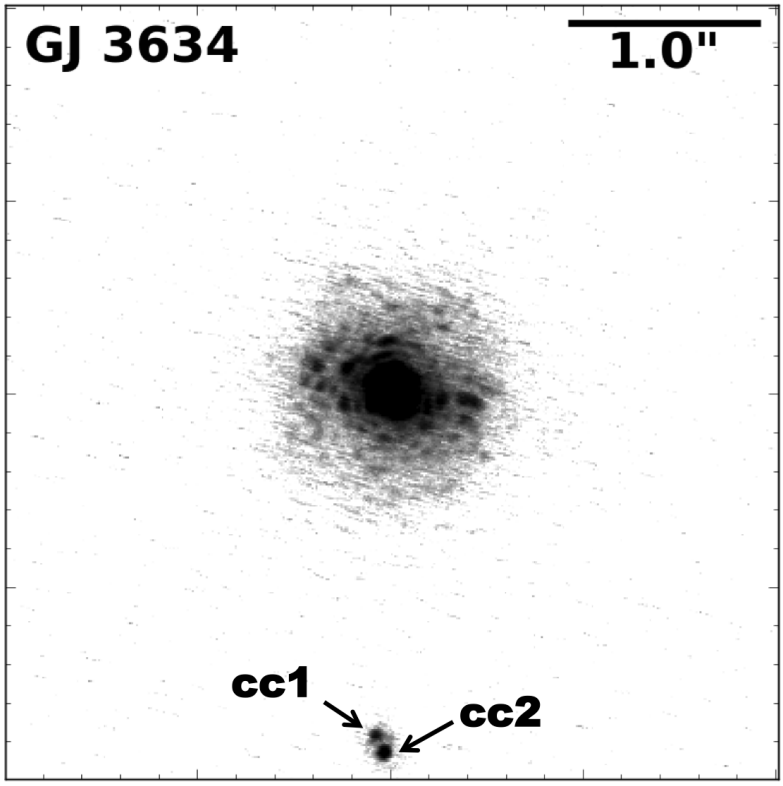

Figure 5.2: Reduced Keck/NIRC2 K_c-band image of GJ 3634 showing two candidate companions, labeled cc1 and cc2. Note the image is shown on a log scale, and is aligned with North corresponding to up and East corresponding to left.

explain the observed RV trend using the equation from Torres (1999):

$$M_{\rm comp} = 5.34 \times 10^{-6} M_{\odot} \left(\frac{d}{\rm pc} \frac{\rho}{\rm arcsec} \right)^2 \times \left| \frac{\dot{v}}{ms^{-1}yr^{-1}} \right| F(i, e, \omega, \phi). \tag{5.2}$$

In this equation, d is the distance to the star, ρ is the projected separation of the companion and the star on the sky, $\dot{v}$ is the radial velocity trend, and $F(i, e, \omega, \phi)$ is a variable that depends on the orbital parameters of the companion that are currently unconstrained. We use a value of $\sqrt{27}/2$ for F, as discussed in Liu et al. (2002). We then compare this minimum mass to the estimated mass of the candidate companion, which we calculate using the measured brightness ratio under the assumption that the candidate companion is located at the same distance as the primary star. We discuss our results for each individual system below.

Kepler-93 is 96.7 pc away and has a candidate companion with a projected separation of 2″.29 (Furlan et al., 2017). With an RV trend of 12.0 m s^{-1} yr^{-1}, this trend corresponds to a minimum companion mass of 8.2 $M_{\odot}$. We estimate the mass of the

candidate companion using its measured magnitude $M_K = 5.35$ and assuming an age of 1 Gyr. We then use the Baraffe et al. (1998) models to calculate a corresponding mass of 0.57 $M_\odot$ for this companion. This mass is significantly smaller than the minimum mass needed to explain the RV trend, and we therefore conclude that this candidate companion cannot explain the observed RV trend and keep this system in our sample.

Kepler-97 is 414 pc away and has a candidate companion with a projected separation of 0″.385 (Furlan et al., 2017). With an RV trend of 4.5 m s^{-1} yr^{-1}, this trend corresponds to a minimum companion mass of 1.58 $M_\odot$. The candidate companion in this system has a magnitude $M_K = 6.28$, corresponding to an estimated companion mass of 0.4 $M_\odot$ using its estimated age of 8.4 Gyr. As this is smaller than the minimum mass needed to explain the RV trend, we leave this system in our sample.

Kepler-407 is 326 pc away and has a candidate companion with a projected separation of 2″.13 (Furlan et al., 2017). With an RV trend of -155.8 m s^{-1} yr^{-1}, this trend corresponds to a minimum companion mass of 1045 $M_\odot$. Given the companion's measured magnitude of $M_K = 7.0$ and using its estimated age of 7.5 Gyr, the estimated companion mass is 0.3 $M_\odot$. This is several orders of magnitude smaller than would be required in order to explain the observed RV trend, and we therefore leave this system in the sample.

GJ 3634 is 19.8 pc away and has two candidate companions in what appears to be a hierarchical triple system, as discussed above. These two companions are 1″.83 away from GJ 3634 and have a mutual separation of 0.087″. The measured RV trend in this system is 9.6 m s^{-1} yr^{-1}, corresponding to a minimum companion mass of 0.018 $M_\odot$. As discussed earlier, both companions have estimated masses of 0.08 $M_\odot$, indicating that their combined mass could be responsible for the observed RV trend. We thus remove this system from our sample in subsequent analyses. We note that the RV trend in this system was previously published in Bonfils, Gillon, et al. (2011). Given their trend, they estimate a minimum mass of 32 $M_\oplus$ and a minimum period of 200 days. Our AO image is the first to indicate that this trend might be due to the presence of stellar/brown dwarf companions rather than a distant orbiting planet.

GJ 15A is 3.6 pc away and has a confirmed stellar companion with a projected separation of 20″.28 (Howard, Marcy, D. A. Fischer, et al., 2014). With an RV trend of -0.44 m s^{-1} yr^{-1}, this corresponds to a minimum companion mass of 0.074 $M_\odot$. The stellar companion in this system has an absolute magnitude of $M_K = 8.17$,

corresponding to an estimated companion mass of 0.175 $M_\odot$ for an age of 1 Gyr. As this estimated companion mass is larger than the minimum companion mass needed to account for the trend, we exclude this system from our subsequent analysis.

Finally, GJ 676 is 15.9 pc away (Gaia Collaboration, Prusti, et al., 2016; Gaia Collaboration, Brown, et al., 2016) and has a confirmed stellar companion at a separation of 47″. We note that this distance has been updated with a Gaia parallax, and is the only one of these systems with confirmed or candidate stellar companions to have an updated distance from Gaia. With an RV trend of 21.6 m s^{-1} yr^{-1}, this trend corresponds to a minimum companion mass of 167 $M_\odot$. Given an absolute magnitude of M_K = 6.9, the estimated companion mass is 0.3 $M_\odot$ assuming an age of of 1 Gyr. Since this estimated companion mass is well below the minimum mass to account for the observed RV trend, we conclude this companion could not be producing the observed trend and leave this system in our sample.

Trends Due to Stellar Activity

We next consider whether any of the observed trends might be due to stellar activity. We examined each system in order to determine if the measured RV trend exhibits a correlation with the star's emission in Ca II H & K lines as quantified by either the S_{HK} index or logR' (Wright et al., 2004; Isaacson and D. Fischer, 2010). We calculated the Spearman-Rank correlation coefficients between the RV data and this activity indicator after subtracting the orbital solutions for the confirmed inner planets. We considered a correlation coefficient with an absolute value greater than 0.3 to indicate a significant correlation. We find that systems HD 219134, HD 40307, and HD 85512 have significant correlations between stellar activity and the observed RV trend, and remove these system from our subsequent analysis. We also remove HD 1461 from our analysis, as we determined in Bryan et al. (2016) that this system has a fully resolved long period signal that is significantly correlated with stellar activity.

There were three systems with RV trends for which we were not able to obtain stellar activity data, including Corot-24, 55 Cnc, and GJ 3634. We conclude that stellar activity is unlikely to be the cause of the trend in Corot-24, as the amplitude of the observed trend is higher than would be expected for stellar activity signals, and is similarly unlikely to be the cause of the trend in 55 Cnc, as the baseline of this trend is longer than would be expected for most activity cycles without turnover (Isaacson and D. Fischer, 2010; Lovis et al., 2011). Although we cannot determine whether

or not the observed RV trend in the GJ 3634 might be due to stellar activity, we have already removed this system from further analysis due to the presence of candidate stellar companions that could have caused the observed trend.

After removing systems with either stellar or potentially activity-related sources of RV trends, including HD 219134, HD 85512, HD 40307, HD 1461, GJ 15A, and GJ 3634, we are left with ten systems with statistically significant trends that can plausibly be attributed to the presence of a substellar companion. We plot the RV data for each of these systems after subtracting the orbital solutions for the confirmed inner planets in Figures 5.3 and 5.4. Trends for GJ 273 (Astudillo-Defru, Forveille, et al., 2017), GJ 667C (Anglada-Escudé, Arriagada, et al., 2012), GJ 676 (Anglada-Escudé and Tuomi, 2012), Kepler-93 (Dressing, Charbonneau, et al., 2015; Marcy et al., 2014), Kepler-97 (Marcy et al., 2014), Kepler-407 (Marcy et al., 2014), and Kepler-454 (Dressing, Charbonneau, et al., 2015) were previously reported in the published literature.

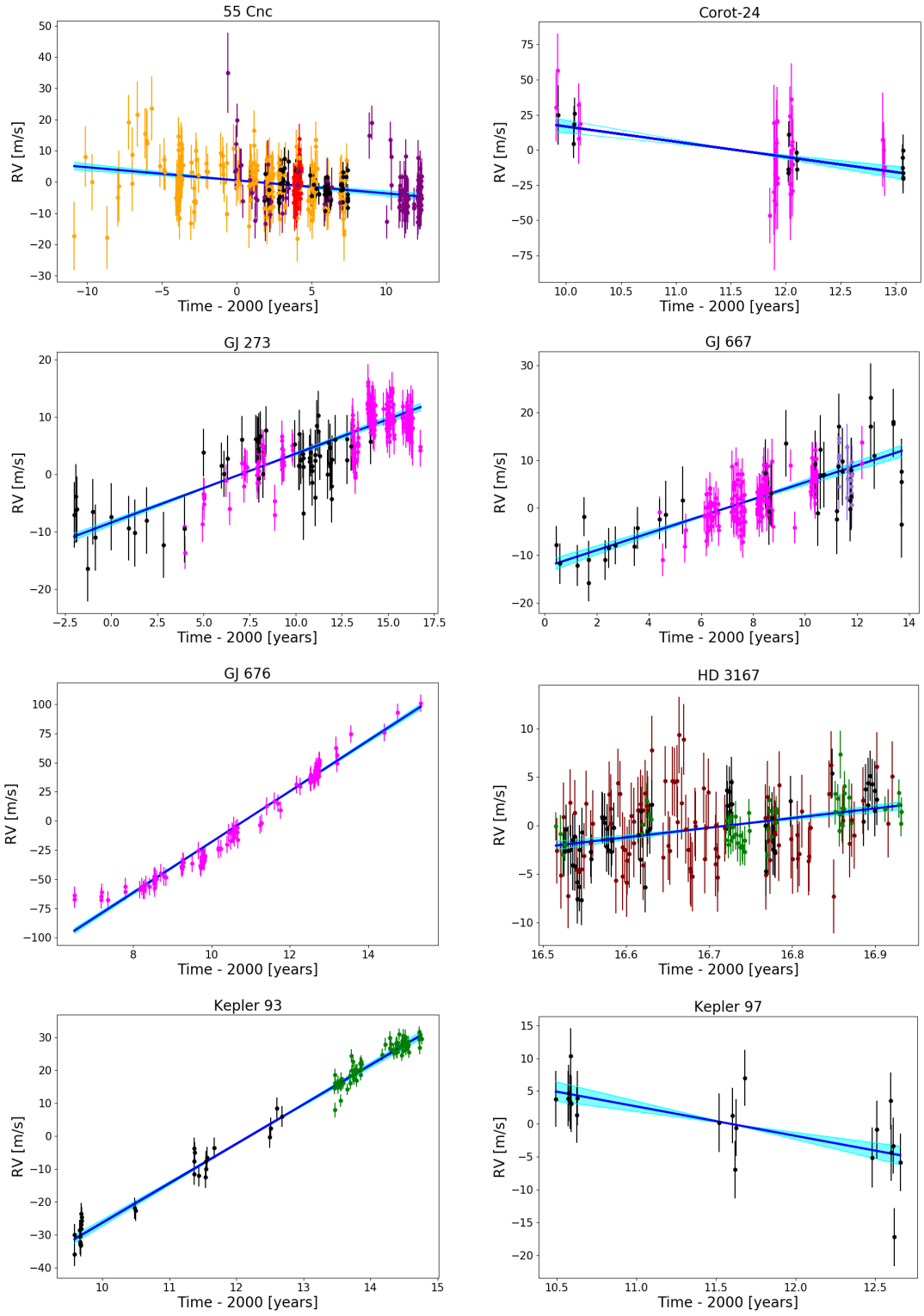

Figure 5.3: Best fit accelerations to the radial velocity data with a 3σ trend. The best fit trend is shown as a solid blue line, the 1σ errors on the slope are presented light blue shaded regions. The different colored data points represent RVs taken using different telescopes: black = HIRES, green = HARPS-N, pink = HARPS, orange = Lick, red = HET, purple = HJST, light purple = PFS, maroon = APF. Note that GJ 676 has a curved trend, which allows us to place much tighter constraints on the mass and separation of the companion producing that trend.

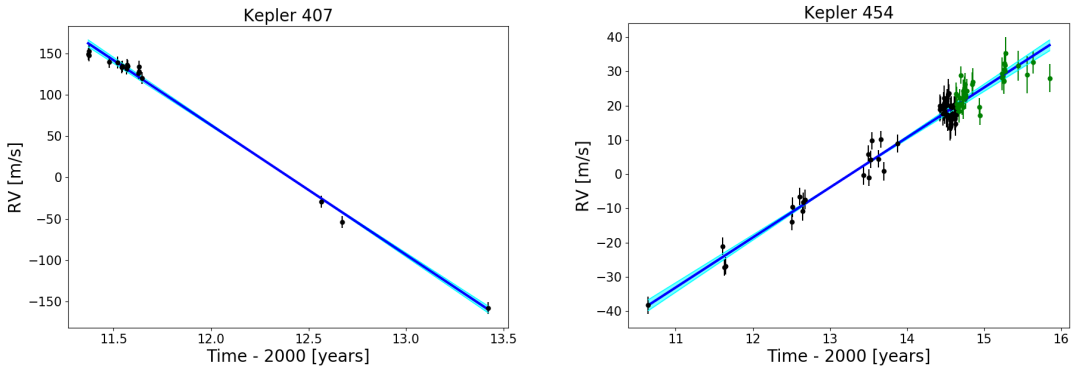

Figure 5.4: Best fit accelerations to the radial velocity data with a 3σ trend. The best fit trend is shown as a solid blue line, the 1σ errors on the slope are presented light blue shaded regions. The different colored data points represent RVs taken using different telescopes: black = HIRES, green = HARPS-N, pink = HARPS, orange = Lick, red = HET, purple = HJST, light purple = PFS, maroon = APF. Note that GJ 676 has a curved trend, which allows us to place much tighter constraints on the mass and separation of the companion producing that trend.

Constraints on Companion Masses and Orbital Semi-Major Axes

We use the RV data to place constraints on the masses and semi-major axes of the long period companions in each system. The duration and shape of the RV trend places a lower limit on the companion's mass and separation, while the lack of a detection in our AO imaging data places a corresponding upper limit on these quantities. As described in Bryan et al. (2016), we calculate two-dimensional probability distributions for each companion using an equally spaced 50×50 grid in logarithmic mass (true mass, not $m \sin i$), and logarithmic semi-major axis spanning a range of 0.3 - 500 M_{Jup} and 0.5 - 500 AU. In each grid cell we inject 500 simulated companions and determine whether or not they are consistent with the RV observations as follows. We first draw a set of orbital parameters for the confirmed inner planets from the previous MCMC fits, and then subtract away this orbital solution to preserve any long-term trend signal. We then draw a mass and semi-major axis value from within the grid box from a uniform distribution in log(M) and log(a), and draw an inclination from a uniform distribution in $\cos i$. We draw our eccentricity values from a beta distribution with $a = 1.12$ and $b = 3.09$, which are derived from a fit to the population of long-period gas giant planets from RV surveys (Kipping, 2013). Given a fixed semi-major axis, mass, and eccentricity for each simulated companion, we then fit for the remaining orbital parameters including time of periastron, argument of periastron, and a velocity zero point and calculate the corresponding log likelihood value of the best-fit solution.

After repeating this process five hundred times in each grid cell, we convert the resulting $50 \times 50 \times 500$ cube of log likelihood values to probabilities and marginalize over our 500 samples in each grid cell to yield a two-dimensional probability distribution in mass and semi-major axis for each system. We calculate two-dimensional probability distributions for all systems in our sample, regardless of whether or not they have statistically significant trends. The only difference between those systems with and without trends is that we use our AO imaging data to place an upper limit on the companion mass and semi-major axis in the trend systems as discussed in Bryan et al. (2016). Figure 5.5 shows the posterior distributions for the ten systems with 3σ trends, while Table 5.4 indicates the corresponding 1σ limits in mass and semi-major axis for each companion.

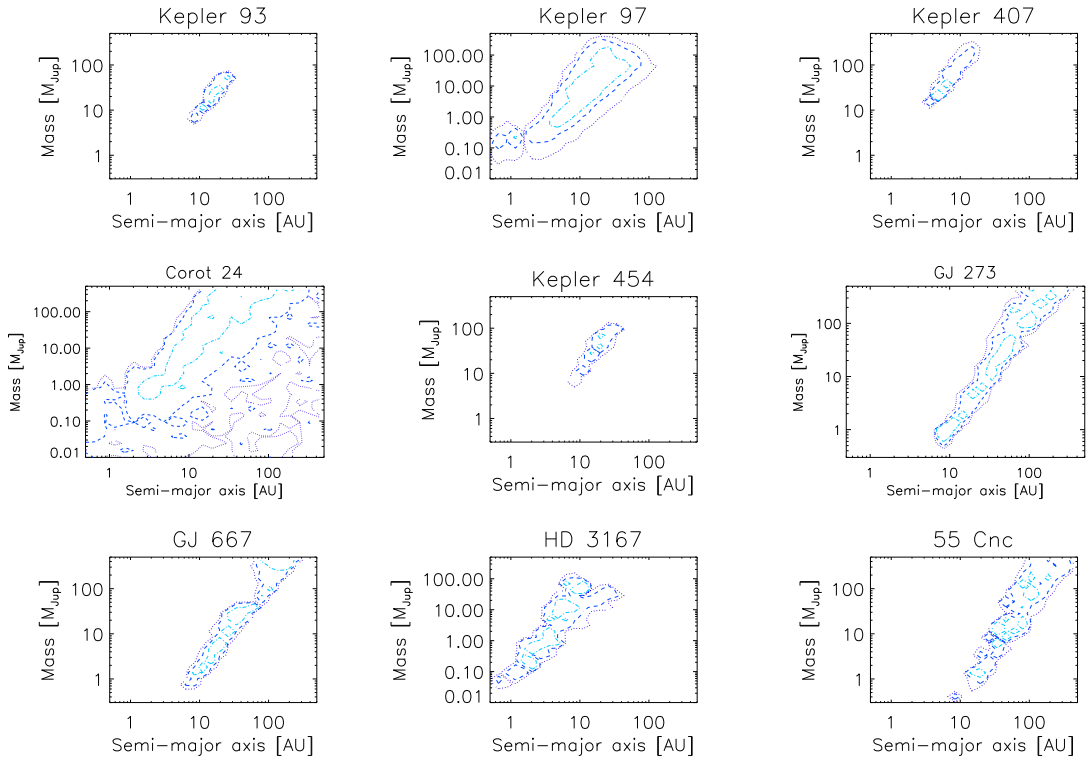

Figure 5.5: Probability distributions for the ten systems with statistically significant trends that are plausibly due to an orbiting substellar companion (i.e., they cannot be explained by either stellar activity or the presence of a distant stellar companion). The three contours define the 1σ, 2σ, and 3σ levels moving outward. We do not show the probability distribution for GJ 676 here, as the probability density is concentrated in just a few grid points and the contours are therefore unresolved.

Table 5.4: Constraints on Companion Properties

Companion	Mass (M_{Jup})	Semi-major Axis (AU)
Kepler 93 c	11.3 - 51.6	9.6 - 25.9
Kepler 97 c	0.18 - 166	1.2 - 60.3
Kepler 407 c	11.4 - 51.6	3.1 - 7.3
Corot 24 d	0.27 - 401	0.5 - 186
Kepler 454 d	7.2 - 81.3	9.6 - 29.8
55 Cnc g	1.0 - 369	15 - 377
GJ 273 d	0.55 - 430	7.3 - 214
GJ 667 h	1.2 - 430	8.4 - 214
HD 3167 e	0.05 - 85	0.8 - 22

Completeness Maps

We evaluate our sensitivity to distant companions in each system by calculating the completeness as a function of mass and orbital semi-major axis after taking into account the time baseline, number of data points, and measurement errors for each dataset. As before, we start with a 50×50 grid in mass and semi-major axis evenly spaced in log space from 0.3 - 500 M_{Jup} and 0.5 - 500 AU. For each grid box we inject 500 simulated companions where we draw a mass and semi-major axis from a uniformly spaced distribution across each grid box, an eccentricity value from the β distribution, inclination from a uniform distribution in $\cos i$, and the remaining orbital elements from uniform distributions. We then calculate the RV signal from this simulated companion at each observation epoch. We then add noise into these simulated RVs by drawn from a Gaussian distribution with a width defined by $\sqrt{\sigma_i^2 + \sigma_{\rm jit}^2}$, where σ_i is the instrumental uncertainty (randomly shuffled from the original dataset) and $\sigma_{\rm jit}$ is the stellar jitter estimated from the earlier MCMC fits. To assess whether a simulated planet would be detected, we fit each simulated set of RVs with a one-planet orbital solution, a linear trend, and a flat line. We compared these model fits using the Bayesian Information Criterion (BIC) (Kass & Rafferty 1995) in order to determine the simplest model that can provide an adequate fit to the data. If the BIC values for either the one-planet model fit or the linear trend were smaller than the BIC value for the flat line by at least 10, we concluded that the simulated planet would have been detected. However, if the flat line was preferred or the difference in BIC was less than 10, we counted this as a non-detection. We repeated this process for each simulated companion injected into each grid box, using our "detected/not detected" determinations to calculate the completeness over the entire grid.

Perhaps unsurprisingly, we find that the average sensitivity to companions in systems with super-Earths discovered via the transit method is significantly less than in

systems with RV-detected super-Earths. This likely reflects the substantially greater investment of RV time required to detect a planet with an unknown orbital period and phase, versus the transit case where these two quantities are known precisely in advance. RV-only detections must also achieve a higher significance in their measurement of the RV semi-amplitude in order to be considered a secure detection (see representative trend system GJ 273 (Butler et al., 2017; Forveille et al., 2009)), whereas for RV follow-up of transiting planets even marginally significant measurements of this quantity still provide useful constraints on the planet density (see representative trend system Kepler 97 (Marcy et al., 2014)). We show the resulting completeness maps in Figure 5, with systems discovered using the transit method plotted separately from systems discovered using RVs in order to illustrate the different average sensitivities of these two samples.

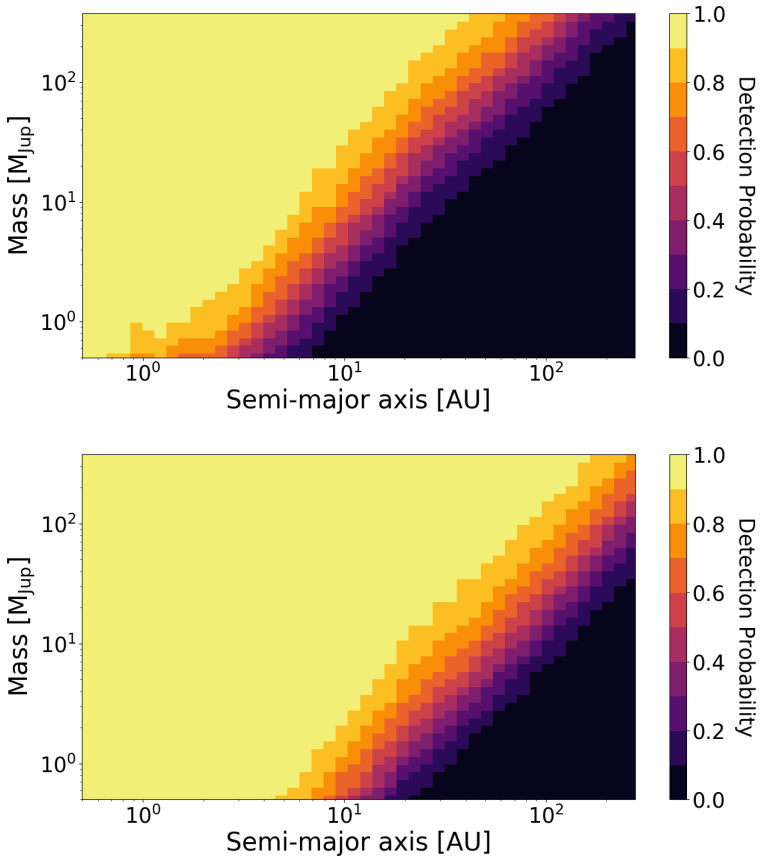

Figure 5.6: Sensitivity maps for the systems with super-Earths discovered using the transit method (left) and radial velocity method (right). Radial velocity detections typically require much more extensive data sets and have longer baselines than observations of transiting planet systems, resulting in different levels of completeness for these two samples.

5.5 Discussion

The Occurrence Rate of Gas Giant Companions

In this section we utilize our probability distributions for each system to determine the underlying distribution and corresponding occurrence rate for the observed population of long period gas giant companions in these systems. We follow the methodology laid out in Bryan et al. (2016), and present a summary of the steps here. We first assume that this population of companions is distributed in mass and semi-major axis space according to a double power law of the form $f(m, a) = Cm^{\alpha}a^{\beta}$ (e.g. Cumming et al., 2008; Tabachnik and Tremaine, 2002). The likelihood for a set of N exoplanet systems is given by:

$$\mathscr{L} = \Pi_{i=1}^{N} p(d_i|C, \alpha, \beta) \tag{5.3}$$

where $p(d_i|C, \alpha, \beta)$ is the probability of the RV dataset given power law coefficients C, α, and β. Assuming that each system has at most one outer companion, this likelihood is then the sum of the probability that a given system contains one planet and the probability that the system contains zero planets. The probability of a system containing zero planets is given by:

$$p(d_i, 0|C, \alpha, \beta) = p(d_i|0)[1 - Z] \tag{5.4}$$

where Z is the probability that the system contains a planet within a range of masses and semi-major axes (determined by integrating the power law distribution over the specified range), and $p(d_i|0)$ is the probability of obtaining the RV dataset given that there is no planet in the system.

The probability of a system having one companion given their distribution in mass and semi-major axis space is:

$$p(d_i, 1|C, \alpha, \beta) = \int_{a_1}^{a_2} d\ln a \int_{m_1}^{m_2} d\ln m\ p(d_i|a, m)Cm^{\alpha}a^{\beta} \tag{5.5}$$

where $p(d_i|a, m)$ is the probability of a companion being located at a given mass and semi-major axis, which we know from our previously determined probability distributions (see section 5.3). To determine the likelihood of a given set of C, α, and β given our RV datasets, we combine the probabilities of a system having one planet and a system having zero planets as follows:

$$\mathscr{L} = \Pi_{i=1}^{N} \left[p_i(d_i, 0|C, \alpha, \beta) + p_i(d_i, 1|C, \alpha, \beta) \right] \tag{5.6}$$

As in Bryan et al. (2016), we incorporate the probability distributions for all systems in this framework, not just the distributions for systems that have statistically significant trends. This allows us to treat all systems consistently regardless of whether or not they have a statistically significant trend. Phrased another way, this allows for the possibility of marginal trend detections, rather than assuming a binary classification system in which any star with a less than 3σ trend is counted as a non-detection. We note that for the systems with resolved gas giant companions with masses greater than 0.5 M_{Jup} outside 1 AU we replace the probability distributions calculated from the RV trends with ones where the probability density is concentrate in a single grid point closest to the best fit mass and separation of the resolved companion (see Table 5.2 for these values). We note that the statistically significant trend systems GJ 676, 55 Cnc, and Kepler-454 have resolved gas giant companions greater than 0.5 M_{Jup} outside 1 AU, so the probability distributions calculated from the statistically significant trends were replaced with the resolved companions in these systems. For systems GJ 676 and HD 181433 there are two resolved gas giant planets with masses greater than 0.5 M_{Jup} outside 1 AU. We select the outermost planet in these cases, and note that this selection does not impact the derived power law coefficients or occurrence rates.

We determine the values of C, α, and β that maximize the value of $\mathscr{L}$ by first performing a grid search where we vary each of these power law coefficients, and then carry out a MCMC fit initialized near the location of the optimal grid point. Because these parameters are often poorly constrained and highly correlated, we find that the use of a grid search allows us to reliably identify the global maximum and reduces the convergence time in our MCMC chains.

We can use the results of these power-law fits to calculate an integrated occurrence rate for the observed population of gas giant companions over a range of masses and semi-major axes. We first calculate the integrated companion frequency separately for systems discovered using the transit method versus the radial velocity method. Given the significant differences in completeness for these two samples of systems, this allows us to evaluate the degree to which these sensitivities impact the integrated occurrence rates. We ran the grid search and MCMC analysis of each sample separately. When we calculated the occurrence rates for these two samples of systems over a mass range of 0.5 - 20 M_{Jup} and a semi-major axis range of 1 - 20

Table 5.5: Total Occurrence Rates for Companions

	1 - 10 AU	1 - 20 AU	1 - 50 AU
0.5 - 20 M_{Jup}	38±7%	39±7%	41^{+8}_{-7}%
0.5 - 13 M_{Jup}	36^{+7}_{-6}%	41^{+8}_{-7}%	40^{+8}_{-7}%
1 - 20 M_{Jup}	35±7%	35±7%	38^{+8}_{-7}%
1 - 13 M_{Jup}	34±7%	38±7%	39^{+8}_{-7}%

AU, we found that the occurrence rate of companions in the transiting planet sample is 41^{+10}_{-10}%, and the occurrence rate of the RV planet sample is 34^{+11}_{-10}%, consistent at 0.5σ level. We note that the uncertainties on these occurrence rates are driven by the number of systems in each sample, which are similar (33 for the transiting planet sample, 26 for the RV sample).

We next calculate the frequency of companions for the combined sample over different ranges in mass and semi-major axis in order to assess how occurrence rates depend on our chosen integration ranges. Table 5.5 shows the resulting occurrence rates for the combined sample. We note that, as in Bryan et al. (2016), the values for the power law coefficients α and β vary significantly depending on our chosen integration range as a result of the poorly constrained companion masses and separations in these systems. However, we find that we obtain consistent results for the integrated occurrence rate for these companions across a wide range of integration ranges. This is because the strongest constraint we obtain from these data is the total number of companions in these systems, while their locations are poorly constrained. As a result, we find that the preferred values for C, α, and β in our fits are correlated in a way that preserves the total number of companions regardless of the fitting range used. This stands in contrast to studies examining populations of planets with tightly constrained masses and orbital semi-major axes (e.g. Cumming et al., 2008; B. P. Bowler et al., 2010), where the values of α and β are much better constrained by the data. For these systems, we would expect the integrated occurrence rate to rise as we increase the range in mass and semi-major axis, reflecting our much better knowledge of the planet occurrence rate density. This is an important point to consider when comparing our occurrence rate to those from surveys focusing on planets with fully resolved orbits, as we will discuss below.

Comparison to Published Surveys

We now aim to determine whether the rate of gas giant companions in super-Earth systems is higher or lower than the average occurrence rate for sun-like field stars.

If there is no correlation (positive or negative) between the presence of an inner super-Earth and an outer gas giant companion, we would expect these two rates to be consistent with each other. Conversely, once we have determined the frequency of long period gas giants in super-Earth systems, we can then ask what fraction of the long period gas giants orbiting field stars are drawn from this population (i.e., what fraction of long period gas giants have inner super-Earths?). We can express this probability using Bayes theorem:

$$p(SE|LPG) = \frac{p(LPG|SE) \times p(SE)}{p(LPG)} \tag{5.7}$$

where $p(SE)$ is the probability that a given star hosts a super-Earth and $p(LPG)$ is the probability of hosting a long period gas giant planet. Here we again consider a super-Earth to either have 1 - 10 $M_\oplus$ or 1 - 4 $R_\oplus$, and a long period gas giant planet to have 0.5 - 20 M_{Jup} and a semi-major axis 1 - 20 AU.

There have been several studies that have sought to quantify the frequency of long period gas giant planets, including Wittenmyer, Butler, et al. (2016), Rowan et al. (2016), and Foreman-Mackey et al. (2016). Wittenmyer, Butler, et al. (2016) calculate the occurrence rate of Jupiter analogs over the range 0.3 - 13 M_{Jup} and between 3 - 7 AU for a sample of 202 stars observed as a part of the 17-year Anglo-Australian Planet Search. For their sample of targets, they only consider planets with fully resolved orbits and find an integrated occurrence rate of $6.2^{+2.8}_{-1.6}$% over this range assuming binomial statistics (i.e., they do not fit a power law distribution). Integrating our sample over this same mass and semi-major axis range, we find an occurrence rate of 34±7%, which differs from the Wittenmyer, Butler, et al. (2016) value by 3.7σ. In order to determine whether or not this difference is meaningful, we must consider the possible biases introduced by our decision to consider trends rather than limit our study to companions with fully resolved orbits. Specifically, our occurrence rate is primarily derived from a population of planets with probability distributions extending over a wide range of masses and semi-major axes. This means that when we integrate over the relatively narrow range used in the Wittenmyer study, our occurrence rate may be inflated by the inclusion of planets whose probability distributions overlap with this integration range, even though the planets themselves are in fact located on more distant orbits.

To quantify this effect, we assume that planets in our sample are distributed according to the best-fit power law from Cumming et al. (2008), where $\alpha = -0.31$ and $\beta = 0.26$. This is almost certainly not the case in reality, as these coefficients were derived

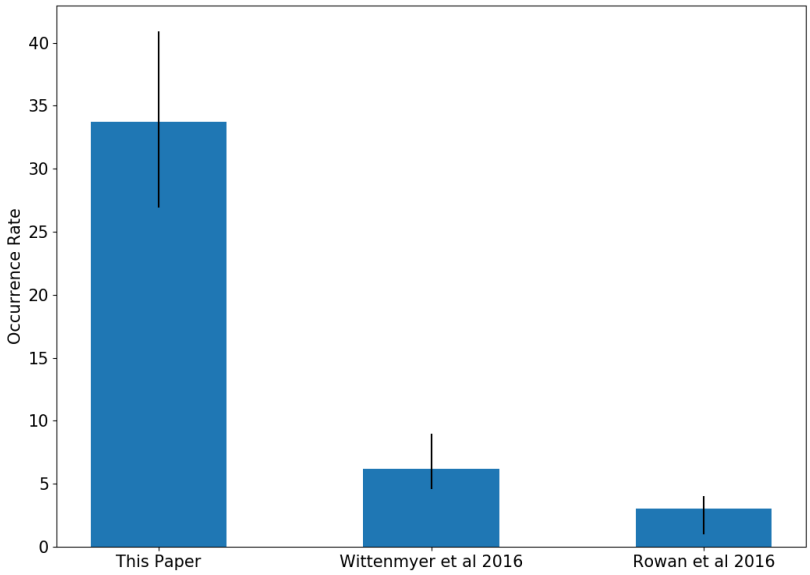

Figure 5.7: Compared to the Jupiter analog occurrence rate estimates published in Wittenmyer, Butler, et al. (2016) and Rowan et al. (2016), this study finds a higher occurrence rate of distant gas giant planets in super-Earth systems than would be expected just based on chance.

from a fit to the population of gas giant planets inside 3 AU. This fit indicates that the frequency of these planets rises with increasing semi-major axis, but this distribution must flatten or even turn over at larger semi-major axes, as we discuss below. Nonetheless, this power law provides a useful upper bound on the possible rate of contamination in our 3 – 7 AU occurrence rate from companions located outside 3 – 7 AU.

For each of the 8 systems with a statistically significant trend that do not have a resolved companion in this mass and semi-major axis range, we draw from the Cumming et al. power law distribution until we have generated a sample of 100 simulated planets with a cutoff mass of 20 M_{Jup} that lie within the favored region of mass/semi-major axis parameter space where the probability of there existing a planet given the RV trend is greater than the probability of there being no planet given the RV trend. For each system we then count the fraction of planets that fall within the range 3 – 7 AU and 0.3 – 13 M_{Jup}. For the resolved companions, we count four companions that fall within this range, and five that fall outside. For each of the resolved companions we either indicate that all 100 planets fall inside the box, or all 100 fall outside. Averaging across all of the trend and resolved companion systems, we find that 75% of our simulated planet population lies inside this range. If we rescale our occurrence rate to account for the fact that 1/4 of our occurrence right might be attributed to companions outside the 3 - 7 AU semi-major axis range,

we would then derive a corrected occurrence rate of 25% ± 5% for our sample over this semi-major axis range. This reduced occurrence rate is inconsistent with the Wittenmyer et al. value at the 3.3σ level.

While this correction could reduce the occurrence rate of companions in our sample, the revised occurrence would still not be consistent with that of Wittenmyer et al. Furthermore, we note that this power law distribution is inconsistent with current constraints from both RV and direct imaging surveys (Bryan et al., 2016; B. P. Bowler, 2016; Clanton and Gaudi, 2016; Brendan P. Bowler and Nielsen, 2018), which prefer much flatter distributions at large semi-major axes. In Bryan et al. (2016) we found that for the population of gas giant planets with long-period companions, the occurrence rate of these companions decreases with increasing semi-major axis. While the current small sample size of directly imaged planets makes it difficult to determine their mass and semi-major axis distribution, their overall low occurrence rate indicates that a rising power law in semi-major axis is likely not applicable at wide separations. We therefore conclude that our occurrence rate is likely higher than the rate from this study as well, with the same caveats as for the Wittenmyer et al. comparison.

For our last comparison we turn to Foreman-Mackey et al. (2016), who calculated the frequency of long period planets between $1.5 - 9$ AU and $0.01 - 20$ M_{Jup} using transit detections from the Kepler photometry. Unlike the previous two radial velocity studies, a majority of the long period planets in their sample have just one observed transit. Although this study is able to place some loose constraints on the orbital periods of these planets based on their measured transit durations, these constraints are nearly as broad as those for our radial velocity trend systems. For this parameter space Foreman-Mackey et al. (2016) find an occurrence rate density of 0.068±0.019, corresponding to an integrated occurrence rate of 92.5 ± 25.7%. Over a similar semi-major axis range and a more limited mass range ($1 - 10$ AU and $0.5 - 20$ M_{Jup}), we find an occurrence rate density of 0.045 ± 0.009 and an integrated occurrence rate of 38±7%. While these two occurrence rate densities are formally consistent, three-quarters of Foreman-Mackey et al. (2016)'s sample consists of planets whose estimated masses are less than 0.2 M_{Jup}, whereas all of our candidate companions have minimum masses higher than this threshold. We therefore conclude that there is relatively small overlap between the two planet samples, making this comparison less relevant than the studies by Wittenmyer, Butler, et al. (2016) and Rowan et al. (2016).

Implications of Our Results for Super-Earth Formation and Migration Models

Although it is difficult to make quantitative comparisons without a better understanding of the power law distribution for the long period gas giant planets in our sample, our results indicate that there is a higher occurrence rate for gas giants in systems hosting inner super-Earths than for field stars. This suggests that gas giant companions do not hinder super-Earth formation, either by cutting off the flow of solids to the inner disk, stirring up the velocity distribution of these solids, or by preventing super-Earths formed at larger separations from migrating inward (Batygin and Laughlin, 2015; Walsh et al., 2011; Moriarty and D. Fischer, 2015; Izidoro et al., 2015). If the scenario for the solar system presented in Batygin and Laughlin (2015) is correct, this would also suggest that the giant planets in these systems did not undergo a dramatic in-and-then-out again migration, as this would similarly disrupt planet formation in the inner disk. However, our current data do not provide any constraints on the multiplicity of long period giant planets, and it is therefore not currently possible to evaluate the likelihood of dynamical interactions between pairs of outer gas giant planets in these systems.

The presence of an outer gas giant may instead be a reflection of the properties of protoplanetary disks that are particularly amenable to planet formation. Large solid mass content is considered one such property, facilitating the growth of grains to planetesimals (e.g. Youdin and E. I. Chiang, 2004; Birnstiel, Klahr, and Ercolano, 2012), accelerating the growth of cores by pebble accretion (e.g. Ormel and Kobayashi, 2012; Lambrechts and Johansen, 2014), and speeding up the final assembly by giant impact (e.g. Dawson, E. Chiang, and Lee, 2015).[1] Observationally, both gas giants and super-Earths (here defined as planets with mass of 1–10 $M_\oplus$ and/or with radii of 1–4 $R_\oplus$) are found to occur more frequently around metal-rich stars (D. A. Fischer and Valenti, 2005; Petigura, Marcy, et al., 2018). Here we consider whether the metallicity of the host star—used as a proxy of the total solid content in the natal disk—is correlated with the occurrence of gas giant companions to inner super-Earths.

As a test of this question, we divide our sample into systems that have greater than 3σ trends ("Trend Systems") and resolved companions and those that do not ("No Trend Systems"), and compare the error weighted averages of the stellar metallicities between these two samples. For the transiting planet sample, we find average

[1] To be more precise, the growth of planetesimals and cores is governed by the "local" concentration of solids; in other words, what matters is the solid-to-gas mass ratio at the site of such growth, not necessarily the bulk mass ratio.

metallcities of 0.210±0.020 and -0.010±0.012 for the trend/no trend systems, a 9.4σ difference. This suggests that super-Earth systems around metal-rich sun-like stars may be more likely to have outer companions than their metal-poor counterparts. We find that for the RV sample, the average metallicities are -0.034±0.055 and -0.079±0.024 for the trend/no trend systems, a 0.7σ difference. We note that the sample of stars in the RV sample typically have lower masses and correspondingly lower metallicities than stars in the transiting planet sample, with an error weighted average metallicity of -0.065±0.022 and 0.060±0.010 for the RV and transiting samples respectively. The lack of a correlation in this sample is surprising, as previous trend studies targeting M stars found that the occurrence rate of gas giant planets in systems with M star hosts is strongly correlated with stellar metallicity (Montet et al., 2014). We speculate that this difference between the transit and RV sample metallicity trends could be driven by differences in gas giant companion separation. Taking the innermost semi-major axis 1σ limits for the trend systems from Table 4 and the resolved companion semi-major axes from Table 2, we note that the average semi-major axis of gas giant companions in the transiting planet sample is 2.9 AU, in comparison to 5.9 AU for the RV sample. This could reflect a weaker correlation between the occurrence of gas giant planets at wider separations with metallicity (Buchhave, Bitsch, et al., 2018).

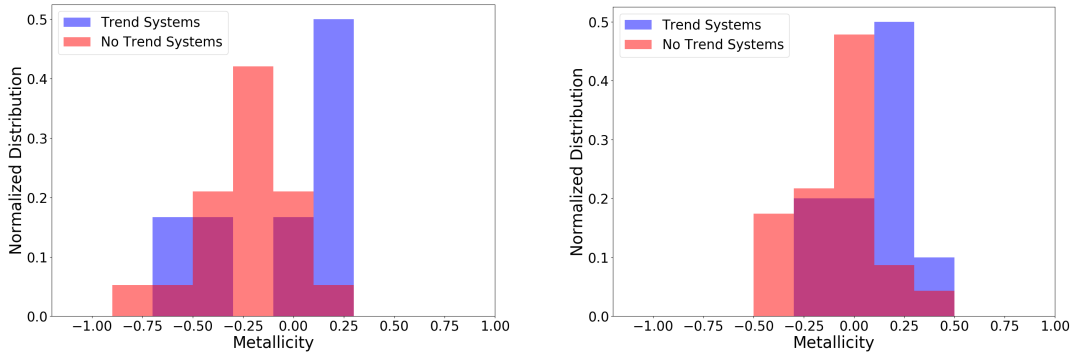

Figure 5.8: Distributions of stellar metallicities for systems with and without > 3σ trends and resolved companions. Top: RV only sample. Bottom: Transit only sample.

We next consider whether or not there is any correlation between the presence of a long-term trend and the mass of the host star. This could potentially affect our estimates of the companion frequency in RV versus transiting planet systems, as these two samples have different stellar mass distributions. We find that while only one star in the transiting planet sample is an M dwarf (LHS 1140), ten targets are M dwarfs in the RV sample. We calculate the occurrence rate for the combined RV and

transiting planet samples without the M stars over an integration range of 0.5 - 20 M_{Jup} and 1 - 20 AU, and find an occurrence rate of 37±8%. This is consistent with the occurrence rate of the total sample including the M stars of 39±7% to $< 0.1\sigma$.

Could outer gas giants actually help the formation of inner super-Earths? For their masses, super-Earths have small radii, characterized by typically just a few percent by mass envelope (e.g. Wolfgang and Lopez, 2015). Such small envelope mass fraction points toward late-time formation, whereby cores of a few Earth masses assemble out of smaller protocores during the late stage of disk evolution when the core-to-core stirring have a fighting chance against eccentricity damping by gas dynamical friction (e.g. Lee, E. Chiang, and Ormel, 2014; Lee and E. Chiang, 2016; Ogihara et al., 2018). This core-to-core stirring may be invigorated by the presence of outer gas giants (e.g. Mustill, Davies, and Johansen, 2017; Hansen, 2017; Pu and Lai, 2018), kick-starting the final assembly of super-Earth cores earlier.

If we take our integrated occurrence rate of 34±7% between $3 - 7$ AU and $0.3 - 13$ M_{Jup} at face value, as well as the overall occurrence rates of super-Earths and long-period gas giant planets (Wittenmyer, Butler, et al., 2016; Rowan et al., 2016; Howard, Marcy, Johnson, et al., 2010; Fressin et al., 2013; Petigura, Howard, and Marcy, 2013; Zhu et al., 2018), Equation 5.7 would suggest that a significant majority of long period gas giant planets have inner super-Earths.

5.6 Conclusions

We collected published RV data for a sample of 65 systems hosting at least one inner super-Earth planet in order to search for massive, long-period companions. We detect these distant companions as long term trends in the RV data when the orbital period of the companion is shorter than the system RV baseline. Out of our sample of 65 systems, we found 15 systems that had statistically significant trends. Two of these systems had resolved stellar companions that could potentially have caused the observed trends, while three more systems had trends that were likely due to stellar activity. We removed these five systems from subsequent analysis, leaving ten systems with statistically significant trends indicating the presence of an outer companion. Three of these trends are identified here for the first time, while seven were previously reported in the literature. We also identify 11 previously published resolved gas giant companions (> 0.5 M_{Jup} and 1 - 20 AU) in our sample of systems, as well as two new candidate planets in systems HD 156668 and HD 175607 (which we do not include in our statistical analysis due to their candidate nature).

We compute 2D probability distributions in mass and semi-major axis space for each system in our sample with a radial velocity trend, where we use the duration and shape of the trends to place lower limits on allowed ranges of mass and separation. We use a combination of new and archival AO imaging at infrared wavelengths to place a corresponding upper limit on the allowed masses and separations of these companions. We fit these distributions with a double power law in mass and semi-major axis, and integrate this power law over 0.5 - 20 M_{Jup} and 1 - 20 AU to find an occurrence rate of 39 ± 7%. We then compare our occurrence rate for these companions to similar occurrence rates for long period gas giant planets from radial velocity surveys of sun-like field stars. We find that super-Earth systems appear to have more gas giant companions than we would expect to see by chance alone, even after accounting for the additional uncertainty introduced by our inability to pinpoint the precise locations of these companions.

We therefore conclude that the presence of an outer gas giants does not hinder super-Earth formation, as proposed in some previous theoretical studies. To the contrary, our data suggest that these companions may either actively facilitate super-Earth formation or simply serve as a fossil record of early disk conditions that were particularly favorable for planet formation over a wide range of semi-major axes.

References

Affer, L. et al. (2016). "HADES RV program with HARPS-N at the TNG GJ 3998: An early M-dwarf hosting a system of super-Earths". In: *A&A* 593, A117, A117. DOI: 10.1051/0004-6361/201628690. arXiv: 1607.03632 [astro-ph.EP].

Almenara, J. M. et al. (2015). "A HARPS view on K2-3". In: *A&A* 581, L7, p. L7. DOI: 10.1051/0004-6361/201525918. arXiv: 1509.02917 [astro-ph.EP].

Alonso, R. et al. (2014). "Transiting exoplanets from the CoRoT space mission. XXVI. CoRoT-24: a transiting multiplanet system". In: *A&A* 567, A112, A112. DOI: 10.1051/0004-6361/201118662. arXiv: 1406.1270 [astro-ph.EP].

Anglada-Escudé, G., P. J. Amado, et al. (2016). "A terrestrial planet candidate in a temperate orbit around Proxima Centauri". In: *Nature* 536, pp. 437–440. DOI: 10.1038/nature19106. arXiv: 1609.03449 [astro-ph.EP].

Anglada-Escudé, G., P. Arriagada, et al. (2012). "A Planetary System around the nearby M Dwarf GJ 667C with At Least One Super-Earth in Its Habitable Zone". In: *ApJL* 751, L16, p. L16. DOI: 10.1088/2041-8205/751/1/L16. arXiv: 1202.0446 [astro-ph.EP].

Anglada-Escudé, G. and M. Tuomi (2012). "A planetary system with gas giants and super-Earths around the nearby M dwarf GJ 676A. Optimizing data analysis

techniques for the detection of multi-planetary systems". In: *A&A* 548, A58, A58. DOI: 10.1051/0004-6361/201219910. arXiv: 1206.7118 [astro-ph.EP].

Anglada-Escudé, G., M. Tuomi, et al. (2013). "A dynamically-packed planetary system around GJ 667C with three super-Earths in its habitable zone". In: *A&A* 556, A126, A126. DOI: 10.1051/0004-6361/201321331. arXiv: 1306.6074 [astro-ph.EP].

Astudillo-Defru, N., X. Bonfils, et al. (2015). "The HARPS search for southern extra-solar planets. XXXVI. Planetary systems and stellar activity of the M dwarfs GJ 3293, GJ 3341, and GJ 3543". In: *A&A* 575, A119, A119. DOI: 10.1051/0004-6361/201424253. arXiv: 1411.7048 [astro-ph.EP].

Astudillo-Defru, N., T. Forveille, et al. (2017). "The HARPS search for southern extra-solar planets. XLI. A dozen planets around the M dwarfs GJ 3138, GJ 3323, GJ 273, GJ 628, and GJ 3293". In: *A&A* 602, A88, A88. DOI: 10.1051/0004-6361/201630153. arXiv: 1703.05386 [astro-ph.EP].

Baraffe, I. et al. (1998). "Evolutionary models for solar metallicity low-mass stars: mass-magnitude relationships and color-magnitude diagrams". In: *A&A* 337, pp. 403–412. eprint: astro-ph/9805009.

Batygin, K. and G. Laughlin (2015). "Jupiter's decisive role in the inner Solar System's early evolution". In: *Proceedings of the National Academy of Science* 112, pp. 4214–4217. DOI: 10.1073/pnas.1423252112. arXiv: 1503.06945 [astro-ph.EP].

Berta-Thompson, Z. K. et al. (2015). "A rocky planet transiting a nearby low-mass star". In: *Nature* 527, pp. 204–207. DOI: 10.1038/nature15762. arXiv: 1511.03550 [astro-ph.EP].

Birnstiel, T., H. Klahr, and B. Ercolano (2012). "A simple model for the evolution of the dust population in protoplanetary disks". In: *A&A* 539, A148, A148. DOI: 10.1051/0004-6361/201118136. arXiv: 1201.5781 [astro-ph.EP].

Bonfils, X., X. Delfosse, et al. (2005). "Metallicity of M dwarfs. I. A photometric calibration and the impact on the mass-luminosity relation at the bottom of the main sequence". In: *A&A* 442, pp. 635–642. DOI: 10.1051/0004-6361:20053046. eprint: astro-ph/0503260.

Bonfils, X., M. Gillon, et al. (2011). "A short-period super-Earth orbiting the M2.5 dwarf GJ 3634. Detection with HARPS velocimetry and transit search with Spitzer photometry". In: *A&A* 528, A111, A111. DOI: 10.1051/0004-6361/201015981. arXiv: 1102.1420 [astro-ph.EP].

Bonfils, X., G. Lo Curto, et al. (2013). "The HARPS search for southern extra-solar planets. XXXIV. A planetary system around the nearby M dwarf <ASTROBJ>GJ 163</ASTROBJ>, with a super-Earth possibly in the habitable zone". In: *A&A* 556, A110, A110. DOI: 10.1051/0004-6361/201220237. arXiv: 1306.0904 [astro-ph.EP].

Borucki, W. J., E. Agol, et al. (2013). "Kepler-62: A Five-Planet System with Planets of 1.4 and 1.6 Earth Radii in the Habitable Zone". In: *Science* 340, pp. 587–590. DOI: 10.1126/science.1234702. arXiv: 1304.7387 [astro-ph.EP].

Borucki, W. J., D. G. Koch, et al. (2012). "Kepler-22b: A 2.4 Earth-radius Planet in the Habitable Zone of a Sun-like Star". In: *ApJ* 745, 120, p. 120. DOI: 10.1088/0004-637X/745/2/120. arXiv: 1112.1640 [astro-ph.EP].

Bouchy, F. et al. (2009). "The HARPS search for southern extra-solar planets. XVII. Super-Earth and Neptune-mass planets in multiple planet systems HD 47 186 and HD 181 433". In: *A&A* 496, pp. 527–531. DOI: 10.1051/0004-6361:200810669. arXiv: 0812.1608.

Bowler, B. P. (2016). "Imaging Extrasolar Giant Planets". In: *PASP* 128.10, p. 102001. DOI: 10.1088/1538-3873/128/968/102001. arXiv: 1605.02731 [astro-ph.EP].

Bowler, B. P. et al. (2010). "Retired A Stars and Their Companions. III. Comparing the Mass-Period Distributions of Planets Around A-Type Stars and Sun-Like Stars". In: *ApJ* 709, pp. 396–410. DOI: 10.1088/0004-637X/709/1/396. arXiv: 0912.0518 [astro-ph.EP].

Bowler, Brendan P. and Eric L. Nielsen (2018). "Occurrence Rates from Direct Imaging Surveys". In: *ArXiv e-prints*, arXiv:1802.10132, arXiv:1802.10132. arXiv: 1802.10132.

Bryan, M. L. et al. (2016). "Statistics of Long Period Gas Giant Planets in Known Planetary Systems". In: *ApJ* 821, 89, p. 89. DOI: 10.3847/0004-637X/821/2/89. arXiv: 1601.07595 [astro-ph.EP].

Buchhave, L. A., B. Bitsch, et al. (2018). "Jupiter Analogs Orbit Stars with an Average Metallicity Close to That of the Sun". In: *ApJ* 856, 37, p. 37. DOI: 10.3847/1538-4357/aaafca. arXiv: 1802.06794 [astro-ph.EP].

Buchhave, L. A., M. Bizzarro, et al. (2014). "Three regimes of extrasolar planet radius inferred from host star metallicities". In: *Nature* 509, pp. 593–595. DOI: 10.1038/nature13254. arXiv: 1405.7695 [astro-ph.EP].

Butler, R. P. et al. (2017). "The LCES HIRES/Keck Precision Radial Velocity Exoplanet Survey". In: *AJ* 153, 208, p. 208. DOI: 10.3847/1538-3881/aa66ca. arXiv: 1702.03571 [astro-ph.EP].

Christiansen, J. L. et al. (2017). "Three's Company: An Additional Non-transiting Super-Earth in the Bright HD 3167 System, and Masses for All Three Planets". In: *AJ* 154, 122, p. 122. DOI: 10.3847/1538-3881/aa832d. arXiv: 1706.01892 [astro-ph.EP].

Clanton, C. and B. S. Gaudi (2016). "Synthesizing Exoplanet Demographics: A Single Population of Long-period Planetary Companions to M Dwarfs Consistent with Microlensing, Radial Velocity, and Direct Imaging Surveys". In: *ApJ* 819, 125, p. 125. DOI: 10.3847/0004-637X/819/2/125. arXiv: 1508.04434 [astro-ph.EP].

Correia, A. C. M. et al. (2010). "The HARPS search for southern extra-solar planets. XIX. Characterization and dynamics of the GJ 876 planetary system". In: *A&A* 511, A21, A21. DOI: 10.1051/0004-6361/200912700. arXiv: 1001.4774 [astro-ph.EP].

Crida, A., A. Morbidelli, and F. Masset (2006). "On the width and shape of gaps in protoplanetary disks". In: *Icarus* 181, pp. 587–604. DOI: 10.1016/j.icarus.2005.10.007. eprint: astro-ph/0511082.

Cumming, A. et al. (2008). "The Keck Planet Search: Detectability and the Minimum Mass and Orbital Period Distribution of Extrasolar Planets". In: *PASP* 120, p. 531. DOI: 10.1086/588487. arXiv: 0803.3357.

Dai, F. et al. (2015). "Doppler Monitoring of the WASP-47 Multiplanet System". In: *ApJL* 813, L9, p. L9. DOI: 10.1088/2041-8205/813/1/L9. arXiv: 1510.03811 [astro-ph.EP].

Dawson, R. I., E. Chiang, and E. J. Lee (2015). "A metallicity recipe for rocky planets". In: *MNRAS* 453, pp. 1471–1483. DOI: 10.1093/mnras/stv1639. arXiv: 1506.06867 [astro-ph.EP].

Delfosse, X. et al. (2013). "The HARPS search for southern extra-solar planets. XXXIII. Super-Earths around the M-dwarf neighbors Gl 433 and Gl 667C". In: *A&A* 553, A8, A8. DOI: 10.1051/0004-6361/201219013. arXiv: 1202.2467 [astro-ph.EP].

Desch, S. J., A. Kalyaan, and C. M. O. Alexander (2017). "The Effect of Jupiter's Formation on the Distribution of Refractory Elements and Inclusions in Meteorites". In: *ArXiv e-prints*. arXiv: 1710.03809 [astro-ph.EP].

Diaz, R. F. et al. (2016). "The HARPS search for southern extra-solar planets. XXXVIII. Bayesian re-analysis of three systems. New super-Earths, unconfirmed signals, and magnetic cycles". In: *A&A* 585, A134, A134. DOI: 10.1051/0004-6361/201526729. arXiv: 1510.06446 [astro-ph.EP].

Dittmann, J. A. et al. (2017). "A temperate rocky super-Earth transiting a nearby cool star". In: *Nature* 544, pp. 333–336. DOI: 10.1038/nature22055. arXiv: 1704.05556 [astro-ph.EP].

Dressing, C. D. and D. Charbonneau (2015). "The Occurrence of Potentially Habitable Planets Orbiting M Dwarfs Estimated from the Full Kepler Dataset and an Empirical Measurement of the Detection Sensitivity". In: *ApJ* 807, 45, p. 45. DOI: 10.1088/0004-637X/807/1/45. arXiv: 1501.01623 [astro-ph.EP].

Dressing, C. D., D. Charbonneau, et al. (2015). "The Mass of Kepler-93b and The Composition of Terrestrial Planets". In: *ApJ* 800, 135, p. 135. DOI: 10.1088/0004-637X/800/2/135. arXiv: 1412.8687 [astro-ph.EP].

Dumusque, X. et al. (2014). "The Kepler-10 Planetary System Revisited by HARPS-N: A Hot Rocky World and a Solid Neptune-Mass Planet". In: *ApJ* 789, 154, p. 154. DOI: 10.1088/0004-637X/789/2/154. arXiv: 1405.7881 [astro-ph.EP].

Endl, M. et al. (2012). "Revisiting ρ^1 Cancri e: A New Mass Determination of the Transiting Super-Earth". In: *ApJ* 759, 19, p. 19. DOI: 10.1088/0004-637X/759/1/19. arXiv: 1208.5709 [astro-ph.EP].

Ercolano, B. and C. J. Clarke (2010). "Metallicity, planet formation and disc lifetimes". In: *MNRAS* 402, pp. 2735–2743. DOI: 10.1111/j.1365-2966.2009.16094.x. arXiv: 0910.5110 [astro-ph.EP].

Fischer, D. A., G. W. Marcy, et al. (2008). "Five Planets Orbiting 55 Cancri". In: *ApJ* 675, 790-801, pp. 790–801. DOI: 10.1086/525512. arXiv: 0712.3917.

Fischer, D. A. and J. Valenti (2005). "The Planet-Metallicity Correlation". In: *ApJ* 622, pp. 1102–1117. DOI: 10.1086/428383.

Foreman-Mackey, D. et al. (2016). "The Population of Long-period Transiting Exoplanets". In: *AJ* 152, 206, p. 206. DOI: 10.3847/0004-6256/152/6/206. arXiv: 1607.08237 [astro-ph.EP].

Forveille, T. et al. (2009). "The HARPS search for southern extra-solar planets. XIV. Gl 176b, a super-Earth rather than a Neptune, and at a different period". In: *A&A* 493, pp. 645–650. DOI: 10.1051/0004-6361:200810557. arXiv: 0809.0750.

Fressin, F. et al. (2013). "The False Positive Rate of Kepler and the Occurrence of Planets". In: *ApJ* 766, 81, p. 81. DOI: 10.1088/0004-637X/766/2/81. arXiv: 1301.0842 [astro-ph.EP].

Fulton, B. J., E. A. Petigura, et al. (2018). "RadVel: The Radial Velocity Modeling Toolkit". In: *PASP* 130.4, p. 044504. DOI: 10.1088/1538-3873/aaaaa8. arXiv: 1801.01947 [astro-ph.IM].

Fulton, B. J., L. M. Weiss, et al. (2015). "Three Super-Earths Orbiting HD 7924". In: *ApJ* 805, 175, p. 175. DOI: 10.1088/0004-637X/805/2/175. arXiv: 1504.06629 [astro-ph.EP].

Furlan, E. et al. (2017). "The Kepler Follow-up Observation Program. I. A Catalog of Companions to Kepler Stars from High-Resolution Imaging". In: *AJ* 153, 71, p. 71. DOI: 10.3847/1538-3881/153/2/71. arXiv: 1612.02392 [astro-ph.SR].

Gaia Collaboration, A. G. A. Brown, et al. (2016). "Gaia Data Release 1. Summary of the astrometric, photometric, and survey properties". In: *A&A* 595, A2, A2. DOI: 10.1051/0004-6361/201629512. arXiv: 1609.04172 [astro-ph.IM].

Gaia Collaboration, T. Prusti, et al. (2016). "The Gaia mission". In: *A&A* 595, A1, A1. DOI: 10.1051/0004-6361/201629272. arXiv: 1609.04153 [astro-ph.IM].

Gautier III, T. N. et al. (2012). "Kepler-20: A Sun-like Star with Three Sub-Neptune Exoplanets and Two Earth-size Candidates". In: *ApJ* 749, 15, p. 15. DOI: 10.1088/0004-637X/749/1/15. arXiv: 1112.4514 [astro-ph.EP].

Gettel, S. et al. (2016). "The Kepler-454 System: A Small, Not-rocky Inner Planet, a Jovian World, and a Distant Companion". In: *ApJ* 816, 95, p. 95. DOI: 10.3847/0004-637X/816/2/95. arXiv: 1511.09097 [astro-ph.EP].

Gillon, M. et al. (2017). "Two massive rocky planets transiting a K-dwarf 6.5 parsecs away". In: *Nature Astronomy* 1, 0056, p. 0056. DOI: 10.1038/s41550-017-0056. arXiv: 1703.01430 [astro-ph.EP].

Hansen, B. M. S. (2017). "Perturbation of Compact Planetary Systems by Distant Giant Planets". In: *MNRAS* 467, pp. 1531–1560. DOI: 10.1093/mnras/stx182. arXiv: 1608.06300 [astro-ph.EP].

Hasegawa, Y. and R. E. Pudritz (2011). "The origin of planetary system architectures - I. Multiple planet traps in gaseous discs". In: *MNRAS* 417, pp. 1236–1259. DOI: 10.1111/j.1365-2966.2011.19338.x. arXiv: 1105.4015 [astro-ph.EP].

Howard, A. W., G. W. Marcy, D. A. Fischer, et al. (2014). "The NASA-UC-UH ETA-Earth Program. IV. A Low-mass Planet Orbiting an M Dwarf 3.6 PC from Earth". In: *ApJ* 794, 51, p. 51. DOI: 10.1088/0004-637X/794/1/51. arXiv: 1408.5645 [astro-ph.EP].

Howard, A. W., G. W. Marcy, J. A. Johnson, et al. (2010). "The Occurrence and Mass Distribution of Close-in Super-Earths, Neptunes, and Jupiters". In: *Science* 330, p. 653. DOI: 10.1126/science.1194854. arXiv: 1011.0143 [astro-ph.EP].

Howell, S. B. et al. (2012). "Kepler-21b: A 1.6 REarth Planet Transiting the Bright Oscillating F Subgiant Star HD 179070". In: *ApJ* 746, 123, p. 123. DOI: 10.1088/0004-637X/746/2/123. arXiv: 1112.2165 [astro-ph.SR].

Huang, Chelsea X., Cristobal Petrovich, and Emily Deibert (2017). "Dynamically Hot Super-Earths from Outer Giant Planet Scattering". In: *AJ* 153. DOI: 10.3847/1538-3881/aa67fb.

Isaacson, H. and D. Fischer (2010). "Chromospheric Activity and Jitter Measurements for 2630 Stars on the California Planet Search". In: *ApJ* 725, pp. 875–885. DOI: 10.1088/0004-637X/725/1/875. arXiv: 1009.2301 [astro-ph.EP].

Izidoro, A. et al. (2015). "Gas Giant Planets as Dynamical Barriers to Inward-Migrating Super-Earths". In: *ApJL* 800, L22, p. L22. DOI: 10.1088/2041-8205/800/2/L22. arXiv: 1501.06308 [astro-ph.EP].

Johnson, J. A. et al. (2010). "Giant Planet Occurrence in the Stellar Mass-Metallicity Plane". In: *PASP* 122, p. 905. DOI: 10.1086/655775. arXiv: 1005.3084 [astro-ph.EP].

Kipping, D. M. (2013). "Parametrizing the exoplanet eccentricity distribution with the Beta distribution". In: *MNRAS* 434, pp. L51–L55. DOI: 10.1093/mnrasl/slt075. arXiv: 1306.4982 [astro-ph.EP].

Kley, W. and R. P. Nelson (2012). "Planet-Disk Interaction and Orbital Evolution". In: *ARA&A* 50, pp. 211–249. DOI: 10.1146/annurev-astro-081811-125523. arXiv: 1203.1184 [astro-ph.EP].

Knutson, H. A. et al. (2014). "Friends of Hot Jupiters. I. A Radial Velocity Search for Massive, Long-period Companions to Close-in Gas Giant Planets". In: *ApJ* 785, 126, p. 126. DOI: 10.1088/0004-637X/785/2/126. arXiv: 1312.2954 [astro-ph.EP].

Lambrechts, M. and A. Johansen (2014). "Forming the cores of giant planets from the radial pebble flux in protoplanetary discs". In: *A&A* 572, A107, A107. DOI: 10.1051/0004-6361/201424343. arXiv: 1408.6094 [astro-ph.EP].

Lambrechts, M., A. Johansen, and A. Morbidelli (2014). "Separating gas-giant and ice-giant planets by halting pebble accretion". In: *A&A* 572, A35, A35. DOI: 10.1051/0004-6361/201423814. arXiv: 1408.6087 [astro-ph.EP].

Lee, E. J. and E. Chiang (2016). "Breeding Super-Earths and Birthing Super-puffs in Transitional Disks". In: *ApJ* 817, 90, p. 90. DOI: 10.3847/0004-637X/817/2/90. arXiv: 1510.08855 [astro-ph.EP].

Lee, E. J., E. Chiang, and C. W. Ormel (2014). "Make Super-Earths, Not Jupiters: Accreting Nebular Gas onto Solid Cores at 0.1 AU and Beyond". In: *ApJ* 797, 95, p. 95. DOI: 10.1088/0004-637X/797/2/95. arXiv: 1409.3578 [astro-ph.EP].

Léger, A. et al. (2009). "Transiting exoplanets from the CoRoT space mission. VIII. CoRoT-7b: the first super-Earth with measured radius". In: *A&A* 506, pp. 287–302. DOI: 10.1051/0004-6361/200911933. arXiv: 0908.0241 [astro-ph.EP].

Lenzen, R. et al. (2003). "NAOS-CONICA first on sky results in a variety of observing modes". In: *Instrument Design and Performance for Optical/Infrared Ground-based Telescopes*. Ed. by M. Iye and A. F. M. Moorwood. Vol. 4841. Proc. SPIE, pp. 944–952. DOI: 10.1117/12.460044.

Lin, D. N. C. and J. Papaloizou (1986). "On the tidal interaction between protoplanets and the protoplanetary disk. III - Orbital migration of protoplanets". In: *ApJ* 309, pp. 846–857. DOI: 10.1086/164653.

Liu, M. C. et al. (2002). "Crossing the Brown Dwarf Desert Using Adaptive Optics: A Very Close L Dwarf Companion to the Nearby Solar Analog HR 7672". In: *ApJ* 571, pp. 519–527. DOI: 10.1086/339845. eprint: astro-ph/0112407.

Lo Curto, G. et al. (2010). "The HARPS search for southern extra-solar planets . XXII. Multiple planet systems from the HARPS volume limited sample". In: *A&A* 512, A48, A48. DOI: 10.1051/0004-6361/200913523.

López-Morales, M. et al. (2016). "Kepler-21b: A Rocky Planet Around a V = 8.25 Magnitude Star". In: *AJ* 152, 204, p. 204. DOI: 10.3847/0004-6256/152/6/204. arXiv: 1609.07617 [astro-ph.EP].

Lovis, C. et al. (2011). "The HARPS search for southern extra-solar planets. XXVIII. Up to seven planets orbiting HD 10180: probing the architecture of low-mass planetary systems". In: *A&A* 528, A112, A112. DOI: 10.1051/0004-6361/201015577. arXiv: 1011.4994 [astro-ph.EP].

Marcy, G. W. et al. (2014). "Masses, Radii, and Orbits of Small Kepler Planets: The Transition from Gaseous to Rocky Planets". In: *ApJS* 210, 20, p. 20. DOI: 10.1088/0067-0049/210/2/20. arXiv: 1401.4195 [astro-ph.EP].

Masset, F. S. et al. (2006). "Disk Surface Density Transitions as Protoplanet Traps". In: *ApJ* 642, pp. 478–487. DOI: 10.1086/500967.

Mayor, M., X. Bonfils, et al. (2009). "The HARPS search for southern extra-solar planets. XVIII. An Earth-mass planet in the GJ 581 planetary system". In: *A&A* 507, pp. 487–494. DOI: 10.1051/0004-6361/200912172. arXiv: 0906.2780 [astro-ph.EP].

Mayor, M., M. Marmier, et al. (2011). "The HARPS search for southern extra-solar planets XXXIV. Occurrence, mass distribution and orbital properties of super-Earths and Neptune-mass planets". In: *ArXiv e-prints*. arXiv: 1109.2497 [astro-ph.EP].

Meshkat, T. et al. (2014). "Optimized Principal Component Analysis on Coronagraphic Images of the Fomalhaut System". In: *ApJ* 780, 17, p. 17. DOI: 10.1088/0004-637X/780/1/17. arXiv: 1310.8577 [astro-ph.EP].

Montet, B. T. et al. (2014). "The TRENDS High-contrast Imaging Survey. IV. The Occurrence Rate of Giant Planets around M Dwarfs". In: *ApJ* 781, 28, p. 28. DOI: 10.1088/0004-637X/781/1/28. arXiv: 1307.5849 [astro-ph.EP].

Morbidelli, A., B. Bitsch, et al. (2016). "Fossilized condensation lines in the Solar System protoplanetary disk". In: *Icarus* 267, pp. 368–376. DOI: 10.1016/j.icarus.2015.11.027. arXiv: 1511.06556 [astro-ph.EP].

Morbidelli, A. and A. Crida (2007). "The dynamics of Jupiter and Saturn in the gaseous protoplanetary disk". In: *Icarus* 191, pp. 158–171. DOI: 10.1016/j.icarus.2007.04.001.

Morbidelli, A., J. I. Lunine, et al. (2012). "Building Terrestrial Planets". In: *Annual Review of Earth and Planetary Sciences* 40, pp. 251–275. DOI: 10.1146/annurev-earth-042711-105319. arXiv: 1208.4694 [astro-ph.EP].

Morbidelli, A. and D. Nesvorny (2012). "Dynamics of pebbles in the vicinity of a growing planetary embryo: hydro-dynamical simulations". In: *A&A* 546, A18, A18. DOI: 10.1051/0004-6361/201219824. arXiv: 1208.4687 [astro-ph.EP].

Moriarty, J. and D. Fischer (2015). "Building Massive Compact Planetesimal Disks from the Accretion of Pebbles". In: *ApJ* 809, 94, p. 94. DOI: 10.1088/0004-637X/809/1/94. arXiv: 1507.08215 [astro-ph.EP].

Mortier, A. et al. (2016). "The HARPS search for southern extra-solar planets. XXXIX. HD 175607, the most metal-poor G dwarf with an orbiting sub-Neptune". In: *A&A* 585, A135, A135. DOI: 10.1051/0004-6361/201526905. arXiv: 1511.03941 [astro-ph.EP].

Mustill, A. J., M. B. Davies, and A. Johansen (2017). "The effects of external planets on inner systems: multiplicities, inclinations and pathways to eccentric warm Jupiters". In: *MNRAS* 468, pp. 3000–3023. DOI: 10.1093/mnras/stx693. arXiv: 1609.08058 [astro-ph.EP].

Neveu-VanMalle, M. et al. (2016). "Hot Jupiters with relatives: discovery of additional planets in orbit around WASP-41 and WASP-47". In: *A&A* 586, A93, A93. DOI: 10.1051/0004-6361/201526965. arXiv: 1509.07750 [astro-ph.EP].

Ngo, H., H. A. Knutson, M. L. Bryan, et al. (2017). "No Difference in Orbital Parameters of RV-detected Giant Planets between 0.1 and 5 au in Single versus Multi-stellar Systems". In: *AJ* 153, 242, p. 242. DOI: 10.3847/1538-3881/aa6cac. arXiv: 1704.02326 [astro-ph.EP].

Ngo, H., H. A. Knutson, S. Hinkley, et al. (2015). "Friends of Hot Jupiters. II. No Correspondence between Hot-jupiter Spin-Orbit Misalignment and the Incidence of Directly Imaged Stellar Companions". In: *ApJ* 800, 138, p. 138. DOI: 10.1088/0004-637X/800/2/138. arXiv: 1501.00013 [astro-ph.EP].

O'Brien, D. P., A. Morbidelli, and H. F. Levison (2006). "Terrestrial planet formation with strong dynamical friction". In: *Icarus* 184, pp. 39–58. DOI: 10.1016/j.icarus.2006.04.005.

Ogihara, M. et al. (2018). "Formation of close-in super-Earths in evolving protoplanetary disks due to disk winds". In: *ArXiv e-prints*. arXiv: 1804.01070 [astro-ph.EP].

Ormel, C. W. and H. Kobayashi (2012). "Understanding How Planets Become Massive. I. Description and Validation of a New Toy Model". In: *ApJ* 747, 115, p. 115. DOI: 10.1088/0004-637X/747/2/115. arXiv: 1112.0274 [astro-ph.EP].

Pepe, F. et al. (2011). "The HARPS search for Earth-like planets in the habitable zone. I. Very low-mass planets around HD 20794, HD 85512, and HD 192310". In: *A&A* 534, A58, A58. DOI: 10.1051/0004-6361/201117055. arXiv: 1108.3447 [astro-ph.EP].

Petigura, E. A., A. W. Howard, and G. W. Marcy (2013). "Prevalence of Earth-size planets orbiting Sun-like stars". In: *Proceedings of the National Academy of Science* 110, pp. 19273–19278. DOI: 10.1073/pnas.1319909110. arXiv: 1311.6806 [astro-ph.EP].

Petigura, E. A., A. W. Howard, G. W. Marcy, et al. (2017). "The California-Kepler Survey. I. High-resolution Spectroscopy of 1305 Stars Hosting Kepler Transiting Planets". In: *AJ* 154, 107, p. 107. DOI: 10.3847/1538-3881/aa80de. arXiv: 1703.10400 [astro-ph.EP].

Petigura, E. A., G. W. Marcy, et al. (2018). "The California-Kepler Survey. IV. Metal-rich Stars Host a Greater Diversity of Planets". In: *AJ* 155, 89, p. 89. DOI: 10.3847/1538-3881/aaa54c. arXiv: 1712.04042 [astro-ph.EP].

Petigura, E. A., E. Sinukoff, et al. (2017). "Four Sub-Saturns with Dissimilar Densities: Windows into Planetary Cores and Envelopes". In: *AJ* 153, 142, p. 142. DOI: 10.3847/1538-3881/aa5ea5. arXiv: 1702.00013 [astro-ph.EP].

Pollack, J. B. et al. (1996). "Formation of the Giant Planets by Concurrent Accretion of Solids and Gas". In: *Icarus* 124, pp. 62–85. DOI: 10.1006/icar.1996.0190.

Pu, B. and D. Lai (2018). "Eccentricities and Inclinations of Multi-Planet Systems with External Perturbers". In: *MNRAS*. DOI: 10.1093/mnras/sty1098. arXiv: 1801.06220 [astro-ph.EP].

Queloz, D. et al. (2009). "The CoRoT-7 planetary system: two orbiting super-Earths". In: *A&A* 506, pp. 303–319. DOI: 10.1051/0004-6361/200913096.

Raymond, S. N. (2006). "The Search for Other Earths: Limits on the Giant Planet Orbits That Allow Habitable Terrestrial Planets to Form". In: *ApJL* 643, pp. L131–L134. DOI: 10.1086/505596. eprint: astro-ph/0605136.

Raymond, S. N. and A. Izidoro (2017). "Origin of water in the inner Solar System: Planetesimals scattered inward during Jupiter and Saturn's rapid gas accretion". In: *Icarus* 297, pp. 134–148. DOI: 10.1016/j.icarus.2017.06.030. arXiv: 1707.01234 [astro-ph.EP].

Rice, W. K. M. et al. (2006). "Dust filtration at gap edges: implications for the spectral energy distributions of discs with embedded planets". In: *MNRAS* 373, pp. 1619–1626. DOI: 10.1111/j.1365-2966.2006.11113.x. eprint: astro-ph/0609808.

Rodriguez, D. R. et al. (2015). "Stellar multiplicity and debris discs: an unbiased sample". In: *MNRAS* 449, pp. 3160–3170. DOI: 10.1093/mnras/stv483. arXiv: 1503.01320 [astro-ph.SR].

Rousset, G. et al. (2003). "NAOS, the first AO system of the VLT: on-sky performance". In: *Adaptive Optical System Technologies II*. Ed. by P. L. Wizinowich and D. Bonaccini. Vol. 4839. Proc. SPIE, pp. 140–149. DOI: 10.1117/12.459332.

Rowan, D. et al. (2016). "The Lick-Carnegie Exoplanet Survey: HD 32963 - A New Jupiter Analog Orbiting a Sun-like Star". In: *ApJ* 817, 104, p. 104. DOI: 10.3847/0004-637X/817/2/104. arXiv: 1512.00417 [astro-ph.EP].

Sahlmann, J. et al. (2016). "The mass of planet GJ 676A b from ground-based astrometry. A planetary system with two mature gas giants suitable for direct imaging". In: *A&A* 595, A77, A77. DOI: 10.1051/0004-6361/201628854. arXiv: 1608.00918 [astro-ph.EP].

Sato, T., S. Okuzumi, and S. Ida (2016). "On the water delivery to terrestrial embryos by ice pebble accretion". In: *A&A* 589, A15, A15. DOI: 10.1051/0004-6361/201527069. arXiv: 1512.02414 [astro-ph.EP].

Schlaufman, K. C. and G. Laughlin (2010). "A physically-motivated photometric calibration of M dwarf metallicity". In: *A&A* 519, A105, A105. DOI: 10.1051/0004-6361/201015016. arXiv: 1006.2850 [astro-ph.EP].

Service, M. et al. (2016). "A New Distortion Solution for NIRC2 on the Keck II Telescope". In: *PASP* 128.9, p. 095004. DOI: 10.1088/1538-3873/128/967/095004.

Sinukoff, E. et al. (2017). "K2-66b and K2-106b: Two Extremely Hot Sub-Neptune-size Planets with High Densities". In: *AJ* 153, 271, p. 271. DOI: 10.3847/1538-3881/aa725f. arXiv: 1705.03491 [astro-ph.EP].

Suárez Mascareño, A. et al. (2017). "A super-Earth orbiting the nearby M dwarf GJ 536". In: *A&A* 597, A108, A108. DOI: 10.1051/0004-6361/201629291. arXiv: 1611.02122 [astro-ph.EP].

Tabachnik, S. and S. Tremaine (2002). "Maximum-likelihood method for estimating the mass and period distributions of extrasolar planets". In: *MNRAS* 335, pp. 151–158. DOI: 10.1046/j.1365-8711.2002.05610.x. eprint: astro-ph/0107482.

Tanner, A. M., C. R. Gelino, and N. M. Law (2010). "A High-Contrast Imaging Survey of SIM Lite Planet Search Targets". In: *PASP* 122, p. 1195. DOI: 10.1086/656481. arXiv: 1007.4315 [astro-ph.SR].

Torres, G. (1999). "Substellar Companion Masses from Minimal Radial Velocity or Astrometric Information: a Monte Carlo Approach". In: *PASP* 111, pp. 169–176. DOI: 10.1086/316313.

Tsiganis, K. et al. (2005). "Origin of the orbital architecture of the giant planets of the Solar System". In: *Nature* 435, pp. 459–461. DOI: 10.1038/nature03539.

Uehara, S. et al. (2016). "Transiting Planet Candidates Beyond the Snow Line Detected by Visual Inspection of 7557 Kepler Objects of Interest". In: *ApJ* 822, 2, p. 2. DOI: 10.3847/0004-637X/822/1/2. arXiv: 1602.07848 [astro-ph.EP].

Vogt, S. S., R. P. Butler, et al. (2005). "Five New Multicomponent Planetary Systems". In: *ApJ* 632, pp. 638–658. DOI: 10.1086/432901.

Vogt, S. S., R. A. Wittenmyer, et al. (2010). "A Super-Earth and Two Neptunes Orbiting the Nearby Sun-like Star 61 Virginis". In: *ApJ* 708, pp. 1366–1375. DOI: 10.1088/0004-637X/708/2/1366. arXiv: 0912.2599 [astro-ph.EP].

Wallace, J., S. Tremaine, and J. Chambers (2017). "Collisional Fragmentation Is Not a Barrier to Close-in Planet Formation". In: *AJ* 154, 175, p. 175. DOI: 10.3847/1538-3881/aa8c08. arXiv: 1705.08932 [astro-ph.EP].

Walsh, K. J. et al. (2011). "The Asteroid Belt and Mars' Small Mass Explained by Large-Scale Gas-Driven Migration of Jupiter". In: *Lunar and Planetary Science Conference*. Vol. 42. Lunar and Planetary Inst. Technical Report, p. 2585.

Weiss, L. M. and G. W. Marcy (2014). "The Mass-Radius Relation for 65 Exoplanets Smaller than 4 Earth Radii". In: *ApJL* 783, L6, p. L6. DOI: 10.1088/2041-8205/783/1/L6. arXiv: 1312.0936 [astro-ph.EP].

Whipple, F. L. (1972). "On certain aerodynamic processes for asteroids and comets". In: *From Plasma to Planet*. Ed. by A. Elvius, p. 211.

Wittenmyer, R. A., R. P. Butler, et al. (2016). "The Anglo-Australian Planet Search XXIV: The Frequency of Jupiter Analogs". In: *ApJ* 819, 28, p. 28. DOI: 10.3847/0004-637X/819/1/28. arXiv: 1601.05465 [astro-ph.EP].

Wittenmyer, R. A., M. Tuomi, et al. (2014). "GJ 832c: A Super-Earth in the Habitable Zone". In: *ApJ* 791, 114, p. 114. DOI: 10.1088/0004-637X/791/2/114. arXiv: 1406.5587 [astro-ph.EP].

Wolfgang, A. and E. Lopez (2015). "How Rocky Are They? The Composition Distribution of Kepler's Sub-Neptune Planet Candidates within 0.15 AU". In: *ApJ* 806, 183, p. 183. DOI: 10.1088/0004-637X/806/2/183. arXiv: 1409.2982 [astro-ph.EP].

Wright, J. T. et al. (2004). "Chromospheric Ca II Emission in Nearby F, G, K, and M Stars". In: *ApJS* 152, pp. 261–295. DOI: 10.1086/386283. eprint: astro-ph/0402582.

Yasui, C. et al. (2010). "Short Lifetime of Protoplanetary Disks in Low-metallicity Environments". In: *ApJL* 723, pp. L113–L116. DOI: 10.1088/2041-8205/723/1/L113. arXiv: 1010.1668 [astro-ph.SR].

Youdin, A. N. and E. I. Chiang (2004). "Particle Pileups and Planetesimal Formation". In: *ApJ* 601, pp. 1109–1119. DOI: 10.1086/379368. eprint: astro-ph/0309247.

Zhu, W. et al. (2018). "About 30% of Sun-like Stars Have Kepler-like Planetary Systems: A Study of their Intrinsic Architecture". In: *ArXiv e-prints*. arXiv: 1802.09526 [astro-ph.EP].

Chapter 6

SUMMARY AND FUTURE DIRECTIONS

6.1 Summary

This thesis explores the impact of outer gas giant planets on inner exoplanet systems, and probes the origins of supermassive gas giant planets at wide separations. To address these questions, we used radial velocity, direct imaging, and high-resolution spectroscopy techniques in four distinct studies.

In Chapter 2, we describe a dedicated search for massive, long-period companions to 123 known exoplanetary systems using the radial velocity method. In addition to detecting eight new long-period planets, we found 20 systems with statistically significant RV trends. After using AO imaging to rule out stellar companions as the source of the trends, we used these data to produce the first statistical analysis of the frequency of outer gas giant companions in systems hosting inner gas giant planets. These companions appear to be common, with an occurrence rate of 52±5% for planets between 1 - 20 M_{Jup} and 5 - 20 AU. When we split the sample into systems that had inner hot Jupiters (a<0.1 AU), inner warm Jupiters (0.1<a<1AU), and inner cold Jupiters (1<a<5AU), we found that systems hosting hot Jupiters are more likely than warm and cold Jupiters (2.3σ and 2.4σ respectively) to have an outer gas giant companion. This enhanced companion fraction for short-period planets is consistent with the predictions of dynamical migration models. Alternatively, this enhanced companion fraction could indicate that hot Jupiters are found in disks that were particularly efficient at producing gas giant planets. Although most hot Jupiters have tidally circularized orbits, we found that planets between 0.1-5 AU in multi-body systems have higher average eccentricities than isolated planets. While previous studies found that multi-planet systems have lower eccentricities, they were typically only sensitive to a 1 M_{Jup} planet out to 3-5 AU, in comparison to our survey completeness out to 20 AU. Thus if the separation between inner and outer planets is larger for cases where the inner planet has a large eccentricity, many of the multi-body systems detected in our survey would have been misclassified as single planet systems in these previous surveys. This result suggests that dynamical interactions among gas giant planets play an important role in the evolution of most planetary systems, not just those with hot Jupiters.

Chapter 3 discusses our first look into the formation histories of wide-separation planetary-mass companions. One possible solution is to argue that these planets did not form in situ, but were instead scattered outward from their original formation locations via interactions with another body in the system. With this hypothesis in mind, beginning in 2014 we carried out a near-infrared imaging survey using NIRC2 at Keck to search for close-in substellar companions to a sample of seven systems with confirmed planetary-mass companions on wide orbits. While we initially identified eight candidate companions, a second epoch of astrometry confirmed all eight to be background objects. From these new epochs of astrometry we also found that two of the previously confirmed companions showed evidence for orbital motion, which we used to place constraints on their orbital eccentricities. We found that the eccentricity distributions for both companions favored low to moderate eccentricities, contradicting predictions from scattering simulations. Taken together, these two pieces of evidence present a compelling argument against scattering as the explanation for the wide orbits of these planetary-mass companions.

Chapter 4 describes a study where we used near-IR high-resolution spectroscopy to measure rotational line broadening of three young (2-300 Myr) planetary-mass companions and combined these measurements with published rotation rates for two additional companions to provide the first look at the spin distribution of these objects. We compared this distribution to complementary rotation rate measurements for six brown dwarfs with masses < 20 M_{Jup} (three of which we measured) to determine whether there was any systematic offset between the two sets of rotation rates. We found that these spin distributions are indistinguishable, suggesting either that these two populations formed via the same mechanism, or that processes regulating rotation rates are largely independent of formation history. We also found that the rotation rates for both populations are well below their break-up velocities and do not evolve significantly during the first few hundred million years after the end of accretion. This suggests that rotation rates are set early in a planetary-mass object's lifetime, possibly by interactions with a circumplanetary disk. Although we would expect both bound and free-floating planetary-mass objects to host such disks, previous models had suggested that their properties might vary depending on formation mechanism and/or birth environment; these observations therefore place constraints on the disk properties of these two populations. This result has important implications for our understanding of the processes regulating the angular momentum evolution of young planetary-mass objects, and of the physics of gas accretion and disk coupling in the planetary-mass regime.

In Chapter 5, we use radial velocity observations to search for massive, long-period gas giant companions in 65 systems hosting inner super-Earth ($1 - 4$ $R_\oplus$, $1 - 10$ $M_\oplus$) planets in order to constrain formation and migration scenarios for this population. We consistently re-fit all published radial velocity datasets for these stars and find 10 systems with statistically significant trends indicating the presence of an outer companion. We combine these radial velocity data with AO images in order to constrain the allowed masses and semi-major axes of these companions. We quantify our sensitivity to the presence of long period companions in these system by fitting the sample with a power law distribution and find an estimated occurrence rate of 39±7% for companions between $0.5 - 20$ M_{Jup} and $1 - 20$ AU. Half of our systems were discovered by the transit method and the other half were discovered by the RV method. While differences in RV baselines and number of data points between the two samples lead to different sensitivities to distant companions, we find that the occurrence rates of gas giant companions in each sample is consistent at the 0.5σ level. A quantitative comparison to previous determinations of the frequency of Jupiter analogs indicates that the occurrence rate of Jupiter analogs in super-Earth systems appears to be higher than the occurrence rate of gas giant planets around field stars. We conclude that the presence of outer gas giant planets does not suppress the formation of inner super-Earths, and may instead facilitate their formation. The presence of these outer companions also places an upper limit on the distance super-Earths in these systems might have migrated from their formation locations, as well as the range of migration the gas giant companions could have experienced.

6.2 Future Directions

Leveraging the suite of observational techniques developed over the course of this thesis, I look to exciting new directions that can be explored.

High-Resolution Spectroscopy: Measuring Atmospheric Abundances and Rotation Rates

One avenue that I plan on developing is harnessing near-IR high-resolution spectroscopy to study the atmospheric compositions of directly imaged, wide-separation planetary-mass companions. Clues to past formation histories are imprinted on these spectra — while the core accretion model predicts planets should have non-stellar atmospheric carbon to oxygen (C/O) ratios and metallicities, in both the disk instability and turbulent fragmentation models the planet interior and atmosphere

are formed simultaneously with a stellar C/O ratio (Alibert et al., 2005; Guillot and Hueso, 2006). While attempts have been made to place constraints on atmospheric compositions of directly imaged planets at lower resolutions (R~<4000), these studies have all been hindered by degeneracies due to the presence of high altitude cloud layers in many of the objects, which limit achievable abundance constraints (Konopacky et al., 2013; Barman et al., 2015; Lavie et al., 2017). The advantage of going to higher resolutions is that individual molecular lines can be resolved, and thus abundances can be determined directly from ratios of line depths, breaking degeneracies with cloud properties. I will use NIR high-resolution spectra to compare the atmospheric C/O ratios of directly imaged companions to those of their host stars, thereby placing stringent constraints on their possible origins.

This line of investigation is aided by planned developments for instruments and telescopes. For example, the imminent NIRSPEC upgrade will increase the spectral resolution from R~25,000 to R~37,500, enabling greater precision on abundance constraints. On a longer timescale, there are ongoing efforts with multiple instruments to couple high contrast imaging with high-resolution spectroscopy (e.g. KPIC + NIRSPEC at Keck, SPHERE + CRIRES on the VLT, and SCExAO + IRD on Gemini). These efforts are ideally suited for high-resolution abundance studies of young planets, and will enable observations of lower mass planets at smaller separations.

Another direction I plan to continue to explore is expanding my sample of rotation rate measurements in the planetary mass regime. Using the same high-resolution NIR spectra as examined to constrain atmospheric abundances, I will more than double the number of planets with measured rotational line broadening in order to investigate how rotation rates vary as a function of orbital separation. Because the various competing formation mechanisms each operate more effectively at a different range of orbital separations, this study will allow me to determine whether this population is consistent with formation via a single channel or is instead a mixture of several. With this larger sample size I can also explore how rotation rates of bound planetary-mass companions vary based on companion to star mass ratio. Because the different formation mechanisms produce companions more effectively with different companion to star mass ratios, assessing how rotation rates vary with mass ratio will also shed light on whether these companions form via one or more formation mechanisms. Additionally, since many of the directly imaged planetary-mass companions that have been discovered to date are young (<10 Myr

old), more than doubling the number of rotation rate measurements at these early ages will allow me to place novel constraints on the initial scatter in rotation rates. In Bryan et al. (2018) I found that based on the angular momentum evolution of planetary-mass objects, spin is set very early on in the planetary mass regime. It then seems possible that measuring the scatter of rotation rates at early ages will place interesting constraints on the mechanism responsible for regulating and setting these spins.

As with the line of investigation into atmospheric compositions, upcoming instruments both short and long term will benefit these efforts. The NIRSPEC upgrade to higher resolution will enable greater precision of these rotation rate measurements, and the future coupling of high contrast imaging with high-resolution spectroscopy as well as high-resolution spectrographs on future 30-meter class telescopes will allow me to measure rotation rates of smaller, closer-in directly imaged planetary-mass companions.

Direct Imaging: Probing Smaller Masses At Smaller Separations

New and upcoming advances in state-of-the-art imaging techniques are expanding the parameter space accessible to direct imaging. One avenue that I will leverage in the immediate future is to use the recently commissioned vector vortex coronagraph (Mawet et al., 2013) in L-band with NIRC2 at Keck to obtain deep images of ∼100 members of the Taurus star forming region. Both the young age of Taurus (1 - 3 Myr old) (Kraus et al., 2011) and the shift to L-band (young planets are brighter in L-band than K-band), enable greater sensitivities to smaller masses. Furthermore, the inner working angle (IWA) of the vortex coronagraph is 0.07 arcseconds. Given a distance of 145 pc to Taurus, this translates to a physical separation of only ∼10 AU. For comparison, the IWA of the coronagraph used in the survey described in Chapter 3 is 0.3 arcseconds, which would translate to a physical separation of ∼45 AU. Taken together, the choice of star forming region plus instrumentation will allow me to consistently probe masses as small as 1 - 2 M_{Jup} outside 20 AU, making this the deepest direct imaging survey to date. While Taurus has been targeted by previous imaging surveys, this one will be sensitive to substantially lower masses at smaller separations, probing new regions of parameter space and potentially providing new targets for detailed characterization studies.

Radial Velocities: Gas Giant Frequencies in Terrestrial and Ice Giant Systems

I will further investigate the role gas giants play in shaping inner exoplanet systems by adapting the statistical framework presented in chapters 2 and 5 to determine the frequency of gas giant planets in systems with terrestrial and ice giant planets. These occurrence rates can inform questions such as: Are gas giant companions more common in systems with low-density, volatile-rich inner planets or those with rocky planets? For systems with inner transiting gas giant planets, how does the presence of an outer companion affect the inner planet's core mass fraction? More broadly, these statistical conclusions will allow me to constrain the extent to which gas giants interact with and impede the flow of material into inner regions of the disk, as well as the subsequent dynamical evolution of these systems.

These kinds of studies require statistical leverage to reach robust conclusions. The statistical significance of an individual radial velocity trend is determined by the time baseline of the observations, the number of observations taken, and the uncertainties on each observation, while the significance of the overall statistical analysis is dependent on the number of systems in the sample of interest. In addition to the current state-of-the-art precision RV instruments (i.e. HIRES, HARPS, HARPS-N, APF), in the next few years there will be even more new RV instruments coming online (i.e. HPF, SPIRou, NIRPS, NEID, ESPRESSO). The combination of new targets from TESS with this significant increase in resources to follow up many of these systems will lead to a wealth of RV data for new systems as well as the necessary statistical leverage to answer these questions. Furthermore, as RV baselines on systems increase, I can use these RV trends to probe system architectures farther and farther away from the host stars. These RV trend studies provide our best chance of overlapping in mass/semi-major axis parameter space with direct imaging studies.

References

Alibert, Y. et al. (2005). "Models of giant planet formation with migration and disc evolution". In: *A&A* 434, pp. 343–353. DOI: 10.1051/0004-6361:20042032. eprint: astro-ph/0412444.

Barman, T. S. et al. (2015). "Simultaneous Detection of Water, Methane, and Carbon Monoxide in the Atmosphere of Exoplanet HR8799b". In: *ApJ* 804, 61, p. 61. DOI: 10.1088/0004-637X/804/1/61. arXiv: 1503.03539 [astro-ph.EP].

Bryan, M. L. et al. (2018). "Constraints on the spin evolution of young planetary-mass companions". In: *Nature Astronomy* 2, pp. 138–144. DOI: 10.1038/s41550-017-0325-8. arXiv: 1712.00457 [astro-ph.EP].

Guillot, T. and R. Hueso (2006). "The composition of Jupiter: sign of a (relatively) late formation in a chemically evolved protosolar disc". In: *MNRAS* 367, pp. L47–L51. DOI: 10.1111/j.1745-3933.2006.00137.x. eprint: astro-ph/0601043.

Konopacky, Q. M. et al. (2013). "Detection of Carbon Monoxide and Water Absorption Lines in an Exoplanet Atmosphere". In: *Science* 339, pp. 1398–1401. DOI: 10.1126/science.1232003. arXiv: 1303.3280 [astro-ph.EP].

Kraus, A. L. et al. (2011). "Mapping the Shores of the Brown Dwarf Desert. II. Multiple Star Formation in Taurus-Auriga". In: *ApJ* 731, 8, p. 8. DOI: 10.1088/0004-637X/731/1/8. arXiv: 1101.4016 [astro-ph.SR].

Lavie, B. et al. (2017). "HELIOS-RETRIEVAL: An Open-source, Nested Sampling Atmospheric Retrieval Code; Application to the HR 8799 Exoplanets and Inferred Constraints for Planet Formation". In: *AJ* 154, 91, p. 91. DOI: 10.3847/1538-3881/aa7ed8. arXiv: 1610.03216 [astro-ph.EP].

Mawet, D. et al. (2013). "L'-band AGPM vector vortex coronagraph's first light on VLT/NACO. Discovery of a late-type companion at two beamwidths from an F0V star". In: *A&A* 552, L13, p. L13. DOI: 10.1051/0004-6361/201321315. arXiv: 1304.0930 [astro-ph.IM].